1-1-2015

Protein Dynamics and Entropy: Implications for Protein-Ligand Binding

Kyle William Harpole
University of Pennsylvania, kharpole@mail.med.upenn.edu

Recommended Citation

Harpole, Kyle William, "Protein Dynamics and Entropy: Implications for Protein-Ligand Binding" (2015). *Publicly Accessible Penn Dissertations*. 1756.
http://repository.upenn.edu/edissertations/1756

Protein Dynamics and Entropy: Implications for Protein-Ligand Binding

Abstract

The nature of macromolecular interactions has been an area of deep interest for understanding many facets of biology. While a great deal of insight has been gained from structural knowledge, the contribution of protein dynamics to macromolecular interactions is not fully appreciated. This plays out from a thermodynamic perspective as the conformational entropy. The role of conformational entropy in macromolecular interactions has been difficult to address experimentally. Recently, an empirical calibration has been developed to quantify the conformational entropy of proteins using solution NMR relaxation methods. This method has been demonstrated in two distinct protein systems. The goal of this work is to expand this calibration to assess whether conformational entropy can be effectively quantified from NMR-derived protein dynamics. First, we demonstrate that NMR dynamics do not correlate well between the solid and solution states, suggesting that the relationship between the conformational entropy of proteins is limited to solution state-derived NMR dynamics. We hypothesize that this may be partially due to the role of hydration of the protein in its dynamics. Next, we expand our empirical calibration to over 30 distinct protein systems and demonstrated that the relationship between NMR dynamics and conformational entropy is both robust and general. Furthermore, we demonstrate that conformational entropy plays a significant role in macromolecular interactions. Using our empirical calibration, we then look to address if conformational entropy could be an important contribution to drug design. The latter process is often a brute force approach, and subsequent optimization of initial drug candidates is often a guess and check process. In silico drug design was thought to offer a more efficient and rational approach, but often relies on static structures. This minimizes or completely neglects the role that conformational entropy may play in binding. Here we experimentally determine the role of conformational entropy in the drug target p38a MAPK in binding to two potent inhibitors. We demonstrate evidence that conformational entropy may represent a tunable parameter in affinity optimization of lead compounds. This has important implications for lead optimization and strongly suggests that the role of conformational entropy be considered in drug design efforts.

Degree Type
Dissertation

Degree Name
Doctor of Philosophy (PhD)

Graduate Group
Biochemistry & Molecular Biophysics

First Advisor
A. Joshua Wand

Keywords
Drug Design, Entropy, Protein Dynamics, Protein-Ligand Binding

Subject Categories
Biochemistry | Biophysics

PROTEIN DYNAMICS AND ENTROPY: IMPLICATIONS FOR PROTEIN-LIGAND BINDING

Kyle William Harpole

A DISSERTATION

in

Biochemistry and Molecular Biophysics

Presented to the Faculties of the University of Pennsylvania

in

Partial Fulfillment of the Requirements for the

Degree of Doctor of Philosophy

2015

Supervisor of Dissertation

____

A. Joshua Wand, Ph.D., Benjamin Rush Professor of Biochemistry and Biophysics

Graduate Group Chairperson

____

Kim A. Sharp, Ph.D., Associate Professor

Dissertation Committee

Ronen Marmorstein, Ph.D., Professor of Biochemistry and Biophysics
Yale E. Goldman MD, Ph.D., Professor of Physiology
Jeffery G. Saven, Professor of Chemistry
Kim A. Sharp, Ph.D., Associate Professor of Biochemistry and Biophysics
Gregory D. Van Duyne, Ph.D., Jacob Gershon-Cohen Professor of Medical Science
Andrew L. Lee, Ph.D., Professor, Division of Chemical Biology and Medicinal Chemistry

PROTEIN DYNAMICS AND ENTROPY: IMPLICATIONS FOR PROTEIN-LIGAND BINDING

Kyle William Harpole

To my wife, Grace, for her unyielding love and support.

ACKNOWLEDGMENT

First, I must acknowledge my thesis mentor, Josh Wand, for all of his guidance and support over the course of my graduate career. I imagine that being a successful mentor takes a number of essential skills. The mentor must be patient. The mentor must also challenge. Often the mentor must also do both simultaneously. However, I feel that one of the marks of a great mentor is to believe in their students and the work they do, even when the student may not believe in themselves at times. This is something that Josh has done for me on various occasions, and I will always owe a great deal of success to him in this regard. I also wish to thank Kathy Valentine for teaching me the basics of NMR as a technique. I must also thank her for her support and assistance, both scientific and otherwise. Like Josh, she has dedicated a good deal of her career to foster both the scientific and personal development of all members of the lab. I thank my committee – Ronen Marmorstein, Yale Goldman, Jeff Saven, and Kim Sharp, for challenging my ideas and pushing me in the direction of good science. Also thanks to Greg Van Duyne for supplementing my committee for the final defense and Andrew Lee for serving as an external examiner. I thank the members of the Wand Laboratory, both past and present. I must especially thank a few members of the lab who played a variety of important roles: Jakob Dogan and Vonni Moorman for assistance during the early days of my graduate career, Christine Jorge for her insightful discussion but also for her knowledge of the table of contents function in Microsoft Word. I thank Bryan Marques, Jack Wee Lim, Nathaniel Nucci, Evan O'Brien, Alfredo Caro, and fellow Oklahoma expat Brian Fuglestad for helpful scientific discussions. I thank Matt Stetz for his deep knowledge of NMR relaxation. Special thanks to him for the development of pulse sequences and software that had a significant positive impact on the lab as a whole, including many crucial aspects of this dissertation. I thank Vignesh Kasinath, fellow architect of the entropy meter, for discussion of conformational entropy and all aspects of life, several of which were, like both of us, a bit quirky. I thank Sabrina Bédard for all-around support in all aspects of my graduate career.

Further thanks to BMB administrators extraordinaire, Ruth Keris and Angie Young. You made me blissfully unaware of all of the paperwork that I must have required. I must thank several friends, especially Sandya Ajith, Helen Chen, Rob Culik, Sam Getchell , and Bridgin Lee for their support during the mutual endeavor of graduate school. I also thank a number of folks that served in various capacities toward my scientific development. Old mentors and colleagues from summers doing research at ConocoPhillips: Bernie Baldwin, James Howard, Jim Stevens , Amy Briggs, and Rachel Stryffeler. Coming from those 2 MHz magnets, I can truly say that I have come from humble magnetic beginnings. Mentors and colleagues from my undergraduate research lab at the University of Iowa: Heejin Lee, Sean Gu, and Lawrence Gray, and my undergraduate advisor Shahram Khademi.

Of course, I would not be where I am without the unconditional love and support of my parents. My father, always the inquisitive engineer, sought to understand the details of my research and even playfully challenge it at times. I like to think that he only saw a prototypical version of the ‘entropy meter’ (Chapter 3) and, upon reviewing this work, is now more or less convinced that it is real. My mother’s support was also always important, even when she didn’t understand precisely what it was I was doing, she always encouraged me to discover great things. I believe that the work enclosed provides a great deal of support for these wishes.

Finally, I must thank my wife Grace. She has seen me through the latter half of my graduate career and all that it has entailed. She played a crucial role in this work, though no scientific contributions were offered. Her role in my personal development is easily of comparable magnitude to the role that Josh played in my professional development. My life would be far more entropic without her.

ABSTRACT

PROTEIN DYNAMICS AND ENTROPY: IMPLICATIONS FOR PROTEIN-LIGAND BINDING

Kyle William Harpole

A. Joshua Wand, Ph.D.

The nature of macromolecular interactions has been an area of deep interest for understanding many facets of biology. While a great deal of insight has been gained from structural knowledge, the contribution of protein dynamics to macromolecular interactions is not fully appreciated. This plays out from a thermodynamic perspective as the conformational entropy. The role of conformational entropy in macromolecular interactions has been difficult to address experimentally. Recently, an empirical calibration has been developed to quantify the conformational entropy of proteins using solution NMR relaxation methods. This method has been demonstrated in two distinct protein systems. The goal of this work is to expand this calibration to assess whether conformational entropy can be effectively quantified from NMR-derived protein dynamics. First, we demonstrate that NMR dynamics do not correlate well between the solid and solution states, suggesting that the relationship between the conformational entropy of proteins is limited to solution state-derived NMR dynamics. We hypothesize that this may be partially due to the role of hydration of the protein in its dynamics. Next, we expand our empirical calibration to over 30 distinct protein systems and demonstrate that the relationship between NMR dynamics and conformational entropy is both robust and general. Furthermore, we demonstrate that conformational entropy plays a significant role in macromolecular interactions. Using our empirical calibration, we then look to address if conformational entropy could be an important contribution to drug design. The latter process is often a brute force approach, and subsequent optimization of initial drug candidates is often a guess and check process. *In silico* drug design was thought to offer a more efficient and rational approach, but often relies on static structures. This minimizes or completely neglects the role that conformational entropy may play in binding. Here we experimentally determine the role of conformational entropy in the drug target p38a MAPK in binding to two potent inhibitors. We demonstrate evidence that conformational entropy may represent a tunable parameter in affinity optimization of lead compounds. This has important implications for lead optimization and strongly suggests that the role of conformational entropy be considered in drug design efforts.

TABLE OF CONTENTS

LIST OF TABLES

LIST OF FIGURES

CHAPTER 1: Introduction

Proteins and their interactions

Proteins power even the most basic functions of our cells. A seemingly simple polymer comprised of twenty amino acids has vast importance in the promotion of life. The prevalence of biophysical techniques such as X-ray crystallography and, more recently, protein NMR spectroscopy have allowed an unprecedented look into the intricacies of these molecules on an atomic level. This has revolutionized the field as we strive to deeply understand the world around us and, to a great extent, within us. Yet still we strive for a deeper understanding of these molecules known as proteins. Proteins demonstrate much of their functional prowess in the cell as part of a network where associations with other molecules (ions, small molecules, nucleic acids, and other proteins) power the cell through a multitude of functions. The models by which proteins interact with other molecules have evolved significantly, from the early 'lock-and-key' model to the 'induced-fit' and later the 'conformational selection' model [1-3]. While these models help us visualize the nature of protein-ligand interactions, the association of protein and their ligands is ultimately dictated by the Gibbs-Helmholtz equation:

$$\Delta G = \Delta H - T\Delta S \qquad \text{Equation 1-1}$$

This equation is fundamental to protein-ligand association. The free energy, ΔG, which dictates the affinity, is expressed in terms of the change in enthalpy (ΔH) and entropy ($-T\Delta S$) resulting from a binding event. The understanding of these relative contributions has been the subject of extensive study in the field of biology. Of these two thermodynamic quantities, far more is understood about the enthalpic contributions of binding, which has been greatly enhanced by three dimensional structures of proteins in complex with their ligands [4]. The components of the enthalpy include van der Waals interactions as well as hydrogen bonding and other electrostatic interactions [5]. The entropy has remained far more nebulous to understand in the context of biology, often because it is difficult to measure experimentally. Despite this, entropy plays a fundamental role in the thermodynamics of the world around us and has recently been invoked to explain a new theory on the origin of life [6]. This highlights the fact that a detailed knowledge of entropy is essential for completing the thermodynamic understanding of macromolecular association. Calorimetric methods such as ITC are able to indirectly determine entropy [7], but cannot provide detailed information about its individual components. The major components of entropy in macromolecular interactions are outlined below:

$$-T\Delta S = -T\left[\Delta S_{solvent} + \Delta S_{conf} + \Delta S_{RT}\right] \qquad \text{Equation 1-2}$$

In Equation 1-2, $\Delta S_{\mathrm{solvent}}$,ΔS_{conf}, and ΔS_{RT} represent the solvent entropy, conformational entropy, and rotational-translation (RT) entropy, respectively. In the context of protein-ligand binding, solvent entropy in the form of the hydrophobic effect was historically thought to dwarf other contributions [8]. Changes in conformational and RT entropy were considered to be negligible. This view has evolved, as several theoretical and experimental measurements have argued that solvent entropy only represents part of the entropic equation and that contributions from conformational entropy and RT entropy cannot be simply ignored [9-14].

Of particular interest in this dissertation is the contribution of conformational entropy to protein-ligand association. This quantity has hitherto resisted experimental measurement. The conformational entropy of proteins is intrinsically linked to their dynamics. NMR relaxation techniques can provide site-specific dynamic information and is uniquely positioned to probe this thermodynamic quantity.

Solution NMR relaxation as a tool to study protein dynamics

It is well known that proteins, as polymers in solution, are not static. In fact, they are quite dynamic on a multitude of timescales [15]. The dynamic timescales at which NMR provides dynamic information are vast, ranging from picoseconds to hours or even days. (Figure 1-1). This allows for the collection of detailed dynamic information that has been invaluable for understanding protein folding and function [16-20].

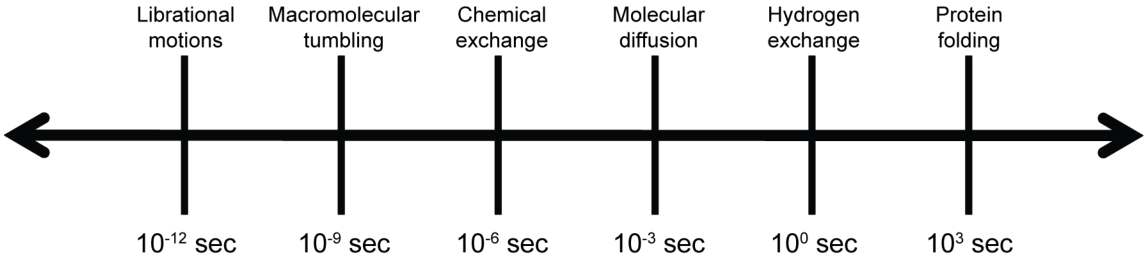

Figure 1-1: Timescales and motions of proteins that NMR can report on.

Here we are interested in motions occurring on the ps-ns timescale, which can be probed by solution NMR spin relaxation techniques. The relaxation of nuclear spins inherently contains information about the dynamics of both the overall protein molecule and the individual bond vectors within the protein. Spin relaxation occurs through a variety of mechanisms depending on the nucleus being probed. The primary relaxation mechanisms considered here are dipole-dipole interactions, chemical shift anisotropy, and (in the case of ^{2}H nuclei) quadrupolar relaxation. The measured relaxation rates have well defined dependencies on the underlying spectral density function, J , which corresponds to the probability of motions occurring at a given Larmor frequency, ω. Appendix A outlines the spectral density equations for the relaxation mechanisms outlined in this dissertation. It was shown over three decades ago by Lipari and Szabo [21] that J(ω) for isotropic motion is defined as:

$$J(\omega) = \frac{2}{5}\left(\frac{O^2\tau_m}{1+(\tau_m\omega)^2} + \frac{(1-O^2)\tau}{1+(\tau\omega)^2}\right), \text{ where } \frac{1}{\tau} = \frac{1}{\tau_m} + \frac{1}{\tau_e} \qquad \text{Equation 1-3}$$

In Equation 1-3, τ_m refers to the overall rotational correlation time of the molecule, O^2 is the squared generalized order parameter (described below), and τ_e refers to the rate of motion described by the order parameter. The Lipari-Szabo order parameter, O^2, represents the degree of flexibility of a given bond vector in the context of the molecular frame. O^2 can range in value from 0, indicating completely isotropic disorder with respect to the molecular frame, to 1, indicating no internal motion of the bond vector. Of particular interest here is the squared generalized order parameter O^2, as it represents the degree of motion of an individual bond vector in the context of the molecular frame. More formally, the order parameter is the secondorder Legendre polynomial of cosine θ, where θ is the tip angle. A more intuitive way of considering the order parameter is that it is the limiting value of the autocorrelation function of a given bond vector's position at infinite time (Figure 1-2). The area under the curve (τ_e) represents the timescale of fluctuations of the bond vector. By measuring multiple nuclear spin relaxation rates at different magnetic fields (ω) and fitting Equation 1-3, one is able to obtain information about the overall motions of the protein (τ_m) as well as information about the overall motions of the molecules (τ_e, O^2). We now consider how solution NMR relaxation studies of proteins can be used to characterize these motions.

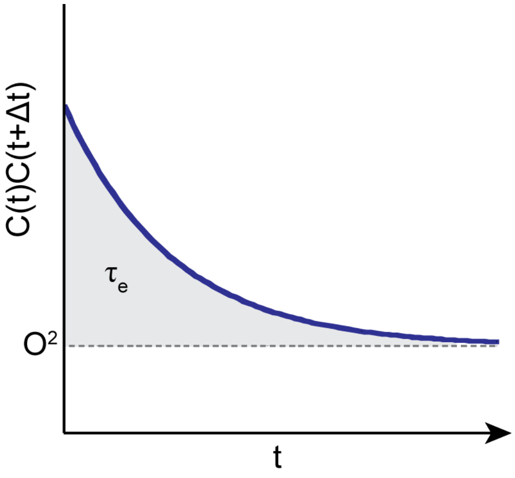

Figure 1-2: Illustration of O^2.
The autocorrelation function of bond vector position at infinite time converges to the value of O^2.

Backbone and methyl side chain order parameters

Experimentally, the order parameters of the backbone and methyl side chains are probed. Recently, methods have been developed to measure the order parameters of aromatic side chains [22], though these will not be discussed here. The order parameters of the amide backbone are obtained from the ^{15}N T_1 and T_2 rates as well as the H-N steady-state NOE. It is well established that the motions of the protein backbone are highly restricted by any sort of secondary structural element. Typically the only dynamic regions of the

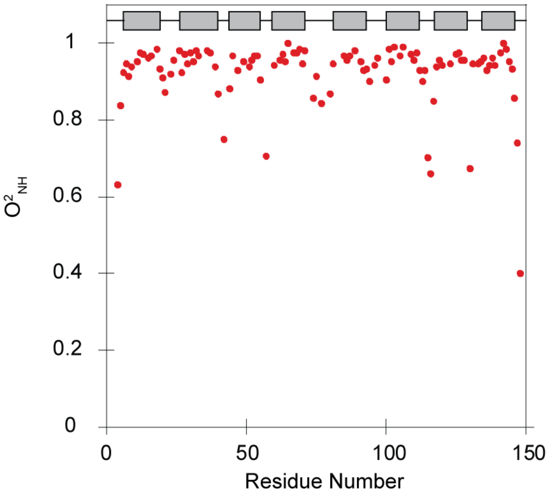

Figure 1-3: Backbone order parameters of the calmodulin:smMLCK(p) complex.
Secondary structure elements (helices) are shown in grey.

backbone are in the termini of the protein and in unstructured regions such as loops (Figure 1-3). While some insight can be obtained through changes in backbone dynamics, recent simulations have suggested the changes in backbone order parameter (O^2_{NH}) upon ligand binding are often very small and contribute little to the change in entropy, which is of interest here [23].

Motions of the methyl side chains are typically obtained through either ^2H or ^{13}C relaxation techniques. The relaxation of amides relies on a relatively simple AX spin system (where A=^{15}N and X=^1H_N). Methyl groups, however, are natively an AX_3 spin system. This significantly complicates the relaxation mechanism. For experimental simplicity, the spin systems of methyl groups are reduced to an AXY_2 spin system. In the case of ^2H relaxation, the CH_2D isotopomer is selectively enriched (A=^{13}C,X=^2H, Y=^1H). In this case, the underlying relaxation mechanism is dominated by the quadrupolar relaxation, with very minor (~2.5%) contributions from dipole-dipole relaxation from the ^1H atoms in the methyl group [24]. Because of the simplicity of analysis and relative affordability of reagents, ^2H relaxation is often the ideal method for measuring side chain dynamics of proteins. These experiments, however, are quite sensitive to the macromolecular tumbling of the molecule. For molecules with a molecular tumbling time longer than ~20ns, INEPT-based coherence transfers in these experiments compete strongly with the rapid T_2 relaxation that is characteristic of slowly tumbling molecules. This leads to a severe degradation of the signal. For this reason, ^{13}C relaxation methods can be employed for large proteins [25]. These experiments rely on the relaxation properties of the CHD_2 isotopomer (AX_2Y; A=^{13}C,X=^2H,Y=^1H). In this case, the relaxation mechanism of the ^{13}C-H spin pair is dominated by dipolar and CSA interactions. The bonded ^2H nuclei do not significantly affect the dipolar reactions of the ^{13}C spin. A detailed review of these and other methods for measuring side chain dynamics can be found elsewhere [16].

The order parameters of methyl groups are often considered with respect to the methyl symmetry axis (O^2_{axis}) [16]. It has been shown that, in contrast to the backbone, the methyl side chains display a manifold of order parameters (Figure 1-4). One might intuit that methyl order parameters show a correlation to metrics such as crystallographic B-factor or burial depth.

Igumenova *et al.* have examined several factors such as this and no correlation has been observed [16]. Thus the motions of protein methyl side chains have been shown to be quite non-intuitive.

The distribution of methyl order parameters across a protein has been shown to be tri-Gaussian [26]. This observation was recently corroborated by using a Bayesian approach to show that methyl order parameters segment into three distinct dynamic "bands" [27]. The so-called J-class is distinguished by extensive rotamer interconversion on the ps-ns timescale that results in O^2_{axis} values centered on ~0.35, while the ω-class corresponds to highly restricted motion within a single and likely narrower rotameric well potential that gives rise to O^2_{axis} values centered on ~0.8 [16, 27]. An intermediate class, with O^2_{axis} values centered on ~0.5, involves larger amplitude motion within a rotamer well that is accompanied by limited rotameric barrier crossing [27]. The relative population of each class varies significantly across proteins, even for the same protein involved in various complexes [10, 16, 27] (Figure 1-5). This dynamic banding can be rationalized in terms of packing interactions, which naturally lead to a segregation of order parameters.

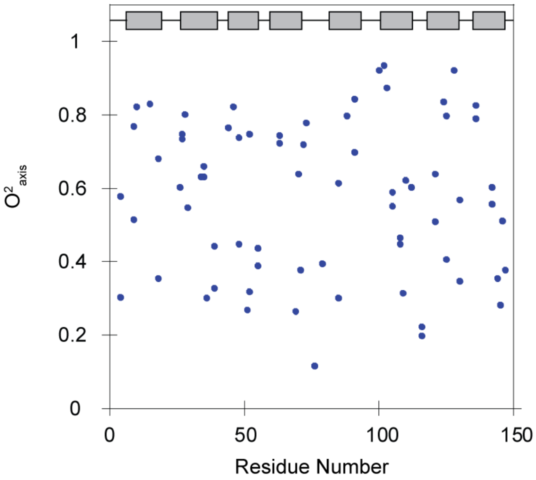

Figure 1-4: Side chain methyl order parameters of the calmodulin:smMLCK(p) complex.
Secondary structure elements (helices) are shown in grey.

Measurement of conformational entropy from protein dynamics

As the order parameter reports on localized bond fluctuations, there is an intuitive connection between the order and the conformational entropy of a protein. Different approaches have been taken to establish a relationship between the order parameter and conformational entropy. Various motional models including a harmonic oscillator and an infinite square well potential have been invoked, leading to initial quantifications of the conformational entropy [28-29]. These theoretical measurements laid the groundwork for quantification of protein entropy using NMR dynamics as a proxy for conformational entropy. This relationship was first explored by Frederick *et al.*, who used the harmonic oscillator model to determine

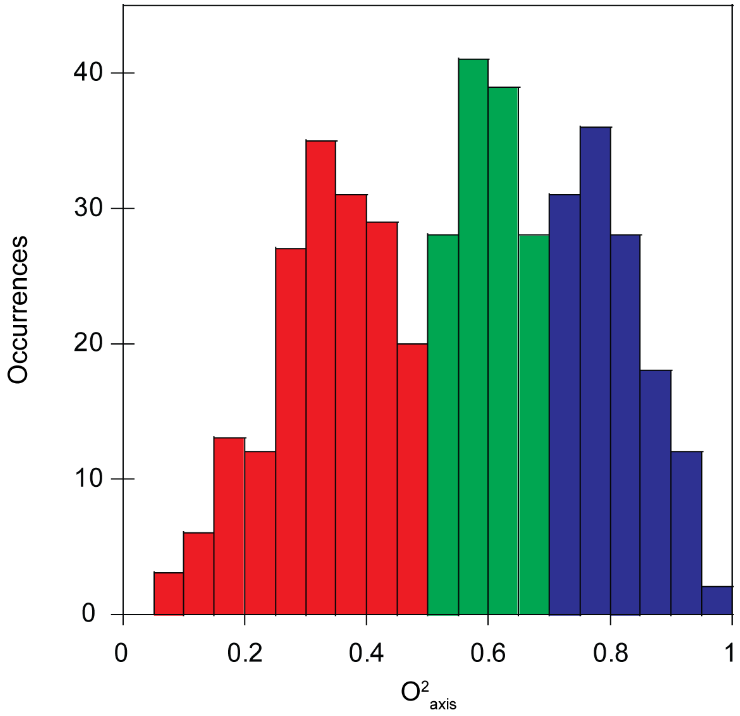

Figure 1-5: Distribution of methyl order parameters into three distinct "bands" of motion.
The methyl order parameters for Ca^{2+}-bound calmodulin and six calmodulin-peptide complexes are compiled here. Three distinct bands of motion can be observed. These bands have been termed J(red), α (green), and ω (blue).

changes in conformational entropy for the binding of Calmodulin (CaM) to CaM-binding peptides [10]. It was demonstrated that there was a linear relationship between the change in total binding entropy measured from calorimetry and the change in conformational entropy deduced from NMR relaxation measurements (Figure 1-5). This was an unprecedented and unanticipated result, strongly suggesting that conformational entropy was a significant contributor to the total binding entropy and could no longer be ignored in macromolecular interactions. It should be noted that the use of a specific potential function has several criticisms. Among them are the effects of correlated motions and the completeness of the oscillator count [30]. This warranted an empirical calibration. Using the CaM data set and estimating the solvent entropy based on the burial of surface area [31], a linear relationship was assumed between ΔO^2_{axis} and ΔS_{conf} in the following form:

$$\Delta S_{total} - \Delta S_{solvent} = m\left[\left(N_{res}^{protein}\Delta\left\langle O_{axis}^{2}\right\rangle^{protein}\right)+\left(N_{res}^{ligand}\Delta\left\langle O_{axis}^{2}\right\rangle^{ligand}\right)\right]+\Delta S_{RT}+\Delta S_{other}$$

Equation 1-4

It was anticipated from Equation 1-4 that if no such linear relationship exists, it would be readily apparent in this analysis. However, the results showed a very clear linear relationship between the measured ΔO^2_{axis} and ΔS_{conf} (Figure 1-6).

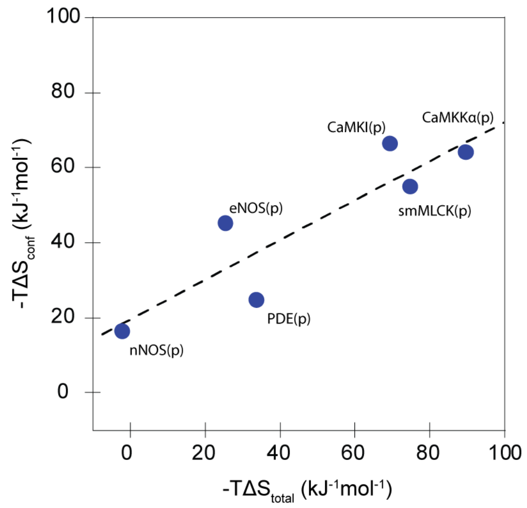

Figure 1-5: The relationship between total binding entropy and conformational entropy using a harmonic oscillator potential

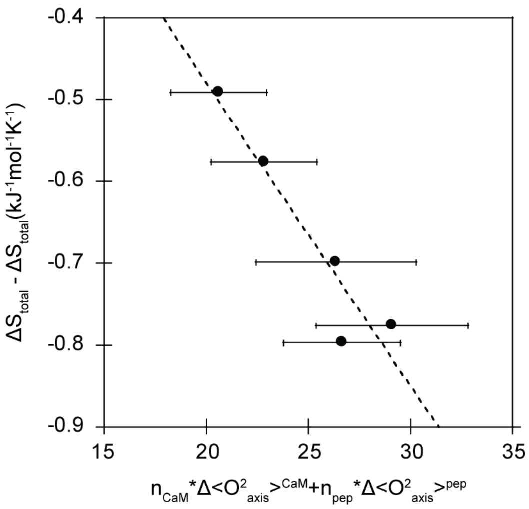

Figure 1-6: The first empirical callibration between methyl order parameter and conformational entropy.

A similar linear relationship was demonstrated with the catabolite activator protein binding to double-stranded DNA [13]. It should be noted that in this study, the contribution from $\Delta S_{solvent}$ was found to be identical between the 11 CAP-DNA complexes. This implies that the differences in total binding entropy can be reflected almost exclusively in the changes in conformational entropy measured by NMR. Taken together, these studies combine to suggest not only that conformational entropy plays an important role in macromolecular interactions, but also that it can be effectively quantified by NMR relaxation methods.

Measurement of methyl dynamics by solid state NMR spectroscopy

While the focus of this dissertation will be protein dynamics derived from solution state NMR, analogous studies of protein dynamics have been performed using solid state NMR [32]. In one such study, deuterium spin echo NMR was used to probe the dynamics of the 36-residue subdomain of the villin headpiece [33]. Applying a specific model for the motion, conformational entropies were determined for individual methyl groups. This suggests an additional technique for probing conformational entropy, but does warrant some degree of caution. It is clear that solid state NMR generally offers one advantage over solution state NMR in that protein dynamics can be observed over a wider temperature range. This allows the energy functions underlying biophysical phenomena such as entropy and heat capacity to be more robustly defined. One must consider, however, that physiological relevance must always be held paramount when exploring the intricacies of protein thermodynamics. Typically, solid state NMR studies are performed on hydrated protein powders, which may not be fully analogous to the fully hydrated state. Recently, studies on the SH3 domain of α-spectrin compared protein dynamics in the solution and solid states. Their results suggested that the internal ps-ns motions of this protein are essentially identical [34-35]. However, we believe that additional studies are needed on how observations observed in the solid state translate to the solution state. Of particular interest here is the relationship between solution state and solid state dynamics in the context of measuring protein conformational entropy. This will be addressed in Chapter 2 of this dissertation.

Drug discovery and the potential role of conformational entropy

The ultimate goal of drug design is to identify compounds that bind with high affinity and specificity to a protein target of interest. This is a multi-step process. Typically, the structure of the target protein is determined experimentally, though homology modeling can be used for proteins that resist structural characterization [36]. To identify initial "hits" for binding, libraries of small molecules, often numbering in the millions, are tested against a protein target of interest [37]. These molecules typically bind with low to mid µM affinity. Their affinities are further optimized to produce a “lead compound” which will often bind with low nM affinity [38]. The process of lead optimization is essential to early stage drug development. It is essential to identify a molecule that is both potent and selective for the protein target of interest. Several approaches are available to the drug designer in this regard.

The simplest and most economical approaches are computational methods to aid in lead generation and optimization. This involves the computational design and screening of compounds based on the known structure of the protein target [39]. In such approaches, molecules are typically "docked" to a protein structure of interest *in silico* and the affinity is calculated to identify potential leads [40]. One must make a trade-off between computational rigor and the size of the screen. Many computational methods that are used to rapidly screen a number of drug candidates employ static structures in their calculations. This completely neglects the role of conformational entropy. These methods are seldom successful in identifying potent drug candidates, as they are plagued with false negatives in which potential drug candidates are lost in the vast expanse of the library [41]. The importance of accounting for both protein and ligand flexibility for a robust calculation is well established [42-43], highlighting the need to account for conformational entropy in such calculations. However, attempts to computationally calculate conformational entropy in a robust manner would require unrealistic computational expense [44]. Thus, despite advances in computing such as GPU technology [45], successful computational approaches to drug design still seem out of reach.

In practice, many of these computational approaches also rely solely on free energy calculations and cannot reliably discern the thermodynamic signature (*i.e.,* the relative contributions of enthalpy and entropy to the free energy). This is primarily a result of convergence issues in the molecular simulation [38]. Knowledge of the thermodynamic signature is far more valuable than simply knowing the overall affinity, as it allows one to optimize the affinity in a rational way [44]. It should be noted that being able to determine the thermodynamic signature of binding does not deem the process of drug optimization “rational,” as the interplay between enthalpy and entropy is poorly understood. Attempts to optimize one aspect of the thermodynamics (*e.g.,* the enthalpy) often results in a penalty in the other (*e.g.,* the entropy). This results in optimization attempts to thermodynamically “break even” and not lead to an increase in affinity. This is often attributed to enthalpy-entropy compensation [46-47] and appears to be a major barrier for lead optimization [48].

In this regard, biocalorimetric techniques have proven valuable in the optimization of lead compounds [49]. Recently, Freire and colleagues demonstrated a framework for lead optimization that allows one to semi-rationally overcome the barrier of enthalpy-entropy compensation [50]. In their approach, both the affinity and thermodynamic signature of a compound are determined. All chemical modifications to a compound are then benchmarked for both affinity and thermodynamic signature. This method, while very powerful, is essentially a means of guess and check with respect to the underlying thermodynamics of binding. While one can retroactively rationalize the thermodynamic effects, it is advantageous to gain a deeper understanding of the subcomponents of enthalpy and entropy. In general, the goal of the drug designer is to optimize the enthalpy without a consequent entropic penalty [51]. The contribution from conformational entropy in drug design is considered to almost always be unfavorable [52]. While this seems intuitive, it has not been experimentally validated. Furthermore, the relative contribution of conformational entropy to the overall binding thermodynamics is not known, as conformational entropy has resisted experimental measurement. Of particular interest in this dissertation is an experimental measure of conformational entropy to assess its potential role in the drug design process.

Dissertation objectives

This dissertation explores the role protein dynamics and conformational entropy play in the native state and in protein-ligand interactions. First, we compare protein methyl dynamics in the solid state and in the solution state using the 36-residue villin headpiece subdomain (Chapter 2). We find a poor correlation between methyl dynamics measured in the two states. More interestingly, we discover that the native state dynamic of the protein display a remarkable spatial segmentation of different classes of motion which has not been observed previously with NMR relaxation techniques. Next, we establish a strong empirical relationship between solution NMR-derived protein dynamics and conformational entropy. The relationship is shown to apply to a wide variety of protein-ligand interactions. It not only allows for a measurement of the conformational entropy, but also establishes an empirical relationship between solvent entropy and burial of polar and nonpolar surface area (Chapter 3). Finally, with an experimental readout of conformational entropy, we examine its potential role in the drug design process. Here we find that conformational entropy may be an additional parameter that can be tuned during the process of lead optimization, potentially leading to a new and distinct class of pharmaceutical drugs (Chapter 4). Together, this work represents a large step forward for the use of NMR relaxation to not only characterize the dynamics of proteins, but also to probe protein thermodynamics, especially in the context of protein-ligand binding.

CHAPTER 2: The unusual internal motion of the villin headpiece subdomain

Contributions of this Chapter pertaining to MD simulations were performed by Evan S. O'Brien, a graduate student in the Wand laboratory.

Abstract

The thermostable 36-residue subdomain of the villin headpiece (HP36) is the smallest known cooperatively folding protein. Though the folding and internal dynamics of HP36 and close variants have been extensively studied there has not been a comprehensive investigation of side-chain motion in this protein. Here, the fast motion of methyl-bearing amino acid side chains are explored over a range of temperatures using site-resolved solution NMR deuterium relaxation. The squared generalized order parameters of methyl groups extensively spatially segregate according to motional classes. This has not been observed before in any protein studied using this methodology. The class segregation is preserved from 275K to 305K. Motions detected in helix 3 suggest a fast timescale of conformational heterogeneity that has not been previously observed but is consistent with a range of folding and dynamics studies. Finally, a comparison between the order parameters in solution with previous results based on solid-state NMR deuterium line shape analysis of HP36 in partially hydrated powders shows a clear disagreement for half of the sites. This result has significant implications for the interpretation of data derived from a variety of approaches that rely on partially hydrated protein samples.

Introduction

Recent advances in experiment and simulation have begun to indicate that the internal motion of proteins and the entropy that it represents can significantly impact the thermodynamics underlying various functions and states of proteins [11] . NMR spectroscopy has contributed centrally to this effort and has revealed previously unrecognized physical attributes and patterns of internal motion within the three-dimensional structure of the protein native state [16]. Methyl-bearing amino acid side chains have been comprehensively examined in several dozen protein systems using deuterium or carbon relaxation methods [16]. These studies have shown that many proteins display three classes of motion that involve various degrees of rotameric interconversion on the picosecond-nanosecond timescale [27]. Of particular interest is that these motions appear to report on the changes in conformational entropy associated with a change in protein functional state [10, 28-29]. Indeed, recent advances indicate that appropriate use of NMR relaxation methodologies can quantitatively access this important thermodynamic feature of protein molecules [30, 53]. These types of investigations have been carried out almost exclusively in the solution state. However, protein powders hydrated to various degrees are often employed in biophysical investigations using techniques such as neutron scattering [54-55]. Thus it is of interest to compare the internal dynamics of fully solvated and partially hydrated protein molecules. Here we use a small subdomain of the villin headpiece (HP36) and employ deuterium relaxation to illuminate the dynamics of the protein in free aqueous solution and compare them to those observed in a partially hydrated powder.

HP36 is comprised of residues 791-825 of the intact chicken villin protein and is the smallest known cooperatively folding protein domain [56]. The protein is comprised of three short helices stabilized by a well packed hydrophobic core [57] (Figure 2-1). HP36 has been extensively studied using a variety of techniques [58-68]. While much is known about the folding and conformational dynamics of HP36 including the dynamics of the backbone, site-specific information at side-chains locations remains somewhat limited. Many site-resolved experimental studies of the dynamics of HP36 have hitherto been

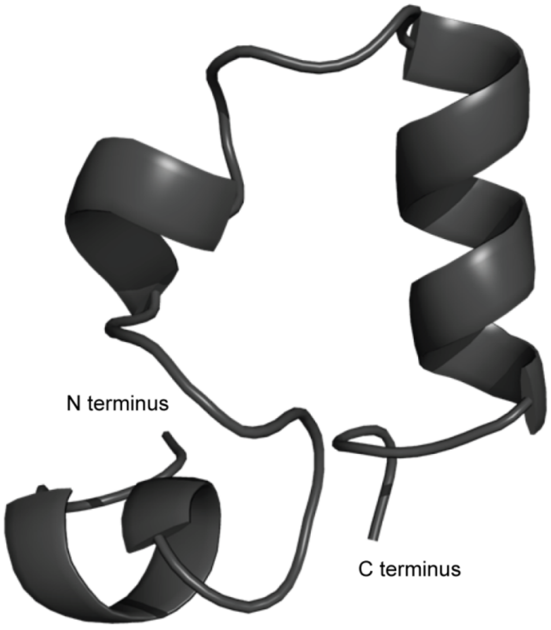

Figure 2-1: Structure of Villin HP36 (PDB:1VII)

primarily confined to solid-state NMR. While several NMR dynamics studies have been performed to characterize the conformational distribution and thermodynamics of HP36, [33, 59, 66, 69-72] no comprehensive study of side chain motion has been performed in solution. Here we further characterize the native state ensemble of HP36 by probing the sub-ns methyl dynamics in solution across a wide range of temperatures. We then compare these results to those obtained from a partially hydrated powder across a comparable temperature range to determine if the underlying thermodynamics based on NMR observables are translatable from the partially hydrated solid state to the solution state.

Results and Discussion

Methyl-bearing side chain dynamics in solution

The fast dynamics of the methyl-bearing residues in HP36 were characterized at six temperatures ranging from 275K to 305K. Lipari-Szabo [21] squared generalized order parameters for the methyl symmetry axis (O^2_{axis}) and the associated effective correlation time (τ_e) were determined for the 18 methyl groups of HP36. The N-terminal methionine residue (M41) was omitted from further analysis, as it displayed O^2_{axis} values around 0.05, suggesting it is entirely disordered. It should be noted that this residue is a result of recombinant protein expression and is not present in the native sequence of the protein. At the lower temperatures examined, the methyl groups of one Alanine and one Threonine display O^2_{axis} values near the theoretical limit of 1 indicating that they are essentially rigid within the molecular frame. The remaining methyl groups show O^2_{axis} values over nearly the full theoretical range. The temperature

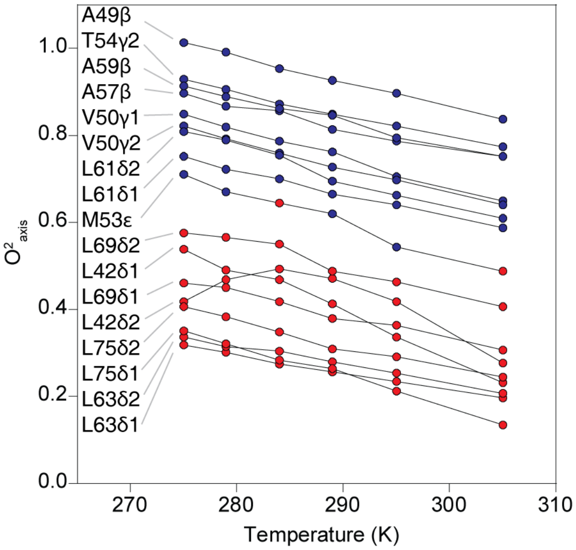

Figure 2-2: Plots of dO^2_{axis}/dT for the methyl groups of HP36. Most methyl groups displayed a clear linear dependence with temperature. All methyls fall within the J(red) and ω(blue) bands of motion.

dependences of the O^2_{axis} and τ_e parameters display a clear linear trend. The plots of dO^2_{axis}/dT for the methyl groups of HP36 are shown in Figure 2-2. In contrast to previous studies of methyl dynamics across different temperatures [26, 73-74], a particularly sharp temperature dependence of O^2_{axis} is observed, with an average value of $-5.9 \pm 1.5 \times 10^{-3}$ K^{-1} across methyl residues. This value is significantly larger than previous studies on ubiquitin and a calmodulin-peptide complex where the observed dO^2_{axis}/dT values were -2.3×10^{-3} K^{-1} and -2.5×10^{-3} K^{-1}, respectively [26, 73]. The distribution of these residues is shown in Figure 2-3. The reason for this difference is not clear, but has implications for the heat capacity of the protein. A linear trend in τ_e values is also seen (not shown), though this parameter is complex as it involves convolved motions of the methyl axis as well as methyl rotation motions and is also scaled by the order parameter [21].

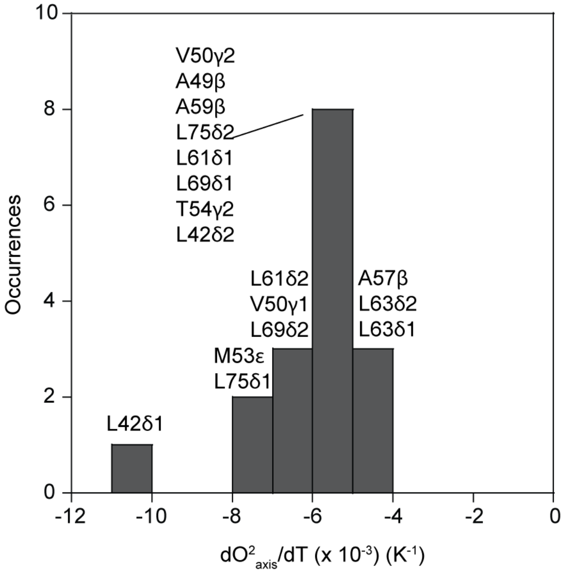

Figure 2-3: Histogram of dO^2_{axis}/dT values

Banding of O^2_{axis} parameters

As outlined in Chapter 1, methyl-bearing amino acid side chains undergo three classes of motion that are often manifested as a tri-modal distribution or banding of the amplitude of motion represented by the O^2_{axis} parameter [16] . The banding can be rationalized in terms of simple packing interactions that naturally lead to a segregation of order parameters [27]. The so-called J-class is distinguished by extensive rotamer interconversion while the ω-class corresponds to highly restricted motion within a single and likely narrower rotameric well potential [27]. An intermediate class involves larger amplitude motion within a rotamer well that is accompanied by limited rotameric barrier crossing [27]. The relative population of each class varies significantly across proteins, even for the same protein involved in various complexes [10, 16, 27]. To determine the presence of banding of the distribution of O^2_{axis} parameters within HP36, we used a Bayesian statistical analysis that is described in detail elsewhere [27]. This approach makes no assumptions about the presence of distinct classes of motions. We applied this approach to each set of methyl order parameters at each temperature at which data was determined, *i.e.* the presence and number of dynamic bands was determined independently for each temperature. We observe two roughly equally populated bands are maintained at each temperature across the entire temperature range (Figure 2-2). At 295K, the two band centers correspond to O^2_{axis} values of 0.35 and 0.78, which conform to the previously described J- and ω-bands, respectively [16, 27]. Most residues do not move to different bands over this temperature range ,*i.e.*, they qualitatively maintain the same character of motion. The sole exception is M53Cε, which is in between the band centers at higher temperature and falls statistically into the ω-band at 284K and again at 305K. Visually, there appears to be a spatial gap between the M53Cε (the most dynamic ω-band residue) and L69Cδ2 (the least dynamic J-band residue) that separates the two bands of motion in Figure 2-2. Despite this, M53Cε statistically into different bands across the temperature range. It is unclear if this has any physical significance or is merely a consequence of having a methyl order parameter that falls roughly between the two band centers. Mapping the distribution of the various classes of motion onto the structure of HP36 reveals that they are spatially segmented and are separated by the three aromatic residues (F47, F51 and F58) that comprise the hydrophobic core of this protein (Figure 2-4).

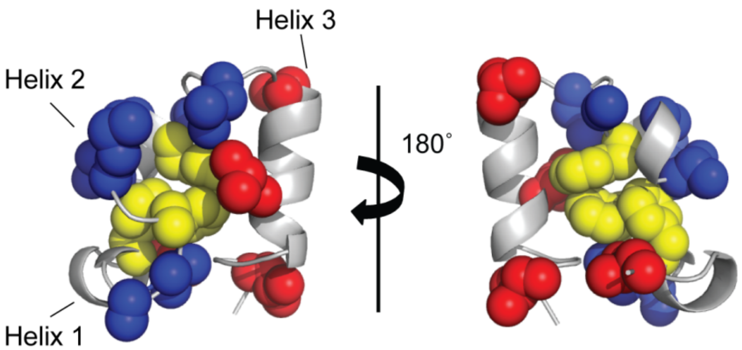

Figure 2-4: Spatial clustering of HP36 dynamics.
The side chains in the J band (red) and the ω band (blue) at 295K are mapped onto the structure of HP36. The side chains of three phenylalanine residues that comprise the hydrophobic core (F47,F51, and F58) are shown in yellow and roughly separate the two bands.

The bulk of the J-band is found in helix 3, whereas the ω-band is centered on helices 1 and 2. Such distinct spatial clustering of dynamic motion has not been observed previously. Though some spatial clustering of O^2_{axis} values is seen within protein molecules it is generally obscure and limited [16, 27]. In this regard, the spatial distribution of internal motion of the methyl-bearing side chain dynamics seen for HP36 is quite striking. It must be noted that the low number of methyl-bearing residues in HP36 may bias the banding by amino acid type [16, 75-76]. For example, the J-band is comprised entirely of leucines. However, the ω-band contains both a leucine (L61) and a methionine residue (M53), which are often associated with relatively low order parameters due to a higher number of side chain degrees of freedom. Thus, the spatial clustering of these bands seems to have significance beyond the degrees of freedom offered by the side chain of a particular amino acid type.

The spatial clustering of the J- and ω-bands in the structure of HP36 is consistent with the proposed energy landscape of the protein. The three helices of HP36 are all known to be unstructured in isolation [60]. However, a construct that comprised both helix 1 and 2 was shown to have significant secondary structure by both CD and NMR [60, 62]. Furthermore, triplet-triplet energy transfer (TTET) and 2D IR experiments have unveiled conformational heterogeneity in the C-terminal helix 3 [63-64, 67]. This manifests itself in what is described as a reversible “unlocking” of helix 3 from the helices 1 and 2, followed by large structural fluctuations of helix 3. TTET experiments have shown that these motions occur on the ns-us timescale and are considered to be on the native side of the major folding barrier of HP36. Cross-correlated NMR relaxation measurements have also indicated enhanced motions in the backbone of helix 3 [70]. The ω-band encompasses helices 1 and 2, which is consistent with them forming the core structural unit of this protein. In contrast, the J-band is localized almost entirely to helix 3. This suggests that in addition to more global fluctuations within the helix, there are also large side chain fluctuations occurring on a timescale several orders of magnitude faster than what has been previously observed. Taken together, the segregation of methyl dynamics in HP36 into spatially distinct bands provide additional insight into the native state ensemble of the protein.

Comparison of solution state and solid state dynamics

Recently, Vugmeyster and colleagues performed a study of the dynamics of a partially hydrated powder of HP36 across a wide range of temperature using deuterium spin echo NMR [33]. They performed deuterium line shape analysis and fit the data to a motional model containing three contributions that describe fast 3-site jumps of the methyl group, restricted diffusion along on an arc, and rotameric jumps. There are two important distinctions between the solution and solid-state studies: the level of hydration and the broader sensitivity of the averaging of the deuterium quadrupolar tensor into the microsecond time regime. The level of hydration (h=0.4g H_2O/g protein) used for the solid state studies corresponds to partial hydration – the roughly 100 water molecules per protein molecule will cover only about half of the molecular surface of the folded protein – while the solution studies employ a fully hydrated protein. Deuterium lineshape analysis is sensitive to motion on the order of and faster than the breadth of methyl deuterium quadrupolar tensor, with the motionally averaged values of one third of 167 kHz,[75] or on the order of 20 μs. In contrast, deuterium relaxation in solution will report only on internal motion that are faster than overall tumbling, which in this case is on the order of 3 ns. Thus, even if motion in the solid state sample is identical on the nanosecond timescale, order parameters derived from deuterium lineshape analysis can potentially be smaller than those seen by classical relaxation due to contributions from motions in the μs to ns time regime. However, they cannot be larger in this situation. The O^2_{axis} values obtained from these studies are compared to the solution O^2_{axis} values at 295K for the partially hydrated powder (h ≈ 0.4 grams H_2O/gram protein) (Figure 2-5). The pro-chiral isopropyl methyls of Val and Leu are not resolved in the solid state data allowing comparison of only six methyl groups, which yielded a quite poor correlation ($R^2 = 0.003$, RMSD = 0.172). Of the 6 methyl groups compared, only those of L42, V50 and L75 display a reasonable correlation between the solution and solid states. These residues are spatially clustered. The remaining methyl groups do not show a systematically higher O^2_{axis} values in the solution state as would be expected if the solid state analysis was reporting on motions on a slower timescale. L63 is the only side-chain probed in the solid-state that is not buried in the hydrophobic core and, thus, its higher value of the order parameter in the powder state could be caused by inter-molecular contacts. The only hydrophobic core residues for which the values of the order parameter are larger in the solid-state is L69. The temperature dependence of the O^2_{axis} parameters is also shown in Figure 2-5. The average temperature derivative of the O^2_{axis} values obtained in the solid state data is $-2.2 \pm 1.2 \times 10^{-3}\ K^{-1}$ and compares to $-5.9 \pm 1.5 \times 10^{-3}\ K^{-1}$ obtained in solution. Interestingly, the slope of the solid-state data correlates very well with previous studies of temperature dependent methyl dynamics in the solution state [26, 73-74].

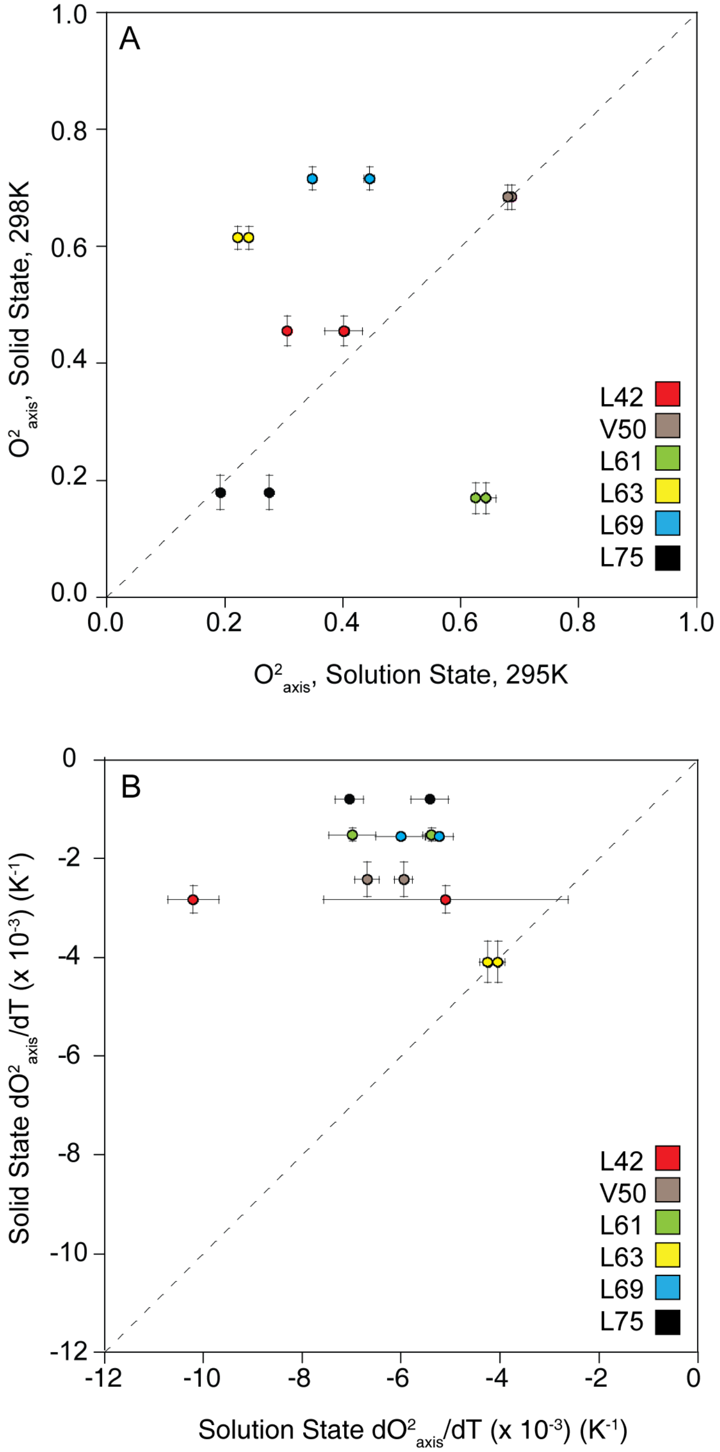

Figure 2-5: Comparison of solution state and solid state dynamics of HP36.
Correlation plots are shown for O^2_{axis} (A) and dO^2_{axis}/dT (B). Unity lines are shown in both plots.

Vugmeyster and coworkers[59] have developed an analytical parameter (Λ) to help characterize the underlying energy potential governing the temperature dependence:

$$\Lambda = \frac{d\ln(1-O)}{d\ln T}$$

Equation 3-1

Λ is ≤ 1 for a simple harmonic oscillator. Both amide N-H and methyl groups are generally found to have a non-harmonic component to their temperature dependent motion. For example, ubiquitin has average Λ values of 7.1 and 2.3 for the backbone and side chain atoms, respectively [73]. Higher values of lambda (Λ > ~5) were ascribed to highly restricted angular motions and barrier heights on the order of 5 kcal/mol. Lower values of lambda were inferred to typify large angular excursions with low barrier heights, *i.e.*, consistent with rotameric interconversion. The correlation plot for solution and solid-state lambda values for HP36 are shown in Figure 2-6**.** Once again, we note that the timescale and/or level of hydration may explain the differences in the temperature dependence of the dynamics. Comparison of dynamics in solid and solution states is a topic of active investigation. Most studies focus on hydrated proteins in micro-crystalline state and show general correspondence between dynamics in solution and solid-state when probed by relaxation measurements [34]. However, mobile regions of the proteins can be affected by crystalline environments and display differences in ns-ms time scale dynamics when probed by dipolar coupling measurements [77]. Our work underscores the need for further detailed investigations to compare the dynamics in the solution

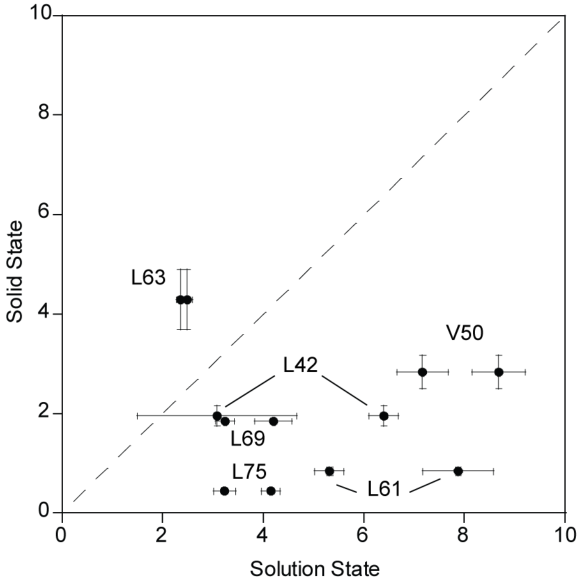

Figure 2-6: Comparison of Λ values between solid state and solution state dynamics.
Note that two solution state values correspond to one solid state value, as the pro-chiral isopropyl methyls are not resolved in solid state experiments.

and various levels of hydration in the solid state using a variety of techniques that can match the time scales probed in the two phases.

Molecular dynamics simulation of HP36

The accuracy of simulations of internal protein motion continues to improve and now provides generally semi-quantitative and, in some cases, quantitative prediction of experimentally obtained measures of side chain motion. [53, 78-80] In an effort to illuminate the origins of the apparent discrepancy between the view of methyl-bearing side chain motion in the solution and solid-state studies, we carried out a 120 ns molecular dynamics simulation of HP36 in explicit solvent (Figure 2-7). The order parameters predicted by the simulation correlate well with solution state data (R^2 = 0.86) but poorly with those obtained in the partially hydrated solid-state sample (R^2 = 0.24).

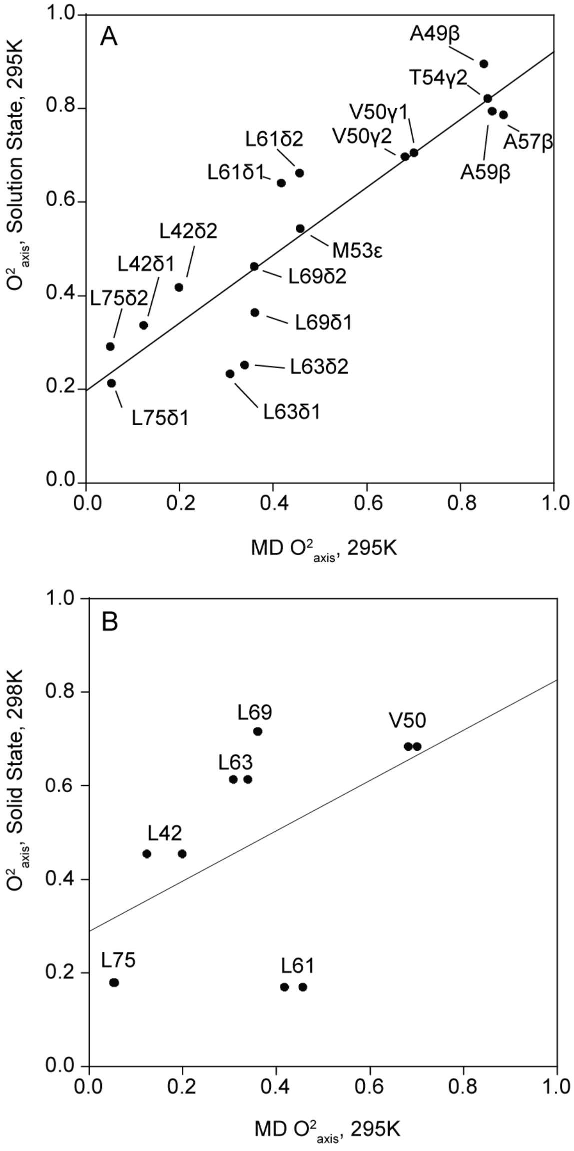

Figure 2-7: Correlation between experimentally-derived and MD-derived methyl order parameters. Methyl order parameters from a 120ns MD simulation of HP36 and experimentally determined methyl order parameters from either (A) solution state NMR or (B) solid state NMR are shown. The linear fits for each correlation are shown in each plot.

Implications for studies involving partially hydrated proteins

A protein hydration level of h ~ 0.4 has been the widely accepted level at which protein internal motions closely resemble native motions [81]. Previous studies utilizing neutron scattering as well as solid state NMR have shown that hydration has a very large effect on protein dynamics in the range of h between 0 and around 0.4, after which most dynamic changes plateau [81-82]. In one such study, however, the quasielastic neutron scattering of lysozyme in the 2-6 GHz (ps-ns) range showed a hydration dependence that continued to increase up to at least h=0.8 [83], suggesting that perhaps not all dynamic processes of proteins are activated at the level of 40% hydration. It should be noted that a hydration level of h ~ 0.8 would constitute one full hydration layer of HP36. The data presented in this work further supports the idea that some native state motions may require a greater level of hydration than has been previously shown.

Conclusions

The side chain methyl dynamics of Villin HP36 have been measured across a wide range of temperatures. Curiously, the methyl dynamics of HP36 reside in spatially distinct bands of motion. While such a clear clustering of dynamics has not been previously observed to our knowledge, these dynamics are consistent with the proposed native state ensemble. Our results also point to conformational heterogeneity of side chains of helix 3 occurring at a sub-ns timescale, which has not been observed previously. The majority of methyl-bearing residues show clear differences in dynamics in fully hydrated aqueous solution from that observed in partially hydrated powders. These differences may be partially explained by a difference in timescales that are represented within the order parameters as well as by inter-molecular contacts for solvent-exposed side chains, but also suggest that there may be inherent differences between partially hydrated proteins and proteins in free aqueous solution. This has implications for the interpretation of many neutron scattering and solid-state NMR studies that utilize partially hydrated protein samples. This suggests that the dynamical proxy to be discussed in the following chapter likely does not apply to solid state-derived NMR dynamics.

CHAPTER 3: Development of a universal entropy meter

This chapter represents a curation and analysis of a large pool of experimental data. While all of the final data analysis and fitting were performed by this author, earlier contributions to the data analysis were made by Vignesh Kasinath, former graduate student of the Wand Lab. Additionally, experimental data pertaining to the HBP(D24R)-Histamine and Barnase-dCGAC complexes were contributed by Jack Wee Lim and Vignesh Kasinath, respectively.

Abstract

Molecular recognition by proteins is fundamental to molecular biology. Dissection of the thermodynamic landscape governing protein-ligand interactions has proven difficult[84]. Determination of the individual entropic contributions is particularly elusive. Recently, NMR relaxation based measurements have suggested that changes in conformational entropy can be quantitatively obtained through a dynamical proxy [11, 30, 53]. Here we use 32 different protein-ligand complexes to show a general relationship between measures of fast side chain motion and the underlying conformational entropy. We find that the contribution of conformational entropy can range from favorable to unfavorable, which demonstrates the potential of this key thermodynamic variable to modulate protein-ligand interactions. The dynamical “entropy meter” also refines our understanding of the contributions of solvent entropy [31] and directly determines the loss in rotational-translational entropy [85] that occurs upon formation of high affinity complexes. Collectively, these results provide a comprehensive and unified view of the role of entropy in high affinity molecular recognition by proteins.

Introduction

At the most fundamental level biological processes are controlled using molecular recognition by proteins. Protein-ligand interactions impact critical events ranging from the catalytic action of enzymes, assembly of macromolecular structures, complex signaling and allostery, transport phenomena, force generation and so on. Indeed, efforts at pharmaceutical intervention in disease have largely centered on the manipulation of molecular recognition by proteins.

The physical origin of high affinity interactions involving proteins has been the subject of intense investigation for decades. Structural analysis at atomic resolution has helped illuminate in great detail the role played by enthalpy in molecular recognition by proteins. Of interest here is the role of the entropy, in particular the protein conformational entropy, in modulating the free energy of association of protein with a ligand. Because this entropy arises from the distribution between different conformational states of the protein, it is effectively invisible in a static, structure based view of proteins. Moreover, the recognition and binding of ligands by proteins often involves dozens of amino acids and thousands of square Ångstroms of contact area [86]. The contribution of a particular amino acid residue to the affinity varies greatly from complex to complex, and also within each complex, which greatly hinders the computation of the free energy of binding by taking inventory of interactions or from analysis of static structures alone [84, 87]. While potential roles for conformational entropy in protein function have been speculated about and simulated for some time [84, 88-92], a comprehensive quantitative experimental demonstration of the extent and variation of its importance has been lacking.

Experimental insight into entropy generally begins from a calorimetric perspective where the heat or enthalpy (ΔH_{total}) and free energy (ΔG_{total}) are measured and the total binding entropy (ΔS_{total}) is determined by:

$$\Delta G_{total} = \Delta H_{total} - T\Delta S_{total} = \Delta H_{total} - T\left(\Delta S_{conf}^{protein} + \Delta S_{conf}^{protein} + \Delta S_{solvent} + \Delta S_{RT} + \Delta S_{other}\right)$$

Equation 3-1

The challenge is to quantify the various microscopic contributions to the free energy of binding. Detailed atomic resolution structural models provide great insight into the origins of the enthalpy of binding. Much less certain are the various contributions to the total binding entropy. In principle, several types of entropy are potentially important (see right side of Equation 3-1). Historically, entropy has most often entered the discussion in terms of the changes in the entropy of solvent water ($\Delta S_{solvent}$) and framed in terms of the so-called “hydrophobic effect” [31, 93].

$\Delta S_{solvent}$ has, with some success, been related empirically to changes in accessible surface area (ΔASA) of the protein and ligand upon complexation [94]. Changes in the conformational entropy (ΔS_{conf}) and the rotational-translation entropy (ΔS_{RT}) of the interacting species have received far less attention, presumably because they have resisted experimental measurement. Contributions to binding entropy from unrecognized sources (ΔS_{other}) are also included in Equation 3-1 for purposes of experimental validation (see below).

Some time ago it was recognized that fast sub-nanosecond timescale motion between conformational states might provide access to various thermodynamic features [95], especially conformational entropy [28-29]. Application of this idea has been thwarted by a number of technical limitations [11, 16], but has nevertheless led to the strong suggestion that dynamical proxies made available by NMR relaxation measurements could provide access to measures of conformational entropy [10]. More recently, efforts have been taken to overcome these technical barriers and limitations and render this approach to protein entropy quantitative [30, 53]. The resulting NMR-based "dynamical proxy" for conformational entropy or "entropy meter" takes a simple form that requires few assumptions, particularly about the nature of the underlying motion [53]:

$$\Delta S_{total} - \Delta S_{solvent} = s_d \left[\left(N_{\chi}^{protein} \Delta \left\langle O_{axis}^2 \right\rangle^{protein} \right) + \left(N_{\chi}^{ligand} \Delta \left\langle O_{axis}^2 \right\rangle^{ligand} \right) \right] + \Delta S_{RT} + \Delta S_{other}$$

Equation 3-2

where ΔO^2_{axis} is a measure of the degree of spatial restriction of the methyl group symmetry axis and varies between 0, which represents complete isotropic disorder and 1, which corresponds to no internal motion within the molecular frame [21] and is measured in various ways [16]. $\Delta\langle O^2_{axis}\rangle$ is the change in order parameter averaged over all the methyl groups in the protein. s_d is the sought after relationship (conversion) between measures of fast internal motion and conformational entropy [30, 53]. To avoid issues associated with statements about absolute entropy we restrict this treatment to changes in entropy upon a perturbation ,*e.g,*. binding of a ligand. In principle all internal degrees of freedom of the protein contribute to ΔS_{conf}, namely bond lengths, angles and torsions. In practice, empirical and computational studies show that changes upon binding are largely restricted to the softer, torsional modes [14, 96]. Thus Eqn. 2 contains just the total number of torsion angles in the molecule (N_X). Scaling $\Delta\langle O^2_{axis}\rangle$ by the total number of torsions essentially projects the entropy change detected via the motion of methyl-bearing amino acid side chains across the entire protein molecule. $\Delta S_{solvent}$ is generally calculated from the structures of the free and complexed states using empirically determined scaling of changes in apolar and polar accessible surface area [94]. The conformational entropy meter approach has thus far been applied to two protein-ligand systems: calcium activated calmodulin binding peptides representing the domains of regulated proteins [30] and a series of mutants of the catabolite activator protein binding DNA [13]. Here, we expand this initial set of protein-ligand interactions to 32 protein-ligand complexes that span a broad range of binding affinities (K_d : 10^{-4} to 10^{-10} M)

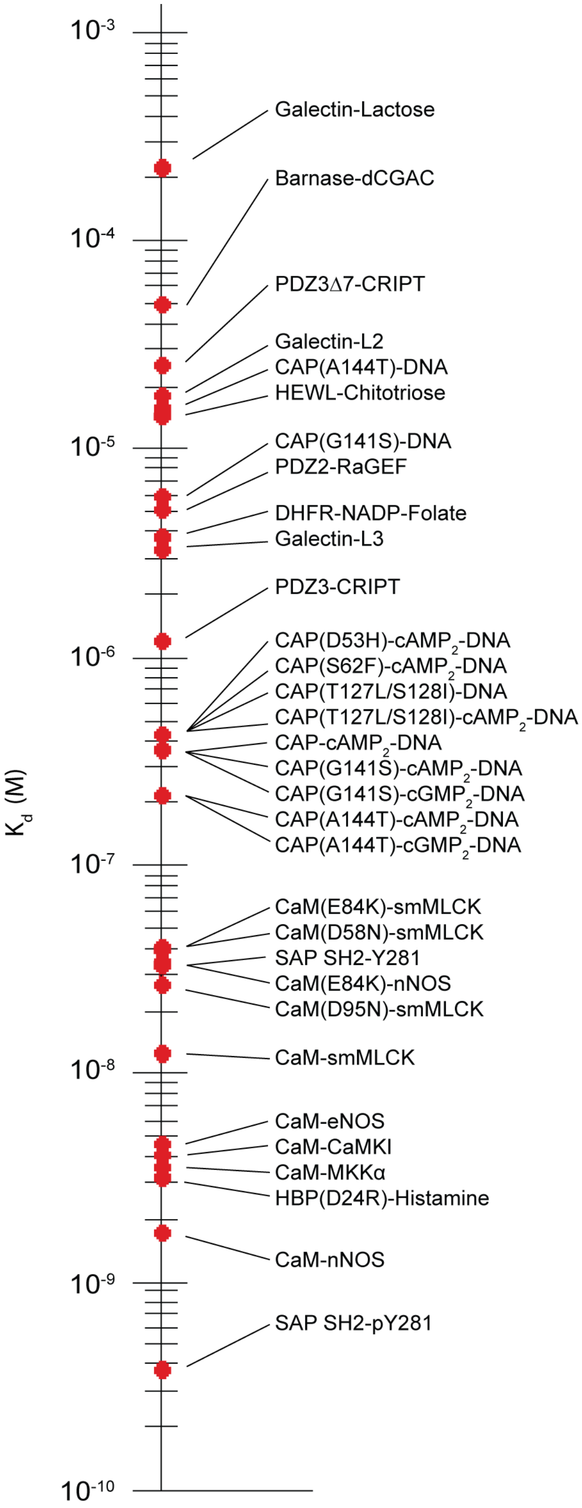

Figure 3-1: Range of affinities represented in the entropy meter.

and ligand types (nucleic acids, enzyme substrates & cofactors, carbohydrates, peptides & proteins) (Figure 3-1: Table C-1). We set out to test the hypothesis that the “entropy meter” is universally applicable ,*i.e.*, that the scaling (s_d) between changes in fast motion and changes in conformational entropy is constant. There are now roughly two-dozen published studies of the change in methyl-bearing side chain dynamics that are sufficiently complete to use to test this idea (Tables C-9 through C-70). We have complemented several of these by measuring the binding thermodynamics using isothermal titration calorimetry. A number of new examples, including additional variants of calmodulin in complex with a peptide corresponding to the calmodulin-binding domain of the smooth muscle myosin light chain kinase, were also examined. The curated data set is summarized in Tables C-1 and C-2.

Results and discussion

Simultaneous calibration of conformational entropy and solvent entropy

Usually the contribution of solvent entropy to the thermodynamics of an equilibrium is calculated using empirically determined coefficients relating changes in accessible polar and apolar surface area [94]. These coefficients have been derived with various assumptions about the nature of conformational entropy. In addition, these coefficients were determined in the context of protein-unfolding, where conformational entropy may behave different. This suggests that the previously determined coefficients for determining solvent entropy may be inappropriate in the context of protein-ligand binding. Fortunately, the unprecedented extent of the dynamical dataset used here allowed us to fit directly for these solvent entropy coefficients. In addition, the intercept of Equation 3-2 contains the loss in rotational-translational entropy upon formation of the complex. We therefore recast Equation 3-2 as:

$$\Delta S_{total} = s_d \left[\left(N_{\chi}^{protein} \Delta \left\langle O_{axis}^2 \right\rangle^{protein} \right) + \left(N_{\chi}^{ligand} \Delta \left\langle O_{axis}^2 \right\rangle^{ligand} \right) \right] + \left[a_1(T) \Delta ASA_{apolar} + a_2(T) \Delta ASA_{polar} \right] + \Delta S_{RT} + \Delta S_{other}$$

Equation 3-3

Should unaccounted contributions to the binding entropy be insignificant (*i.e.,* <ΔS_{other}> ~ 0) then ΔS_{RT} will dominate the ordinate intercept. Violations of the few assumptions used to construct the calibration line for the entropy meter will result in deviation from linearity. These include the assumptions that methyl-groups are sufficiently numerous, are well distributed and are adequately coupled to non-methyl bearing amino acids that their motions provide comprehensive coverage of internal motion in the protein. These assumptions are strongly supported by simulation [96]. Fitting of Equation 3-3 to the dynamical data summarized in Table C-1 gives an R^2 of 0.76 and yields the values s_d, ΔS_{RT}, a_1, a_2 listed in Table 3-1 (Figure 3-2).

Table 3-1: Calibration of the dynamic proxy for conformational entropy*

Coefficient	Value
Ordinate intercept (ΔS_{RT} + ΔS_{other})	$-(1.0 \pm 0.1) \times 10^{-1}$ kJ mol^{-1}K^{-1}
Slope (s_d)¶	$-(5.1 \pm 0.4) \times 10^{-3}$ kJ mol^{-1}K^{-1}
Hydration heat capacity – apolar (dCp_1)	$+(31.5 \pm 8.6) \times 10^{-5}$ kJ mol^{-1}K^{-1} Å^{-2}
Hydration heat capacity – polar (dCp_2)	$-(6.2 \pm 0.5) \times 10^{-5}$ kJ mol^{-1}K^{-1} Å^{-2}
Solvent entropy coefficient‡ – apolar (a_1) at 298K	$-(8.06 \pm 2.2) \times 10^{-5}$ kJ mol^{-1}K^{-1} Å^{-2}
Solvent entropy coefficient‡ – polar (a_2) at 298K	$-(3.28 \pm 0.26) \times 10^{-5}$ kJ mol^{-1}K^{-1} Å^{-2}

* Derived from a global fit of NMR-derived dynamical data summarized in Appendix C to Equation 3-3. Stated precision determined by Monte Carlo sampling. Binding data were collected at different temperatures for different protein systems - see Table C-2. Significant heat capacity changes accompany hydration of apolar and polar groups , so the area coefficients a1 and a2 in Eqn. 3-3 for hydration entropy will differ somewhat between the proteins studied at different temperatures. However, this temperature variation is well described experimentally by the relations a1 = dCp1 ln(T/385K) and a2 = dCp2 ln(T/176K) where dCp1 and dCp2 are the hydration heat capacities per unit area of apolar and polar surface, respectively. Substituting these relations for a1 and a2 into Eqn. 3, we globally fit for the parameters dCp1, dCp2, ΔSRT, and sd, using the experimental binding entropy changes, order parameter changes, and known experimental temperatures. Best-fit parameters and uncertainties determined by Monte Carlo sampling are given in Table 3-1. Values for the solvent entropy coefficients per unit area are also tabulated at the standard temperature of 298 K.

¶ The entropic contribution of the backbone is not included. Unfortunately, the backbone dynamics data that accompanies the side chain database (Tables C-1 and C-2) is ill suited for the analysis due to limited dynamic range with relatively large error, incompleteness and inadequate reporting. Simulations indicate that it will be small (< 5% of ΔS_{conf}).

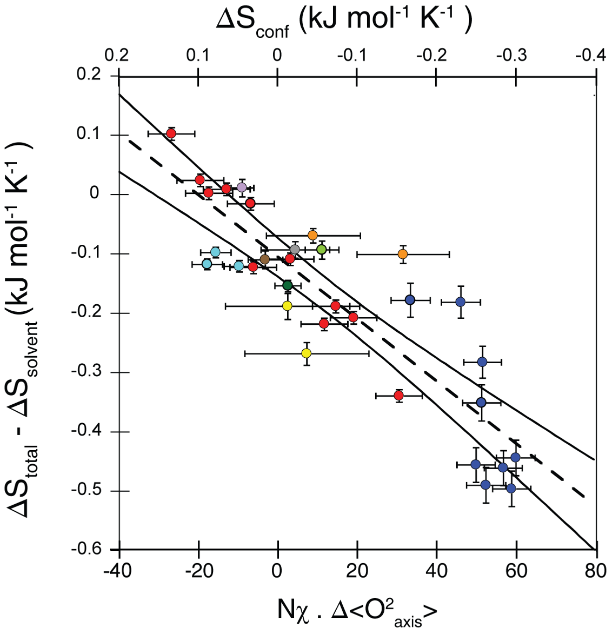

Figure 3-2: Calibration of the dynamical proxy for protein conformational entropy.
Fitting of equation 3-3 to data provided by 32 protein-ligand association. The difference in the measured total binding entropy and calculated solvent entropy is plotted against the change in the dynamical proxy is the average Lipari-Szabo squared generalized order parameter of methyl group symmetry axes (<O$^2_{axis}$>). The dashed line indicated the linear regression line. Solid lines indicate the 95% confidence intervals of the linear fit. The protein-ligand complexes are: (●) CaM-peptide, (●) CAP-DNA, (●) Galectin-L2/L3/lactose, (●) SAPSH2-Y281/pY281, (●) HEWL-chitotriose, (●) PDZ3/PDZ3Δ7-CRIPT, (●) DHFR-NADP-folate, (●) PDZ2-RaGEF, (●) Barnase-dCGAC, and (●) HBP(D24R)-Histamine. Error bars in the abscissa represent the standard deviation of <O$^2_{axis}$>, which for our data is 0.01. For SAPSH2-Y281/pY281, PDZ/PDZΔ7-CRIPT, PDZ2-RaGEF, and Barnase-dCGAC, the uncertainty of the contribution of the peptide or ssDNA ligand also contributes additional error (see Appendix C). The ordinate error represents the propagated quadrature error of ΔS_{tot}, ΔS_{solv}, and ΔS_{RT}. The former is derived from experimental error and the latter two are derived from errors in the fitted coefficients in Table 3-1. In the case of CAP-DNA and HEWL-Chitotriose, experimental errors of ΔS_{tot} were unavailable, and the ordinate error is assumed to be the quadrature error of only ΔS_{solv} and ΔS_{RT} . The fitted slope (s_d) of -0.0053 ± 0.0003 kJ mol^{-1}K^{-1} allows for the conversion of measured changes in methyl-bearing side chain motion and the associated conformational entropy. Other parameters of Equation 3-3 are summarized in Table 3-1.

The parameter of central interest (s_d) is well determined and provides for the first time a robust and apparently general means to experimentally obtain the change in conformational entropy upon protein-ligand association. In this treatment we have ignored the contribution to the binding entropy from the backbone of the protein. Recent simulations suggest that the binding of ligands by structured proteins will involve little contribution from the polypeptide chain [23]. Unfortunately, only six of the complexes used in Figure 3-2 have sufficiently characterized dynamics to allow backbone motion be included in our analysis. We have attempted to fit these data to a modification of Equation 3-3 that includes the contribution of backbone entropy:

$$\begin{aligned}\Delta S_{total} = {} & s_d^{sc}\left[\left(N_\chi^{protein}\Delta\left\langle O_{axis}^2\right\rangle^{protein}\right)+\left(N_\chi^{ligand}\Delta\left\langle O_{axis}^2\right\rangle^{ligand}\right)\right]\\ & +s_d^{bb}\left[\left(N_{res}^{protein}.\ \Delta\ \log\left\{1-\left\langle O_{NH}^2\right\rangle^{protein}\right\}\right)+\left(N_{res}^{ligand}.\ \Delta\ \log\left\{1-\left\langle O_{NH}^2\right\rangle^{ligand}\right\}\right)\right]\\ & +\left[a_1(T)\Delta ASA_{apolar}+a_2(T)\Delta ASA_{polar}\right]+\Delta S_{RT}+\Delta S_{other}\end{aligned}$$

Equation 3-4

However, when analyzed in a similar fashion this subset cannot be reliably fit. Upon globally fitting this equation in a similar manner to Equation 3-3 (see appendix C), the backbone s_d value is of the wrong sign, erroneously suggesting a decrease in dynamics is entropically favorable. Employing a number of reasonable constraints on the fitting parameters does not alter this result, supporting the idea that the contribution by the backbone to the binding entropy is indeed small. Utilizing the determined value of s_d we can establish that the contribution of conformational entropy to molecular recognition by proteins is quite variable between complexes. Conformational entropy can highly disfavor, have no effect, or strongly favor association, and is often a large determinant of the thermodynamics of binding (Figure 3-3).

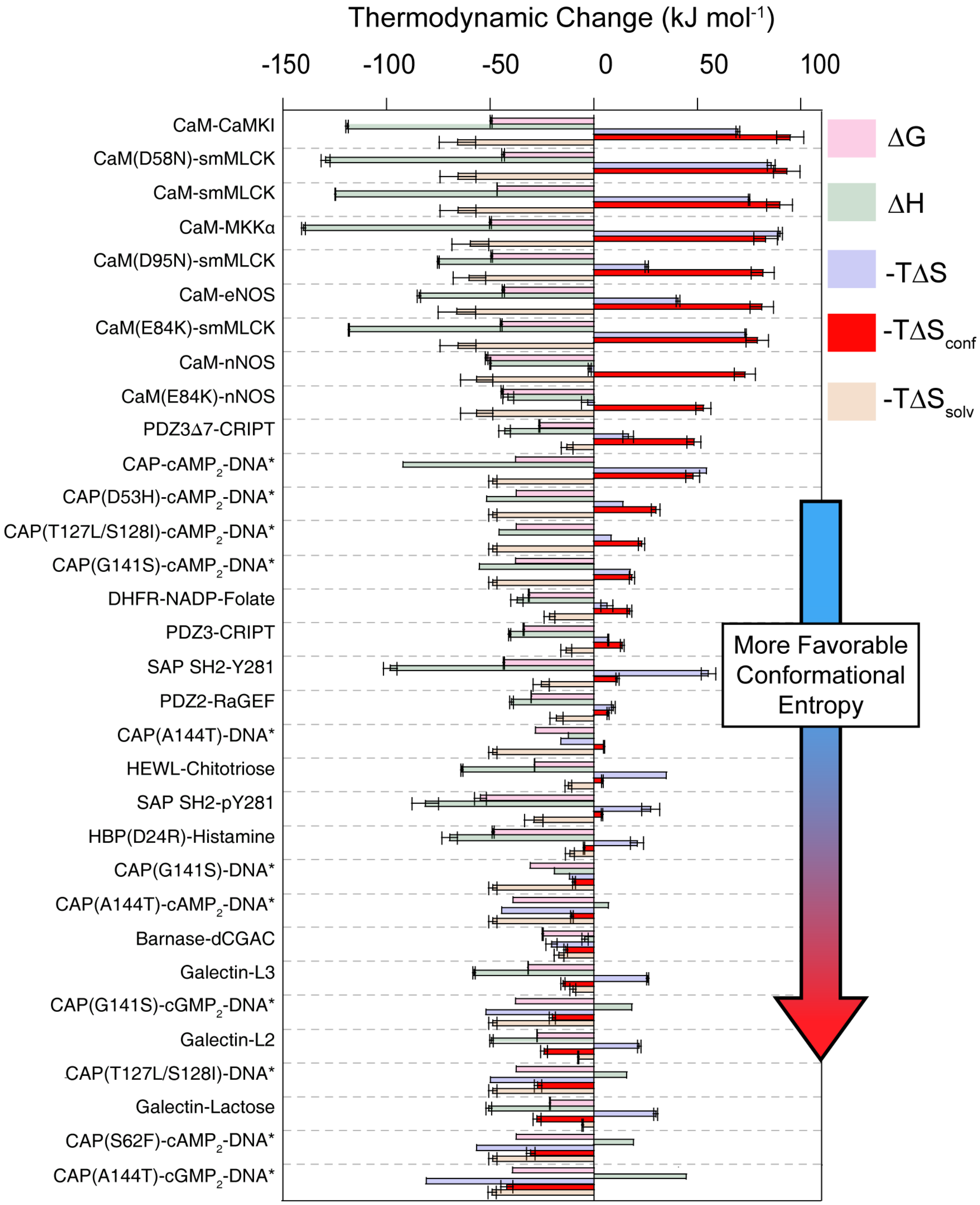

Figure 3-3: Binding Energetics for the different protein-ligand complexes
The broad spectrum of thermodynamic signatures of the different protein-ligand complexes demonstrates an excellent reposity for understanding the role played by protein conformational entropy in binding. The thermodynamic parameters are summarized in Appendix C. Error bars correspond to reported experimental error for ΔG, ΔH, and -TΔS. Error bars for -TΔS$_{conf}$ and -TΔS$_{solv}$ are based on the error for the fitted coefficients in Table 3-1. Data for which error is not available are indicated by an asterisk (*). Note that -TΔS$_{conf}$ and -TΔS$_{solv}$ will not add up to -TΔS due to the contribution of -TΔS$_{RT}$ and deviation from the linear fit in Figure 3-1.

Other entropic contributions to protein-ligand associations are also made accessible by the approached summarized by Figure 3-2 and Equation 3-3. Equation 3-3 allows that there may be other unknown sources of entropy. These might include, for example, (de)protonation events associated with binding [97]. Clearly, if ΔS_{other} is both significant and varies between complexes then the linearity of Equation 3 will be degraded. The observed linear correlation strongly suggests that this is not the case. Thus, if ΔS_{other} is small relative to ΔS_{conf} and $\Delta S_{\mathrm{solvent}}$ then the ordinate intercept represents the loss in rotational-translational entropy (ΔS_{RT}) upon formation of high affinity complexes. ΔS_{RT} has been the subject of extensive theoretical debate but, like conformational entropy, has resisted experimental definition. Here we find that the apparent ΔS_{RT} is -0.10 ± 0.1 kJ $\mathrm{mol}^{-1}\mathrm{K}^{-1}$, which compares quite well to that recently obtained through molecular dynamics simulations [9]. Finally, prior to this work, the contribution of solvent entropy to processes involving proteins has been empirically derived from changes in solvent accessible surface area. Underlying such approaches have been strong assumptions regarding conformational entropy [94], which are not required here. We find that burial of apolar and polar surfaces upon binding both produce a positive (favorable) change in entropy. This is because hydration of polar groups, like that of apolar groups, has a negative entropy of hydration at physiological temperatures, in agreement with a wide range of thermodynamic data on solute, ion and protein hydration [98-100]. We determined the surface area coefficients for apolar (a_1) and polar (a_2) desolvation entropy at 298 K to be +0.081 ± 0.022 J $\mathrm{mol}^{-1}\mathrm{K}^{-1}\,\text{Å}^{-2}$ and +0.033 ± 0.0026 J $\mathrm{K}^{-1}\,\text{Å}^{-2}$, respectively (Table 3-1). The corresponding hydration heat capacity surface area coefficients are also listed in Table 3-1. Burial of hydrophobic area stabilizes the complex through the usual hydrophobic effect. Concomitantly, burial of polar area also stabilizes the complex via release of its hydrating water into the bulk, less ordered state. These coefficient values are markedly different from those obtained previously. This is unsurprising, as the contributions to conformational entropy were explicitly accounted for in this fit.

Implications for the heat capacity of proteins

Several fundamental properties of protein molecules in solution are related to their heat capacity (C_p). The most pertinent definition of C_p here is the derivative of the entropy with respect to the natural logarithm of the temperature:

$$C_p = \frac{\Delta S_{conf}}{d \ln T} \qquad \text{Equation 3-5}$$

Thus, establishment of the "entropy meter" along with suitable temperature dependence data allows the protein conformational contribution to C_p changes to be determined. The relative importance of conformational and solvation contributions to ΔC_p of binding, like that of ΔS,, has been the subject of considerable debate [101], because previously there was no experimental way to isolate the different contributions. The temperature dependence of fast methyl-bearing side chain motion has been examined for only two proteins, ubiquitin [73, 102] and a calmodulin-peptide complex[26]. By combining Equations 3-5 and 3-3, we can probe the contribution of amino acid side chains to the overall protein heat capacity as:

$$C_p^{sc} = s_d N_\chi^{protein} \left\langle \frac{dO_{axis}^2}{d \ln T} \right\rangle \qquad \text{Equation 3-6}$$

From Equation 3-6, we find that the amino acid side chains contribute only a small fraction (~5-6%) to the total heat capacity measured by differential scanning calorimetry (Table C-8). This reinforces the expectation that the vast majority of heat capacity comes from solvent-protein interactions [93, 101, 103].

Conformational entropy of mutant calmodulin-peptide complexes

As part of the entropy meter calibration, we have fully characterized both the dynamics and thermodynamics of binding of three previously studied CaM mutants (D58N, D95N and E84K) [104] in complex with target peptides by ITC and NMR. Specifically, we have measured the binding of smMLCK(p) to D58N and D95N as well as the binding of nNOS(p) to E84K. The thermodynamic data, including contributions from conformational entropy, are shown in Table

3-2.

Table 3-2: Thermodynamics of mutant CaM-peptide binding.

Complex	ΔG (kJ/mol)	ΔH (kJ/mol)	$-T\Delta S_{total}$ (kJ/mol)	$-T\Delta S_{conf}$[b] (kJ/mol)
CaM:smMLCK(p)[a]	-46.6 ± 0.1	-124.7 ± 0.2	+75.0 ± 0.3	-89.8 ± 6.2
CaM(D58N):smMLCK(p)	-43.7 ± 0.6	-129.4 ± 2.2	+85.7 ± 1.9	-93.2 ± 6.4
CaM(D95N):smMLCK(p)	-44.6 ± 0.4	-118.1 ± 0.2	+73.4 ± 0.4	-79.0 ± 5.4
CaM:nNOS(p)[a]	-51.7 ± 0.6	-49.9 ± 0.3	-1.9 ± 0.7	-73.0 ± 5.0
CaM(E84K):nNOS(p)	-44.1 ± 0.6	-41.2 ± 2.7	-2.9 ± 3.1	-52.9 ± 3.6

[a] Data taken from Frederick et al. [11]

[b] Calculated from the entropy meter. Includes both protein and target peptide.

We find that despite the fact that D58N and D95N mutants are pseudo-symmetric, the dynamic response of smMLCK(p) binding varies for these two mutants. While D58N displays nearly identical conformational entropy of binding with respect to wild type, D95N displays a notably smaller value upon binding. In both cases, the smMLCK(p) peptide displays a larger entropic penalty upon binding than the wild-type complex, suggesting that perhaps the entropic penalty of peptide binding is increased when mutant CaM binds a native CaM binding domain. In the case of E84K binding the nNOS(p), E84K experiences a significantly smaller entropic penalty upon binding with respect to wild-type. Curiously, this is partially compensated for by a much larger entropic penalty observed in nNOS(p) upon binding. Looking at the overall conformational entropy change upon binding of these three mutant complexes, we see that calorimetric data correlates well with our observations in changes in dynamics and conformational entropy. In the case of D58N:smMLCK(p), the binding is less favorable entropically but more favorable enthalpically with respect to wild-type. The increased entropic penalty upon binding is consistent with the large decrease in conformational entropy as measured by the dynamical proxy. The opposite trend is observed in D95N:smMLCK(p), where the decreased entropic penalty agrees with the lower conformational entropy of binding. Curiously, E84K:nNOS(p) follows the same qualitative trends as D95N:smMLCK(p) with respect to its wild-type complex, but results in a notable loss of binding affinity. It is also interesting to note that the affinity of all three mutant protein-ligand complexes is nearly identical (Kd ≈ 40nM). These results together with previously characterized CaM-peptide complexes [30] suggest that CaM has evolved to bind different targets with fairly similar affinity even in the presence of perturbing mutations by simultaneously modulating the changes in enthalpy and conformational entropy, portraying a robust thermodynamic landscape.

Conclusions

The range of ligand types employed here suggest that the relationship between fast internal side chain motion and the underlying conformational entropy documented in Fig. 3-2 is universal and represents a fundamental property of proteins. There is no apparent structural relationship for the dynamical (entropic) response to molecular recognition by proteins. The connection between structure, and the enthalpy that it represents, and the conformational entropy and dynamics presents an immediate challenge to our current understanding of protein thermodynamics and function. The experimental approach presented here provides a means to quantify the role of protein conformational entropy and will hopefully both guide refinement of computational approaches and allow experimental access to this crucial component underlying the action of protein molecules.

CHAPTER 4: Conformational entropy of p38α-inhibitor binding: Implications for drug design

This chapter makes extensive use of non-uniformly sampled NMR pulse sequences. These experiments were written by Matthew Stetz, graduate student in the Wand lab.

Abstract

In silico drug discovery has long held the promise to revolutionize the way drugs are designed, but has largely failed to deliver. Historically inhibitors were designed based mainly on static structures that emphasized interaction energetics but ignored potential contributions from conformational entropy. This issue has been difficult to address experimentally. Recently, we have developed an NMR-based approach that employs measures of motion as a proxy for the conformational entropy. Using an empirical calibration, we have shown that the resulting "entropy meter" is both robust and general. We hypothesize that conformational entropy represents a critical "missing piece" in rational drug design. Using the "entropy meter," we examine the effect of conformational entropy on protein-inhibitor interactions using the drug target mitogen-activated protein kinase (MAPK) p38α as a model system. We have assigned the majority of methyl resonances and measured the methyl dynamics of this protein both in the apo state and bound to either a competitive or a non-competitive (allosteric) inhibitor. Using NMR methods, the structural and dynamic effects of inhibitor binding were examined. The effects of binding were found to be structurally localized to the binding sites as well as the so-called catalytic spine region of the protein. In contrast, dynamic perturbations occurred on a much more global scale across the protein. We then applied our dynamical proxy to determine the role of conformational entropy in the binding of both inhibitors. Intriguingly, the conformational entropy change upon binding was found to roughly scale with the total binding entropy. This suggests that conformational entropy may be a tunable parameter in the drug design process. These results promote further studies to understand how small molecule inhibitors may modulate the

dynamics and entropy of protein targets, and how this information can be used to design better lead compounds

Introduction

Protein kinases perform the simple yet essential task of phosphorylating macromolecules in the cell. This task is essential in nearly all processes in the cell, from regulation of cell proliferation to stress responses [105-106]. To date, over 6000 kinase have been added to the PDB database [107]. The structures of these proteins are highly conserved, consisting of N and C terminal lobes connected by a hinge region [108]. Taylor and Kornev have shown that two structurally conserved “spines” play an essential role on the catalytic activity of kinases [109]. While a wealth of structural information exists, numerous studies have demonstrated that protein kinases are highly dynamic molecules with multitudes of complexity in their regulation [110-115]. The majority of studies that have been performed address only the dynamics of the protein in the native state or in the context of native substrates, and most focus on the dynamics of the backbone or on μs-ms timescales typically associated with catalysis. Few studies have dealt with the dynamic effects of the binding of kinase inhibitors.

Because of their roles in several cellular processes, kinases are often sought after drug targets for a wide range of diseases ranging from cancer to inflammatory diseases to hypertension to Parkinson’s disease [116]. Design of both potent and selective inhibitors for such structurally conserved proteins represents a challenge [117]. Thus the ability to design and optimize such inhibitors of protein kinases is of considerable interest. As discussed in Chapter 1, “rational” design of inhibitors has proven difficult, as such design efforts cannot sufficiently address the role of entropy, particularly conformational entropy. The contribution of conformational entropy is often assumed to be almost always unfavorable [52] , yet its contribution has been difficult to address experimentally. Furthermore, computational methods are not able to robustly determine the conformational entropy of protein-ligand binding due to the inability to sample the vast degrees of freedom of a protein-ligand complex [43]. We seek to examine the effect of conformational entropy on protein ligand binding using our NMR-based approach. Here we use the drug target mitogen-actived protein kinase (MAPK) p38α to explore the role of conformational entropy in drug design.

p38α MAPK is involved in inflammation pathways [118] and is a current drug target for inflammatory diseases such as COPD and Rhematoid Arthritis [119-121]. p38α is activated by dual phosphorylation in the TGY motif of the activation loop [122]. Here we examine the binding of the resting state (non-phosphorylated) p38α to two potent inhibitors with distinct binding modes to determine if conformational entropy plays an appreciable role in the energetics of binding. The first of these inhibitors is the pyridinyl imidazole inhibitor SB203580, which is known to be a type I (ATP competitive) inhibitor of p38α [123]. The second inhibitor, the diaryl urea compound BIRB796, is an allosteric inhibitor of p38α, binding to an inactive conformation of the kinase and resulting in a conformational change in the conserved DFG loop of the kinase [124]. This ligand has previously been shown by NMR to bind with a conformational selection mechanism [125]. The structures of these complexes are shown in Figure 4-1. We first perform calorimetry to determine the overall thermodynamic of binding of two inhibitors with distinct binding modes. We then assess the structural and dynamic changes that occur upon inhibitor binding in the context of knowledge of these highly tuned molecular machines. Finally, we consider the observed dynamic changes in the context of the ‘entropy meter’ to determine if conformational entropy plays a significant role in protein-inhibitor interactions and thus may be a tunable parameter in drug design.

Results and discussion

Overall thermodynamics of binding

We first determined the overall binding thermodynamics of p38α to the two inhibitors using ITC (Figure 4-2). We find that both molecules bind with low nM affinity (Kd=17.6 ± 8.5nM and 1.9 ± 4.2nM for SB203580 and BIRB796, respectively. These numbers are in general agreement with the literature [125]. Unsurprisingly, the affinity of each compound is driven almost entirely by enthalpy. Calorimetric studies have shown that in most optimization efforts, an

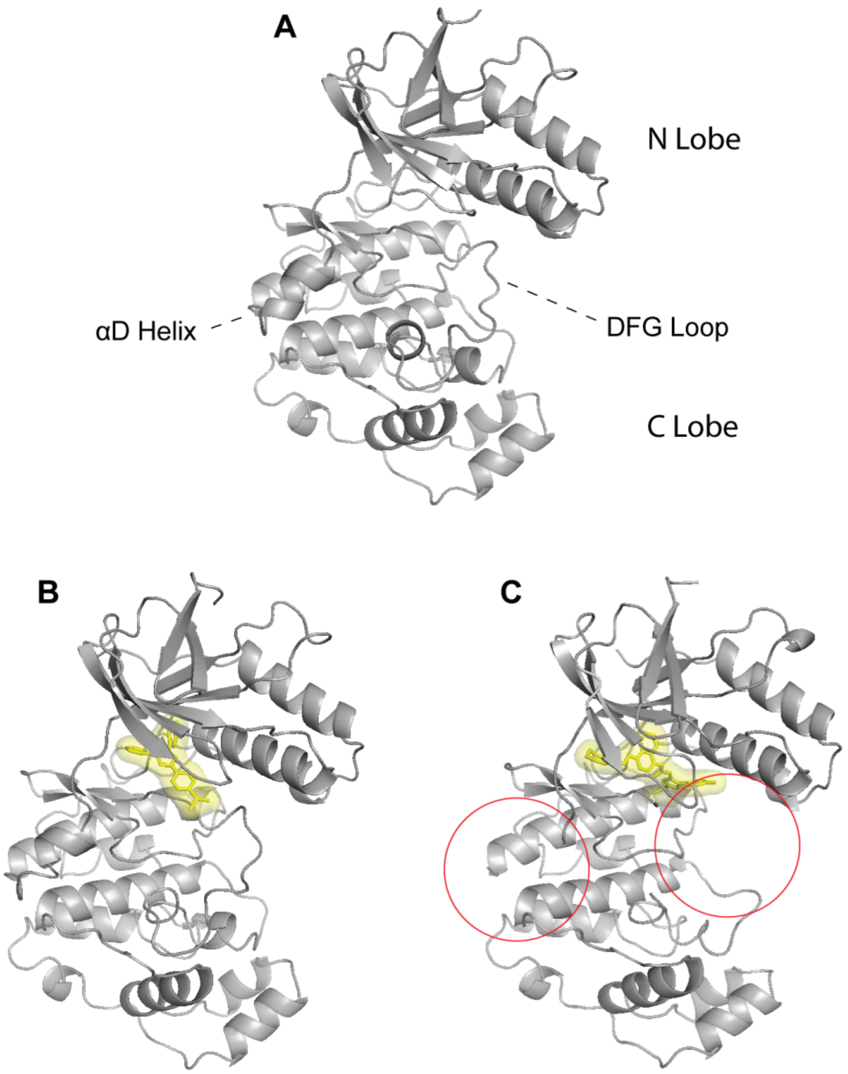

Figure 4-1: Structures of resting state p38α in the apo form (A:1P38) and bound to two inhibitors of interest, SB203580 (B:1A9U) and BIRB796 (C:1KV2).
Note that the αD helix and the DFG loop are both disordered in the BIRB796-bound complex (red circles). However, αD helix has extremely high crystallographic B factors in 1P38 and 1A9U, suggesting this may be an artifact of crystallographic refinement.

optimized drug will display a favorable enthalpy [52]. The binding entropy of these two compounds differs, with SB203580 binding being associated with a slightly favorable binding entropy (-TΔS= -0.48kcal/mol), whereas BIRB 796 is associated with a slightly unfavorable entropy of binding (-TΔS= +1.11 kcal/mol). The latter is more than compensated by a largely favorable enthalpy of binding, resulting in a roughly 10-fold higher affinity for BIRB 796 than for SB203580. It is notable that the total binding entropies of these two compounds differ in sign. The available thermodynamic data suggest that the difference in binding modes does not display a general trend in terms of thermodynamic signature [126-127]. Furthermore, no information is available on the contributions of the various components of the binding entropy, namely the solvent entropy or conformational entropy. It is well established that the burial of both polar and apolar surface area is entropically favorable [128], but the magnitude of this contribution is unclear. Could this partially explain the difference in binding entropy? The contribution of conformational entropy is also unclear. To address the role of the entropic subcomponents in these binding interactions, we employ NMR relaxation techniques and our recently established dynamical proxy.

Resonance assignments

Assignments of the backbone and ILV methyl side chains of resting state apo p38α MAPK have been reported previously[129-130]. We have largely confirmed these assignments using a suite of backbone and side chain experiments. Backbone assignments of the apo protein were confirmed using TROSY HNCA and agree very well with previously published assignments. Backbone assignments of the drug-bound complexes were performed using non-uniform sampled (NUS) [131] versions of the TROSY HNCA and HN(CA)CB. More information about non-uniform sampling is provided in Appendix D.

ILV methyl side chain assignments of all three states were performed using either Cartesian or NUS versions of the methyl “Divide and Conquer” experiments [132-133] as well as Cartesian 4D $^{13}C/^{13}C$ and in the case of the apo protein $^{13}C/^{15}N$ -HSQC-NOESY-HSQC experiments. Methyl assignment statistics can be found in Table 4-1.

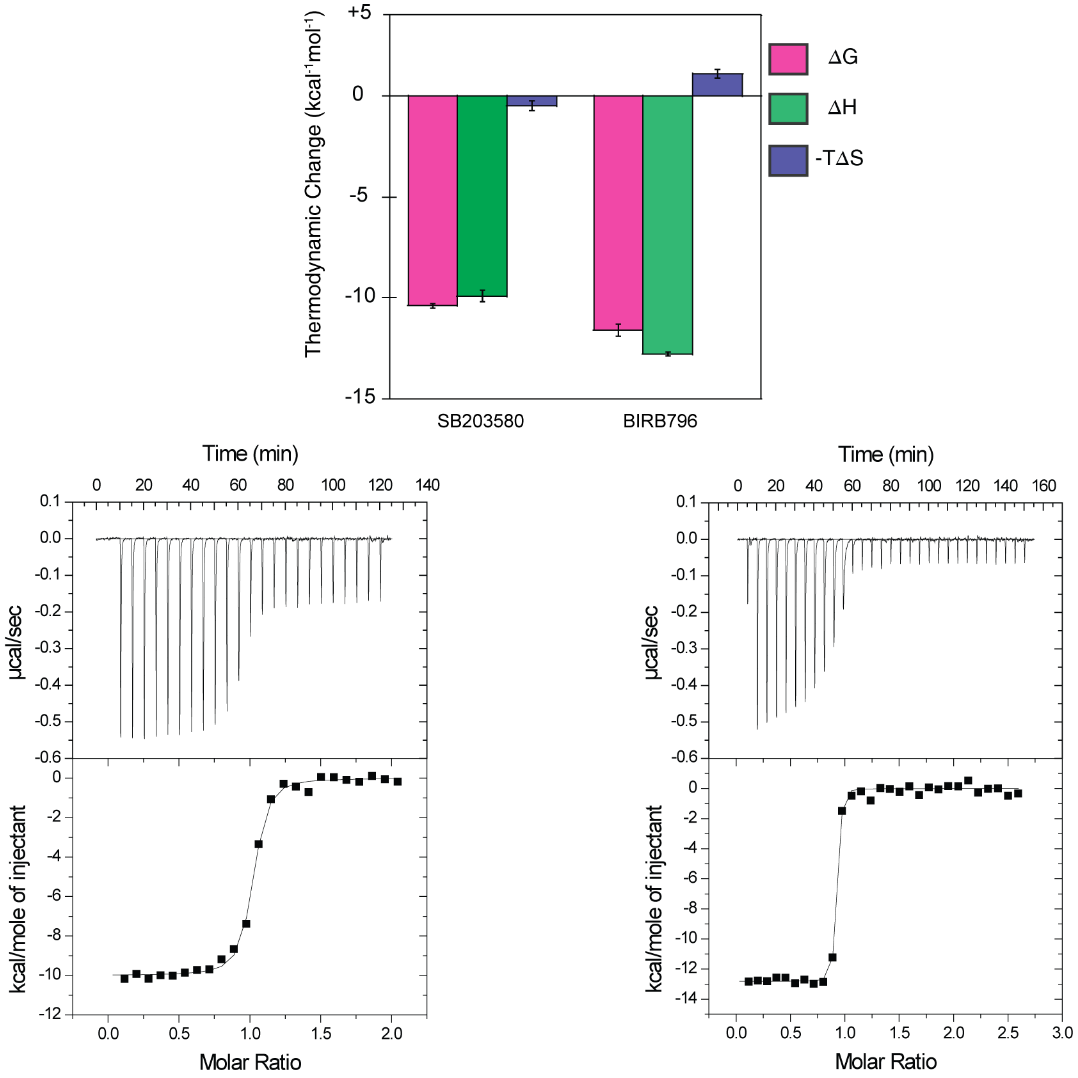

p38α-SB203580

p38α-BIRB796

Figure 4-2: Thermodynamics of p38α-inhibitor binding.
Experiments were performed in triplicate. Error bars represent the standard deviation between experiments. Example thermograms and titration curves are shown for each of the inhibitors. The correction for the heat of dilution have been performed for each titration curve. Experimental details are outlined in Appendix D.

Table 4-1: Methyl assignment statistics of apo and inhibitor-bound p38α

	Observed Methyls[a]	Assigned and Observed	Resolved Methyls[b]	Resolved and Assigned	Methyl Coverage[c]
p38α	139/150	138/139	98/139	96/98	98/150(65%)
p38α-SB203580	131/150	130/131	97/131	95/97	97/150(65%)
p38α-BIRB796	138/150	132/138	110/138	102/110	110/150(73%)

[a] Peaks that are detected in a ^{13}C HMQC spectrum, including peaks that are degenerate
[b] Peaks that are non-degenerate and can be analyzed by NMR spin relaxation
[c] The percentage of methyl groups in the protein that can be used to report on its overall dynamics

Structural changes upon inhibitor binding

With a significant portion of the backbone and methyl resonances assigned in both the apo and inhibitor bound states, we can assess the site-specific structural perturbations that occur upon binding these inhibitors. The methyl and backbone chemical shift perturbations (CSPs) are mapped onto the structure of the inhibitor-bound complexes in Figure 4-3. Unsurprisingly, a large amount of chemical shift perturbations (CSPs) occurred near the inhibitor binding sites. Both inhibitors exhibit large chemical shift perturbations in the proximity of the αD helix and the β7-β8 region of the protein. This region of the protein has been shown to be a docking site for both upstream and downstream substrates of p38α [134]. This region of the protein is also notable, as several residues in this region comprise one of two “hydrophobic spines” that are conserved across protein kinases [108]. These spines are proposed to be regions of the protein that allow communication between the N and C lobes. Regions of αD and β7-β8 comprise the catalytic spine (C-spine). This spine is not structurally contiguous in the apo protein and is completed by the binding of ATP into the active site. Analyzing the structures of p38α, we observe several residues both within and directly surrounding the C-spine experience very large CSPs, corresponding to $\Delta\delta_{\text{weighted}}$ >0.4ppm, where:

$$\Delta\delta_{weighted} = \sqrt{(\Delta\delta_H)^2 + \left(\Delta\delta_X \frac{\gamma_X}{\gamma_H}\right)^2} \qquad \text{Equation 4-1}$$

In Equation 4-1, X corresponds to either ^{13}C or ^{15}N and γ corresponds to the gyromagnetic ratio. The resulting CSPs suggest a localized structural rearrangement of the residues around this conserved structural unit. Recently, Shimada and colleagues showed that essentially no spectral change occurs when the native substrate, ATP, binds to inactive p38α [130]. This suggests that the structural rearrangement we observe is not simply a result of the completion of the C-spine by a ligand. It is curious to note that no significant structural differences are observed between the crystal structures of the apo and inhibitor-bound states (Backbone RMSD <0.8 Å). Concomitantly, the crystallographic B-factors of the αD helix in the apo and SB203580-bound structure are on

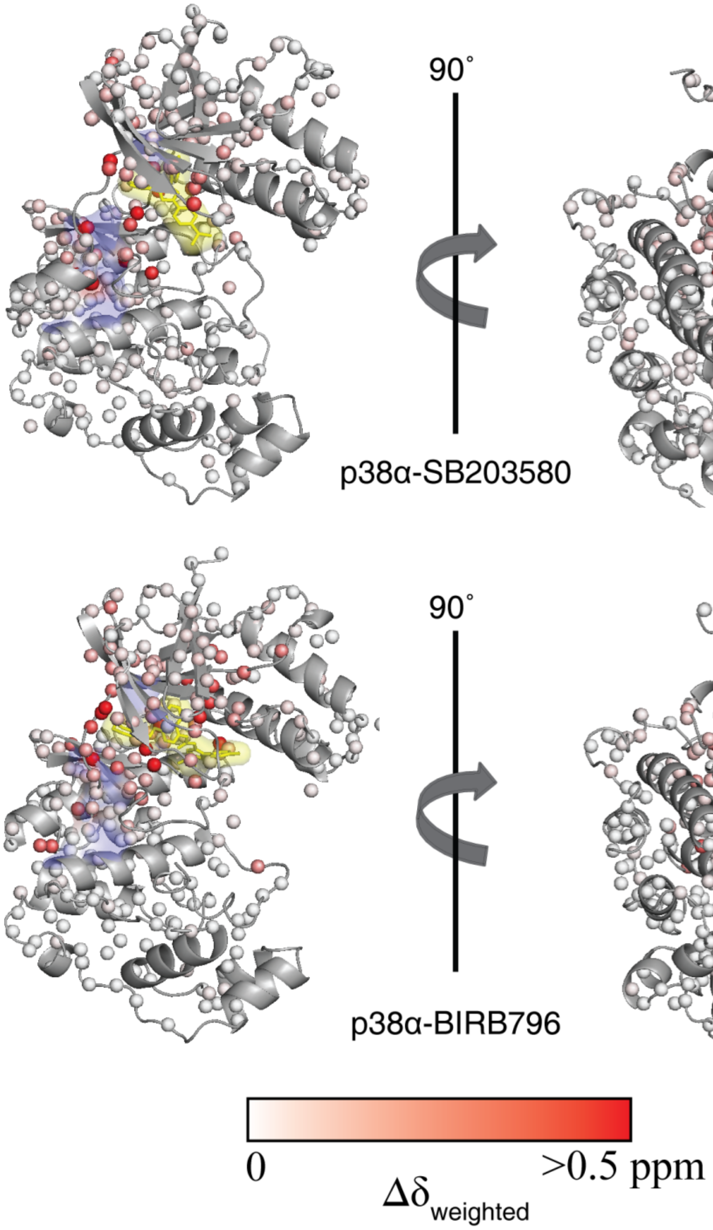

Figure 4-3: Chemical shift perturbations of inhibitor binding to p38α MAPK. Spheres represent backbone amide nitrogens and ILV methyl carbons that have been assigned for each complex. Ligands are shown in yellow. The hydrophobic "C-spines" are mapped in blue.

the order of 60-95 $Å^2$ and in the BIRB796 bound structure, this region is entirely unresolved. This suggests a large degree of conformational equilibrium in this region, which may be perturbed or disrupted by inhibitor binding. To further address this, we have determined dynamic perturbations of the protein by NMR relaxation methods.

Characterization of macromolecular tumbling

We have used NUS-sampled [131] versions of standard TROSY-detected ^{15}N backbone relaxation experiments to determine the overall tumbling of resting state p38α both in its apo and inhibitor bound states[135]. The rotational correlation times and backbone dynamics of all three states were determined from ^{15}N T_1 and T_2 measurements at 14.1T and 17.6T. Data were fit to the Lipari-Szabo model free formalism[21]. For each complex, a data set of approximately 115 resonances was used to calculate τ_m values. Full details can be found in appendix D.

It should be noted that one would not expect *a priori* for the macromolecular tumbling of the protein to change significantly when binding a small molecule drug. High-resolution crystal structures show minimal structural perturbation in both the absence and presence of ligand [123-124, 136]. Based on analysis of the ^{15}N relaxation, all three states were found to tumble isotropically. The tumbling times were determined to be 32.5ns, 30.8ns, and 33.0ns for apo, SB203580-bound, and BIRB796-bound p38, respectively. These molecular tumbling times are all notably longer than what has been previously observed for the activated form of p38α [137]. This is not surprising, given a difference in experimental temperature and the consequent difference in the viscosity of the solvent. While the BIRB 796 complex displays a comparable τ_m to the apo state, SB203580 shows a notably lower (~7%) tumbling time than apo p38. The reasons for this are not clear. One potential cause of the different τ_m values could be related to the fidelity of the NUS reconstruction of data (see Appendix D), which is a source of controversy in the literature [138]. It has been noted in particular, that a higher peak density may warrant the need for a higher sampling percentage than is employed in this study. To confirm that this confounding issue does not significantly distort the τ_m , it was recalculated using a sparse set of peaks that excluded any ^{15}N resonances within two times the line width of one another in the NUS (^{15}N) dimension. If significant NUS reconstruction artifacts were present, we would expect a significant impact on the experimentally determined τ_m using this subset of our data. However, the resulting τ_m values were within 1% of the original value. This confirms that the NUS sampling schedule and sampling density employed here can be used to determine a τ_m value of a moderately sized (40kDa) protein. Unfortunately, this does not resolve the issue of deviant macromolecular tumbling. Furthermore, we speculate that the presence of slower timescale motions may also distort the τ_m of the p38-SB203580 complex. These motions can be detected through the T_1T_2 product for ^{15}N relaxation peaks [139], though no deviant behavior was detected in this case. The notably lower τ_m in the p38-SB203580 complex remains quite puzzling and is not supported by theoretical hydrodynamic calculations such as the boundary element method or HYDRONMR [140-143]. We speculate that another factor not detectable by our NMR relaxation data may be contributing to the deviant τ_m. This prevents a robust analysis of site-specific dynamic perturbations of the amide backbone, and the backbone dynamics will not be explored further. As notable differences in the τ_m are not anticipated, we have used the average τ_m value for all three complexes (32.1ns) for analysis of side chain relaxation.

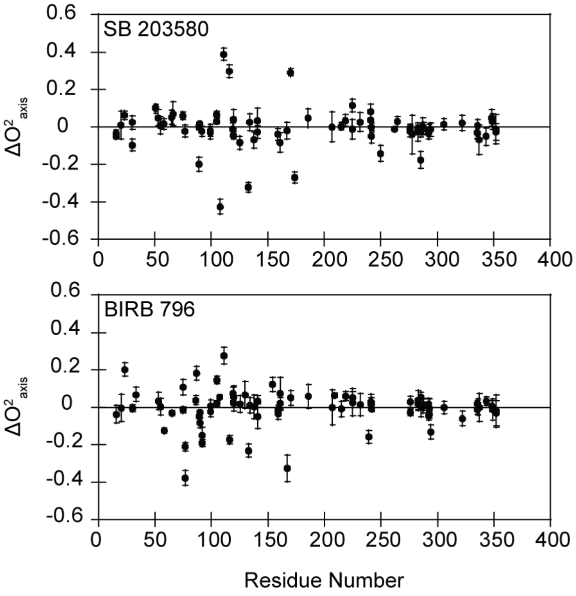

Figure 4-4: Changes in ILV methyl dynamics upon inhibitor binding.

Methyl dynamics of p38a

Carbon methyl axis generalized order parameters (O^2_{axis}) of ILV methyl resonances were calculated from the $^{13}CHD_2$ isotopomer from 13C T_1 and T_2 relaxation rates at 14.1T and 17.6T. Additional details are available in appendix D. A large degree of spectral degeneracy is present in the methyl spectra, and several functionally interesting residues are obscured. Approximately 100 (74%) of the 135 observed methyls are resolved in each of the three states. Despite this, we are still able to make pairwise comparisons of O^2_{axis} for 80 methyl sites in p38α upon binding these inhibitors. Plots for ΔO^2_{axis} can be found in Figure 4-4. A number of residues display large changes in ΔO^2_{axis} upon binding. Surprisingly, these dynamic changes do not correspond to an increase in rigidity as is often thought intuitively in protein-drug interactions. Instead, both increases and decreases in dynamics are observed near the active site (Figure 4-5). Furthermore, propagation of dynamic changes throughout the protein is apparent in both states. If we examine the spatial distribution of dynamic changes as a function of proximity to the inhibitor, we find that there are several significant changes in regions of the protein in the C lobe, quite distal to the active site (Figure 4-6). This suggests a complex network of dynamics across the protein. It is also interesting to note that the extent of overall dynamic perturbation is larger for BIRB796, supporting the fact that an allosteric inhibitor will, by definition, have a more global effect on the dynamic state of the protein.

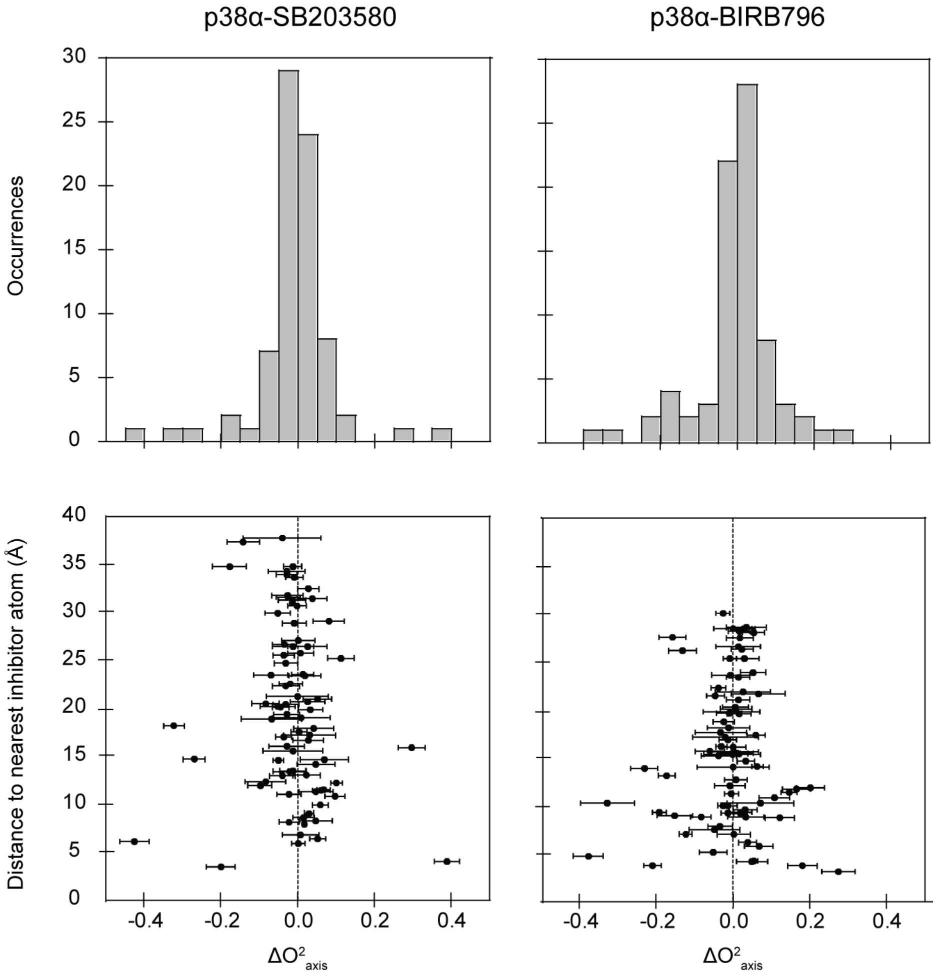

Figure 4-5: Distance dependence of dynamic perturbations of p38α-inhibitor binding.

As we observed with the structural perturbations, a large deal of dynamic perturbations occur in the "peri-spinal region" (Figure 4-6). Several residues on the αE helix flanking the base of the C-spine become more dynamic, while other residues, namely Leu 113, display differential dynamic trends between binding of the competitive and allosteric inhibitor. This residue is one of two hydrophobic residues that faces downward to contact residues on the αF helix at the "base" of the C-spine. Upon binding SB203580, Leu 113 becomes very rigid ($O^2_{axis} \approx 0.9$) and is flanked by several residues which become dynamic. Curiously, upon binding BIRB796, the Leu 113 becomes notably more dynamic and the residues flanking it become more rigid. This result suggests that this residue, as part of the hydrophobic spine, displays dynamics that report on the overall state of the protein. We speculate that in the case of the ATP-competitive inhibitor, the enzyme may not be able to fully distinguish a native substrate from its inhibitor and rigidifies the hydrophobic spine in preparation for catalysis. A similar result has been observed with the binding of the enzyme dihydrofolate reductase to a folate-competitive inhibitor, where the protein displays some motions typically associated with native substrate binding [144]. We must note, however, that we do not have any information regarding dynamic pertubations that occur upon native substrate binding. Such studies would be valuable in distinguishing dynamic perturbations that are associated with substrate binding from those that are associated with potential dynamic modes of inhibition. Outside of the "peri-spinal region," several changes in dynamics are observed in both the N and C lobes upon inhibitor binding. On the whole, it seems that significant dynamic changes are well dispersed across the protein. Several more subtle dynamic changes occur in the C lobe of the protein, quite far from the binding site (Figure 4-6). For both inhibitors, the overall change in methyl dynamics across the protein is small ($\Delta\langle O^2_{axis}\rangle = +0.004\pm0.036$ and $+0.012\pm0.037$ for SB203580 and BIRB796, respectively). It appears that, in this regard, the binding of these inhibitors does not greatly affect the dynamics of the protein. This has interesting implications for the overall conformational entropy change upon inhibitor binding.

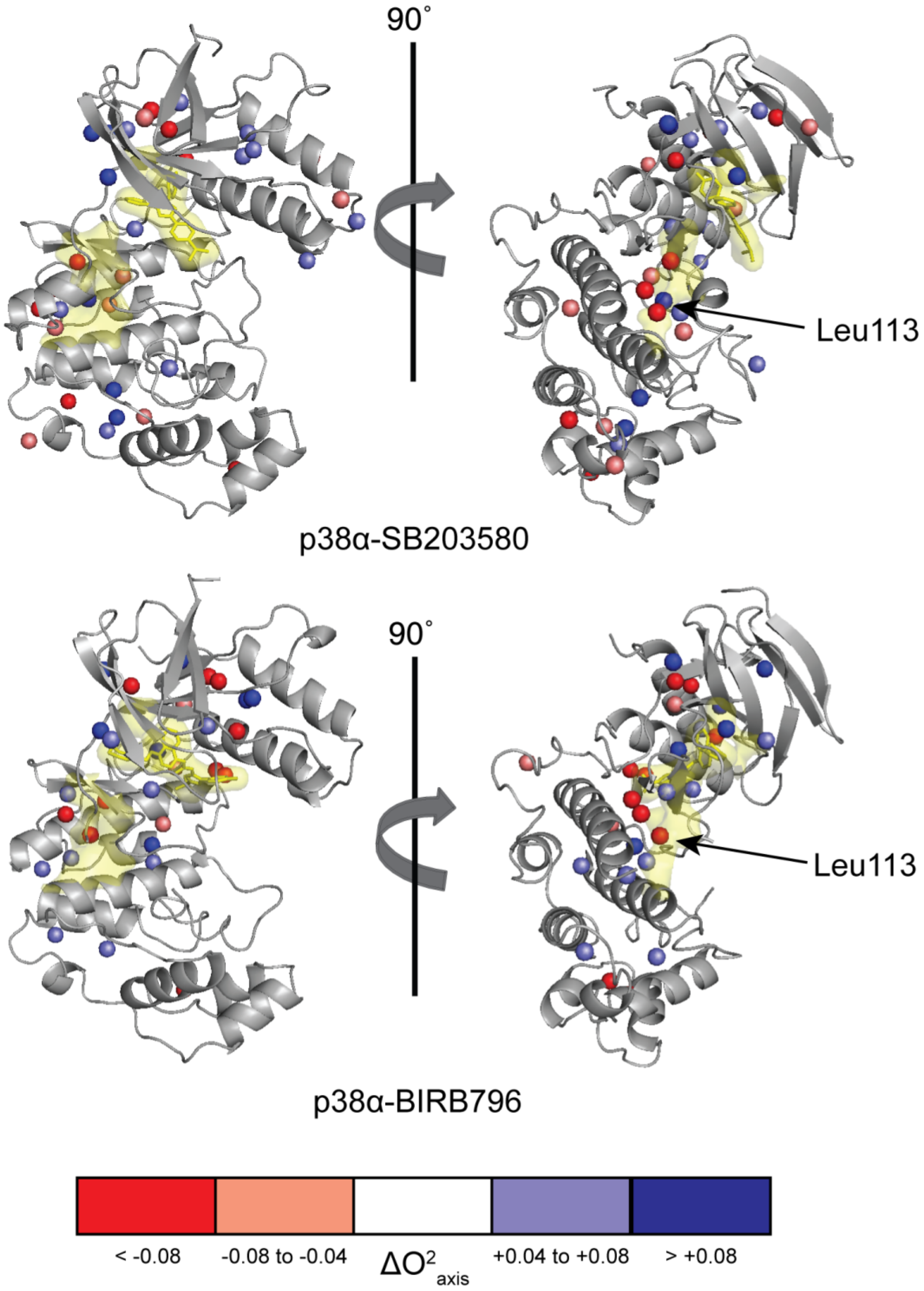

Figure 4-6: Statistically significant perturbations of dynamics for the binding of two p38a inhibitors.
Several residues become either more dynamic (red) or more rigid (blue) upon inhibitor binding. Dynamic changes in the protein are distributed throughout the protein. The ligand is shown in yellow with a yellow surface. The catalytic (C) spine is also shown as a yellow surface, demonstrating how each ligand "completes" the C-spine, but result in differential dynamical responses. Leucine 113 is highlighted, which displays differential dynamics between the two inhibitors.

Conformational entropy of binding: implications for drug design

As described in Chapter 3, we developed a conformational “entropy meter” to discern conformational entropy changes from NMR dynamics. This method employed a data set of 32 protein-ligand complexes with a manifold of binding partners to empirically calibrate not only the change in conformational entropy, but also the change in solvent entropy derived from changes in polar and apolar surface area. Combining the NMR and ITC data collected here with changes in acessible surface area from the published crystal structures, we find that both p38-inhibitor complexes fit on the entropy meter (Figure 4-7), suggesting that we can use it to dissect the ΔS_{total} measured from NMR relaxation. Analyzing the crystal structures of the apo and p38-inhibitor complexes, we determine that the changes in solvent entropy are almost identical ($-T\Delta S_{solv}$=-5.1 ±0.6 kcal/mol and =-5.1 ±0.8 kcal/mol for SB203580 and BIRB796, respectively). This implies that solvent entropy does not explain the difference in ΔS_{total} observed from ITC. This is somewhat surprising given the changes in conformation of the DFG loop between the two inhibitors. It has been suggested that the change in ΔS_{RT} is essentially constant for tight-binding macromolecular interactions [9] . The 'entropy meter' outlined in Chapter 3 supports this. Could conformational entropy be a differentiating factor?

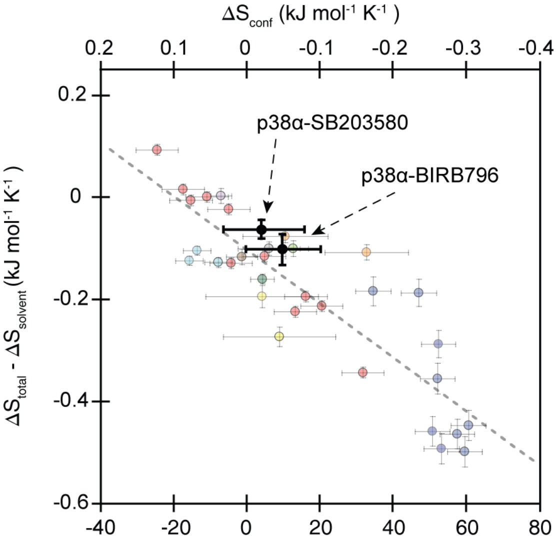

Figure 4-7: Position of the p38α-inhibitor complexes on the conformational entropy meter.
The error bars are as described in Figure 3-2.

Using the measured changes in dynamics, we can apply the dynamical proxy to determine the conformational entropy of binding of these two complexes. It must be noted that the methyl coverage for the protein is somewhat low (~65%). This might suggest that our NMR-derived order parameters may not be able to appropriately represent the overall dynamic state of the protein. The $\Delta\langle O^2_{axis}\rangle$ values may be biased by the lack of available probes in the analysis. This has implications for the conformational entropy of the protein, as larger proteins are more sensitive to errors in the measurement of ΔO^2_{axis}. This is due to the fact that the observed dynamic change is scaled by $N_{\chi,}$, which increases with increasing size. The sensitivity of the measurement to limited methyl coverage is highlighted by calculating the dynamic changes in another way, namely the average of the pairwise changes in O^2_{axis}, or $<\Delta O^2_{axis}>$ instead of $\Delta<O^2_{axis}>$. The results are shown in Table 4-2.

Table 4-2: Overall dynamic changes upon p38a-inhibitor binding

		NON-PAIRWISE COMPARISON			PAIRWISE COMPARISON		
	$<O^2_{axis}>$	$\Delta<O^2_{axis}>$	Methyl probes (free, bound)	Methyl Coverage (free, bound)	$<\Delta O^2_{axis}>$	Probe pairs	Methyl Coverage
p38α	0.582 ± 0.025	-	-	-	-	-	-
p38α-SB203580	0.586 ± 0.025	0.004 ± 0.036	98,97	65%, 64%	-0.012 ± 0.037	79	52%
p38α-BIRB796	0.593 ± 0.027	0.012 ± 0.037	98,110	65%, 74%	-0.004 ± 0.038	83	55%

Note that the two methods result in opposite signs for dynamic changes, but the trend of BIRB 796 having a larger dynamical penalty upon binding is upheld. It should be noted that a pairwise comparison ($<\Delta O^2_{axis}>$) omits more methyl probes and thus exacerbates the issue of methyl coverage across the protein. The pairwise comparison of methyl probes is a function of the overlap of the NMR spectrum, which we assume is essentially random. Thus the difference between $<\Delta O^2_{axis}>$ and $\Delta<O^2_{axis}>$ may then be due simply to omission of an additional 20% of the data. To address this, we pseudorandomly omitted up to 25% of methyl probes for both the free and bound states and calculated the resulting $\Delta<O^2_{axis}>$. The results of this simulation are shown in Figure 4-8. Indeed, we find that the value of $<\Delta O^2_{axis}>$ (pairwise) is almost precisely one standard deviation of $\Delta<O^2_{axis}>$ with 20% of the data omitted.

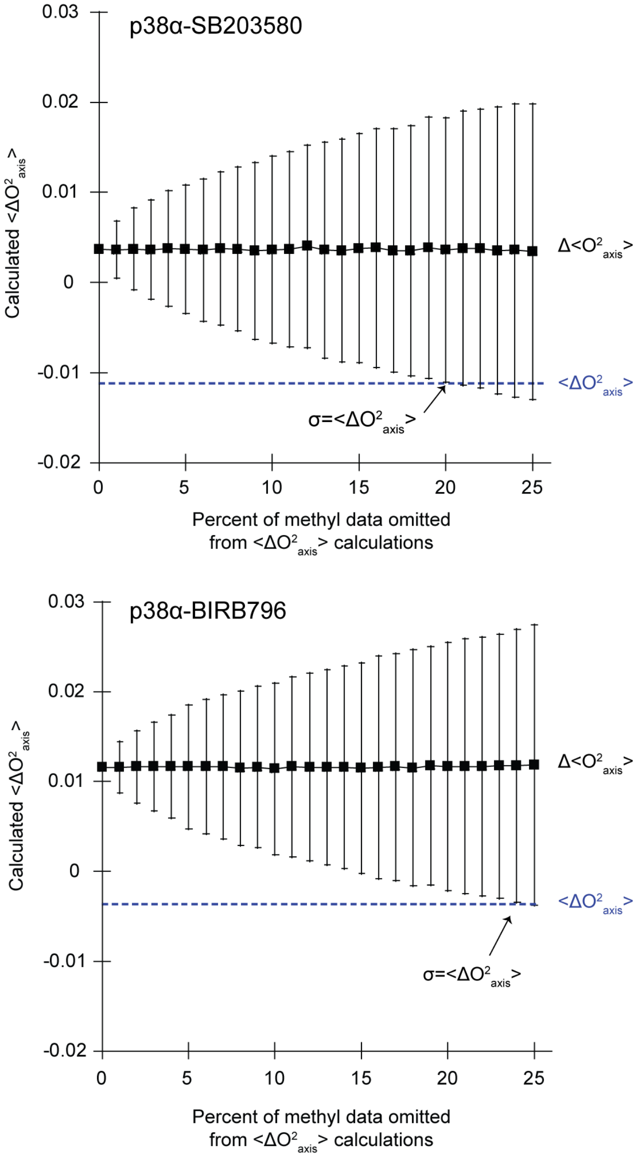

Figure 4-8: Reconciliation between $\Delta\langle O^2_{axis}\rangle$ and $\langle \Delta O^2_{axis}\rangle$ values.
Using the O^2_{axis} values for the free and bound states, a set percentage of methyl probes were randomly thrown out and $\langle \Delta O^2_{axis}\rangle$ was calculated for the binding of both inhibitors. The points and error bars represent the mean and standard deviation σ (respectively) in $\langle \Delta O^2_{axis}\rangle$ for 10,000 subsamples at which x% of date were omitted. The corresponding value of $\Delta\langle O^2_{axis}\rangle$ is shown as a blue dotted line. The point at which $\sigma=\langle \Delta O^2_{axis}\rangle$ corresponds to the percentage of data that is omitted from the calculation of $\Delta\langle O^2_{axis}\rangle$ versus $\langle \Delta O^2_{axis}\rangle$

This suggests that the observed difference between $<\Delta O^{2}_{axis}>$ and $\Delta<O^{2}_{axis}>$ is simply due to a decrease in effective methyl coverage. The issue of the precision of $\Delta<O^{2}_{axis}>$ remains. We make the conservative assumption that the error can be reflected with respect to the difference between $\Delta<O^{2}_{axis}>$ and $<\Delta O^{2}_{axis}>$. For both inhibitors, this corresponds to an error in $\Delta<O^{2}_{axis}>$ of 0.015. In this regard, we acknowledge that propagation of the error will consequently lead to large errors in conformational entropy, which will be reflected in our analysis.

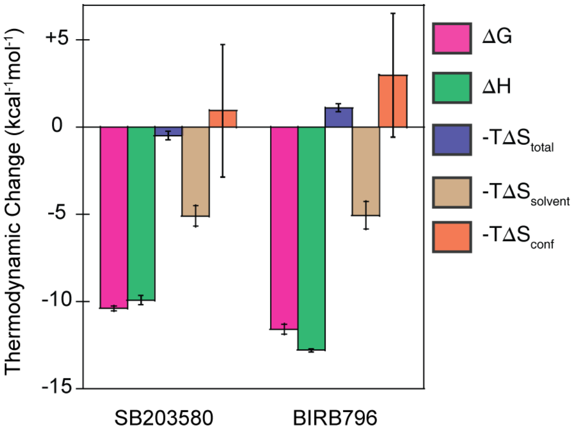

Figure 4-9: Thermodynamics of p38α-inhibitor binding, including contributions for conformational and solvent entropies.
Errors in ΔG, ΔH, and -TΔS are as in Figure 4-2. The error in $-T\Delta S_{solvent}$ comes from the error in the solvent entropy coefficients from the entropy meter. The error in $-T\Delta S_{conf}$ is derived from the uncertainty in $\Delta<O^{2}_{axis}>$ as expressed in Figure 4-7.

Using the entropy meter, we find that the conformational entropy of inhibitor binding is appreciable ($-T\Delta S_{conf}$=0.9 ± 3.7 kcal/mol and 2.9 ± 3.7 kcal/mol for SB203580 and BIRB796 respectively). It is interesting to note that despite the large uncertainties outlined above, the differences in ΔS_{conf} between the two inhibitors appears to scale roughly with the differences in ΔS_{total} from ITC (Figure 4-9). This suggests that conformational entropy accounts for the difference in binding entropy for the two inhibitors. This is supported by the fact that the solvent entropy, often a major contributor in the total binding entropy, does not vary between the two inhibitors. Taken together, these results provide evidence that while conformational entropy is often unfavorable as observed here, it may be a tunable parameter in drug design.

Conclusions

We have found that in the case of p38α MAPK, dynamic changes that occur across the protein can lead to a more shallow conformational entropy change upon binding than one might expect *a priori*. In some regard, this is encouraging to the drug designer, as conformational entropy may be less of a threat to high affinity binding. Concomitantly. this also adds to the complexity of considerations in drug design. The “rules” for tuning conformational entropy have not yet been established, and thus an “entropically optimized” compound cannot yet be designed. A study of two notably different compounds with distinct binding modes cannot provide a thorough prescriptive knowledge of how to optimize conformational entropy. Follow-up studies will be needed to determine if the addition of a given functional group can significantly affect the overall conformational entropy of binding of a compound. Given this, it is curious to speculate that conformational entropy may be an important consideration in overcoming the barrier of enthalpy-entropy compensation often encountered in drug design [50, 145].

In summary, conformational entropy presents yet another layer of complexity with respect to lead optimization in drug discovery, but also opens the possibility of a new class of drugs whose binding can be supported if not driven by a favorable conformational entropy of binding.

CHAPTER 5: Conclusions

Summary

The goal of this work was to establish the relationship between protein dynamics and conformational entropy and apply this relationship in the context of rational drug design. Chapter 2 demonstrated the curious nature of protein side chain dynamics. In the case of the villin headpiece subdomain, spatially segregated classes of motions can occur. This unprecedented result demonstrates an interesting case study for the spatial distribution of different motional classes in proteins. It also provides further insight into the native state conformational ensemble of the highly studied protein, and may have interesting implications for the thermodynamics of folding of this protein. Furthermore, it highlights the need for a full hydration layer to recapitulate the native state dynamics of proteins, and precludes its analysis using the dynamical proxy between NMR dynamics and entropy. Chapter 3 demonstrated that solution state methyl dynamics can reliably report on the conformational entropy. This has allowed for the calibration of an ‘entropy meter’ that provides a quantitative estimate of both the conformational entropy and solvent entropy of a binding event. Furthermore, it provides insight into the relative distribution of protein heat capacity from the protein, which challenges previous calculations [146]. This demonstrates the power of the entropy meter to provide a deeper understanding of the underlying thermodynamics of proteins. Chapter 4 demonstrated that the binding of inhibitors to p38a MAPK have distinct structural and dynamic effects on the kinase, particularly in the structurally conserved hydrophobic spine regions. It also demonstrated that two different classes of p38α kinase inhibitors exhibit differential dynamic changes upon binding. These dynamic changes are not uniformly unfavorable, as traditional drug design efforts might assume. Instead, the protein appears to adapt to the binding of inhibitors through a complex dynamic network that exists across this protein. This likely diminishes the entropic penalty of binding. Furthermore, the total binding entropy of these two compounds appears to roughly scale with the calculated conformational entropy determined from NMR dynamics. This suggests that conformational entropy may represent an additional tool in the toolbox for the drug designer. Taken together, this work further demonstrates the complexity of protein dynamics and their implications in the underlying thermodynamics of protein-ligand interactions.

Future Directions

The relationship between solution NMR-derived dynamics and conformational entropy has been shown to be both robust and general. However, the relationship is purely empirical and as such offers a means of further exploration. The ordinate intercept of the entropy meter represents the quantity (ΔS_{RT}+ΔS_{other}), where ΔS_{other} represents contributions to the entropy that have not been accounted for, such as the entropy of (de)protonation upon binding[97]. As highlighted in Chapter 3, if ΔS_{other} represents a significant contribution to the overall binding entropy the linear relationship will be degraded. We have clearly demonstrated this is not the case. It is curious to note that the value of (ΔS_{RT}+ ΔS_{other}) across the data set agrees very well with an approximation of the RT entropy alone from molecular dynamics. This quantity was argued to be constant for high-affinity protein-ligand complexes [9]. Therefore one could interpret the ordinate intercept of the entropy meter as the constant ΔS_{RT} and the observed "scatter" in the entropy meter containing information about ΔS_{other}. We expect that as various theoretical and experimental determinations of the various terms of ΔS_{other} are more robustly defined, this observed scatter will further decrease for our data set. The work presented in Chapter 3 provides an excellent benchmark to account for additional entropic terms in the context of the full entropic equation.

The application of the entropy meter to drug design presents an exciting line of inquiry, as we have shown conformational entropy may be a tunable parameter in this context. The work presented here provides preliminary evidence of conformational entropy's role in lead optimization, but further work will be required to begin to understand the "rules of the game" with respect to entropic optimization. Of particular interest would be to explore the consequences of the addition of functional groups to a lead candidate by both biocalorimetry and NMR relaxation methods similar to those employed in Chapter 4. This would complement previous studies only employing the former [50] by allowing a deeper understanding of the entropic side of binding. Such work would begin to allow the drug designer to more deeply understand the consequences of given functional groups at the interface of structure and dynamics to ultimately begin to "rationalize" rational drug design.

APPENDIX A: Chapter 1

Spectral density equations for ^{13}C and ^{15}N relaxation.

$$\frac{1}{T_1} = \frac{1}{4} d^2 \left\{ J(\omega_H - \omega_X) + 3(\omega_X) + 6(\omega_H + \omega_X) \right\} + c^2 J(\omega_X)$$

$$\frac{1}{T_2} = \frac{1}{8} d^2 \left\{ J(\omega_H - \omega_X) + 3(\omega_X) + 6(\omega_H + \omega_X) + 4J(0) + 6J(\omega_H) \right\} + \frac{c^2}{6} [4J(0) + 3J(\omega_X)] + R_{ex}$$

$$NOE = 1 + \frac{T_1 d^2}{4} \frac{\gamma_H}{\gamma_X} \left\{ 6J(\omega_H + \omega_X) - J(\omega_H - \omega_X) \right\}$$

$$c = \frac{(\omega_H \Delta\sigma)^2}{3}$$

$$d = \frac{1}{4} \left(\frac{\mu_0}{4\pi} \right)^2 \frac{(\hbar \gamma_H \gamma_X)^2}{r^6}$$

Where μ_o is the permeability of free space, γ_H and γ_X are the gyromagnetic ratios of H and X (^{15}N or ^{13}C) respectively, $\hbar$ is Planck's constant divided by 2π, r is the effective bond length, and Δσ is the chemical shift anisotropy in ppm.

Spectral density equations for ^{2}H relaxation.

$$\frac{1}{T_1(D)} = \frac{3}{16} \left(\frac{e^2 qQ}{\hbar} \right)^2 \left[J(\omega_D) + 4J(2\omega_D) \right]$$

$$\frac{1}{T_{1\rho}(D)} = \frac{1}{32} \left(\frac{e^2 qQ}{\hbar} \right)^2 \left[9J(0) + 15J(\omega_D) + 6J(2\omega_D) \right]$$

Where $\frac{e^2 qQ}{h}$ is the quadrupolar coupling constant and h is Planck's constant ($h = 2\pi\hbar$). It has been suggested that the dipolar contribution to the relaxation mechanism will contribute less than 2.5% to the relaxation mechanism as is neglected here [24].

APPENDIX B: Chapter 2

Materials and methods

Sample preparation:

The experiments were performed on homogenously $^{13}C/^{15}N$ –labeled and partially deuterated sample stemming from expression in 65% D_2O/35% H_2O. This leads to methyl group isotopomers distribution with the CH_2D isotopomer detected by the relaxation experiments. The expression, according to the method of Bi. et al., relies on a fusion of HP36 via a factor Xa cleavage sequence to the C-terminus of the N-terminal domain of the ribosomal protein L9.[147] As described by Marley et al., BL21 (DE3) cells were transformed with the L9-HP36 fusion plasmid were grown in 4 L of Luria Broth to an OD_{600} of 0.8, then harvested by centrifugation and washed once with M9 salts.[148] The resulting pellet was re-suspended in 1 L M9T minimal media with 0.8 g/L $^{15}NH_4Cl$, 3 g/L ^{13}C-glucose and in 65% D_2O/35% H_2O. Cells were allowed 1 hour to recover, then protein expression was induced by addition of Isopropyl β-D-1-thiogalactopyranoside to a final concentration of 1 mM. The cells were harvested after 12 hrs. The cells were lysed with lysozyme treatment and sonication and the spun at 300,000 g for 1hr. The supernatant was applied to a Sephadex G75 column (2 cm x 100 cm) run in 20 mM tris(hydroxymethyl)aminomethane, 100 mM NaCl, 5 mM $CaCl_2$, and 0.01% azide, pH 7.5 (cleavage buffer) at 0.5 – 1 ml/min. Fractions containing the L9-HP36 fusion protein were pooled and lyophilized. The lyophilized powder was resuspended in water and further purified by high performance liquid chromatography (HPLC) and a C18 column (Vydac) eluted with a linear water-acetonitrile gradient with 0.1% trifluoroacetic acid throughout. Fractions containing the fusion protein were pooled and lyophilized. The fusion protein was resuspended in cleavage buffer and treated with 8 units of factor Xa per mg of protein at room temperature overnight. The cleaved HP36 was then purified by HPLC. The HP36 fractions were lyophilized and stored at -20 ^{o}C. The identity and purity of the sample was confirmed by mass spectroscopy, ^{15}N NMR HSQC spectrum, and reverse- phase high performance liquid chromatography. The sample was resuspended in 90%:10% H_2O:D_2O. The resulting buffer conditions were 50 mM Sodium Acetate-d_3, pH 5.4. A 4 mM HP36 sample was used for collecting NMR assignments, which was adjusted to 2 mM HP36 for collection of relaxation experiments.

NMR Spectroscopy

All NMR experiments were collected using Bruker Avance III NMR spectrometers equipped with cryogenic probes. Assignments of the methyl groups in HP36 were determined by collection of a (H)CC(CO)NH-TOCSY[149] and a 2D H-H NOESY[150] experiments. Our assignments are in good agreement with the previously published assignments for a similar construct, HP67.[151] NMR relaxation data of methyl side chain CH_2D isotopomers were collected at 14.1T and 17.6T using the IzCz-compensated $I_zC_zD_z$ and $I_zC_zD_y$ experiments.[24, 152] These experiments were carried out at 275, 279, 284, 289, 295, and 305K. Temperatures were calibrated before each set of experiments using a methanol-d3 standard sample. For each pseudo-3D relaxation experiment, nine delays were collected with three duplicate points to estimate the error in the decay rates. The relaxation delays for these experiments ranged from 1.5 – 60 ms and 0.6 – 27.5 ms for $I_zC_zD_z$ and $I_zC_zD_y$, respectively.

Relaxation Data Analysis

The rotational correlation time of HP36 at each temperature was calculated using the boundary element method, which has been described elsewhere and has been shown to be a robust method for determination of macromolecular tumbling [140-142]. The molecular surface of Villin HP36 (1VII) was constructed using in-house software.[153] The viscosity of the solution was determined from standard values of water at each experimental temperature.[154] The resulting rotational correlation times at 275, 279, 284, 289, 295, and 305K were 5.40 ns, 4.68 ns, 3.96 ns, 3.40 ns, 2.87 ns, and 2.22 ns, respectively. The N-terminal methionine residue was removed for these calculations as it is known to be unstructured in solution and its inclusion leads to large (~10%) biases in the macromolecular tumbling time. Exponential decays were fit using in-house software to determine T_1 and T_{1p} rates. Model free parameters (O^2 and τ_e) were determined using a grid search approach[155] utilizing software and parameters as described elsewhere.[156] Errors were determined using the Monte Carlo method. O^2_{axis} values were obtained by division by 0.111, which assumes a tetrahedral geometry of the methyl groups.

Banding analysis

To determine the "banding" of the O^2_{axis} parameters at each temperature, a Bayesian approach was used as described previously [27] using in-house software. The approach was performed separately for a data set of all methyl order parameters at each temperature. No assumptions about the number (or even existence) of bands was made. In each case, a two-band model was the best fit to the data set. The N-terminal residue, Met41, was excluded from this analysis. If included, the Bayesian approach identified three bands, with the population of the third band having a band center near the theoretical lower limit of O^2_{axis} and populated only by Met41.

Molecular dynamics simulation and determination of in silico order parameters

A molecular dynamics simulation of the villin headpiece (PDB: 1VII) was performed using NAMD2[157] with the CHARMM27 [158] all-atom parameters and an explicit TIP3P water potential.[159] Hydrogen atoms were added to the villin headpiece crystal structure with VMD.[160] The protein was centered in a TIP3P water box such that the initial minimum protein-boundary distance was 6 Å. The simulation was conducted with a 2 fs timestep. Bonds to hydrogen atoms were constrained with the SHAKE algorithm.[161] A switching distance of 10 Å and cutoff distance of 12 Å were used for nonbonded interactions, along with a particle mesh Ewald summation (1 Å grid spacing) for long-range electrostatic interactions. The simulation utilized the Langevin method to ensure constant temperature and pressure (1 atm). The simulation was performed at 295K to match experimental conditions of the solution state measurements. Following a 200 ps equilibration run, a production run of 120 ns was performed. Lipari-Szabo order parameters were determined from the simulation as described previously.[53]

Data tables and figures

Figure B-1: Methyl assignments of HP36 at 293K

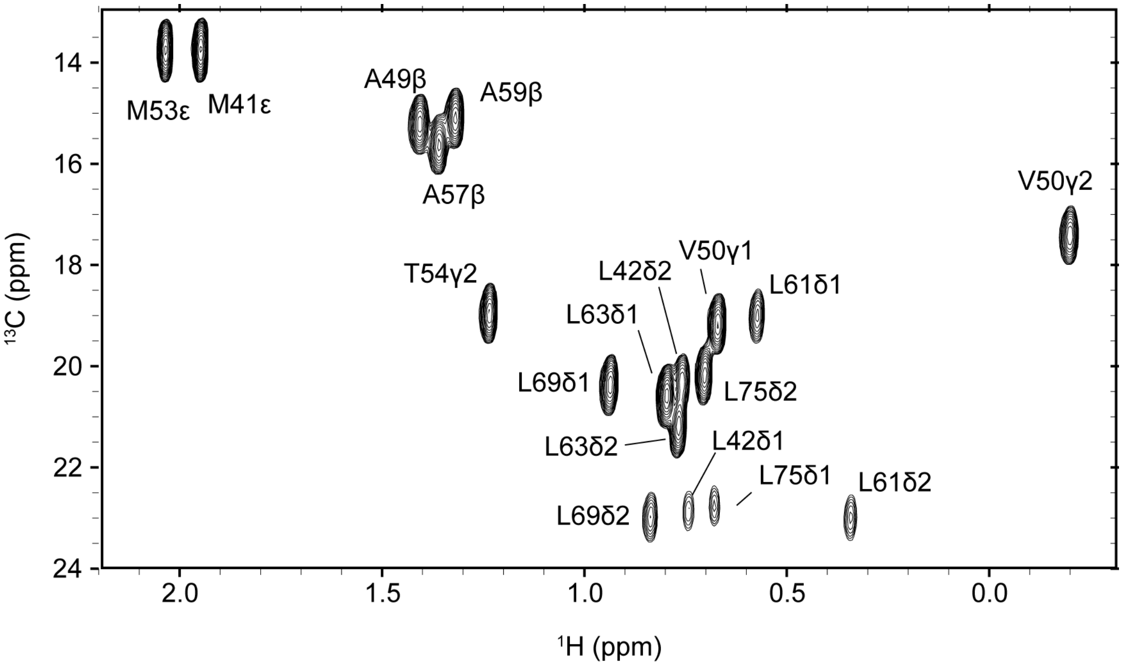

Table B-1: Methyl order parameters of HP36 at 275K, 279K, 284K, 289K, 295K, and 305K

	O^{2}_{axis}					
	275K	**279K**	**284K**	**289K**	**295K**	**305K**
Met41Cε	0.062±0.02	0.049±0.019	0.065±0.024	0.067±0.003	0.105±0.012	0.216±0.007
Leu42Cδ1	0.539±0.02	0.49±0.014	0.469±0.016	0.412±0.002	0.337±0.006	0.232±0.008
Leu42Cδ2	0.418±0.066	0.469±0.037	0.493±0.026	0.472±0.004	0.418±0.032	0.278±0.032
Ala49Cβ	1.013±0.013	0.992±0.008	0.954±0.01	0.927±0.002	0.897±0.011	0.838±0.01
Val50Cγ1	0.849±0.002	0.819±0.001	0.787±0.007	0.763±0.001	0.706±0.002	0.649±0.001
Val50Cγ2	0.822±0.007	0.792±0.005	0.76±0.006	0.728±0.001	0.698±0.007	0.641±0.008
Met53Cε	0.711±0.016	0.671±0.012	0.644±0.015	0.62±0.002	0.544±0.019	0.488±0.014
Thr54Cγ2	0.93±0.003	0.905±0.002	0.873±0.009	0.849±0.001	0.822±0.002	0.773±0.012
Ala57Cβ	0.897±0.001	0.868±0.001	0.857±0.006	0.814±0.001	0.787±0.001	0.752±0.003
Ala59Cβ	0.913±0.012	0.889±0.008	0.862±0.017	0.846±0.001	0.795±0.009	0.752±0.007
Leu61Cδ1	0.752±0.004	0.722±0.003	0.701±0.014	0.666±0.001	0.641±0.003	0.587±0.011
Leu61Cδ2	0.808±0.029	0.79±0.018	0.754±0.016	0.695±0.003	0.663±0.018	0.609±0.018
Leu63Cδ1	0.318±0.002	0.302±0.002	0.275±0.011	0.256±0.002	0.234±0.001	0.197±0.019

	O^2_{axis}					
	275K	**279K**	**284K**	**289K**	**295K**	**305K**
Leu63Cδ2	0.337±0.007	0.315±0.005	0.304±0.005	0.28±0.001	0.253±0.003	0.207±0.004
Leu69Cδ1	0.461±0.008	0.45±0.007	0.418±0.005	0.38±0.001	0.364±0.004	0.307±0.007
Leu69Cδ2	0.577±0.013	0.566±0.011	0.55±0.009	0.488±0.001	0.463±0.009	0.407±0.011
Leu75Cδ1	0.35±0.008	0.321±0.008	0.283±0.009	0.264±0.001	0.213±0.005	0.135±0.015
Leu75Cδ2	0.407±0.021	0.383±0.017	0.348±0.012	0.31±0.001	0.291±0.001	0.245±0.001

Table B-2: Internal correlation times of HP36 at 275K, 279K, 284K, 289K, 295K, and 305K

	τ_e (ps)					
	275K	**279K**	**284K**	**289K**	**295K**	**305K**
Met41Cε	10±4.3	10±3.6	7.5±3.6	7.5±4.5	5±3.1	2.5±3
Leu42Cδ1	112.5±3.4	102.5±1.8	90±2	80±2.8	70±1.6	60±1.1
Leu42Cδ2	57.5±1.2	50±1.7	45±0.8	40±1.6	37.5±0.3	35±0.2
Ala49Cβ	65±2.1	57.5±1.1	52.5±1.4	47.5±1.3	42.5±0.9	37.5±0.5
Val50Cγ1	37.5±4.5	35±2.3	32.5±2.1	30±2.8	30±2.1	27.5±1.5
Val50Cγ2	97.5±5.7	87.5±3	80±2.9	72.5±4.1	65±3.2	55±2.4
Met53Cε	7.5±2.5	7.5±1.6	7.5±3.8	7.5±4.1	10±1.5	10±1
Thr54Cγ2	42.5±2.6	40±1.4	37.5±1.7	35±1.9	32.5±1.4	30±1.2
Ala57Cβ	75±2.7	70±1.5	62.5±2	60±2.1	55±1.4	47.5±1.1
Ala59Cβ	40±0.4	37.5±0.2	35±1.3	32.5±1.5	32.5±0.2	30±0.7
Leu61Cδ1	45±1.1	42.5±0.7	40±1	37.5±0.9	35±0.7	32.5±0.5
Leu61Cδ2	62.5±0.5	57.5±0.5	55±0.8	50±0.7	47.5±0.5	42.5±0.8
Leu63Cδ1	62.5±0.4	57.5±0.3	52.5±1.8	47.5±0.3	42.5±0.1	35±0.3
Leu63Cδ2	70±0.8	65±0.6	57.5±1.2	52.5±0.4	47.5±0.2	40±0.3
Leu69Cδ1	57.5±6.4	52.5±3.4	50±2.5	47.5±3.3	42.5±2.4	37.5±1.7
Leu69Cδ2	152.5±4.7	137.5±4.7	120±1.9	107.5±4.1	92.5±1.9	75±2.1
Leu75Cδ1	72.5±3.5	65±3.7	60±1.4	52.5±2.8	47.5±0.6	42.5±1.7

	τ_e (ps)					
	275K	**279K**	**284K**	**289K**	**295K**	**305K**
Leu75Cδ2	47.5±1.8	42.5±1.6	40±1.2	37.5±1.2	32.5±0.1	27.5±0.9

APPENDIX C: Chapter 3

Materials and Methods

Sample preparation

Calmodulin mutants and target peptides and complexes were prepared in 20 mM imidazole (pH 6.5), 100 mM KCl, 6 mM $CaCl_2$ and 0.02% (w/v) NaN_3 as described elsewhere [30, 162]. The SAP SH2 domain was prepared as described[163]. The pY281 (Ac-RKSLTIYAQVQK-COOH) and pY281 (Ac-KKSLTIpYAQVQK-COOH) peptides were obtained from Genscript (Piscataway, NJ). The ecDHFR:folate binary complex was prepared as described previously and refolded to remove endogenous ligands[164]. The genes coding for both barnase and barstar were cloned into a pETDUET vector with both barnase and barstar under the control of their own T7 promoter. Barnase contained a N-terminal His_{6x}-tag followed by a Factor Xa cleavage site while Barstar remained untagged. Barstar was also expressed separately from a pET-15b vector containing N-terminal His_{6x}-tag. The barnase-barstar complex was isolated by Ni-NTA affinity chromatography and further purified by size-exclusion chromatography. Free barnase was isolated from the purified barnase-barstar complex by denaturation in 9 M urea pH 7.4 at 25°C for 4 hours and purification on a DEAE anion exchange column equilibrated at pH 7.4. Barnase (pI 9.0) was collected from the flow through and subjected to multiple rounds of dialysis followed by size-exclusion chromatography. dCGAC was purchased from Integrated DNA Technologies (Coralville, IA) . NMR and calorimetry experiments with barnase and its complex were done with samples prepared in 20 mM potassium phosphate pH 6.6, 1 mM DTT, 10% D_2O and 0.02% NaN_3 (azide). Histamine-binding protein (HBP) with a D24R mutation (to abolish the second histamine binding site) was expressed from pET-15b vector with an N-terminal His_{6x}-tag followed by a thrombin cleavage site. HBP(D24R) was isolated using a cobalt resin column with a pH gradient from 7.5 to 5.0 using 50 mM sodium phosphate with 300 mM NaCl further purified using size-exclusion chromatography. NMR and calorimetry experiments with HBP(D24R) and its complex with histamine were done with samples prepared in 50 mM potassium phosphate pH 7.3, 5% D_2O and 0.02% NaN_3 (azide).

Isothermal Titration Calorimetry

Isothermal titration calorimetry (ITC) measurements were carried out on a VP-ITC instrument (Microcal) at the same temperature and buffer conditions as the corresponding NMR relaxation data. In cases where DTT is present in the buffer (SAP SH2-Y281/pY281 and DHFR:Folate-$NADP^+$), The DTT concentration was lowered to 0.1-0.2mM. All samples were prepared as described above and centrifuged at 4000 RPM for 10 mins to remove precipitate. ITC experiments of Calmodulin Mutant-peptide binding were performed as described previously [30]. For SAP SH2-peptide binding, samples were centrifuged at 4000 RPM for 10 minutes to remove any precipitate. 5-25μM SAP SH2 domain was titrated with 265-365μM peptide. For ecDHFR:Folate-$NADP^+$ binding, 60uM ecDHFR pre-bound to 360uM folate was titrated with 935-995μM $NADP^+$. 4-6μL injections were used. Data analysis was performed using the Origin software. Data were corrected for the heat of dilution as necessary. Example thermograms and fits of all protein-ligand complexes described above can be found in Figure C-1.

NMR Spectroscopy

Free proteins and their complexes were assigned using standard triple resonance strategies. The resonance assignments have been deposited in the BMRB under accession numbers 25727, 25728, 26619 and 26620. Barnase relaxation studies employed ^{13}C-relaxation using the $^{13}CHD_2$ isotopomer [165] essentially as described elsewhere[166]. Calmodulin and histamine binding protein relaxation studies utilized deuterium relaxation [24] essentially as described elsewhere [156]. O^2_{axis} parameters were determined from T_1 and $T_{1\rho}$ relaxation measured at two magnetic fields. Rotational correlation times and O^2_{NH} were determined from ^{15}N relaxation obtained at two magnetic fields. Model-free parameters [21] were determined using a

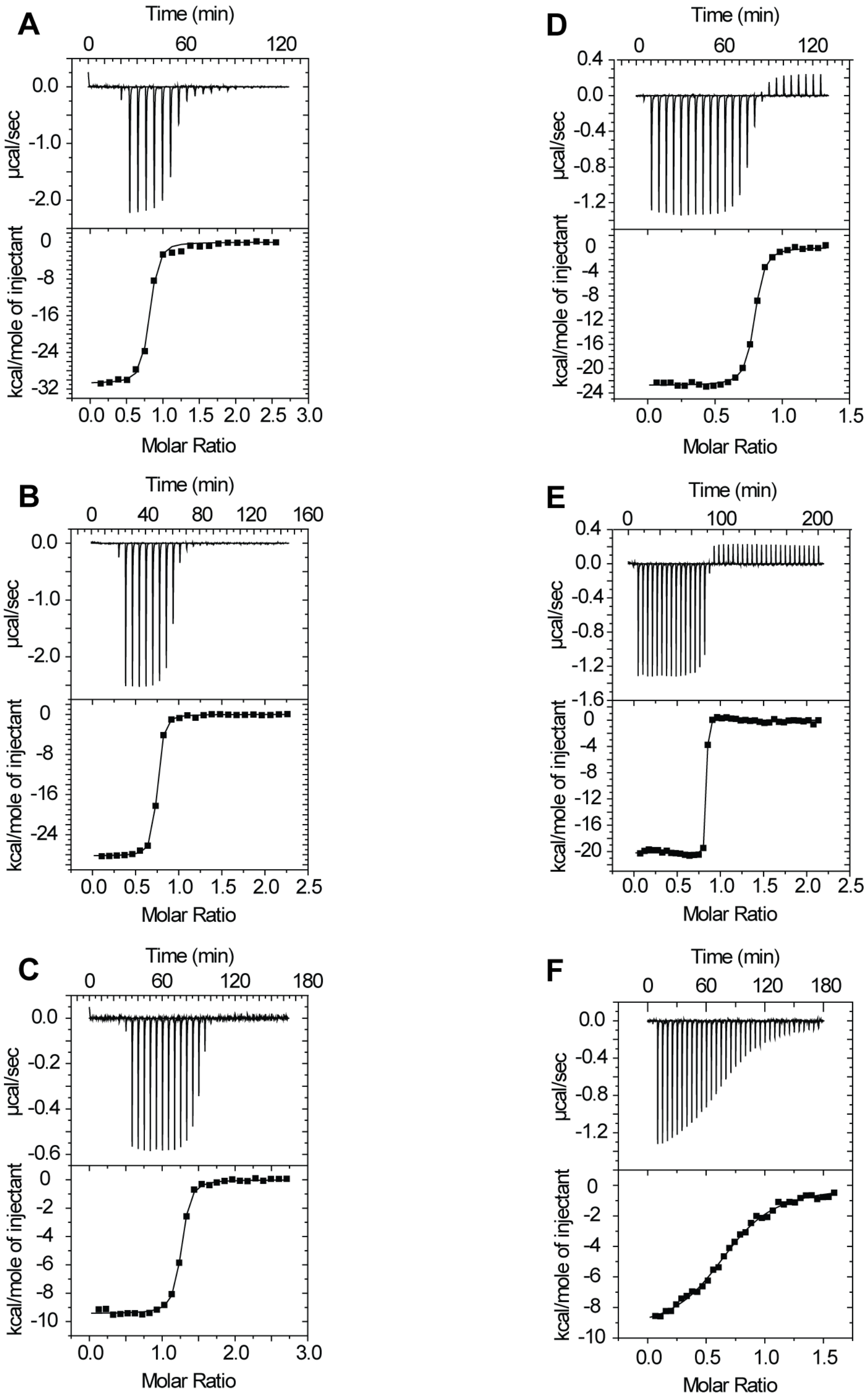

Figure C-1: ITC thermograms and fits of complexes measured in Chapter 3.
Example thermograms for (A) CaM(D58N)-smMLCK(p), (B) CaM(D95N)-smMLCK(p), (C) CaM(E84K)-nNOS(p), (D) SAP SH2-Y281, (E) SAP SH2-pY281, and (F) ecDHFR:Folate-NADP$^+$. All experiments were performed in triplicate. Thermodynamic parameters for these and other protein-ligand complexes are found in Tables C-1 and C-2.

grid search approach using a quadrupolar coupling constant of 167 kHz, an effective N-H bond length of 1.04 Å and a general ^{15}N tensor breadth of 170 p.p.m. O^2_{axis} and O^2_{NH} parameters have been deposited in the BMRB under accession numbers 26619, 26620, 26621 and 26622. The appropriate tumbling model was identified through statistical analysis.

Fitting of the entropy meter

The optimization and statistical analysis of the parameters obtained for the empirical calibration of the entropy meter (Table 3-1) was performed using nonlinear least-squares regression analysis by fitting to Equation 3-3. The errors in the fitted parameters were estimated using Monte Carlo sampling (N=100,000) where the fitting procedure was repeated taking into account the errors in $\Delta\langle O^2_{axis}\rangle$. This error was assumed to be 10%. Changes in polar and apolar accessible surface area were calculated using AREAIMOL[167] as described previously [30]. Further details are provided in the Supplementary Tables below.

Data Tables

Table C-1: Protein-Ligand Complexes Used

Index	Protein:Ligand	K_d (M)[§]	PDB Code	Reference
1	CaM:CaMKKα(p)	$3.6 \pm 0.7 \times 10^{-9}$	1XO2, 1CKK	[10, 30]
2	CaM:smMLCK(p)	$1.3 \pm 0.5 \times 10^{-8}$	1XO2, 1CDL	[10, 30]
	CaM(E84K):smMLCk(p)	$4.1 \pm 0.8 \times 10^{-8}$	1XO2, 1CDL	[10, 30]
4	CaM:CaMKI(p)	$4.1 \pm 0.8 \times 10^{-9}$	1XO2, 1MXE	[10, 30]
5	CaM:eNOS(p)	$4.6 \pm 0.5 \times 10^{-9}$	1XO2, 1NIW	[10, 30]
6	CaM:nNOS(p)	$1.7 \pm 0.4 \times 10^{-9}$	1XO2, 2O60	[10, 30]
7	CAP:cAMP2:DNA	3.6×10^{-7} ± NA	1G6N, 1CGP	[13]
8	CAP(D53H):cAMP2:DNA	4.2×10^{-7} ± NA	1G6N, 1CGP	[13]
9	CAP(S62F):cAMP2:DNA	4.2×10^{-7} ± NA	1G6N, 1CGP	[13]
10	CAP(T127LS128I):DNA	4.2×10^{-7} ± NA	1G6N, 1CGP	[13]
11	CAP(T127LS128I):cAMP2:DNA	4.2×10^{-7} ± NA	1G6N, 1CGP	[13]
12	CAP(G141S):DNA	5.9×10^{-6} ± NA	1G6N, 1CGP	[13]
13	CAP(G141S):cAMP2:DNA	3.6×10^{-7} ± NA	1G6N, 1CGP	[13]

14	CAP(G141S):cGMP2:DNA	3.6×10^{-7} ± NA	1G6N, 1CGP	[13]
15	CAP(A144T):DNA	1.6×10^{-5} ± NA	1G6N, 1CGP	[13]
16	CAP(A144T):cAMP2:DNA	2.2×10^{-7} ± NA	1G6N, 1CGP	[13]
17	CAP(A144T):cGMP2:DNA	2.2×10^{-7} ± NA	1G6N, 1CGP	[13]
18	Galectin:L2	$1.8 \pm 0.1 \times10^{-5}$	1A3K[c], 2XG3	[168]
19	Galectin:L3	$3.3 \pm 0.1 \times10^{-6}$	1A3K[c], 1KJR	[168]
20	Galectin:Lactose	$2.3 \pm 0.2 \times10^{-4}$	1A3K[c], 2NN8	[168]
21	HEWL:Chitotriose	$1.5 \pm 0.0 \times10^{-5}$	1LZA, 1LZB	[156, 169]
22	PDZ3:CRIPT	$1.2 \pm 0.1 \times10^{-6}$	1BFE, 1BE9	[170]
23	PDZ3Δ7:CRIPT	$2.6 \pm 0.4 \times10^{-5}$	1BFE, 1BE9	[170]
24	DHFR:NADP:Folate[f]	$3.8 \pm 0.4 \times10^{-6}$	1RX7, 1RX2	[171][a]
25	SAP SH2:Y281	$3.4 \pm 0.4 \times10^{-8}$	1D1Z, 1D4T	[163][a]
26	SAP SH2:pY281	$3.8 \pm 5.5 \times10^{-10}$	1D1Z, 1D4W	[163][a]
27	PDZ2:RA-GEF2	$5.1 \pm 0.2 \times10^{-6}$	3LNX, 3LNY	[172-173][e]
28	CaM(D58N):smMLCK(p)	$4.0 \pm 0.9 \times10^{-8}$	1XO2, 1CDL[d]	[104][a,b]
29	CaM(D95N):smMLCK(p)	$2.7 \pm 0.5 \times10^{-8}$	1XO2, 1CDL[d]	[a,b]
30	CaM(E84K):nNOS(p)	$3.3 \pm 0.8 \times10^{-8}$	1XO2, 2O60[d]	[a,b]
31	Barnase-dCGAC	$5.0 \pm 0.6 \times10^{-5}$	1BNI,1BRN	[a,b]
32	HBP(D24R):Histamine	$3.2 \pm 0.7 \times10^{-9}$	3GAQ,3G7X	[a,b]

[§] For some complexes information regarding the precision of the determined K_d was not available from the cited literature and is indicated by "NA".

[a] The calorimetric measurements were carried out in this study

[b] The NMR relaxation measurements were carried out in this study

[c] The unliganded structure of this protein is not available. The ligand was manually removed from the indicated coordinates of the complex and used for accessible surface area calculations without further adjustment.

[d] Structures were not available for these mutant calmodulin-peptide complexes. The corresponding structures of wild-type calmodulin were used for accessible surface area calculations.

[e] The RA-GEF2 peptide used in the calorimetric study (Ac-YADSEADENEQVSAV-COOH) is longer than that used in the NMR relaxation study (Ac-ENEQVSAV-COOH). The solution structure of the complex with the longer peptide (PDB code: 1D5G [174]) shows that only the five C terminal residues of the peptide contact the protein. Accessible surface area calculations used the shorter peptide.

[f] The "free state" is the DHFR:folate binary complex and the binding of NADP$^+$ to form a ternary complex that is the "bound" state.

Table C-2: Summary of the thermodynamic association of protein complexes

Index	$\Delta G^{total}_{binding}$ (kJ/mol)	$\Delta H^{total}_{binding}$ (kJ/mol)	$-T\Delta S^{total}_{binding}$ (kJ/mol)	T (K)	Ref
1	-49.8 ± 0.5	-140.0 ± 0.9	+90.0 ± 1.0	308	[10]
2	-46.6 ± 0.1	-124.7 ± 0.2	+75.0 ± 0.3	308	[10]
3	-43.6 ± 0.5	-84.3 ± 0.8	+40.7 ± 0.9	308	[30]

4	-49.5 ± 0.5	-119 ± 0.6	+69.6 ± 0.9	308	[10]
5	-49.2 ± 0.3	-74.9 ± 0.4	+25.7 ± 0.8	308	[10]
6	-51.7 ± 0.6	-49.9 ± 0.3	-1.9 ± 0.7	308	[10]
7	-37.7 ± NA	-92.0 ± NA	+54.4 ± NA	305	[13]
8	-37.2 ± NA	-51.5 ± NA	+14.2 ± NA	305	[13]
9	-37.2 ± NA	+19.2 ± NA	-56.5 ± NA	305	[13]
10	-37.2 ± NA	+15.9 ± NA	-49.8 ± NA	305	[13]
11	-37.2 ± NA	-45.6 ± NA	+8.4 ± NA	305	[13]
12	-30.5 ± NA	-18.8 ± NA	-11.7 ± NA	305	[13]
13	-37.7 ± NA	-55.2 ± NA	+17.6 ± NA	305	[13]
14	-37.7 ± NA	+18.4± NA	-51.9 ± NA	305	[13]
15	-28.0 ± NA	-12.1 ± NA	-15.9 ± NA	305	[13]
16	-38.9 ± NA	+7.1 ± NA	-44.4 ± NA	305	[13]
17	-38.9 ± NA	+44.4 ± NA	-80.3 ± NA	305	[13]
18	-27.3 ± 0.1	-49.3 ± 0.8	+22.0 ± 0.8	301	[168]
19	-31.6 ± 0.1	-57.7 ± 0.5	+26.1 ± 0.5	301	[168]
20	-21.0 ± 0.2	-50.6 ± 1.4	+30.0 ± 1.0	301	[168]
21	-28.5 ± 0.04	-63.6 ± 0.4	+35.1 ± NA	308	[169]
22	-34 ± 0.2	-40.6 ± 0.5	+6.9 ± 0.3	298	[170]
23	-26.2 ± 0.3	-43.0 ± 2.8	+16.7 ± 2.5	298	[170]
24	-31.3 ± 0.3	-37.0 ± 3.0	+6.4 ± 2.9	302	[a]
25	-43.3 ± 0.3	-98.1 ± 3.2	+55.4 ± 3.5	303	[a]
26	-54.7 ± 2.9	-81.2 ± 6.4	+27.5 ± 4.3	303	[a]
27	-30.2 ± 0.1	-39.6 ± 0.9	+9.4 ± 0.9	298	[173]
28	-43.7 ± 0.6	-129.4 ± 2.1	+85.7 ± 1.9	308	[a]
29	-44.6 ± 0.4	-118.1 ± 0.2	+73.4 ± 0.4	308	[a]
30	-44.1 ± 0.6	-41.2 ± 2.7	-2.9 ± 3.1	308	[a]
31	-24.6 ± 0.3	-4.2 ± 1.5	-20.4 ± 2.7	298	[a]
32	-48.5 ± 0.5	-69.5 ± 3.7	+21.0 ± 3.1	298	[a]

[§] Precision listed as the standard deviation between experiments. In some cases, the precision of the measurements was not available from the literature and is indicated as "NA."

[a] This work.

Table C-3: Effective rotational correlation times for calcium-saturated calmodulin mutants and their complexes at 308K

Protein	**Domain**[a]	**τ_m (ns)**[b]
Free CaM (D58N)	N-term	8.9
Free CaM (D58N)	C-term	7.8
Free CaM (D95N)	N-term	9.5

Free CaM (D95N)	C-term	8.9
Free CaM (E84K)[c,d]	N-term	9.5
Free CaM (E84K)[c,d]	C-term	8.5
CaM (D58N):smMLCK(p)	N/A	7.7
CaM (D95N):smMLCK(p)	N/A	8.2
CaM (E84K):nNOS(p)[d]	N/A	9.4

[a] The rotational correlation times for the individual domains of free (calcium-saturated) calmodulin were analyzed separately. The N-terminal domain was defined as residues 1-79 and the C-terminal domain was defined as residues 80-148. For the complexes, rotational correlation times considered all residues. All proteins were found to tumble isotropically.

[b] Tumbling model selected from isotropic, axially symmetric and fully anisotropic models using standard statistical tests. See Moorman et al[166] for further details. Monte Carlo analysis indicated that the error in τ_m is 0.2 ns.

[c] These data were recollected for this study.

[d] These data were collected using mixed $^{15}N/^{14}N-^{13}C-55\%^2H$ samples. The overall concentration of the samples was 1.4 mM and contained 1 mM of $^{14}N-^{13}C-55\%^2H$ labeled protein and 55% fractionally deuterated protein and 0.4 mM ^{15}N labeled protein, allowing for measurement of both backbone and side chain relaxation on the same sample.

Table C-4: $<O^2_{axis}>$ of mutant calmodulin-peptide complexes at 308K

Complex	**Free CaM**	**Bound CaM**	**Bound Target**
CaM:smMLCK(p)[b]	0.439 ± 0.010	0.543 ± 0.014	0.634 ± 0.042[c]
CaM(D58N):smMLCK(p)	0.465 ± 0.023	0.569 ± 0.015[c]	0.687 ± 0.013
CaM(D95N):smMLCK(p)	0.474 ± 0.030	0.557 ± 0.031[c]	0.629 ± 0.012
CaM:nNOS(p)[b]	0.439 ± 0.010	0.526 ± 0.010	0.628 ± 0.032[d]
CaM(E84K):nNOS(p)	0.435 ± 0.022	0.461 ± 0.028	0.543 ± 0.011

Alanines were not included in the calculation of $<O^2_{axis}>$ since they do not have a meaningful side chain χ angle. Errors were determined using Monte Carlo sampling.

[b] Data from Frederick et al. 2007 [10].

[c] Data from Igumenova et al. 2005[104].

[d] Data from Marlow et al. 2010[30].

Table C-5: Effective rotational correlation times for barnase and histamine binding protein (D24R) and their complexes at 298 K.

Protein	τ_m^{iso} [a] (ns)	Tumbling[b] Model	D_{avg} (x10^7 s^{-1})	$\frac{2D_z}{(D_x+D_y)}$	$\frac{D_x}{D_y}$	ϕ (deg)	θ (deg)	ψ (deg)
Barnase (Bn) (1mM)	8.0	Axial	2.00	1.17	1.00	76	10	-
Bn-dCGAC (0.7mM)	7.9	Axial	2.11	1.16	1.00	1	4	11
HBP(D24R) apo	9.2	Axial	1.82	1.11	1.00	68	1	-
HBP(D24R):histamine	9.3	Anisotropic	1.80	1.01	1.13	292	74	115

[a] Monte Carlo analysis indicated that the error is 0.2 ns.

[b] Tumbling model selected from isotropic, axially symmetric and fully anisotropic models using standard statistical tests. See Moorman et al[166] for further details.

Table C-6: Dynamics of barnase and histamine binding protein and their complexes at 298 K.

Protein	$< O^2_{axis} >$ [a]
Barnase	0.745 ± 0.025
Barnase-dCGAC	0.645 ± 0.020
HBP(D24R)	0.559 ± 0.036
HBP(D24R):histamine	0.549 ± 0.029

[a] Alanines were not included in the calculation of <O^2_{axis}> since they do not have a meaningful side chain χ angle. Errors were determined using Monte Carlo sampling.

Table C-7: Entropy and NMR relaxation parameters for the calibration of the entropy meter[§].

Index	ΔS_{total} (J mol^{-1} K^{-1})	ΔASA^{a}_{polar} (Å^2)	ΔASA^{a}_{apolar} (Å^2)	$\Delta S^{b}_{solvent}$ (J mol^{-1} K^{-1})	$N\chi\left\langle O^2_{axis}\right\rangle$ [c]	ΔS_{conf} (J mol^{-1} K^{-1})
1	-290 ± 3	-1778	-1965	193 ± 29	+52.7 ± 5.7[f]	-269 ± 18
2	-240 ± 1	-1824	-2433	213 ± 28	+57.1 ± 5.1[f]	-292 ± 20
3	-130 ± 3	-1867	-2386	214 ± 29	+51.6 ± 7.6[f]	-264 ± 18
4	-230 ± 3	-1836	-2421	213 ± 28	+60.2 ± 6.8[f]	-308 ± 21
5	-83 ± 3	-1661	-2248	195 ± 26	+51.9 ± 5.0[f]	-265 ± 18
6	+ 6.2 ± 2	-1618	-2000	183 ± 25	+46.4 ± 4.0[f]	-237 ± 16
7	-180 ± N/A	-745[d]	-3070[d]	160 ± 6	+30.7 ± 24.5	-157 ± 11
8	-47 ± N/A	-745[d]	-3070[d]	160 ± 6	+19.2 ± 22.1	-98 ± 7
9	+190 ± N/A	-745[d]	-3070[d]	160 ± 6	-19.5 ± 25.2	+100 ± 7
10	+160 ± N/A	-745[d]	-3070[d]	160 ± 6	-17.3 ± 30.6	+88 ± 6
11	-27 ± N/A	-745[d]	-3070[d]	160 ± 6	+14.8 ± 28.8	-76 ± 5
12	+38 ± N/A	-745[d]	-3070[d]	160 ± 6	-6.1 ± 40.5	+31 ± 2
13	-58 ± N/A	-745[d]	-3070[d]	160 ± 6	+11.9 ± 46.3	-61 ± 4
14	+170 ± N/A	-745[d]	-3070[d]	160 ± 6	-12.8 ± 56.8	+65 ± 4

15	+52 ± N/A	-745 [d]	-3070 [d]	160 ± 6	+3.3 ± 35.0	-17 ± 1
16	+150 ± N/A	-745 [d]	-3070 [d]	160 ± 6	-6.7 ± 28.6	+34 ± 2
17	+260 ± N/A	-745 [d]	-3070 [d]	160 ± 6	-26.8 ± 26.4	+137 ± 9
18	-73 ± 3	-113	-471	24 ± 1	-15.6 ± 9.3	+79 ± 5
19	-87 ± 2	-272 [e]	-368 [e]	33 ± 5	-9.6 ± 9.7	+49 ± 3
20	-100± 3	-95	-304	18 ± 1	-17.7 ± 10.3	+91 ± 6
21	-110 ± N/A	-342	-445	39 ± 5	+2.6 ± 7.7	-14 ± 1
22	-23 ± 1	-442	-271	44 ± 9	+9.1 ± 14.4 [f]	-46 ± 3
23	-56 ± 8	-451	-212	43 ± 9	+31.8 ± 16.5 [f]	-162 ± 11
24	-21 ± 10	-524	-903	71 ± 9	+11.3 ± 15.2	-58 ± 4
25	-183 ± 12	-731	-842	83 ± 13	+7.4 ± 22.2 [f]	-38 ± 3
26	-91 ± 14	-833	-967	95 ± 15	+2.6 ± 24.4 [f]	-13 ± 1
27	-32 ± 3	-539	-509	60 ± 11	+4.5 ± 12.8 [f]	-23 ± 2
28	-280 ± 6	-1824	-2433	213 ± 28	+59.2 ± 8.2 [f]	-302 ± 21
29	-240 ± 1	-1824	-2433	213 ± 28	+50.2 ± 12.7 [f]	-256 ± 18
30	+9 ± 10	-1618	-2000	183 ± 25	+33.6 ± 10.8 [f]	-172 ± 12
31	+68 ± 9	-436	-636	56 ± 8	-8.9 ± 8.1 [g]	+45 ± 3
32	-70 ± 10	-351	-318	39 ± 7	-3.04 ± 14.1	+16 ± 1

[§] In some cases, the error value was not available in the cited literature and is indicated as "NA."

[a] The change in accessible surface areas (ASA) was calculated for both the protein and the ligand using AREAIMOL[167]. For cases where the residues within the deposited crystal structure had two conformations, the "A" conformer was always used. For non-peptide ligands the free ligand ASA was determined using the structure of the ligand in the complex. For peptide ligands (index # 1-6, 22, 23, 25-30), an extended structure was used to model the free ligand[175]. For double-stranded DNA ligands (index # 7-17), the DNA in the crystal structure (1CGP) is structurally distorted in the complex. To obtain an approximate model structure of the DNA in its free state, the DNA from the crystal structure was hydrated *in silico* and molecular dynamics simulations run using the CHARMM27[ref.] [158] standard nucleic acid parameters to allow the DNA to relax to a stable apo structure. The DNA reached a stable structure after 1.2 ns of simulation time and the total simulation was continued to 3.6 ns. The RMSD between the starting and final structure was 6.85 Å.

[b] The changes in solvent entropy were obtained by the simultaneous optimization of the conformational entropy and the solvent entropy using Equation 3-3 (see main text).

[c] Alanines were not included in the calculation of $N\chi <O^2_{axis}>$ since they do not have a meaningful side chain χ angle. The N_χ values correspond to the species used in the NMR relaxation experiments. The effective error between experimental replicates of $<O^2_{axis}>$ is generally less (± 0.01) than that calculated in quadrature from error estimated by Monte Carlo analysis of individual order parameters. An additional uncertainty is introduced by the nature of the ligand (see legend to Figure 1 in main text and footnote f below).

[d] The CAP complexes were found experimentally to not involve a change in solvent entropy[13], which implies that they also have identical changes in accessible surface area upon binding.

[e] The ligand in this complex contains fluorine atoms, which are not recognized by AREAIMOL. To accommodate this the fluorine atoms were changed to oxygen atoms, which have nearly identical atomic radii.

[f] These complexes contain a peptide ligand. In all cases the dynamics of the free peptide were not characterized. As discussed elsewhere[175], $< O^2_{axis} >$ for the free peptide is taken as 0.05, which is reflective of the disorder of small unstructured peptides. In some cases, the dynamics of the peptide in the complex was measured (Index # 1-6,28-30) but in other cases not (Index # 22,23,25-27). In the latter situation, the contribution of the peptide to $\Delta<O^2_{\mathrm{axis}}>$ was conservatively taken to range between 0 (corresponding to the peptide maintaining the disorder of the free peptide while in the bound state) and 0.9 (corresponding to the attaining an average order parameter in the bound state of 0.95). The midpoint of this range was used for the contribution of the peptide to $N\chi <O^2_{axis}>$. The reported error in these complexes combines the error of the measured $<O^2_{\mathrm{axis}}>$ and the uncertainty arising from the peptide contribution. In the former situation (the CaM-peptide complexes), the $<O^2_{\mathrm{axis}}>$ in the bound state is known and thus the error is treated in quadrature for both the protein and the peptide.

[g] This complex contains a small single-stranded DNA, which has not been dynamically characterized. The contribution of the DNA to $\Delta<O^2_{\mathrm{axis}}>$ was conservatively taken to range between 0 (corresponding to the DNA maintaining the disorder of the free DNA while in the bound state) and 0.9 (corresponding to the attaining an average order parameter in the bound state of 0.95). Nχ was derived as 1 angle per nucleotide, corresponding to that between the base and the sugar-phosphate backbone.

Table C-8: Contribution of amino acid side chains to the heat capacity of protein solutions.

	Ubiquitin	**CaM:smMLCK(p)**
$\left\langle dO^2_{axis} / d\ln T \right\rangle^a$	-0.80 ± 0.15 [b]	-0.96 ± 0.09[c]
N_{res}	76	170
Nχ	161	343
C_p^{sc} **(J/mol/K)**	680 ± 130	1750 ± 170
C_p^{sc} **(J/g/K)**	0.080 ± 0.014	0.091± 0.009
C_p^{total} **(cal/g/K)**	1.47[d]	1.46[e]

[a] Only residues whose linear fit displayed an $R^2 > 0.7$ were included in this analysis. Alanines were excluded since they do not have a meaningful side chain χ angle. The error in $<dO^2_{\mathrm{axis}}/d\ln T>$ is the average of the regression errors for each probe.

[b] Data taken from Song et al. (2007) [73].

[c] Data taken from Lee et al. (2001)[26]. Data for the smMLCK(p) peptide was not collected in this study, so it is assumed that the peptide methyls display the identical $<dO^2_{\mathrm{axis}}/d\ln T>$ value.

[d] Wintrode et al.[176]

[e] Canonical value from Gomez et al.[146]

Table C-9: Methyl Order Parameters of Ca^{2+}-bound CaM

ID	O^2_{axis}	Err
l4d1	0.412	0.018
i9d1	0.39	0.007
i9g2	0.786	0.018
a10b	0.793	0.016
a15b	0.934	0.042
l18d1	0.171	0.004
l18d2	0.256	0.004
t26g2	0.489	0.008
i27g2	0.617	0.021
t29g2	0.376	0.006
l32d1	0.32	0.006
l32d2	0.256	0.012
v35g2	0.687	0.017
m36e	0.249	0.002
m51e	0.171	0.005
i52d1	0.334	0.006
i52g2	0.673	0.017
v55g1	0.567	0.013
v55g2	0.567	0.013
t62g2	0.793	0.033
i63d1	0.504	0.012
i63g2	0.715	0.021
l69d1	0.355	0.017
t70g2	0.595	0.012
m71e	0.164	0.004
m72e	0.277	0.003
m76e	0.094	0.003
i85d1	0.32	0.005
i85g2	0.553	0.009
a88b	0.836	0.029
v91g1	0.68	0.015
v91g2	0.68	0.012
i100g2	0.737	0.022
a102b	0.949	0.025
m109e	0.136	0.005
l116d1	0.285	0.01
l116d2	0.299	0.005
v121g1	0.553	0.008
v121g2	0.553	0.009
m124e	0.186	0.001
i125d1	0.207	0.003
i125g2	0.567	0.008
a128b	0.779	0.018
i130d1	0.327	0.005
i130g2	0.489	0.006
v136g2	0.723	0.018
v142g1	0.715	0.014
v142g2	0.61	0.011
m144e	0.115	0
m145e	0.2	0.001
t146g2	0.433	0.005
a147b	0.327	0.005

Table C-10: Methyl Order Parameters of CaM bound to CaMKKα(p)

ID	O^2_{axis}	Err
l4d1	0.341	0.01
l4d2	0.348	0.007
i9d1	0.405	0.006
i9g2	0.708	0.011
a10b	0.871	0.016
a15b	0.899	0.044
l18d1	0.313	0.006
l18d2	0.299	0.022
i27d1	0.751	0.048
i27g2	0.843	0.034
t28g2	0.829	0.027
t29g2	0.306	0.005

ID	O^2_{axis}	Err
l32d1	0.666	0.039
l32d2	0.659	0.051
t34g2	0.595	0.013
v35g1	0.793	0.028
v35g2	0.744	0.024
m36e	0.39	0.004
l39d1	0.553	0.027
l39d2	0.595	0.024
t44g2	0.369	0.006
a46b	0.786	0.011
l48d1	0.68	0.047
m51e	0.652	0.009
i52d1	0.263	0.006
i52g2	0.786	0.018
v55g1	0.602	0.026
v55g2	0.779	0.03
a57b	0.864	0.016
i63d1	0.602	0.029
i63g2	0.786	0.036
l69d1	0.228	0.012
l69d2	0.171	0.009
t70g2	0.553	0.008
m71e	0.39	0.005
m72e	0.383	0.004
a73b	0.864	0.018
m76e	0.285	0.004
i85d1	0.617	0.014
i85g2	0.8	0.022
v91g2	0.814	0.022
i100d1	0.829	0.048

ID	O^2_{axis}	Err
i100g2	0.836	0.031
a102b	0.885	0.022
a103b	0.885	0.019
l105d1	0.108	0.004
l105d2	0.186	0.004
v108g1	0.313	0.006
v108g2	0.292	0.004
m109e	0.595	0.005
t110g2	0.433	0.004
l112d1	0.426	0.018
l112d2	0.398	0.012
l116d1	0.518	0.013
l116d2	0.574	0.016
v121g1	0.758	0.016
v121g2	0.779	0.023
m124e	0.878	0.023
i125d1	0.277	0.005
i125g2	0.843	0.018
a128b	0.963	0.045
i130d1	0.32	0.005
i130g2	0.525	0.005
v136g1	0.504	0.013
v136g2	0.546	0.011
v142g1	0.532	0.008
v142g2	0.546	0.009
m144e	0.504	0.005
m145e	0.348	0.005
t146g2	0.511	0.008
a147b	0.412	0.005

Table C-11: Methyl Order Parameters of CaM bound to smMLCK(p)

ID	O^2_{axis}	Err
l4d1	0.304	0.011
l4d2	0.579	0.021
i9d1	0.516	0.008
i9g2	0.77	0.014
a10b	0.823	0.017

ID	O^2_{axis}	Err
a15b	0.83	0.032
l18d1	0.682	0.061
l18d2	0.354	0.011
t26g2	0.604	0.011
i27d1	0.749	0.033

ID	O^2_{axis}	Err
i27g2	0.735	0.021
t28g2	0.801	0.01
t29g2	0.548	0.012
t34g2	0.632	0.013
v35g1	0.66	0.015
v35g2	0.632	0.012
m36e	0.301	0.003
l39d1	0.442	0.022
l39d2	0.329	0.019
t44g2	0.766	0.01
a46b	0.823	0.015
l48d1	0.449	0.018
l48d2	0.738	0.03
m51e	0.269	0.003
i52d1	0.318	0.006
i52g2	0.749	0.018
v55g1	0.438	0.006
v55g2	0.389	0.008
i63d1	0.724	0.018
i63g2	0.745	0.021
l69d1	0.265	0.016
t70g2	0.639	0.012
m71e	0.378	0.004
m72e	0.72	0.013
a73b	0.78	0.017
m76e	0.117	0.002
t79g2	0.396	0.005
i85d1	0.301	0.006
i85g2	0.615	0.012
a88b	0.798	0.028
v91g1	0.699	0.017
v91g2	0.844	0.015
i100d1	0.922	0.036
a102b	0.935	0.024
a103b	0.875	0.017
l105d1	0.59	0.023
l105d2	0.551	0.025
v108g1	0.466	0.009
v108g2	0.449	0.007
m109e	0.315	0.003
t110g2	0.622	0.012
l112d2	0.604	0.022
l116d1	0.199	0.007
l116d2	0.223	0.006
v121g1	0.639	0.011
v121g2	0.509	0.006
m124e	0.837	0.018
i125d1	0.407	0.007
i125g2	0.798	0.018
a128b	0.922	0.033
i130d1	0.347	0.005
i130g2	0.569	0.007
v136g1	0.791	0.026
v136g2	0.826	0.013
v142g1	0.604	0.01
v142g2	0.558	0.011
m144e	0.354	0.005
m145e	0.283	0.004
t146g2	0.512	0.008
a147b	0.378	0.004

Table C-12: Methyl Order Parameters of CaM bound to CaMKI(p)

ID	O^2_{axis}	Err
l4d1	0.475	0.031
l4d2	0.489	0.014
i9d1	0.553	0.012
i9g2	0.765	0.02
a10b	0.934	0.018
a15b	0.8	0.05
l18d1	0.482	0.047
l18d2	0.171	0.007

ID	O^2_{axis}	Err
t26g2	0.595	0.018
i27d1	0.744	0.045
i27g2	0.906	0.047
t29g2	0.624	0.022
l32d1	0.525	0.032
l32d2	0.751	0.058
t34g2	0.638	0.021
v35g1	0.822	0.038
m36e	0.341	0.006
l39d1	0.249	0.008
l39d2	0.659	0.032
m51e	0.285	0.004
i52d1	0.256	0.006
i52g2	0.758	0.026
v55g1	0.412	0.009
v55g2	0.383	0.009
a57b	0.864	0.03
t62g2	0.914	0.028
i63d1	0.723	0.023
i63g2	0.786	0.028
l69d1	0.39	0.036
m71e	0.383	0.006
m72e	0.595	0.012
m76e	0.101	0.004
t79g2	0.61	0.014
i85d1	0.567	0.016
i85g2	0.715	0.023
a88b	1	0.085
v91g1	0.61	0.021

ID	O^2_{axis}	Err
v91g2	0.737	0.022
i100g2	0.899	0.043
a102b	0.906	0.033
a103b	0.885	0.03
l105d1	0.602	0.032
l105d2	0.624	0.059
v108g1	0.496	0.014
v108g2	0.518	0.017
m109e	0.419	0.005
t110g2	0.659	0.019
l116d1	0.292	0.014
l116d2	0.313	0.012
v121g1	0.645	0.018
v121g2	0.504	0.01
m124e	0.906	0.026
i125d1	0.362	0.008
i125g2	0.829	0.031
a128b	0.405	0.016
i130d1	0.327	0.006
i130g2	0.581	0.009
v136g1	0.412	0.008
v136g2	0.751	0.02
v142g1	0.645	0.018
v142g2	0.652	0.018
m144e	0.285	0.005
m145e	0.341	0.006
t146g2	0.617	0.014
a147b	0.447	0.007

Table C-13: Methyl Order Parameters of CaM bound to eNOS(p)

ID	O^2_{axis}	Err
l4d1	0.39	0.011
l4d2	0.525	0.006
i9g2	0.694	0.01
a10b	0.836	0.013
a15b	0.793	0.022
l18d1	0.178	0.002

ID	O^2_{axis}	Err
l18d2	0.178	0.003
t26g2	0.489	0.007
i27d1	0.602	0.022
i27g2	0.715	0.019
t29g2	0.348	0.004
l32d1	0.44	0.012

ID	O^2_{axis}	Err
l32d2	0.44	0.018
t34g2	0.673	0.011
v35g1	0.666	0.014
l39d1	0.723	0.117
l39d2	0.56	0.021
a46b	0.772	0.011
l48d1	0.588	0.04
l48d2	0.511	0.008
i52d1	0.242	0.005
i52g2	0.68	0.011
v55g1	0.567	0.009
v55g2	0.581	0.009
a57b	0.08	0
t62g2	0.779	0.02
i63d1	0.518	0.007
i63g2	0.617	0.01
l69d1	0.433	0.015
l69d2	0.496	0.018
t70g2	0.624	0.01
m71e	0.15	0.004
m72e	0.482	0.004
a73b	0.723	0.011
m76e	0.143	0
i85g2	0.765	0.014
a88b	0.871	0.025
v91g1	0.758	0.019

ID	O^2_{axis}	Err
i100d1	0.885	0.033
i100g2	0.864	0.023
a102b	0.906	0.017
l105d1	0.489	0.009
l105d2	0.44	0.016
v108g1	0.723	0.016
v108g2	0.723	0.013
m109e	0.383	0.004
t110g2	0.327	0.005
l112d1	0.398	0.02
v121g1	0.595	0.006
v121g2	0.652	0.012
i125d1	0.341	0.005
i125g2	0.701	0.013
a128b	0.878	0.021
i130d1	0.313	0.004
i130g2	0.532	0.006
v136g2	0.765	0.018
v142g1	0.56	0.007
v142g2	0.539	0.007
m144e	0.553	0.006
m145e	0.383	0.003
t146g2	0.588	0.008
a147b	0.461	0.004

Table C-14: Methyl Order Parameters of CaM bound to nNOS(p)

ID	O^2_{axis}	Err
l4d1	0.362	0.003
l4d2	0.744	0.017
i9d1	0.419	0.003
i9g2	0.715	0.01
a10b	0.822	0.013
l18d1	0.221	0.002
l18d2	0.27	0
t26g2	0.553	0.003
i27d1	0.8	0.034

ID	O^2_{axis}	Err
i27g2	0.8	0.026
t29g2	0.355	0.005
l32d1	0.433	0.007
t34g2	0.581	0.007
v35g1	0.758	0.02
m36e	0.249	0.004
l39d2	0.779	0.034
l48d1	0.602	0.027
l48d2	0.631	0.015

ID	O^2_{axis}	Err
m51e	0.285	0.002
i52d1	0.242	0.005
i52g2	0.645	0.009
v55g1	0.489	0.002
v55g2	0.419	0.005
a57b	0.051	0.005
t62g2	0.871	0.009
i63d1	0.652	0.015
i63g2	0.744	0.018
l69d1	0.376	0.009
t70g2	0.532	0.006
m71e	0.193	0
m72e	0.348	0.003
a73b	0.772	0.016
m76e	0.178	0
t79g2	0.32	0
i85d1	0.433	0.005
i85g2	0.723	0.014
a88b	0.885	0.026
v91g1	0.793	0.019
i100d1	0.708	0.024
i100g2	0.793	0.027
a102b	0.906	0.02
l105d1	0.285	0.004
l105d2	0.256	0.002
v108g1	0.595	0.008
v108g2	0.56	0.007
m109e	0.334	0
t110g2	0.624	0.007
l112d2	0.482	0.009
l116d1	0.235	0.009
l116d2	0.263	0.004
v121g2	0.511	0.005
m124e	0.383	0.005
i125d1	0.306	0.002
a128b	0.963	0.022
i130d1	0.306	0
i130g2	0.518	0.004
v136g2	0.814	0.025
v142g1	0.574	0.005
v142g2	0.574	0.007
m144e	0.68	0.009
m145e	0.454	0.004
t146g2	0.56	0.005
a147b	0.433	0.002

Table C-15: Methyl Order Parameters of CaMKKα(p) bound to CaM

ID	O^2_{axis}	Err
l3d1	0.133	0.004
l3d2	0.155	0.003
i4d1	0.252	0.005
i4g2	0.341	0.007
t8g2	0.587	0.022
t9g2	0.888	0.073
v10g1	0.608	0.029
v10g2	0.621	0.024
i11d1	0.349	0.013
i11g2	0.697	0.029
l12d1	0.273	0.016
l12d2	0.265	0.011
v13g1	0.786	0.034
v13g2	0.723	0.038
m16e	0.252	0.004
l17d1	0.667	0.119
l17d2	0.371	0.024

Table C-16: Methyl Order Parameters of smMLCK(p)bound to CaM

ID	O^2_{axis}	Err
a1b	0.693	0.033
t8g2	0.583	0.028
a11b	0.667	0.046
v12g1	0.744	0.054
v12g2	0.744	0.034

ID	O^2_{axis}	Err
a14b	0.693	0.048
i15d1	0.358	0.011
i15g2	0.646	0.023
l18d1	0.578	0.051
l18d2	0.782	0.094

Table C-17: Methyl Order Parameters of CaMKI(p) bound to CaM

ID	O^2_{axis}	Err
a3b	0.693	0.027
a10b	0.922	0.059
a13b	0.947	0.051
t14g2	0.561	0.02
a15b	0.875	0.05
v16g1	0.744	0.024

ID	O^2_{axis}	Err
v16g2	0.256	0.005
v17g1	0.837	0.04
v17g2	0.744	0.029
m20e	0.248	0.002
l23d1	0.723	0.038
l23d2	0.316	0.02

Table C-18: Methyl Order Parameters of eNOS(p) bound to CaM

ID	O^2_{axis}	Err
t4g2	0.854	0.017
v8g1	0.574	0.008
v8g2	0.557	0.007
a9b	0.723	0.025
a11b	0.837	0.022
v12g1	0.765	0.03
v12g2	0.829	0.02

ID	O^2_{axis}	Err
i14d1	0.578	0.01
i14g2	0.879	0.018
a16b	0.934	0.023
l18d1	0.405	0.006
l18d2	0.434	0.005
m19e	0.324	0.002

Table C-19: Methyl Order Parameters of nNOS(p) bound to CaM

ID	O^2_{axis}	Err
a1b	0.905	0.057
a4b	0.485	0.007
i5d1	0.358	0.008
i5g2	0.417	0.008
l10d1	0.587	0.028
l10d2	0.782	0.072
a13b	0.863	0.044

ID	O^2_{axis}	Err
v14g1	0.782	0.055
v14g2	0.812	0.041
a18b	0.918	0.036
l20d1	0.451	0.019
l20d2	0.481	0.041
m21e	0.333	0.003

Table C-20: Methyl Order Parameters of Ca^{2+}-bound CaM(E84K) for comparison to CaM(E84K):smMLCK(p)

ID	O^2_{axis}	Err
l4d1	0.464	0.013
i9d1	0.426	0.004
i9g2	0.778	0.009
a10b	0.782	0.009
a15b	0.939	0.025
l18d1	0.188	0.002
l18d2	0.273	0.003
m26e	0.252	0.002
t26g2	0.468	0.006
i27g2	0.723	0.017
t29g2	0.375	0.005
l32d1	0.324	0.005
l32d2	0.43	0.015
v35g2	0.706	0.011
m51e	0.18	0.001
i52d1	0.333	0.004
i52g2	0.655	0.009
v55g1	0.591	0.008
v55g2	0.553	0.008
t62g2	0.867	0.027
i63d1	0.502	0.007
i63g2	0.735	0.013
l69d1	0.409	0.012
t70g2	0.553	0.01
m71e	0.155	0
m72e	0.252	0.003
m76e	0.095	0
i85d1	0.341	0.003
i85g2	0.583	0.006
a88b	0.816	0.014
v91g1	0.706	0.009
v91g2	0.697	0.007
i100g2	0.756	0.013
a102b	0.931	0.015
m109e	0.163	0.003
l116d1	0.328	0.009
l116d2	0.299	0.004
v121g1	0.557	0.005
v121g2	0.519	0.005
m124e	0.121	0.001
i125d1	0.21	0.003
i125g2	0.587	0.006
a128b	0.765	0.01
i130d1	0.324	0.003
i130g2	0.502	0.004
v136g2	0.714	0.011
v142g1	0.735	0.009
v142g2	0.617	0.007
m144e	0.201	0.003
m145e	0.197	0.001
t146g2	0.422	0.003
a147b	0.328	0.003

Table C-21: Methyl Order Parameters of CaM(E84K) bound to smMLCK(p)

ID	O^2_{axis}	Err
l4d1	0.349	0.019
i9d1	0.471	0.011
i9g2	0.748	0.018
a10b	0.857	0.022
a15b	0.883	0.052
l18d1	0.241	0.017
l18d2	0.209	0.009
t26g2	0.612	0.026
i27d1	0.794	0.05
i27g2	0.862	0.037
t29g2	0.533	0.022
l32d1	0.544	0.053

ID	O^2_{axis}	Err
t34g2	0.603	0.019
v35g2	0.7	0.029
l39d1	0.615	0.052
l39d2	0.641	0.039
t44g2	0.818	0.027
a46b	0.795	0.023
l48d1	0.66	0.097
l48d2	0.741	0.041
i52g2	0.737	0.023
v55g1	0.456	0.013
v55g2	0.437	0.016
i63d1	0.71	0.026
i63g2	0.803	0.031
l69d1	0.348	0.03
l69d2	0.372	0.053
t70g2	0.632	0.017
m71e	0.257	0.004
m72e	0.554	0.01
a73b	0.837	0.031
m76e	0.169	0.002
t79g2	0.328	0.007
i85g2	0.642	0.02
a88b	0.871	0.046
v91g1	0.604	0.014
v91g2	0.591	0.017
i100d1	0.785	0.048
i100g2	0.83	0.039
a102b	0.925	0.029
a103b	0.889	0.029
l105d1	0.524	0.039
l105d2	0.53	0.031
v108g2	0.503	0.015
m109e	0.363	0.004
t110g2	0.635	0.017
l112d1	0.523	0.05
l116d1	0.285	0.02
l116d2	0.3	0.014
v121g2	0.604	0.015
m124e	0.865	0.018
i125d1	0.335	0.009
i125g2	0.813	0.024
a128b	0.886	0.051
i130d1	0.324	0.007
i130g2	0.53	0.008
v136g2	0.848	0.049
v142g1	0.571	0.014
v142g2	0.581	0.016
m144e	0.329	0.005
m145e	0.416	0.005
t146g2	0.515	0.014
a147b	0.41	0.007

Table C-22: Methyl Order Parameters of smMLCK(p) bound to CaM(E84K)

ID	O^2_{axis}	Err
L18d1	0.379	0.006
L18d2	0.32	0.016
v12g1/g2	0.723	0.01
v12g1/g2	0.718	0.01
t8g	0.638	0.016
a1b	0.723	0.01
a11b	0.769	0.011
a14b	0.863	0.013
i15g2	0.676	0.008
i15d1	0.422	0.007

Table C-23: Methyl Order Parameters of Ca^{2+}-bound CaM(E84K) for comparison to CaM(E84K):nNOS(p)

ID	O^2_{axis}	Err
LEU4CD1	0.388	0.016
LEU4CD2	0.373	0.007
THR5CG2	0.731	0.036
ILE9CG2	0.775	0.042
ILE9CD1	0.353	0.036
ALA10CB	0.82	0.019
ALA15CB	0.994	0.072
LEU18CD1	0.199	0.066
LEU18CD2	0.273	0.036
THR26CG2	0.477	0.021
ILE27CG2	0.224	0.011
THR29CG2	0.383	0.016
LEU32CD1	0.497	0.03
VAL35CG2	0.711	0.035
MET36CE	0.244	0.031
LEU48CD2	0.368	0.033
MET51CE	0.184	0.024
ILE52CG2	0.567	0.02
ILE52CD1	0.333	0.036
VAL55CG1	0.547	0.009
VAL55CG2	0.582	0.036
THR62CG2	0.86	0.038
ILE63CD1	0.497	0.024
ILE63CG2	0.746	0.013
LEU69CD1	0.408	0.009
LEU69CD2	0.343	0.043
THR70CG2	0.621	0.025
MET71CE	0.154	0.017
MET72CE	0.253	0.051
ALA73CB	0.775	0.053
MET76CE	0.089	0.005

ID	O^2_{axis}	Err
THR79CG2	0.298	0.06
ILE85CG2	0.557	0.013
ILE85CD1	0.338	0.042
ALA88CB	0.785	0.007
VAL91CG1	0.716	0.004
VAL91CG2	0.666	0.009
ILE100CG2	0.75	0.019
ALA102CB	0.91	0.04
LEU105CD1	0.373	0.005
LEU105CD2	0.234	0.011
VAL108CG2	0.512	0.012
MET109CE	0.169	0.019
LEU112CD1	0.422	0.005
LEU116CD1	0.308	0.004
LEU116CD2	0.298	0.008
VAL121CG1	0.527	0.002
VAL121CG2	0.542	0.015
MET124CE	0.189	0.038
ILE125CG2	0.596	0.019
ILE125CD1	0.209	0.053
ALA128CB	0.77	0.021
ILE130CG2	0.507	0.01
ILE130CD1	0.343	0.039
VAL136CG2	0.696	0.003
VAL142CG1	0.701	0.006
VAL142CG2	0.631	0.021
MET144CE	0.119	0.001
MET145CE	0.179	0.021
THR146CG2	0.408	0.005
ALA147CB	0.313	0.001

Table C-24: Methyl Order Parameters of CaM(E84K) bound to nNOS(p)

ID	O^2_{axis}	Err
ALA1CB	0.06	0.05
LEU4CD1	0.318	0.007

ID	O^2_{axis}	Err
LEU4CD2	0.343	0.017
ILE9CG2	0.621	0.02

ID	O^2_{axis}	Err
ILE9CD1	0.388	0.044
ALA10CB	0.8	0.051
LEU18CD1	0.239	0.015
LEU18CD2	0.244	0.039
THR26CG2	0.467	0.019
ILE27CD1	0.83	0.012
ILE27CG2	0.83	0.057
THR29CG2	0.308	0.007
THR34CG2	0.512	0.005
VAL35CG1	0.671	0.015
MET36CE	0.288	0.059
LEU39CD2	0.621	0.033
LEU48CD1	0.442	0.021
MET51CE	0.288	0.04
ILE52CD1	0.244	0.027
VAL55CG1	0.502	0.014
VAL55CG2	0.442	0.022
THR62CG2	0.741	0.043
ILE63CD1	0.616	0.036
ILE63CG2	0.686	0.018
LEU69CD1	0.333	0.024
MET71CE	0.219	0.056
MET72CE	0.249	0.049
ALA73CB	0.785	0.026
MET76CE	0.194	0.045
ILE85CG2	0.651	0.043
ILE85CD1	0.408	0.044
ALA88CB	0.989	0.032
VAL91CG1	0.716	0.025
ILE100CG2	0.825	0.025
ILE100CD1	0.741	0.027
ALA102CB	0.934	0.022
LEU105CD1	0.333	0.04
LEU105CD2	0.273	0.05
VAL108CG1	0.646	0.017
MET109CE	0.328	0.055
LEU112CD2	0.427	0.01
LEU116CD1	0.224	0.028
LEU116CD2	0.249	0.045
VAL121CG2	0.462	0.016
MET124CE	0.343	0.012
ILE125CD1	0.293	0.028
ALA128CB	0.77	0.051
ILE130CD1	0.318	0.02
VAL142CG1	0.552	0.02
VAL142CG2	0.542	0.026
MET144CE	0.785	0.031
MET145CE	0.398	0.012
THR146CG2	0.527	0.007
ALA147CB	0.398	0.016

Table C-25: Methyl Order Parameters of nNOS(p) bound to CaM(E84K)

ID	O^2_{axis}	Err
ALA4CB	0.492	0.005
ILE5CG2	0.432	0.006
ILE5CD1	0.343	0.02
LEU10CD1	0.562	0.012
LEU10CD2	0.686	0.019
ALA11CB	0.87	0.002
ALA13CB	0.885	0.012
VAL14CG1	0.785	0.005
VAL14CG2	0.8	0.017
ALA18CB	0.919	0.043
LEU20CD1	0.462	0.002
LEU20CD2	0.462	0.009
MET21CE	0.353	0.012

Table C-26: Methyl Order Parameters of Ca^{2+}-bound CaM(D58N)

ID	O^2_{axis}	Err
LEU4CD1	0.403	0.022
LEU4CD2	0.358	0.036
ILE9CG2	0.726	0.028
ILE9CD1	0.378	0.045
ALA10CB	0.741	0.028
ALA15CB	0.954	0.052
LEU18CD1	0.174	0.038
LEU18CD2	0.239	0.049
THR26CG2	0.696	0.025
ILE27CD1	0.721	0.027
THR29CG2	0.413	0.017
LEU32CD2	0.472	0.016
THR34CG2	0.517	0.019
VAL35CG1	0.676	0.021
VAL35CG2	0.681	0.033
MET36CE	0.229	0.028
LEU39CD1	0.502	0.016
LEU39CD2	0.467	0.018
LEU48CD1	0.497	0.022
LEU48CD2	0.681	0.026
MET51CE	0.154	0.062
ILE52CG2	0.716	0.03
ILE52CD1	0.512	0.017
VAL55CG1	0.646	0.016
VAL55CG2	0.651	0.017
ALA57CB	0.785	0.025
THR62CG2	0.83	0.031
ILE63CD1	0.616	0.023
ILE63CG2	0.775	0.036
LEU69CD1	0.422	0.022
LEU69CD2	0.393	0.023
THR70CG2	0.557	0.024
MET71CE	0.129	0.05
MET72CE	0.219	0.03
MET76CE	0.075	0.044
THR79CG2	0.234	0.028

ID	O^2_{axis}	Err
ILE85CG2	0.572	0.015
ILE85CD1	0.343	0.038
ALA88CB	0.77	0.008
VAL91CG1	0.681	0.005
VAL91CG2	0.641	0.012
ILE100CG2	0.78	0.013
ILE100CD1	0.596	0.037
ALA102CB	0.919	0.042
LEU105CD1	0.343	0.006
LEU105CD2	0.268	0.025
VAL108CG1	0.557	0.008
VAL108CG2	0.462	0.021
MET109CE	0.134	0.028
THR110CG2	0.482	0.007
LEU112CD1	0.373	0.003
LEU112CD2	0.398	0.007
LEU116CD1	0.293	0.003
LEU116CD2	0.298	0.017
VAL121CG1	0.522	0.009
VAL121CG2	0.517	0.026
MET124CE	0.109	0.031
ILE125CG2	0.586	0.031
ILE125CD1	0.199	0.032
ALA128CB	0.741	0.029
ILE130CG2	0.457	0.02
ILE130CD1	0.333	0.051
VAL136CG1	0.78	0.009
VAL136CG2	0.686	0.002
VAL142CG1	0.701	0.007
VAL142CG2	0.626	0.03
MET144CE	0.184	0.007
MET145CE	0.179	0.019
THR146CG2	0.413	0.006
ALA147CB	0.318	0.014

Table C-27: Methyl Order Parameters of CaM(D58N) bound to smMLCK(p)

ID	O^2_{axis}	Err
ALA1CB	0.04	0.008
LEU4CD1	0.338	0.006
LEU4CD2	0.467	0.004
ILE9CD1	0.532	0.025
ALA10CB	0.8	0.006
ALA15CB	0.87	0.025
LEU18CD1	0.472	0.004
LEU18CD2	0.408	0.021
THR26CG2	0.681	0.011
ILE27CD1	0.82	0.014
ILE27CG2	0.919	0.022
THR29CG2	0.606	0.005
LEU32CD1	0.527	0.004
LEU32CD2	0.477	0.02
THR34CG2	0.671	0.002
VAL35CG1	0.656	0.009
VAL35CG2	0.76	0.022
MET36CE	0.318	0.016
LEU39CD1	0.616	0.005
LEU39CD2	0.601	0.013
ALA46CB	0.81	0.007
LEU48CD2	0.726	0.019
MET51CE	0.283	0.046
ILE52CG2	0.81	0.021
ILE52CD1	0.482	0.016
VAL55CG1	0.686	0.006
VAL55CG2	0.591	0.01
ALA57CB	0.368	0.015
ILE63CD1	0.542	0.025
ILE63CG2	0.954	0.035
LEU69CD1	0.318	0.021
THR70CG2	0.691	0.013
MET71CE	0.462	0.014
MET72CE	0.721	0.009
ALA73CB	0.815	0.026
MET76CE	0.08	0.016
THR79CG2	0.363	0.021
ILE85CG2	0.666	0.015
ILE85CD1	0.323	0.021
ALA88CB	0.994	0.021
VAL91CG2	0.76	0.016
ILE100CD1	0.939	0.003
ALA102CB	0.929	0.003
ALA103CB	0.929	0.027
LEU105CD1	0.557	0.006
LEU105CD2	0.656	0.009
VAL108CG2	0.512	0.008
MET109CE	0.338	0.019
THR110CG2	0.611	0.003
LEU112CD1	0.586	0.003
LEU112CD2	0.606	0.014
LEU116CD1	0.189	0.029
VAL121CG2	0.621	0.02
MET124CE	0.954	0.012
ILE125CG2	0.81	0.023
ILE125CD1	0.417	0.048
ALA128CB	0.805	0.017
ILE130CG2	0.582	0.009
ILE130CD1	0.373	0.026
VAL136CG2	0.736	0.008
VAL142CG1	0.631	0.002
VAL142CG2	0.616	0.011
MET144CE	0.398	0.003
MET145CE	0.293	0.015
THR146CG2	0.527	0.007
ALA147CB	0.368	0.002

Table C-28: Methyl Order Parameters of smMLCK(p) bound to CaM(D58N)

ID	O^2_{axis}	Err
ALA1CB	0.78	0.008
THR8CG2	0.681	0.021
ALA11CB	0.88	0.012
VAL12CG1	0.765	0.005
VAL12CG2	0.731	0.014
ALA14CB	0.87	0.018
ILE15CG2	0.701	0.018
ILE15CD1	0.427	0.019
LEU18CD1	0.721	0.012
LEU18CD2	0.785	0.004

Table C-29: Methyl Order Parameters of Ca^{2+}-bound CaM(D95N)

ID	O^2_{axis}	Err
LEU4CD1	0.472	0.032
LEU4CD2	0.393	0.037
THR5CG2	0.775	0.029
ILE9CG2	0.78	0.021
ILE9CD1	0.422	0.049
ALA10CB	0.815	0.031
ALA15CB	0.989	0.053
LEU18CD1	0.209	0.035
LEU18CD2	0.288	0.033
THR26CG2	0.487	0.018
ILE27CD1	0.721	0.026
ILE27CG2	0.611	0.024
THR29CG2	0.398	0.019
LEU32CD1	0.611	0.025
LEU32CD2	0.393	0.023
THR34CG2	0.547	0.021
VAL35CG2	0.75	0.04
MET36CE	0.249	0.035
LEU39CD2	0.482	0.023
ALA46CB	0.825	0.042
LEU48CD2	0.398	0.029
MET51CE	0.189	0.044
ILE52CG2	0.681	0.032
ILE52CD1	0.338	0.028
VAL55CG1	0.586	0.027
VAL55CG2	0.557	0.028
THR62CG2	0.895	0.04
ILE63CD1	0.517	0.03
ILE63CG2	0.716	0.032
LEU69CD1	0.427	0.026
LEU69CD2	0.358	0.026
THR70CG2	0.611	0.026
MET71CE	0.159	0.042
MET72CE	0.253	0.018
MET76CE	0.089	0.026
THR79CG2	0.249	0.027
ILE85CG2	0.606	0.02
ILE85CD1	0.363	0.035
ALA88CB	0.81	0.032
VAL91CG1	0.755	0.014
VAL91CG2	0.731	0.023
ILE100CG2	0.82	0.031
ILE100CD1	0.661	0.028
ALA102CB	0.994	0.059
LEU105CD1	0.358	0.026
LEU105CD2	0.278	0.031
VAL108CG2	0.537	0.024
MET109CE	0.154	0.044
THR110CG2	0.532	0.015
LEU112CD2	0.437	0.015
LEU116CD1	0.348	0.023
LEU116CD2	0.328	0.023
VAL121CG1	0.562	0.02
VAL121CG2	0.532	0.019
MET124CE	0.194	0.051
ILE125CG2	0.636	0.024

ID	O^2_{axis}	Err
ILE125CD1	0.219	0.058
ALA128CB	0.81	0.042
ILE130CG2	0.522	0.022
ILE130CD1	0.318	0.051
VAL136CG2	0.78	0.036
VAL142CG1	0.76	0.034
VAL142CG2	0.651	0.031
MET144CE	0.124	0.042
MET145CE	0.194	0.041
THR146CG2	0.427	0.024
ALA147CB	0.343	0.033

Table C-30: Methyl Order Parameters of CaM(D95N) bound to smMLCK(p)

ID	O^2_{axis}	Err
LEU4CD1	0.333	0.038
ILE9CD1	0.532	0.04
ALA10CB	0.915	0.047
ALA15CB	0.994	0.051
LEU18CD2	0.408	0.042
THR26CG2	0.616	0.023
ILE27CD1	0.8	0.028
ILE27CG2	0.77	0.018
THR29CG2	0.591	0.014
THR34CG2	0.661	0.006
VAL35CG1	0.641	0.014
VAL35CG2	0.691	0.025
MET36CE	0.313	0.033
LEU39CD1	0.542	0.025
LEU39CD2	0.522	0.034
ALA46CB	0.84	0.038
LEU48CD2	0.78	0.038
MET51CE	0.288	0.042
ILE52CD1	0.328	0.043
ILE52CG2	0.775	0.041
VAL55CG1	0.457	0.025
VAL55CG2	0.422	0.036
ILE63CD1	0.81	0.033
ILE63CG2	0.845	0.033
LEU69CD1	0.308	0.044
THR70CG2	0.661	0.025
MET71CE	0.422	0.036
MET72CE	0.731	0.026
ALA73CB	0.83	0.042
MET76CE	0.089	0.066
THR79CG2	0.373	0.03
ILE85CD1	0.303	0.042
ILE85CG2	0.656	0.026
VAL91CG2	0.76	0.024
ILE100CD1	0.865	0.013
ALA102CB	0.959	0.024
ALA103CB	0.929	0.032
LEU105CD2	0.636	0.027
VAL108CG2	0.527	0.018
MET109CE	0.353	0.033
THR110CG2	0.681	0.028
LEU112CD2	0.601	0.022
LEU116CD1	0.189	0.056
VAL121CG2	0.646	0.024
MET124CE	0.835	0.032
ILE125CD1	0.408	0.05
ILE125CG2	0.805	0.027
ALA128CB	0.924	0.036
ILE130CD1	0.363	0.04
ILE130CG2	0.596	0.029
VAL136CG2	0.845	0.04
VAL142CG1	0.611	0.015
VAL142CG2	0.651	0.025
MET144CE	0.398	0.021
MET145CE	0.283	0.026
THR146CG2	0.547	0.021
ALA147CB	0.363	0.026

Table C-31: Methyl Order Parameters of smMLCK(p) bound to CaM(D95N)

ID	O^2_{axis}	Err
ALA1CB	0.731	0.011
THR8CG2	0.626	0.041
ALA11CB	0.83	0.003
VAL12CG1	0.721	0.01
VAL12CG2	0.706	0.012
ALA14CB	0.855	0.011
ILE15CG2	0.656	0.009
ILE15CD1	0.363	0.006
LEU18CD1	0.661	0.004
LEU18CD2	0.671	0.004

Table C-32: Methyl Order Parameters of WT CAP:cAMP$_2$

ID	O^2_{axis}	Err
LEU11d2	0.46	0.04
LEU11d1	0.43	0.04
LEU15d2	0.85	0.06
LEU15d1	0.59	0.02
ILE20d1	0.15	0.03
LEU29d2	0.36	0.04
LEU29d1	0.47	0.04
ILE30d1	0.79	0.04
LEU39d2	0.74	0.03
LEU39d1	0.73	0.03
ILE42d1	0.56	0.04
VAL43g1	0.74	0.07
VAL43g2	0.7	0.04
VAL47g1	0.66	0.03
VAL47g2	0.66	0.05
VAL49g2	0.96	0.04
VAL49g1	0.86	0.03
LEU50d1	0.33	0.06
LEU50d2	0.32	0.04
ILE51d1	0.54	0.04
ILE60d1	0.46	0.02
LEU61d1	0.4	0.04
LEU61d2	0.37	0.04
LEU64d2	0.68	0.03
LEU64d1	0.67	0.03
ILE70d1	0.55	0.06
LEU73d2	0.63	0.05
LEU73d1	0.57	0.03
LEU75d2	0.52	0.04
LEU75d1	0.47	0.04
VAL86g1	0.66	0.09
VAL86g2	0.63	0.05
VAL94g1	0.63	0.04
VAL94g2	0.56	0.03
ILE97d1	0.52	0.02
LEU105d1	0.56	0.03
LEU105d2	0.55	0.03
ILE106d1	0.36	0.04
VAL108g2	0.52	0.03
VAL108g1	0.46	0.03
ILE112d1	0.55	0.07
LEU113d2	0.44	0.07
LEU113d1	0.54	0.06
LEU116d1	0.27	0.05
LEU116d2	0.24	0.04
LEU124d2	0.29	0.03
LEU124d1	0.29	0.02
VAL126g2	0.52	0.04
VAL126g1	0.49	0.03
VAL131g2	0.45	0.05
VAL131g1	0.51	0.05
LEU134d1	0.54	0.05
LEU134d2	0.51	0.07
LEU137d2	0.55	0.07

ID	O^2_{axis}	Err
LEU137d1	0.45	0.04
VAL139g1	0.5	0.04
VAL139g2	0.49	0.04
ILE143d1	0.44	0.04
LEU147d1	0.62	0.08
LEU147d2	0.56	0.08
LEU148d2	0.35	0.04
LEU148d1	0.34	0.07
LEU150d1	0.44	0.14
LEU150d2	0.49	0.06
ILE165d1	0.44	0.05
ILE167d1	0.29	0.06
ILE172d1	0.42	0.05
ILE175d1	0.54	0.05
VAL176g2	0.52	0.05
VAL176g1	0.37	0.05
VAL183g1	0.44	0.07
VAL183g2	0.17	0.05
ILE186d1	0.23	0.04
LEU187d1	0.44	0.06
LEU187d2	0.54	0.05
LEU190d1	0.63	0.05
LEU190d2	0.44	0.09
LEU195d1	0.48	0.05
LEU195d2	0.32	0.06
ILE196d1	0.3	0.1

ID	O^2_{axis}	Err
ILE203d1	0.54	0.11
VAL204g2	0.54	0.05
VAL204g1	0.5	0.04
VAL205g1	0.54	0.05
VAL205g2	0.31	0.04
ALA36	0.9	0.05
ALA48	0.92	0.12
MET59	0.13	0.04
ALA84	0.66	0.19
ALA88	0.86	0.2
ALA91	0.9	0.22
ALA95	0.71	0.22
MET114	0.17	0.1
ALA118	0.62	0.14
MET120	0.24	0.07
ALA121	0.87	0.22
ALA135	0.85	0.2
ALA144	0.93	0.23
ALA151	0.93	0.19
ALA156	0.81	0.17
MET157	0.31	0.18
MET163	0.4	0.19
MET189	0.53	0.09
ALA198	0.74	0.15

Table C-33: Methyl Order Parameters of CAP:cAMP$_2$:DNA

ID	O^2_{axis}	Err
LEU11d2	0.45	0.02
LEU11d1	0.43	0.01
LEU15d2	0.9	0.02
LEU15d1	0.68	0.02
ILE20d1	0.24	0.01
LEU29d2	0.22	0.02
LEU29d1	0.3	0.02
ILE30d1	0.82	0.02
LEU39d2	0.72	0.02

ID	O^2_{axis}	Err
LEU39d1	0.8	0.02
ILE42d1	0.72	0.03
VAL43g1	0.86	0.02
VAL43g2	0.71	0.02
VAL47g1	0.88	0.04
VAL47g2	0.7	0.03
VAL49g2	0.79	0.02
VAL49g1	0.72	0.02
LEU50d1	0.27	0.01

ID	O^2_{axis}	Err
LEU50d2	0.26	0.01
ILE51d1	0.61	0.01
ILE60d1	0.61	0.01
LEU61d1	0.32	0.01
LEU61d2	0.32	0.02
LEU64d2	0.87	0.02
LEU64d1	0.7	0.03
ILE70d1	0.49	0.03
LEU73d2	0.9	0.04
LEU73d1	0.69	0.02
LEU75d2	0.63	0.02
LEU75d1	0.6	0.02
VAL86g1	0.9	0.04
VAL86g2	0.67	0.02
VAL94g1	0.5	0.02
VAL94g2	0.67	0.02
ILE97d1	0.64	0.02
LEU105d1	0.39	0.02
LEU105d2	0.36	0.02
ILE106d1	0.48	0.02
VAL108g2	0.54	0.02
VAL108g1	0.52	0.02
ILE112d1	0.48	0.01
LEU113d2	0.46	0.02
LEU113d1	0.4	0.02
LEU116d1	0.46	0.02
LEU116d2	0.36	0.02
LEU124d2	0.35	0.02
LEU124d1	0.34	0.01
VAL126g2	0.49	0.02
VAL126g1	0.49	0.01
VAL131g2	0.48	0.02
VAL131g1	0.47	0.02
LEU134d1	0.33	0.01
LEU134d2	0.48	0.02
LEU137d2	0.48	0.01
LEU137d1	0.32	0.02
VAL139g1	0.52	0.02
VAL139g2	0.5	0.02

ID	O^2_{axis}	Err
ILE143d1	0.46	0.04
LEU147d1	0.9	0.02
LEU147d2	0.68	0.02
LEU148d2	0.45	0.01
LEU148d1	0.41	0.02
LEU150d1	0.4	0.03
LEU150d2	0.64	0.02
ILE165d1	0.6	0.01
ILE167d1	0.46	0.02
ILE172d1	0.78	0.02
ILE175d1	0.73	0.01
VAL176g2	0.57	0.01
VAL176g1	0.56	0.01
VAL183g1	0.53	0.02
VAL183g2	0.56	0.02
ILE186d1	0.78	0.02
LEU187d1	0.74	0.02
LEU187d2	0.79	0.02
LEU190d1	0.72	0.02
LEU190d2	0.82	0.02
LEU195d1	0.71	0.02
LEU195d2	0.9	0.03
ILE196d1	0.68	0.13
ILE203d1	0.6	0.02
VAL204g2	0.59	0.02
VAL204g1	0.55	0.02
VAL205g1	0.54	0.02
VAL205g2	0.41	0.02
ALA36	0.86	0.1
ALA48	0.91	0.15
MET59	0.29	0.02
ALA84	0.72	0.11
ALA88	0.94	0.08
ALA91	0.71	0.12
ALA95	0.81	0.1
MET114	0.12	0.01
ALA118	0.8	0.14
MET120	0.24	0.03
ALA121	0.86	0.19

ID	O^2_{axis}	Err
ALA135	0.95	0.15
ALA144	0.92	0.18
ALA151	0.92	0.2
ALA156	0.88	0.1

ID	O^2_{axis}	Err
MET157	0.38	0.16
MET163	0.39	0.17
MET189	0.62	0.12
ALA198	0.79	0.12

Table C-34: Methyl Order Parameters of CAP(D53H):cAMP$_2$

ID	O^2_{axis}	Err
LEU11d2	0.24	0.03
LEU11d1	0.23	0.03
LEU15d2	0.47	0.04
LEU15d1	0.48	0.02
ILE20d1	0.13	0.02
LEU29d2	0.35	0.03
LEU29d1	0.3	0.02
ILE30d1	0.64	0.03
LEU39d2	0.72	0.02
LEU39d1	0.65	0.02
ILE42d1	0.7	0.03
VAL43g1	0.78	0.04
VAL43g2	0.77	0.02
VAL47g1	0.76	0.02
VAL47g2	0.74	0.03
VAL49g2	0.82	0.02
VAL49g1	0.88	0.02
LEU50d1	0.25	0.04
LEU50d2	0.25	0.03
ILE51d1	0.61	0.03
ILE60d1	0.24	0.01
LEU61d1	0.34	0.03
LEU61d2	0.34	0.02
LEU64d2	0.77	0.02
LEU64d1	0.76	0.02
ILE70d1	0.64	0.04
LEU73d2	0.71	0.03
LEU73d1	0.7	0.02
LEU75d2	0.57	0.03
LEU75d1	0.47	0.02
VAL86g1	0.75	0.06

ID	O^2_{axis}	Err
VAL86g2	0.71	0.03
VAL94g1	0.72	0.03
VAL94g2	0.7	0.02
ILE97d1	0.58	0.01
LEU105d1	0.69	0.02
LEU105d2	0.66	0.02
ILE106d1	0.3	0.03
VAL108g2	0.58	0.02
VAL108g1	0.45	0.02
ILE112d1	0.66	0.05
LEU113d2	0.6	0.05
LEU113d1	0.37	0.04
LEU116d1	0.15	0.03
LEU116d2	0.15	0.03
LEU124d2	0.2	0.02
LEU124d1	0.18	0.01
VAL126g2	0.57	0.02
VAL126g1	0.51	0.02
VAL131g2	0.56	0.03
VAL131g1	0.44	0.03
LEU134d1	0.59	0.03
LEU134d2	0.56	0.04
LEU137d2	0.64	0.05
LEU137d1	0.43	0.03
VAL139g1	0.55	0.03
VAL139g2	0.51	0.03
ILE143d1	0.43	0.02
LEU147d1	0.7	0.05
LEU147d2	0.69	0.05
LEU148d2	0.26	0.03
LEU148d1	0.26	0.05

ID	O^2_{axis}	Err
LEU150d1	0.51	0.09
LEU150d2	0.41	0.04
ILE165d1	0.4	0.03
ILE167d1	0.22	0.04
ILE172d1	0.34	0.03
ILE175d1	0.58	0.03
VAL176g2	0.38	0.03
VAL176g1	0.33	0.03
VAL183g1	0.58	0.05
VAL183g2	0.53	0.03
ILE186d1	0.54	0.03
LEU187d1	0.62	0.04
LEU187d2	0.51	0.04
LEU190d1	0.4	0.03
LEU190d2	0.39	0.06
LEU195d1	0.48	0.03
LEU195d2	0.68	0.04
ILE196d1	0.7	0.06
ILE203d1	0.61	0.07
VAL204g2	0.62	0.03
VAL204g1	0.51	0.03

ID	O^2_{axis}	Err
VAL205g1	0.61	0.03
VAL205g2	0.46	0.03
ALA36	0.88	0.2
ALA48	0.94	0.1
MET59	0.5	0.22
ALA84	0.93	0.34
ALA88	0.92	0.29
ALA91	0.96	0.33
ALA95	0.96	0.36
MET114	0.54	0.1
ALA118	0.89	0.24
MET120	0.51	0.07
ALA121	0.85	0.23
ALA135	0.88	0.32
ALA144	0.94	0.32
ALA151	0.84	0.34
ALA156	0.77	0.3
MET157	0.27	0.18
MET163	0.45	0.19
MET189	0.33	0.06
ALA198	0.76	0.16

Table C-35: Methyl Order Parameters of CAP(D53H):cAMP$_2$:DNA

ID	O^2_{axis}	Err
LEU11d2	0.23	0.03
LEU11d1	0.21	0.02
LEU15d2	0.5	0.03
LEU15d1	0.52	0.02
ILE20d1	0.14	0.01
LEU29d2	0.41	0.03
LEU29d1	0.34	0.02
ILE30d1	0.71	0.02
LEU39d2	0.73	0.03
LEU39d1	0.72	0.03
ILE42d1	0.72	0.03
VAL43g1	0.83	0.03
VAL43g2	0.86	0.02
VAL47g1	0.84	0.05

ID	O^2_{axis}	Err
VAL47g2	0.74	0.04
VAL49g2	0.9	0.03
VAL49g1	0.9	0.02
LEU50d1	0.25	0.01
LEU50d2	0.24	0.01
ILE51d1	0.65	0.02
ILE60d1	0.21	0.02
LEU61d1	0.37	0.02
LEU61d2	0.36	0.03
LEU64d2	0.77	0.03
LEU64d1	0.9	0.03
ILE70d1	0.71	0.03
LEU73d2	0.8	0.05
LEU73d1	0.73	0.02

ID	O^2_{axis}	Err
LEU75d2	0.59	0.02
LEU75d1	0.5	0.02
VAL86g1	0.74	0.05
VAL86g2	0.72	0.03
VAL94g1	0.72	0.02
VAL94g2	0.73	0.02
ILE97d1	0.61	0.02
LEU105d1	0.72	0.03
LEU105d2	0.72	0.02
ILE106d1	0.31	0.02
VAL108g2	0.6	0.02
VAL108g1	0.5	0.02
ILE112d1	0.72	0.01
LEU113d2	0.64	0.03
LEU113d1	0.42	0.03
LEU116d1	0.14	0.02
LEU116d2	0.13	0.02
LEU124d2	0.18	0.02
LEU124d1	0.15	0.02
VAL126g2	0.59	0.03
VAL126g1	0.54	0.02
VAL131g2	0.58	0.02
VAL131g1	0.5	0.02
LEU134d1	0.64	0.03
LEU134d2	0.56	0.02
LEU137d2	0.68	0.03
LEU137d1	0.49	0.05
VAL139g1	0.55	0.03
VAL139g2	0.54	0.03
ILE143d1	0.48	0.02
LEU147d1	0.67	0.03
LEU147d2	0.72	0.04
LEU148d2	0.3	0.03
LEU148d1	0.29	0.02
LEU150d1	0.52	0.03
LEU150d2	0.46	0.03
ILE165d1	0.44	0.02
ILE167d1	0.43	0.01
ILE172d1	0.41	0.02

ID	O^2_{axis}	Err
ILE175d1	0.61	0.02
VAL176g2	0.61	0.02
VAL176g1	0.59	0.02
VAL183g1	0.73	0.02
VAL183g2	0.71	0.02
ILE186d1	0.68	0.03
LEU187d1	0.67	0.03
LEU187d2	0.72	0.03
LEU190d1	0.52	0.03
LEU190d2	0.5	0.17
LEU195d1	0.75	0.02
LEU195d2	0.71	0.02
ILE196d1	0.77	0.02
ILE203d1	0.66	0.02
VAL204g2	0.66	0.02
VAL204g1	0.54	0.02
VAL205g1	0.65	0.04
VAL205g2	0.5	0.03
ALA36	0.95	0.12
ALA48	0.9	0.16
MET59	0.4	0.19
ALA84	0.96	0.16
ALA88	0.86	0.2
ALA91	0.92	0.28
ALA95	0.95	0.26
MET114	0.59	0.24
ALA118	0.87	0.24
MET120	0.42	0.12
ALA121	0.88	0.14
ALA135	0.94	0.25
ALA144	0.97	0.18
ALA151	0.93	0.18
ALA156	0.92	0.18
MET157	0.32	0.04
MET163	0.41	0.21
MET189	0.39	0.16
ALA198	0.85	0.22

Table C-36: Methyl Order Parameters of CAP(S62F):cAMP$_2$

ID	O^2_{axis}	Err
LEU11d2	0.3	0.05
LEU11d1	0.29	0.04
LEU15d2	0.74	0.06
LEU15d1	0.64	0.04
ILE20d1	0.3	0.02
LEU29d2	0.2	0.06
LEU29d1	0.18	0.04
ILE30d1	0.67	0.04
LEU39d2	0.68	0.06
LEU39d1	0.75	0.05
ILE42d1	0.66	0.07
VAL43g1	0.78	0.06
VAL43g2	0.66	0.04
VAL47g1	0.73	0.09
VAL47g2	0.68	0.08
VAL49g2	0.94	0.05
VAL49g1	0.9	0.05
LEU50d1	0.53	0.03
LEU50d2	0.74	0.03
ILE51d1	0.77	0.04
ILE60d1	0.83	0.03
LEU61d1	0.77	0.03
LEU61d2	0.86	0.05
LEU64d2	0.64	0.05
LEU64d1	0.79	0.05
ILE70d1	0.75	0.05
LEU73d2	0.54	0.1
LEU73d1	0.53	0.04
LEU75d2	0.75	0.05
LEU75d1	0.73	0.04
VAL86g1	0.7	0.09
VAL86g2	0.75	0.05
VAL94g1	0.69	0.05
VAL94g2	0.8	0.04

ID	O^2_{axis}	Err
ILE97d1	0.66	0.05
LEU105d1	0.62	0.05
LEU105d2	0.51	0.04
ILE106d1	0.52	0.04
VAL108g2	0.43	0.04
VAL108g1	0.36	0.05
ILE112d1	0.21	0.03
LEU113d2	0.71	0.06
LEU113d1	0.72	0.06
LEU116d1	0.44	0.04
LEU116d2	0.43	0.04
LEU124d2	0.58	0.04
LEU124d1	0.56	0.03
VAL126g2	0.43	0.05
VAL126g1	0.58	0.04
VAL131g2	0.58	0.04
VAL131g1	0.37	0.04
LEU134d1	0.49	0.05
LEU134d2	0.48	0.04
LEU137d2	0.37	0.05
LEU137d1	0.28	0.09
VAL139g1	0.63	0.06
VAL139g2	0.62	0.06
ILE143d1	0.8	0.04
LEU147d1	0.69	0.06
LEU147d2	0.86	0.08
LEU148d2	0.56	0.05
LEU148d1	0.58	0.04
LEU150d1	0.72	0.05
LEU150d2	0.69	0.05
ILE165d1	0.39	0.03
ILE167d1	0.5	0.03
ILE172d1	0.8	0.03
ILE175d1	0.96	0.04

ID	O^2_{axis}	Err
VAL176g2	0.6	0.04
VAL176g1	0.46	0.04
VAL183g1	0.59	0.04
VAL183g2	0.84	0.04
ILE186d1	0.83	0.05
LEU187d1	0.75	0.06
LEU187d2	0.64	0.05
LEU190d1	0.63	0.07
LEU190d2	0.56	0.33
LEU195d1	0.56	0.05
LEU195d2	0.53	0.04
ILE196d1	0.52	0.04
ILE203d1	0.4	0.04
VAL204g2	0.56	0.04
VAL204g1	0.43	0.04
VAL205g1	0.48	0.08
VAL205g2	0.5	0.06
ALA36	0.66	0.14
ALA48	0.69	0.12
MET59	0.28	0.07
ALA84	0.98	0.1
ALA88	0.89	0.14
ALA91	0.9	0.15
ALA95	0.94	0.15
MET114	0.28	0.07
ALA118	0.82	0.17
MET120	0.45	0.05
ALA121	0.88	0.17
ALA135	0.76	0.18
ALA144	0.99	0.11
ALA151	0.85	0.1
ALA156	0.84	0.16
MET157	0.14	0.02
MET163	0.2	0.05
MET189	0.28	0.1
ALA198	0.76	0.04

Table C-37: Methyl Order Parameters of CAP(S62F):cAMP$_2$:DNA

ID	O^2_{axis}	Err
LEU11d2	0.31	0.02
LEU11d1	0.3	0.02
LEU15d2	0.55	0.02
LEU15d1	0.63	0.01
ILE20d1	0.18	0.01
LEU29d2	0.23	0.02
LEU29d1	0.23	0.01
ILE30d1	0.62	0.02
LEU39d2	0.67	0.01
LEU39d1	0.53	0.01
ILE42d1	0.66	0.02
VAL43g1	0.53	0.03
VAL43g2	0.41	0.01
VAL47g1	0.51	0.01
VAL47g2	0.45	0.02
VAL49g2	0.72	0.01
VAL49g1	0.54	0.01
LEU50d1	0.35	0.02
LEU50d2	0.42	0.02
ILE51d1	0.53	0.02
ILE60d1	0.4	0.01
LEU61d1	0.39	0.02
LEU61d2	0.55	0.01
LEU64d2	0.63	0.01
LEU64d1	0.62	0.01
ILE70d1	0.55	0.02
LEU73d2	0.69	0.02
LEU73d1	0.68	0.01
LEU75d2	0.6	0.02
LEU75d1	0.51	0.01
VAL86g1	0.62	0.04
VAL86g2	0.62	0.02
VAL94g1	0.45	0.02
VAL94g2	0.54	0.01

ID	O^2_{axis}	Err
ILE97d1	0.44	0.01
LEU105d1	0.67	0.01
LEU105d2	0.58	0.01
ILE106d1	0.32	0.02
VAL108g2	0.28	0.01
VAL108g1	0.33	0.01
ILE112d1	0.24	0.03
LEU113d2	0.71	0.03
LEU113d1	0.62	0.02
LEU116d1	0.37	0.02
LEU116d2	0.37	0.02
LEU124d2	0.75	0.01
LEU124d1	0.72	0.01
VAL126g2	0.37	0.01
VAL126g1	0.51	0.01
VAL131g2	0.49	0.03
VAL131g1	0.42	0.03
LEU134d1	0.61	0.02
LEU134d2	0.58	0.02
LEU137d2	0.57	0.02
LEU137d1	0.3	0.01
VAL139g1	0.73	0.03
VAL139g2	0.69	0.03
ILE143d1	0.78	0.02
LEU147d1	0.76	0.03
LEU147d2	0.67	0.05
LEU148d2	0.71	0.02
LEU148d1	0.55	0.02
LEU150d1	0.47	0.02
LEU150d2	0.46	0.02
ILE165d1	0.35	0.02
ILE167d1	0.62	0.02
ILE172d1	0.67	0.02
ILE175d1	0.9	0.03
VAL176g2	0.78	0.02
VAL176g1	0.56	0.02

ID	O^2_{axis}	Err
VAL183g1	0.77	0.02
VAL183g2	0.73	0.02
ILE186d1	0.86	0.02
LEU187d1	0.92	0.03
LEU187d2	0.87	0.02
LEU190d1	0.8	0.02
LEU190d2	0.7	0.04
LEU195d1	0.7	0.04
LEU195d2	0.65	0.02
ILE196d1	0.64	0.02
ILE203d1	0.3	0.02
VAL204g2	0.48	0.02
VAL204g1	0.43	0.01
VAL205g1	0.43	0.05
VAL205g2	0.45	0.02
ALA36	0.62	0.11
ALA48	0.65	0.11
MET59	0.27	0.12
ALA84	0.91	0.09
ALA88	0.75	0.25
ALA91	0.92	0.11
ALA95	0.95	0.09
MET114	0.29	0.03
ALA118	0.86	0.17
MET120	0.43	0.3
ALA121	0.89	0.56
ALA135	0.55	0.11
ALA144	0.9	0.11
ALA151	0.86	0.32
ALA156	0.82	0.14
MET157	0.2	0.16
MET163	0.25	0.19
MET189	0.37	0.15
ALA198	0.76	0.19

Table C-38: Methyl Order Parameters of CAP(T127L/S128I)

ID	O^2_{axis}	Err
LEU11d2	0.56	0.05
LEU11d1	0.48	0.04
LEU15d2	0.96	0.06
LEU15d1	0.72	0.04
ILE20d1	0.22	0.02
LEU29d2	0.71	0.06
LEU29d1	0.38	0.04
ILE30	0.85	0.04
LEU39d2	0.81	0.06
LEU39d1	0.76	0.05
ILE42d1	0.78	0.07
VAL43g1	0.96	0.06
VAL43g2	0.82	0.04
VAL47g1	0.96	0.09
VAL47g2	0.72	0.08
VAL49g2	0.96	0.05
VAL49g1	0.96	0.05
LEU50d1	0.52	0.03
LEU50d2	0.46	0.03
ILE51d1	0.72	0.04
ILE60d1	0.47	0.03
LEU61d1	0.38	0.03
LEU61d2	0.36	0.05
LEU64d2	0.96	0.05
LEU64d1	0.96	0.05
ILE70d1	0.77	0.05
LEU73d2	0.82	0.1
LEU73d1	0.69	0.04
LEU75d2	0.74	0.05
LEU75d1	0.59	0.04
VAL86g1	0.96	0.09
VAL86g2	0.83	0.05
VAL94g1	0.92	0.05
VAL94g2	0.72	0.04
ILE97d1	0.75	0.05
LEU105d1	0.69	0.05
LEU105d2	0.62	0.04

ID	O^2_{axis}	Err
ILE106d1	0.61	0.04
VAL108g2	0.75	0.04
VAL108g1	0.73	0.05
ILE112d1	0.87	0.03
LEU113d2	0.96	0.06
LEU113d1	0.92	0.06
LEU116d1	0.36	0.04
LEU116d2	0.3	0.04
LEU124d2	0.55	0.04
LEU124d1	0.34	0.03
VAL126g2	0.96	0.05
VAL126g1	0.76	0.04
LEU127D1	0.78	0.05
LEU127D2	0.67	0.04
ILE128	0.71	0.04
VAL131g2	0.79	0.04
VAL131g1	0.74	0.04
LEU134d1	0.84	0.05
LEU134d2	0.66	0.04
LEU137d2	0.96	0.05
LEU137d1	0.92	0.09
VAL139g1	0.96	0.06
VAL139g2	0.89	0.06
ILE143d1	0.59	0.04
LEU147d1	0.95	0.06
LEU147d2	0.95	0.08
LEU148d2	0.8	0.05
LEU148d1	0.65	0.04
LEU150d1	0.94	0.05
LEU150d2	0.91	0.05
ILE165d1	0.51	0.03
ILE167d1	0.28	0.03
ILE172d1	0.62	0.03
ILE175d1	0.69	0.04
VAL176g2	0.72	0.04
VAL176g1	0.66	0.04
VAL183g1	0.45	0.04

ID	O^2_{axis}	Err
VAL183g2	0.37	0.04
ILE186d1	0.52	0.05
LEU187d1	0.96	0.06
LEU187d2	0.86	0.05
LEU190d1	0.95	0.07
LEU190d2	0.92	0.33
LEU195d1	0.79	0.05
LEU195d2	0.59	0.04
ILE196d1	0.58	0.04
ILE203d1	0.96	0.04
VAL204g2	0.79	0.04
VAL204g1	0.75	0.04
VAL205g1	0.94	0.08
VAL205g2	0.9	0.06
ALA36	0.62	0.16
ALA48	0.91	0.09
MET59	0.59	0.11

ID	O^2_{axis}	Err
ALA84	0.94	0.14
ALA88	0.8	0.16
ALA91	0.79	0.15
ALA95	0.85	0.13
MET114	0.51	0.11
ALA118	0.61	0.13
MET120	0.48	0.1
ALA121	0.95	0.2
ALA135	0.6	0.16
ALA144	0.94	0.11
ALA151	0.68	0.15
ALA156	0.62	0.11
MET157	0.17	0.09
MET163	0.38	0.09
MET189	0.33	0.1
ALA198	0.45	0.1

Table C-39: Methyl Order Parameters of CAP(T127L/S128I):DNA

ID	O^2_{axis}	Err
LEU11d2	0.62	0.03
LEU11d1	0.53	0.03
LEU15d2	0.84	0.04
LEU15d1	0.6	0.02
ILE20d1	0.19	0.02
LEU29d2	0.74	0.03
LEU29d1	0.45	0.02
ILE30	0.55	0.03
LEU39d2	0.57	0.02
LEU39d1	0.56	0.02
ILE42d1	0.73	0.03
VAL43g1	0.95	0.05
VAL43g2	0.68	0.03
VAL47g1	0.35	0.02
VAL47g2	0.17	0.04
VAL49g2	0.4	0.02
VAL49g1	0.4	0.02
LEU50d1	0.36	0.04

ID	O^2_{axis}	Err
LEU50d2	0.3	0.03
ILE51d1	0.45	0.03
ILE60d1	0.19	0.01
LEU61d1	0.56	0.03
LEU61d2	0.49	0.03
LEU64d2	0.5	0.02
LEU64d1	0.49	0.02
ILE70d1	0.72	0.04
LEU73d2	0.6	0.03
LEU73d1	0.48	0.02
LEU75d2	0.65	0.03
LEU75d1	0.5	0.03
VAL86g1	0.96	0.06
VAL86g2	0.93	0.03
VAL94g1	0.71	0.03
VAL94g2	0.48	0.02
ILE97d1	0.62	0.02
LEU105d1	0.6	0.02

ID	O^2_{axis}	Err
LEU105d2	0.26	0.02
ILE106d1	0.77	0.03
VAL108g2	0.53	0.02
VAL108g1	0.52	0.02
ILE112d1	0.67	0.05
LEU113d2	0.96	0.05
LEU113d1	0.82	0.04
LEU116d1	0.77	0.03
LEU116d2	0.72	0.03
LEU124d2	0.55	0.02
LEU124d1	0.45	0.02
VAL126g2	0.62	0.03
VAL126g1	0.55	0.02
LEU127D1	0.76	0.03
LEU127D2	0.68	0.04
ILE128	0.76	0.03
VAL131g2	0.96	0.05
VAL131g1	0.96	0.05
LEU134d1	0.83	0.03
LEU134d2	0.73	0.03
LEU137d2	0.93	0.03
LEU137d1	0.83	0.03
VAL139g1	0.96	0.06
VAL139g2	0.89	0.06
ILE143d1	0.68	0.03
LEU147d1	0.92	0.05
LEU147d2	0.96	0.09
LEU148d2	0.87	0.04
LEU148d1	0.79	0.03
LEU150d1	0.83	0.04
LEU150d2	0.79	0.03
ILE165d1	0.62	0.03
ILE167d1	0.63	0.03
ILE172d1	0.68	0.03
ILE175d1	0.74	0.05
VAL176g2	0.89	0.04
VAL176g1	0.77	0.03

ID	O^2_{axis}	Err
VAL183g1	0.96	0.04
VAL183g2	0.89	0.04
ILE186d1	0.72	0.03
LEU187d1	0.96	0.06
LEU187d2	0.96	0.03
LEU190d1	0.96	0.04
LEU190d2	0.96	0.06
LEU195d1	0.96	0.07
LEU195d2	0.96	0.03
ILE196d1	0.87	0.03
ILE203d1	0.96	0.03
VAL204g2	0.81	0.03
VAL204g1	0.75	0.02
VAL205g1	0.96	0.08
VAL205g2	0.72	0.03
ALA36	0.75	0.17
ALA48	0.93	0.14
MET59	0.44	0.22
ALA84	0.95	0.24
ALA88	0.83	0.19
ALA91	0.85	0.11
ALA95	0.9	0.12
MET114	0.21	0.15
ALA118	0.76	0.3
MET120	0.23	0.54
ALA121	0.7	0.2
ALA135	0.79	0.2
ALA144	0.81	0.12
ALA151	0.82	0.56
ALA156	0.31	0.06
MET157	0.14	0.1
MET163	0.49	0.16
MET189	0.32	0.27
ALA198	0.74	0.1

Table C-40: Methyl Order Parameters of CAP(T127L/S128I):cAMP$_2$

ID	O^2_{axis}	Err
LEU11d2	0.16	0.05
LEU11d1	0.31	0.04
LEU15d2	0.47	0.06
LEU15d1	0.53	0.04
ILE20d1	0.14	0.02
LEU29d2	0.21	0.06
LEU29d1	0.17	0.04
ILE30	0.3	0.04
LEU39d2	0.45	0.06
LEU39d1	0.53	0.05
ILE42d1	0.58	0.07
VAL43g1	0.47	0.06
VAL43g2	0.45	0.04
VAL47g1	0.54	0.09
VAL47g2	0.64	0.08
VAL49g2	0.5	0.05
VAL49g1	0.46	0.05
LEU50d1	0.17	0.03
LEU50d2	0.16	0.03
ILE51d1	0.48	0.04
ILE60d1	0.12	0.03
LEU61d1	0.3	0.03
LEU61d2	0.29	0.05
LEU64d2	0.46	0.05
LEU64d1	0.34	0.05
ILE70d1	0.45	0.05
LEU73d2	0.2	0.1
LEU73d1	0.34	0.04
LEU75d2	0.3	0.05
LEU75d1	0.28	0.04
VAL86g1	0.69	0.09
VAL86g2	0.51	0.05
VAL94g1	0.54	0.05
VAL94g2	0.53	0.04
ILE97d1	0.57	0.05

ID	O^2_{axis}	Err
LEU105d1	0.45	0.05
LEU105d2	0.43	0.04
ILE106d1	0.47	0.04
VAL108g2	0.34	0.04
VAL108g1	0.47	0.05
ILE112d1	0.45	0.03
LEU113d2	0.51	0.06
LEU113d1	0.53	0.06
LEU116d1	0.19	0.04
LEU116d2	0.23	0.04
LEU124d2	0.31	0.04
LEU124d1	0.3	0.03
VAL126g2	0.56	0.05
VAL126g1	0.56	0.04
LEU127D1	0.67	0.04
LEU127D2	0.57	0.04
ILE128	0.66	0.05
VAL131g2	0.51	0.04
VAL131g1	0.44	0.05
LEU134d1	0.67	0.09
LEU134d2	0.54	0.06
LEU137d2	0.22	0.06
LEU137d1	0.21	0.04
VAL139g1	0.43	0.06
VAL139g2	0.29	0.08
ILE143d1	0.27	0.05
LEU147d1	0.47	0.04
LEU147d2	0.43	0.05
LEU148d2	0.53	0.05
LEU148d1	0.37	0.03
LEU150d1	0.42	0.03
LEU150d2	0.51	0.03
ILE165d1	0.37	0.04
ILE167d1	0.43	0.04
ILE172d1	0.35	0.04

ID	O^2_{axis}	Err
ILE175d1	0.27	0.04
VAL176g2	0.56	0.04
VAL176g1	0.52	0.05
VAL183g1	0.51	0.06
VAL183g2	0.53	0.05
ILE186d1	0.52	0.07
LEU187d1	0.53	0.33
LEU187d2	0.51	0.05
LEU190d1	0.35	0.04
LEU190d2	0.36	0.04
LEU195d1	0.53	0.04
LEU195d2	0.53	0.04
ILE196d1	0.52	0.04
ILE203d1	0.45	0.08
VAL204g2	0.57	0.06
VAL204g1	0.55	0.07
VAL205g1	0.36	0.12
VAL205g2	0.53	0.07
ALA36	0.56	0.05

ID	O^2_{axis}	Err
ALA48	0.7	0.11
MET59	0.25	0.05
ALA84	0.97	0.19
ALA88	0.6	0.04
ALA91	0.67	0.14
ALA95	0.72	0.15
MET114	0.18	0.05
ALA118	0.68	0.05
MET120	0.19	0.03
ALA121	0.85	0.18
ALA135	0.68	0.05
ALA144	0.49	0.1
ALA151	0.43	0.03
ALA156	0.52	0.04
MET157	0.11	0.02
MET163	0.38	0.03
MET189	0.29	0.02
ALA198	0.49	0.03

Table C-41: Methyl Order Parameters of CAP(T127L/S128I):cAMP$_2$:DNA

ID	O^2_{axis}	Err
LEU11d2	0.16	0.03
LEU11d1	0.29	0.03
LEU15d2	0.48	0.04
LEU15d1	0.52	0.02
ILE20d1	0.12	0.02
LEU29d2	0.22	0.03
LEU29d1	0.18	0.02
ILE30	0.3	0.03
LEU39d2	0.44	0.02
LEU39d1	0.44	0.02
ILE42d1	0.53	0.03
VAL43g1	0.47	0.05
VAL43g2	0.42	0.03
VAL47g1	0.63	0.02
VAL47g2	0.64	0.04
VAL49g2	0.4	0.02

ID	O^2_{axis}	Err
VAL49g1	0.4	0.02
LEU50d1	0.21	0.04
LEU50d2	0.21	0.03
ILE51d1	0.45	0.03
ILE60d1	0.14	0.01
LEU61d1	0.33	0.03
LEU61d2	0.32	0.03
LEU64d2	0.4	0.02
LEU64d1	0.34	0.02
ILE70d1	0.44	0.04
LEU73d2	0.26	0.03
LEU73d1	0.31	0.02
LEU75d2	0.26	0.03
LEU75d1	0.24	0.03
VAL86g1	0.73	0.06
VAL86g2	0.6	0.03

ID	O^2_{axis}	Err
VAL94g1	0.53	0.03
VAL94g2	0.55	0.02
ILE97d1	0.57	0.02
LEU105d1	0.43	0.02
LEU105d2	0.47	0.02
ILE106d1	0.48	0.03
VAL108g2	0.32	0.02
VAL108g1	0.47	0.02
ILE112d1	0.48	0.05
LEU113d2	0.54	0.05
LEU113d1	0.6	0.04
LEU116d1	0.19	0.03
LEU116d2	0.13	0.03
LEU124d2	0.29	0.02
LEU124d1	0.28	0.02
VAL126g2	0.89	0.03
VAL126g1	0.76	0.02
LEU127D1	0.74	0.05
LEU127D2	0.7	0.05
ILE128	0.6	0.03
VAL131g2	0.6	0.03
VAL131g1	0.66	0.03
LEU134d1	0.74	0.03
LEU134d2	0.53	0.06
LEU137d2	0.15	0.06
LEU137d1	0.14	0.03
VAL139g1	0.44	0.05
VAL139g2	0.32	0.09
ILE143d1	0.35	0.04
LEU147d1	0.48	0.03
LEU147d2	0.44	0.04
LEU148d2	0.58	0.03
LEU148d1	0.47	0.03
LEU150d1	0.57	0.03
LEU150d2	0.6	0.03
ILE165d1	0.48	0.05
ILE167d1	0.58	0.04
ILE172d1	0.37	0.03
ILE175d1	0.35	0.04

ID	O^2_{axis}	Err
VAL176g2	0.76	0.04
VAL176g1	0.7	0.03
VAL183g1	0.6	0.06
VAL183g2	0.58	0.03
ILE186d1	0.52	0.04
LEU187d1	0.57	0.06
LEU187d2	0.54	0.07
LEU190d1	0.42	0.03
LEU190d2	0.4	0.03
LEU195d1	0.57	0.03
LEU195d2	0.6	0.03
ILE196d1	0.7	0.02
ILE203d1	0.48	0.08
VAL204g2	0.7	0.03
VAL204g1	0.68	0.23
VAL205g1	0.4	0.2
VAL205g2	0.61	0.22
ALA36	0.46	0.14
ALA48	0.73	0.12
MET59	0.27	0.13
ALA84	0.81	0.14
ALA88	0.68	0.52
ALA91	0.78	0.1
ALA95	0.56	0.13
MET114	0.24	0.09
ALA118	0.69	0.18
MET120	0.31	0.06
ALA121	0.51	0.1
ALA135	0.54	0.12
ALA144	0.67	0.07
ALA151	0.94	0.21
ALA156	0.34	0.04
MET157	0.27	0.06
MET163	0.19	0.1
MET189	0.32	0.16
ALA198	0.65	0.11

Table C-42: Methyl Order Parameters of CAP(G141S)

ID	O^2_{axis}	Err
LEU11d2	0.17	0.04
LEU11d1	0.24	0.04
LEU15d2	0.32	0.06
LEU15d1	0.34	0.06
ILE20d1	0.15	0.03
LEU29d2	0.2	0.05
LEU29d1	0.18	0.05
ILE30d1	0.24	0.08
LEU39d2	0.3	0.08
LEU39d1	0.3	0.08
ILE42d1	0.35	0.08
VAL43g1	0.32	0.09
VAL43g2	0.3	0.09
VAL47g1	0.39	0.09
VAL47g2	0.4	0.08
VAL49g2	0.29	0.09
VAL49g1	0.29	0.09
LEU50d1	0.2	0.04
LEU50d2	0.19	0.04
ILE51d1	0.31	0.07
ILE60d1	0.16	0.04
LEU61d1	0.25	0.05
LEU61d2	0.25	0.05
LEU64d2	0.29	0.08
LEU64d1	0.25	0.09
ILE70d1	0.31	0.08
LEU73d2	0.22	0.09
LEU73d1	0.24	0.08
LEU75d2	0.22	0.07
LEU75d1	0.21	0.06
VAL86g1	0.44	0.08
VAL86g2	0.38	0.08
VAL94g1	0.35	0.08
VAL94g2	0.35	0.08
ILE97d1	0.36	0.07
LEU105d1	0.3	0.08
LEU105d2	0.32	0.08
ILE106d1	0.32	0.04
VAL108g2	0.25	0.07
VAL108g1	0.32	0.06
ILE112d1	0.32	0.08
LEU113d2	0.35	0.07
LEU113d1	0.38	0.05
LEU116d1	0.19	0.03
LEU116d2	0.16	0.03
LEU124d2	0.24	0.03
LEU124d1	0.23	0.03
VAL126g2	0.52	0.07
VAL126g1	0.45	0.06
VAL131g2	0.45	0.07
VAL131g1	0.43	0.06
LEU134d1	0.38	0.07
LEU134d2	0.38	0.07
LEU137d2	0.41	0.08
LEU137d1	0.45	0.06
VAL139g1	0.42	0.06
VAL139g2	0.46	0.06
ILE143d1	0.34	0.06
LEU147d1	0.38	0.07
LEU147d2	0.46	0.08
LEU148d2	0.45	0.04
LEU148d1	0.32	0.04
LEU150d1	0.3	0.06
LEU150d2	0.37	0.06
ILE165d1	0.32	0.06
ILE167d1	0.37	0.06
ILE172d1	0.38	0.05
ILE175d1	0.32	0.07
VAL176g2	0.37	0.07
VAL176g1	0.27	0.07
VAL183g1	0.34	0.08
VAL183g2	0.45	0.08

ID	O^2_{axis}	Err
ILE186d1	0.43	0.08
LEU187d1	0.38	0.07
LEU187d2	0.37	0.08
LEU190d1	0.34	0.06
LEU190d2	0.36	0.06
LEU195d1	0.35	0.08
LEU195d2	0.29	0.08
ILE196d1	0.28	0.08
ILE203d1	0.36	0.07
VAL204g2	0.38	0.07
VAL204g1	0.43	0.06
VAL205g1	0.32	0.07
VAL205g2	0.43	0.06
ALA36	0.41	0.1
ALA48	0.28	0.16
MET59	0.38	0.09
ALA84	0.46	0.16
ALA88	0.61	0.1
ALA91	0.3	0.16
ALA95	0.58	0.16
MET114	0.62	0.11
ALA118	0.6	0.11
MET120	0.53	0.09
ALA121	0.28	0.15
ALA135	0.6	0.13
ALA144	0.34	0.17
ALA151	0.5	0.08
ALA156	0.52	0.16
MET157	0.6	0.07
MET163	0.63	0.09
MET189	0.36	0.09
ALA198	0.3	0.15

Table C-43: Methyl Order Parameters of CAP(G141S):DNA

ID	O^2_{axis}	Err
LEU11d2	0.25	0.06
LEU11d1	0.27	0.05
LEU15d2	0.36	0.08
LEU15d1	0.29	0.06
ILE20d1	0.17	0.04
LEU29d2	0.28	0.06
LEU29d1	0.25	0.05
ILE30d1	0.28	0.07
LEU39d2	0.28	0.07
LEU39d1	0.28	0.07
ILE42d1	0.33	0.07
VAL43g1	0.39	0.08
VAL43g2	0.31	0.07
VAL47g1	0.27	0.08
VAL47g2	0.3	0.06
VAL49g2	0.23	0.08
VAL49g1	0.23	0.08
LEU50d1	0.22	0.05
LEU50d2	0.21	0.05
ILE51d1	0.25	0.06
ILE60d1	0.17	0.05
LEU61d1	0.28	0.05
LEU61d2	0.26	0.05
LEU64d2	0.26	0.08
LEU64d1	0.26	0.08
ILE70d1	0.32	0.07
LEU73d2	0.26	0.07
LEU73d1	0.26	0.06
LEU75d2	0.21	0.07
LEU75d1	0.22	0.06
VAL86g1	0.39	0.08
VAL86g2	0.29	0.07
VAL94g1	0.32	0.07
VAL94g2	0.25	0.06
ILE97d1	0.3	0.07
LEU105d1	0.29	0.06
LEU105d2	0.29	0.06
ILE106d1	0.34	0.06

ID	O^2_{axis}	Err
VAL108g2	0.27	0.07
VAL108g1	0.27	0.06
ILE112d1	0.31	0.07
LEU113d2	0.39	0.08
LEU113d1	0.35	0.07
LEU116d1	0.26	0.05
LEU116d2	0.26	0.04
LEU124d2	0.28	0.06
LEU124d1	0.25	0.05
VAL126g2	0.39	0.08
VAL126g1	0.28	0.07
VAL131g2	0.39	0.07
VAL131g1	0.39	0.07
LEU134d1	0.35	0.07
LEU134d2	0.33	0.06
LEU137d2	0.38	0.08
LEU137d1	0.45	0.07
VAL139g1	0.37	0.08
VAL139g2	0.34	0.07
ILE143d1	0.27	0.06
LEU147d1	0.38	0.08
LEU147d2	0.39	0.08
LEU148d2	0.37	0.07
LEU148d1	0.34	0.06
LEU150d1	0.35	0.08
LEU150d2	0.34	0.07
ILE165d1	0.3	0.05
ILE167d1	0.3	0.04
ILE172d1	0.31	0.06
ILE175d1	0.33	0.06
VAL176g2	0.37	0.06
VAL176g1	0.34	0.06
VAL183g1	0.39	0.05
VAL183g2	0.47	0.05
ILE186d1	0.46	0.05
LEU187d1	0.39	0.08
LEU187d2	0.39	0.07
LEU190d1	0.39	0.08
LEU190d2	0.39	0.07
LEU195d1	0.39	0.07
LEU195d2	0.39	0.06
ILE196d1	0.37	0.06
ILE203d1	0.39	0.08
VAL204g2	0.35	0.07
VAL204g1	0.33	0.07
VAL205g1	0.39	0.08
VAL205g2	0.32	0.07
ALA36	0.38	0.07
ALA48	0.39	0.15
MET59	0.24	0.12
ALA84	0.39	0.15
ALA88	0.55	0.09
ALA91	0.39	0.15
ALA95	0.49	0.15
MET114	0.52	0.11
ALA118	0.45	0.09
MET120	0.47	0.11
ALA121	0.32	0.15
ALA135	0.54	0.14
ALA144	0.35	0.15
ALA151	0.38	0.09
ALA156	0.48	0.1
MET157	0.45	0.11
MET163	0.47	0.1
MET189	0.37	0.09
ALA198	0.37	0.08

Table C-44: Methyl Order Parameters of CAP(G141S):cAMP$_2$

ID	O^2_{axis}	Err
LEU11d2	0.39	0.08
LEU11d1	0.36	0.08

ID	O^2_{axis}	Err
LEU15d2	0.53	0.07
LEU15d1	0.39	0.06
ILE20d1	0.32	0.04
LEU29d2	0.39	0.04
LEU29d1	0.34	0.06
ILE30d1	0.55	0.07
LEU39d2	0.48	0.06
LEU39d1	0.47	0.06
ILE42d1	0.47	0.06
VAL43g1	0.65	0.07
VAL43g2	0.67	0.06
VAL47g1	0.66	0.07
VAL47g2	0.58	0.06
VAL49g2	0.71	0.06
VAL49g1	0.71	0.06
LEU50d1	0.32	0.05
LEU50d2	0.24	0.05
ILE51d1	0.5	0.06
ILE60d1	0.43	0.06
LEU61d1	0.27	0.06
LEU61d2	0.26	0.06
LEU64d2	0.6	0.07
LEU64d1	0.7	0.06
ILE70d1	0.55	0.09
LEU73d2	0.62	0.07
LEU73d1	0.57	0.06
LEU75d2	0.45	0.06
LEU75d1	0.38	0.06
VAL86g1	0.57	0.07
VAL86g2	0.56	0.06
VAL94g1	0.56	0.09
VAL94g2	0.57	0.06
ILE97d1	0.47	0.12
LEU105d1	0.56	0.07
LEU105d2	0.56	0.07
ILE106d1	0.37	0.09
VAL108g2	0.46	0.1
VAL108g1	0.37	0.1
ILE112d1	0.36	0.09

ID	O^2_{axis}	Err
LEU113d2	0.49	0.08
LEU113d1	0.45	0.07
LEU116d1	0.3	0.09
LEU116d2	0.24	0.07
LEU124d2	0.24	0.06
LEU124d1	0.28	0.06
VAL126g2	0.45	0.09
VAL126g1	0.41	0.09
VAL131g2	0.44	0.09
VAL131g1	0.37	0.09
LEU134d1	0.49	0.06
LEU134d2	0.42	0.09
LEU137d2	0.52	0.09
LEU137d1	0.36	0.06
VAL139g1	0.42	0.1
VAL139g2	0.41	0.09
ILE143d1	0.36	0.09
LEU147d1	0.51	0.17
LEU147d2	0.56	0.13
LEU148d2	0.34	0.08
LEU148d1	0.52	0.08
LEU150d1	0.39	0.07
LEU150d2	0.34	0.12
ILE165d1	0.37	0.11
ILE167d1	0.47	0.08
ILE172d1	0.47	0.14
ILE175d1	0.3	0.13
VAL176g2	0.24	0.1
VAL176g1	0.41	0.1
VAL183g1	0.39	0.1
VAL183g2	0.46	0.1
ILE186d1	0.44	0.14
LEU187d1	0.47	0.14
LEU187d2	0.4	0.14
LEU190d1	0.35	0.13
LEU190d2	0.37	0.15
LEU195d1	0.59	0.13
LEU195d2	0.55	0.17
ILE196d1	0.6	0.13

ID	O^2_{axis}	Err
ILE203d1	0.51	0.11
VAL204g2	0.51	0.11
VAL204g1	0.41	0.1
VAL205g1	0.5	0.1
VAL205g2	0.37	0.08
ALA36	0.8	0.18
ALA48	0.76	0.17
MET59	0.29	0.07
ALA84	0.75	0.17
ALA88	0.64	0.14
ALA91	0.73	0.18
ALA95	0.75	0.19

ID	O^2_{axis}	Err
MET114	0.45	0.03
ALA118	0.69	0.19
MET120	0.31	0.09
ALA121	0.46	0.09
ALA135	0.64	0.22
ALA144	0.67	0.23
ALA151	0.73	0.23
ALA156	0.6	0.21
MET157	0.22	0.09
MET163	0.3	0.1
MET189	0.28	0.15
ALA198	0.7	0.13

Table C-45: Methyl Order Parameters of CAP(G141S):cAMP$_2$:DNA

ID	O^2_{axis}	Err
LEU11d2	0.41	0.04
LEU11d1	0.37	0.04
LEU15d2	0.59	0.07
LEU15d1	0.48	0.08
ILE20d1	0.25	0.02
LEU29d2	0.48	0.03
LEU29d1	0.32	0.03
ILE30d1	0.54	0.08
LEU39d2	0.52	0.08
LEU39d1	0.5	0.06
ILE42d1	0.51	0.08
VAL43g1	0.7	0.06
VAL43g2	0.71	0.05
VAL47g1	0.77	0.06
VAL47g2	0.66	0.05
VAL49g2	0.71	0.09
VAL49g1	0.77	0.07
LEU50d1	0.39	0.04
LEU50d2	0.36	0.05
ILE51d1	0.48	0.06
ILE60d1	0.48	0.05
LEU61d1	0.32	0.05
LEU61d2	0.31	0.07

ID	O^2_{axis}	Err
LEU64d2	0.59	0.08
LEU64d1	0.65	0.08
ILE70d1	0.5	0.07
LEU73d2	0.53	0.08
LEU73d1	0.58	0.08
LEU75d2	0.57	0.07
LEU75d1	0.42	0.06
VAL86g1	0.54	0.08
VAL86g2	0.52	0.08
VAL94g1	0.57	0.06
VAL94g2	0.48	0.07
ILE97d1	0.5	0.05
LEU105d1	0.47	0.08
LEU105d2	0.43	0.07
ILE106d1	0.43	0.04
VAL108g2	0.49	0.03
VAL108g1	0.49	0.04
ILE112d1	0.55	0.03
LEU113d2	0.59	0.09
LEU113d1	0.57	0.08
LEU116d1	0.31	0.05
LEU116d2	0.29	0.05
LEU124d2	0.4	0.09

ID	O^2_{axis}	Err
LEU124d1	0.3	0.09
VAL126g2	0.59	0.04
VAL126g1	0.5	0.06
VAL131g2	0.51	0.06
VAL131g1	0.46	0.05
LEU134d1	0.48	0.07
LEU134d2	0.52	0.07
LEU137d2	0.54	0.07
LEU137d1	0.45	0.04
VAL139g1	0.37	0.09
VAL139g2	0.36	0.08
ILE143d1	0.31	0.1
LEU147d1	0.48	0.09
LEU147d2	0.5	0.08
LEU148d2	0.3	0.09
LEU148d1	0.41	0.07
LEU150d1	0.37	0.06
LEU150d2	0.33	0.06
ILE165d1	0.45	0.04
ILE167d1	0.59	0.08
ILE172d1	0.57	0.08
ILE175d1	0.38	0.11
VAL176g2	0.27	0.1
VAL176g1	0.43	0.07
VAL183g1	0.47	0.09
VAL183g2	0.48	0.09
ILE186d1	0.46	0.1
LEU187d1	0.48	0.11
LEU187d2	0.48	0.11
LEU190d1	0.39	0.1
LEU190d2	0.45	0.09
LEU195d1	0.55	0.09
LEU195d2	0.59	0.08
ILE196d1	0.58	0.08
ILE203d1	0.51	0.04
VAL204g2	0.42	0.06
VAL204g1	0.41	0.05
VAL205g1	0.59	0.05
VAL205g2	0.51	0.06
ALA36	0.88	0.1
ALA48	0.89	0.14
MET59	0.3	0.07
ALA84	0.89	0.17
ALA88	0.91	0.12
ALA91	0.88	0.15
ALA95	0.86	0.11
MET114	0.44	0.07
ALA118	0.88	0.1
MET120	0.48	0.1
ALA121	0.69	0.11
ALA135	0.69	0.11
ALA144	0.64	0.14
ALA151	0.71	0.15
ALA156	0.64	0.17
MET157	0.19	0.05
MET163	0.18	0.06
MET189	0.34	0.09
ALA198	0.89	0.15

Table C-46: Methyl Order Parameters of CAP(G141S):cGMP$_2$

ID	O^2_{axis}	Err
LEU11d2	0.33	0.08
LEU11d1	0.28	0.07
LEU15d2	0.46	0.11
LEU15d1	0.45	0.12
ILE20d1	0.5	0.08
LEU29d2	0.37	0.15
LEU29d1	0.47	0.11
ILE30d1	0.5	0.17
LEU39d2	0.49	0.07
LEU39d1	0.53	0.12

ID	O^2_{axis}	Err
ILE42d1	0.52	0.12
VAL43g1	0.47	0.11
VAL43g2	0.43	0.08
VAL47g1	0.53	0.11
VAL47g2	0.52	0.14
VAL49g2	0.48	0.11
VAL49g1	0.44	0.13
LEU50d1	0.26	0.1
LEU50d2	0.22	0.04
ILE51d1	0.33	0.08
ILE60d1	0.28	0.06
LEU61d1	0.3	0.06
LEU61d2	0.45	0.13
LEU64d2	0.48	0.16
LEU64d1	0.45	0.17
ILE70d1	0.52	0.12
LEU73d2	0.48	0.14
LEU73d1	0.46	0.15
LEU75d2	0.33	0.09
LEU75d1	0.36	0.1
VAL86g1	0.48	0.17
VAL86g2	0.56	0.12
VAL94g1	0.41	0.11
VAL94g2	0.29	0.13
ILE97d1	0.52	0.1
LEU105d1	0.58	0.1
LEU105d2	0.39	0.07
ILE106d1	0.43	0.11
VAL108g2	0.37	0.06
VAL108g1	0.47	0.06
ILE112d1	0.59	0.13
LEU113d2	0.52	0.08
LEU113d1	0.48	0.17
LEU116d1	0.56	0.05
LEU116d2	0.45	0.17
LEU124d2	0.44	0.15
LEU124d1	0.46	0.12
VAL126g2	0.52	0.09
VAL126g1	0.6	0.12

ID	O^2_{axis}	Err
VAL131g2	0.56	0.12
VAL131g1	0.52	0.09
LEU134d1	0.59	0.12
LEU134d2	0.48	0.14
LEU137d2	0.54	0.11
LEU137d1	0.56	0.15
VAL139g1	0.52	0.11
VAL139g2	0.54	0.08
ILE143d1	0.4	0.15
LEU147d1	0.58	0.18
LEU147d2	0.63	0.05
LEU148d2	0.5	0.07
LEU148d1	0.4	0.06
LEU150d1	0.56	0.06
LEU150d2	0.51	0.08
ILE165d1	0.35	0.14
ILE167d1	0.23	0.13
ILE172d1	0.56	0.13
ILE175d1	0.39	0.08
VAL176g2	0.57	0.13
VAL176g1	0.46	0.17
VAL183g1	0.37	0.08
VAL183g2	0.4	0.14
ILE186d1	0.48	0.08
LEU187d1	0.47	0.18
LEU187d2	0.47	0.13
LEU190d1	0.52	0.07
LEU190d2	0.51	0.17
LEU195d1	0.55	0.06
LEU195d2	0.53	0.05
ILE196d1	0.45	0.08
ILE203d1	0.53	0.1
VAL204g2	0.53	0.04
VAL204g1	0.61	0.04
VAL205g1	0.59	0.1
VAL205g2	0.45	0.06
ALA36	0.54	0.11
ALA48	0.5	0.12
MET59	0.37	0.08

ID	O^2_{axis}	Err
ALA84	0.38	0.07
ALA88	0.6	0.1
ALA91	0.49	0.11
ALA95	0.45	0.13
MET114	0.27	0.08
ALA118	0.39	0.09
MET120	0.3	0.08
ALA121	0.42	0.1

ID	O^2_{axis}	Err
ALA135	0.42	0.15
ALA144	0.56	0.13
ALA151	0.53	0.13
ALA156	0.43	0.11
MET157	0.22	0.05
MET163	0.29	0.1
MET189	0.39	0.09
ALA198	0.48	0.12

Table C-47: Methyl Order Parameters of CAP(G141S):cGMP$_2$:DNA

ID	O^2_{axis}	Err
LEU11d2	0.28	0.05
LEU11d1	0.24	0.06
LEU15d2	0.39	0.06
LEU15d1	0.41	0.14
ILE20d1	0.44	0.06
LEU29d2	0.38	0.1
LEU29d1	0.46	0.12
ILE30d1	0.45	0.13
LEU39d2	0.49	0.05
LEU39d1	0.54	0.04
ILE42d1	0.51	0.04
VAL43g1	0.48	0.11
VAL43g2	0.42	0.13
VAL47g1	0.54	0.1
VAL47g2	0.51	0.07
VAL49g2	0.49	0.06
VAL49g1	0.44	0.13
LEU50d1	0.29	0.08
LEU50d2	0.23	0.13
ILE51d1	0.37	0.05
ILE60d1	0.34	0.05
LEU61d1	0.35	0.03
LEU61d2	0.47	0.12
LEU64d2	0.49	0.1
LEU64d1	0.47	0.03
ILE70d1	0.48	0.03
LEU73d2	0.33	0.03

ID	O^2_{axis}	Err
LEU73d1	0.36	0.07
LEU75d2	0.37	0.05
LEU75d1	0.32	0.06
VAL86g1	0.48	0.13
VAL86g2	0.37	0.08
VAL94g1	0.27	0.14
VAL94g2	0.26	0.12
ILE97d1	0.51	0.08
LEU105d1	0.47	0.07
LEU105d2	0.4	0.04
ILE106d1	0.41	0.1
VAL108g2	0.36	0.03
VAL108g1	0.27	0.1
ILE112d1	0.46	0.03
LEU113d2	0.52	0.15
LEU113d1	0.47	0.04
LEU116d1	0.56	0.05
LEU116d2	0.48	0.07
LEU124d2	0.45	0.03
LEU124d1	0.48	0.15
VAL126g2	0.37	0.04
VAL126g1	0.45	0.05
VAL131g2	0.44	0.03
VAL131g1	0.49	0.14
LEU134d1	0.49	0.13
LEU134d2	0.45	0.03
LEU137d2	0.45	0.06

ID	O^2_{axis}	Err
LEU137d1	0.5	0.14
VAL139g1	0.35	0.07
VAL139g2	0.49	0.13
ILE143d1	0.3	0.1
LEU147d1	0.45	0.1
LEU147d2	0.54	0.07
LEU148d2	0.35	0.12
LEU148d1	0.31	0.08
LEU150d1	0.45	0.11
LEU150d2	0.47	0.1
ILE165d1	0.34	0.12
ILE167d1	0.21	0.06
ILE172d1	0.51	0.15
ILE175d1	0.42	0.12
VAL176g2	0.58	0.12
VAL176g1	0.49	0.1
VAL183g1	0.39	0.05
VAL183g2	0.41	0.07
ILE186d1	0.48	0.07
LEU187d1	0.5	0.08
LEU187d2	0.49	0.13
LEU190d1	0.53	0.11
LEU190d2	0.53	0.11
LEU195d1	0.52	0.14
LEU195d2	0.53	0.08
ILE196d1	0.48	0.09

ID	O^2_{axis}	Err
ILE203d1	0.52	0.09
VAL204g2	0.48	0.13
VAL204g1	0.54	0.05
VAL205g1	0.55	0.03
VAL205g2	0.43	0.1
ALA36	0.54	0.1
ALA48	0.51	0.11
MET59	0.4	0.01
ALA84	0.36	0.09
ALA88	0.55	0.11
ALA91	0.46	0.11
ALA95	0.3	0.01
MET114	0.29	0.07
ALA118	0.45	0.1
MET120	0.35	0.08
ALA121	0.36	0.09
ALA135	0.37	0.09
ALA144	0.51	0.11
ALA151	0.42	0.08
ALA156	0.39	0.05
MET157	0.21	0.06
MET163	0.31	0.08
MET189	0.4	0.1
ALA198	0.46	0.04

Table C-48: Methyl Order Parameters of CAP(A144T)

ID	O^2_{axis}	Err
LEU11d2	0.59	0.07
LEU11d1	0.63	0.05
LEU15d2	0.7	0.08
LEU15d1	0.59	0.06
ILE20d1	0.67	0.03
LEU29d2	0.51	0.09
LEU29d1	0.37	0.05
ILE30d1	0.28	0.06
LEU39d2	0.37	0.08

ID	O^2_{axis}	Err
LEU39d1	0.62	0.07
ILE42d1	0.35	0.09
VAL43g1	0.56	0.08
VAL43g2	0.33	0.06
VAL47g1	0.44	0.13
VAL47g2	0.51	0.1
VAL49g2	0.46	0.07
VAL49g1	0.74	0.06
LEU50d1	0.5	0.04

ID	O^2_{axis}	Err
LEU50d2	0.38	0.04
ILE51d1	0.62	0.05
ILE60d1	0.53	0.04
LEU61d1	0.59	0.04
LEU61d2	0.46	0.07
LEU64d2	0.48	0.07
LEU64d1	0.59	0.07
ILE70d1	0.45	0.07
LEU73d2	0.49	0.13
LEU73d1	0.55	0.06
LEU75d2	0.6	0.06
LEU75d1	0.74	0.06
VAL86g1	0.49	0.13
VAL86g2	0.77	0.07
VAL94g1	0.6	0.06
VAL94g2	0.66	0.06
ILE97d1	0.63	0.06
LEU105d1	0.66	0.07
LEU105d2	0.66	0.06
ILE106d1	0.49	0.05
VAL108g2	0.56	0.05
VAL108g1	0.57	0.06
ILE112d1	0.49	0.04
LEU113d2	0.4	0.08
LEU113d1	0.42	0.07
LEU116d1	0.42	0.05
LEU116d2	0.33	0.05
LEU124d2	0.77	0.06
LEU124d1	0.6	0.04
VAL126g2	0.52	0.07
VAL126g1	0.65	0.05
VAL131g2	0.66	0.06
VAL131g1	0.64	0.05
LEU134d1	0.36	0.07
LEU134d2	0.67	0.06
LEU137d2	0.68	0.07
LEU137d1	0.65	0.13
VAL139g1	0.45	0.08
VAL139g2	0.64	0.08

ID	O^2_{axis}	Err
ILE143d1	0.67	0.05
LEU147d1	0.74	0.08
LEU147d2	0.65	0.11
LEU148d2	0.69	0.07
LEU148d1	0.63	0.05
LEU150d1	0.49	0.07
LEU150d2	0.59	0.07
ILE165d1	0.63	0.05
ILE167d1	0.58	0.04
ILE172d1	0.5	0.05
ILE175d1	0.32	0.05
VAL176g2	0.55	0.06
VAL176g1	0.56	0.05
VAL183g1	0.37	0.06
VAL183g2	0.4	0.06
ILE186d1	0.3	0.07
LEU187d1	0.37	0.08
LEU187d2	0.42	0.07
LEU190d1	0.37	0.09
LEU190d2	0.47	0.44
LEU195d1	0.39	0.06
LEU195d2	0.4	0.06
ILE196d1	0.17	0.05
ILE203d1	0.57	0.06
VAL204g2	0.48	0.06
VAL204g1	0.57	0.06
VAL205g1	0.65	0.11
VAL205g2	0.67	0.09
ALA36	0.38	0.1
ALA48		
MET59	0.2	0.1
ALA84	0.51	0.05
ALA88	0.5	0.08
ALA91	0.56	0.07
ALA95		
MET114	0.13	0.1
ALA118	0.64	0.09
MET120	0.14	0.06
ALA121	0.64	0.35

ID	O^2_{axis}	Err
ALA135	0.66	0.11
A144T		
ALA151	0.28	0.07
ALA156	0.35	0.08
MET157	0.13	0.03
MET163	0.22	0.05

ID	O^2_{axis}	Err
MET189	0.27	0.04
ALA198	0.56	0.06
MET163	0.19	0.1
MET189	0.32	0.16
ALA198	0.65	0.11

Table C-49: Methyl Order Parameters of CAP(A144T):DNA

ID	O^2_{axis}	Err
LEU11d2	0.6	0.03
LEU11d1	0.64	0.03
LEU15d2	0.69	0.05
LEU15d1	0.54	0.02
ILE20d1	0.71	0.03
LEU29d2	0.5	0.04
LEU29d1	0.39	0.03
ILE30d1	0.35	0.03
LEU39d2	0.4	0.02
LEU39d1	0.71	0.02
ILE42d1	0.38	0.04
VAL43g1	0.48	0.06
VAL43g2	0.38	0.03
VAL47g1	0.5	0.02
VAL47g2	0.56	0.04
VAL49g2	0.47	0.03
VAL49g1	0.76	0.02
LEU50d1	0.39	0.05
LEU50d2	0.35	0.03
ILE51d1	0.66	0.04
ILE60d1	0.58	0.02
LEU61d1	0.47	0.03
LEU61d2	0.38	0.03
LEU64d2	0.52	0.02
LEU64d1	0.51	0.03
ILE70d1	0.45	0.04
LEU73d2	0.41	0.04
LEU73d1	0.58	0.02
LEU75d2	0.56	0.03

ID	O^2_{axis}	Err
LEU75d1	0.68	0.03
VAL86g1	0.45	0.08
VAL86g2	0.72	0.04
VAL94g1	0.64	0.03
VAL94g2	0.62	0.03
ILE97d1	0.66	0.02
LEU105d1	0.66	0.02
LEU105d2	0.61	0.02
ILE106d1	0.59	0.03
VAL108g2	0.57	0.02
VAL108g1	0.57	0.03
ILE112d1	0.5	0.06
LEU113d2	0.4	0.06
LEU113d1	0.4	0.05
LEU116d1	0.41	0.04
LEU116d2	0.42	0.03
LEU124d2	0.76	0.03
LEU124d1	0.6	0.02
VAL126g2	0.45	0.03
VAL126g1	0.72	0.03
VAL131g2	0.6	0.06
VAL131g1	0.54	0.06
LEU134d1	0.38	0.03
LEU134d2	0.67	0.03
LEU137d2	0.73	0.04
LEU137d1	0.63	0.03
VAL139g1	0.5	0.07
VAL139g2	0.53	0.07
ILE143d1	0.57	0.03

ID	O^2_{axis}	Err
LEU147d1	0.6	0.06
LEU147d2	0.61	0.11
LEU148d2	0.59	0.05
LEU148d1	0.65	0.04
LEU150d1	0.56	0.05
LEU150d2	0.66	0.04
ILE165d1	0.66	0.04
ILE167d1	0.6	0.04
ILE172d1	0.6	0.04
ILE175d1	0.4	0.06
VAL176g2	0.51	0.04
VAL176g1	0.54	0.04
VAL183g1	0.47	0.05
VAL183g2	0.5	0.04
ILE186d1	0.44	0.04
LEU187d1	0.47	0.07
LEU187d2	0.47	0.04
LEU190d1	0.41	0.05
LEU190d2	0.5	0.08
LEU195d1	0.41	0.09
LEU195d2	0.5	0.04
ILE196d1	0.29	0.04
ILE203d1	0.6	0.04
VAL204g2	0.59	0.03
VAL204g1	0.59	0.03

ID	O^2_{axis}	Err
VAL205g1	0.69	0.1
VAL205g2	0.67	0.03
ALA36	0.38	0.28
ALA48		
MET59	0.11	0.06
ALA84	0.4	0.16
ALA88	0.6	0.31
ALA91	0.6	0.19
ALA95		
MET114	0.14	0.08
ALA118	0.55	0.26
MET120	0.12	0.04
ALA121	0.49	0.18
ALA135	0.59	0.24
A144T		
ALA151	0.32	0.17
ALA156	0.41	0.08
MET157	0.16	0.13
MET163	0.22	0.12
MET189	0.3	0.12
ALA198	0.64	0.14
MET163	0.19	0.1
MET189	0.32	0.16
ALA198	0.65	0.11

Table C-50: Methyl Order Parameters of CAP(A144T):cAMP$_2$

ID	O^2_{axis}	Err
LEU11d2	0.54	0.05
LEU11d1	0.54	0.04
LEU15d2	0.74	0.06
LEU15d1	0.73	0.04
ILE20d1	0.52	0.02
LEU29d2	0.73	0.06
LEU29d1	0.67	0.04
ILE30d1	0.78	0.04
LEU39d2	0.5	0.06
LEU39d1	0.5	0.05

ID	O^2_{axis}	Err
ILE42d1	0.53	0.07
VAL43g1	0.51	0.06
VAL43g2	0.53	0.04
VAL47g1	0.74	0.09
VAL47g2	0.73	0.08
VAL49g2	0.65	0.05
VAL49g1	0.56	0.05
LEU50d1	0.72	0.03
LEU50d2	0.69	0.03
ILE51d1	0.4	0.04

ID	O^2_{axis}	Err
ILE60d1	0.38	0.03
LEU61d1	0.66	0.03
LEU61d2	0.77	0.05
LEU64d2	0.74	0.05
LEU64d1	0.56	0.05
ILE70d1	0.47	0.05
LEU73d2	0.71	0.1
LEU73d1	0.77	0.04
LEU75d2	0.43	0.05
LEU75d1	0.4	0.04
VAL86g1	0.78	0.09
VAL86g2	0.71	0.05
VAL94g1	0.45	0.05
VAL94g2	0.41	0.04
ILE97d1	0.57	0.05
LEU105d1	0.79	0.05
LEU105d2	0.72	0.04
ILE106d1	0.5	0.04
VAL108g2	0.39	0.04
VAL108g1	0.49	0.05
ILE112d1	0.4	0.03
LEU113d2	0.52	0.06
LEU113d1	0.57	0.06
LEU116d1	0.52	0.04
LEU116d2	0.6	0.04
LEU124d2	0.62	0.04
LEU124d1	0.6	0.03
VAL126g2	0.47	0.05
VAL126g1	0.46	0.04
VAL131g2	0.51	0.04
VAL131g1	0.49	0.04
LEU134d1	0.63	0.05
LEU134d2	0.47	0.04
LEU137d2	0.63	0.05
LEU137d1	0.48	0.09
VAL139g1	0.56	0.06
VAL139g2	0.62	0.06
ILE143d1	0.64	0.04
LEU147d1	0.69	0.06

ID	O^2_{axis}	Err
LEU147d2	0.66	0.08
LEU148d2	0.76	0.05
LEU148d1	0.67	0.04
LEU150d1	0.57	0.05
LEU150d2	0.52	0.05
ILE165d1	0.52	0.03
ILE167d1	0.29	0.03
ILE172d1	0.43	0.03
ILE175d1	0.39	0.04
VAL176g2	0.34	0.04
VAL176g1	0.35	0.04
VAL183g1	0.58	0.04
VAL183g2	0.59	0.04
ILE186d1	0.53	0.05
LEU187d1	0.58	0.06
LEU187d2	0.56	0.05
LEU190d1	0.38	0.07
LEU190d2	0.52	0.33
LEU195d1	0.58	0.05
LEU195d2	0.56	0.04
ILE196d1	0.56	0.04
ILE203d1	0.5	0.04
VAL204g2	0.48	0.04
VAL204g1	0.51	0.04
VAL205g1	0.49	0.08
VAL205g2	0.45	0.06
ALA36	0.73	0.11
ALA48		
MET59	0.5	0.07
ALA84	0.79	0.1
ALA88	0.74	0.11
ALA91	0.84	0.12
ALA95		
MET114	0.35	0.07
ALA118	0.97	0.11
MET120	0.5	0.05
ALA121	0.87	0.26
ALA135	0.88	0.18
A144T		

ID	O^2_{axis}	Err
ALA151	0.88	0.15
ALA156	0.68	0.16
MET157	0.28	0.12

ID	O^2_{axis}	Err
MET163	0.41	0.13
MET189	0.38	0.03
ALA198	0.78	0.09

Table C-51: Methyl Order Parameters of CAP(A144T):cAMP$_2$:DNA

ID	O^2_{axis}	Err
LEU11d2	0.57	0.03
LEU11d1	0.61	0.03
LEU15d2	0.8	0.04
LEU15d1	0.79	0.02
ILE20d1	0.45	0.02
LEU29d2	0.58	0.03
LEU29d1	0.56	0.02
ILE30d1	0.75	0.03
LEU39d2	0.62	0.02
LEU39d1	0.6	0.02
ILE42d1	0.57	0.03
VAL43g1	0.65	0.05
VAL43g2	0.66	0.03
VAL47g1	0.66	0.02
VAL47g2	0.62	0.04
VAL49g2	0.75	0.02
VAL49g1	0.71	0.02
LEU50d1	0.67	0.04
LEU50d2	0.66	0.03
ILE51d1	0.5	0.03
ILE60d1	0.46	0.01
LEU61d1	0.71	0.03
LEU61d2	0.71	0.03
LEU64d2	0.76	0.02
LEU64d1	0.7	0.02
ILE70d1	0.65	0.04
LEU73d2	0.55	0.03
LEU73d1	0.61	0.02
LEU75d2	0.47	0.03
LEU75d1	0.41	0.03

ID	O^2_{axis}	Err
VAL86g1	0.62	0.06
VAL86g2	0.56	0.03
VAL94g1	0.61	0.03
VAL94g2	0.59	0.02
ILE97d1	0.59	0.02
LEU105d1	0.64	0.02
LEU105d2	0.59	0.02
ILE106d1	0.26	0.03
VAL108g2	0.47	0.02
VAL108g1	0.56	0.02
ILE112d1	0.38	0.05
LEU113d2	0.49	0.05
LEU113d1	0.54	0.04
LEU116d1	0.57	0.03
LEU116d2	0.61	0.03
LEU124d2	0.59	0.02
LEU124d1	0.59	0.02
VAL126g2	0.47	0.03
VAL126g1	0.44	0.02
VAL131g2	0.46	0.05
VAL131g1	0.37	0.05
LEU134d1	0.49	0.03
LEU134d2	0.45	0.03
LEU137d2	0.52	0.03
LEU137d1	0.37	0.03
VAL139g1	0.45	0.06
VAL139g2	0.44	0.06
ILE143d1	0.51	0.03
LEU147d1	0.53	0.05
LEU147d2	0.57	0.09

ID	O^2_{axis}	Err
LEU148d2	0.67	0.04
LEU148d1	0.67	0.03
LEU150d1	0.43	0.04
LEU150d2	0.36	0.03
ILE165d1	0.36	0.03
ILE167d1	0.35	0.03
ILE172d1	0.48	0.03
ILE175d1	0.3	0.05
VAL176g2	0.47	0.04
VAL176g1	0.46	0.03
VAL183g1	0.61	0.04
VAL183g2	0.57	0.04
ILE186d1	0.52	0.03
LEU187d1	0.51	0.06
LEU187d2	0.6	0.03
LEU190d1	0.43	0.04
LEU190d2	0.37	0.06
LEU195d1	0.63	0.07
LEU195d2	0.54	0.03
ILE196d1	0.63	0.03
ILE203d1	0.5	0.03
VAL204g2	0.51	0.03
VAL204g1	0.45	0.02

ID	O^2_{axis}	Err
VAL205g1	0.49	0.08
VAL205g2	0.38	0.03
ALA36	0.63	0.16
ALA48		
MET59	0.54	0.15
ALA84	0.89	0.17
ALA88	0.67	0.23
ALA91	0.74	0.11
ALA95		
MET114	0.25	0.11
ALA118	0.87	0.21
MET120	0.57	0.26
ALA121	0.96	0.7
ALA135	0.97	0.14
A144T		
ALA151	0.93	0.25
ALA156	0.63	0.1
MET157	0.24	0.07
MET163	0.41	0.12
MET189	0.39	0.19
ALA198	0.79	0.11

Table C-52: Methyl Order Parameters of CAP(A144T):cGMP$_2$

ID	O^2_{axis}	Err
LEU11d2	0.52	0.05
LEU11d1	0.45	0.04
LEU15d2	0.64	0.06
LEU15d1	0.73	0.04
ILE20d1	0.4	0.02
LEU29d2	0.6	0.06
LEU29d1	0.72	0.04
ILE30d1	0.81	0.04
LEU39d2	0.78	0.06
LEU39d1	0.67	0.05
ILE42d1	0.59	0.07
VAL43g1	0.87	0.06

ID	O^2_{axis}	Err
VAL43g2	0.84	0.04
VAL47g1	0.78	0.09
VAL47g2	0.71	0.08
VAL49g2	0.65	0.05
VAL49g1	0.65	0.05
LEU50d1	0.58	0.03
LEU50d2	0.63	0.03
ILE51d1	0.93	0.04
ILE60d1	0.96	0.03
LEU61d1	0.63	0.03
LEU61d2	0.58	0.05
LEU64d2	0.58	0.05

ID	O^2_{axis}	Err
LEU64d1	0.57	0.05
ILE70d1	0.64	0.05
LEU73d2	0.63	0.1
LEU73d1	0.56	0.04
LEU75d2	0.55	0.05
LEU75d1	0.57	0.04
VAL86g1	0.54	0.09
VAL86g2	0.52	0.05
VAL94g1	0.62	0.05
VAL94g2	0.59	0.04
ILE97d1	0.51	0.05
LEU105d1	0.5	0.05
LEU105d2	0.49	0.04
ILE106d1	0.49	0.04
VAL108g2	0.49	0.04
VAL108g1	0.48	0.05
ILE112d1	0.62	0.03
LEU113d2	0.36	0.06
LEU113d1	0.41	0.06
LEU116d1	0.4	0.04
LEU116d2	0.33	0.04
LEU124d2	0.53	0.04
LEU124d1	0.52	0.03
VAL126g2	0.56	0.05
VAL126g1	0.56	0.04
VAL131g2	0.47	0.04
VAL131g1	0.5	0.04
LEU134d1	0.55	0.05
LEU134d2	0.47	0.04
LEU137d2	0.45	0.05
LEU137d1	0.38	0.09
VAL139g1	0.43	0.06
VAL139g2	0.42	0.06
ILE143d1	0.55	0.04
LEU147d1	0.64	0.06
LEU147d2	0.61	0.08
LEU148d2	0.56	0.05
LEU148d1	0.6	0.04
LEU150d1	0.56	0.05

ID	O^2_{axis}	Err
LEU150d2	0.61	0.05
ILE165d1	0.56	0.03
ILE167d1	0.55	0.03
ILE172d1	0.52	0.03
ILE175d1	0.6	0.04
VAL176g2	0.55	0.04
VAL176g1	0.48	0.04
VAL183g1	0.5	0.04
VAL183g2	0.55	0.04
ILE186d1	0.48	0.05
LEU187d1	0.53	0.06
LEU187d2	0.56	0.05
LEU190d1	0.55	0.07
LEU190d2	0.43	0.33
LEU195d1	0.52	0.05
LEU195d2	0.51	0.04
ILE196d1	0.71	0.04
ILE203d1	0.76	0.04
VAL204g2	0.62	0.04
VAL204g1	0.6	0.04
VAL205g1	0.56	0.08
VAL205g2	0.54	0.06
ALA36	0.82	0.07
ALA48		
MET59	0.24	0.07
ALA84	0.82	0.04
ALA88	0.78	0.06
ALA91	0.75	0.05
ALA95		
MET114	0.13	0.07
ALA118	0.82	0.07
MET120	0.45	0.05
ALA121	0.69	0.26
ALA135	0.82	0.08
A144T		
ALA151	0.81	0.05
ALA156	0.53	0.06
MET157	0.24	0.02
MET163	0.41	0.04

ID	O^2_{axis}	Err
MET189	0.17	0.03

ID	O^2_{axis}	Err
ALA198	0.61	0.04

Table C-53: Methyl Order Parameters of CAP(A144T):cGMP$_2$:DNA

ID	O^2_{axis}	Err
LEU11d2	0.54	0.03
LEU11d1	0.54	0.03
LEU15d2	0.55	0.04
LEU15d1	0.56	0.02
ILE20d1	0.6	0.02
LEU29d2	0.7	0.03
LEU29d1	0.54	0.02
ILE30d1	0.34	0.03
LEU39d2	0.38	0.02
LEU39d1	0.4	0.02
ILE42d1	0.4	0.03
VAL43g1	0.42	0.05
VAL43g2	0.44	0.03
VAL47g1	0.45	0.02
VAL47g2	0.43	0.04
VAL49g2	0.68	0.02
VAL49g1	0.68	0.02
LEU50d1	0.63	0.04
LEU50d2	0.7	0.03
ILE51d1	0.74	0.03
ILE60d1	0.69	0.01
LEU61d1	0.25	0.03
LEU61d2	0.43	0.03
LEU64d2	0.42	0.02
LEU64d1	0.29	0.02
ILE70d1	0.38	0.04
LEU73d2	0.44	0.03
LEU73d1	0.43	0.02
LEU75d2	0.39	0.03
LEU75d1	0.35	0.03
VAL86g1	0.44	0.06
VAL86g2	0.39	0.03
VAL94g1	0.57	0.03
VAL94g2	0.55	0.02

ID	O^2_{axis}	Err
ILE97d1	0.47	0.02
LEU105d1	0.32	0.02
LEU105d2	0.34	0.02
ILE106d1	0.44	0.03
VAL108g2	0.5	0.02
VAL108g1	0.44	0.02
ILE112d1	0.54	0.05
LEU113d2	0.42	0.05
LEU113d1	0.5	0.04
LEU116d1	0.46	0.03
LEU116d2	0.42	0.03
LEU124d2	0.54	0.02
LEU124d1	0.54	0.02
VAL126g2	0.26	0.03
VAL126g1	0.48	0.02
VAL131g2	0.55	0.05
VAL131g1	0.55	0.05
LEU134d1	0.48	0.03
LEU134d2	0.46	0.03
LEU137d2	0.46	0.03
LEU137d1	0.46	0.03
VAL139g1	0.47	0.06
VAL139g2	0.49	0.06
ILE143d1	0.54	0.03
LEU147d1	0.61	0.05
LEU147d2	0.57	0.09
LEU148d2	0.59	0.04
LEU148d1	0.51	0.03
LEU150d1	0.55	0.04
LEU150d2	0.54	0.03
ILE165d1	0.64	0.03
ILE167d1	0.61	0.03
ILE172d1	0.56	0.03
ILE175d1	0.54	0.05

ID	O^2_{axis}	Err
VAL176g2	0.6	0.04
VAL176g1	0.5	0.03
VAL183g1	0.5	0.04
VAL183g2	0.64	0.04
ILE186d1	0.51	0.03
LEU187d1	0.57	0.06
LEU187d2	0.6	0.03
LEU190d1	0.56	0.04
LEU190d2	0.44	0.06
LEU195d1	0.51	0.07
LEU195d2	0.49	0.03
ILE196d1	0.68	0.03
ILE203d1	0.7	0.03
VAL204g2	0.57	0.03
VAL204g1	0.56	0.02
VAL205g1	0.55	0.08
VAL205g2	0.53	0.03
ALA36	0.63	0.12

ID	O^2_{axis}	Err
ALA48		
MET59	0.25	0.02
ALA84	0.85	0.12
ALA88	0.59	0.13
ALA91	0.56	0.11
ALA95		
MET114	0.14	0.01
ALA118	0.83	0.17
MET120	0.46	0.18
ALA121	0.4	0.12
ALA135	0.83	0.1
A144T		
ALA151	0.82	0.22
ALA156	0.34	0.04
MET157	0.14	0.01
MET163	0.42	0.1
MET189	0.18	0.03
ALA198	0.62	0.1

Table C-54: Methyl Order Parameters of Apo Galectin

ID	O^2_{axis}	Err
l114d1	0.51	0.02
l114d2	0.48	0.01
i115d1	0.22	0
i115g2	0.44	0.01
v116g1	0.46	0.01
l120d1	0.63	0.03
v126g1	0.78	0.03
v126g2	0.77	0.05
v127g1	0.25	0.01
m130e	0.48	0.01
l131d1	0.51	0.01
i132d1	0.38	0.01
i132g2	0.67	0.02
i134d1	0.82	0.02
l135d2	0.38	0.01
t137g2	0.55	0.01
v138g1	1	0.1

ID	O^2_{axis}	Err
v138g2	0.9	0.03
a142b	0.92	0.05
i145d1	0.77	0.02
i145g2	0.78	0.02
a146b	0.83	0.01
l147d1	0.52	0.08
l147d2	0.28	0.01
v170g1	0.41	0.02
v170g2	0.49	0.01
i171g2	0.85	0.02
v172g1	0.82	0.05
v172g2	0.87	0.03
t175g2	0.96	0.04
v189g2	0.79	0.05
i200d1	0.78	0.02
i200g2	0.8	0.02
v202g1	0.52	0.01

ID	O^2_{axis}	Err
v202g2	0.69	0.06
l203d2	0.62	0.02
v204g1	0.88	0.03
v204g2	0.91	0.03
v211g1	0.85	0.02
a212b	0.97	0.03
v213g1	0.94	0.05
a216b	0.91	0.02
l218d1	0.74	0.06
v225g1	0.76	0.02
v225g2	0.76	0.02
l228d1	0.61	0.03
l228d2	0.62	0.03
i231d1	0.71	0.02
i231g2	0.89	0.03
l234d1	0.71	0.04
l234d2	0.68	0.06
i236g2	0.82	0.02
i240d1	0.57	0.01
l242d1	0.42	0.04
t243g2	0.68	0.04
a245b	0.68	0.03
t248g2	0.62	0.02
m249e	0.45	0.01
i250d1	0.38	0.01
i250g2	0.55	0.01

Table C-55: Methyl Order Parameters of Galectin bound to L2

ID	O^2_{axis}	Err
m113e	0.01	0
l114d1	0.47	0.01
l114d2	0.42	0.01
i115d1	0.21	0
i115g2	0.4	0.01
v116g1	0.44	0.01
l120d1	0.57	0.02
v126g1	0.69	0.02
v126g2	0.67	0.03
v127g2	0.26	0.01
m130e	0.5	0.02
l131d1	0.49	0.01
i132d1	0.39	0.01
i132g2	0.65	0.02
i134d1	0.83	0.07
l135d2	0.32	0
t137g2	0.49	0.01
v138g2	0.82	0.02
a142b	0.83	0.03
i145d1	0.73	0.02
i145g2	0.7	0.02
a146b	0.81	0.02
l147d1	0.29	0.01
l147d2	0.55	0.08
v155g2	0.82	0.04
a156b	0.82	0.05
v170g1	0.41	0.02
i171g2	0.77	0.02
v172g1	0.82	0.03
v172g2	0.72	0.03
v189g2	0.73	0.04
i200d1	0.67	0.01
i200g2	0.77	0.01
v202g2	0.55	0.01
l203d2	0.56	0.02
v204g1	0.82	0.02
v204g2	0.82	0.02
v211g1	0.78	0.02
a212b	0.88	0.02
v213g1	0.84	0.03
a216b	0.88	0.02
l218d1	0.7	0.04
l219d2	0.75	0.06
v225g2	0.71	0.01

ID	O^2_{axis}	Err
l228d1	0.53	0.02
l228d2	0.62	0.02
i231d1	0.63	0.01
i231g2	0.8	0.02
l234d1	0.68	0.03
i236d1	0.53	0.01
i236g2	0.8	0.02
i240d1	0.55	0.01
i240g2	0.63	0.01

ID	O^2_{axis}	Err
l242d1	0.69	0.07
l242d2	0.61	0.03
t243g2	0.46	0.01
a245b	0.73	0.03
t248g2	0.55	0.01
m249e	0.43	0
i250d1	0.48	0.02
i250g2	0.5	0.01

Table C-56: Methyl Order Parameters of Galectin bound to L3

ID	O^2_{axis}	Err
m113e	0.01	0
l114d1	0.51	0.01
l114d2	0.47	0.01
i115d1	0.21	0
i115g2	0.44	0.01
v116g1	0.53	0.02
l120d1	0.56	0.02
v126g1	0.63	0.02
v126g2	0.75	0.03
v127g2	0.25	0.01
m130e	0.47	0
l131d1	0.54	0.01
i132d1	0.43	0.03
i132g2	0.73	0.02
i134d1	0.78	0.02
l135d2	0.35	0.01
t137g2	0.55	0.01
v138g2	0.87	0.03
a142b	0.84	0.04
i145d1	0.75	0.02
i145g2	0.74	0.02
a146b	0.91	0.02
l147d1	0.26	0.01
l147d2	0.27	0.01
v155g2	0.79	0.04
a156b	0.98	0.06

ID	O^2_{axis}	Err
v170g1	0.57	0.08
v170g2	0.54	0.01
i171g2	0.82	0.02
v172g2	0.65	0.04
v189g2	0.64	0.01
i200d1	0.73	0.01
i200g2	0.77	0.02
v202g1	0.75	0.05
v202g2	0.58	0.01
l203d2	0.57	0.02
v204g1	0.89	0.02
v204g2	0.83	0.02
v211g1	0.83	0.02
a212b	0.9	0.02
v213g1	0.84	0.03
a216b	0.88	0.02
l218d1	0.83	0.06
l219d2	0.81	0.08
l228d1	0.65	0.02
l228d2	0.62	0.03
i231d1	0.65	0.01
i231g2	0.84	0.02
l234d1	0.72	0.03
l234d2	0.69	0.05
i236d1	0.64	0.05
i236g2	0.83	0.02

ID	O^2_{axis}	Err
i240d1	0.54	0.01
l242d1	0.88	0.08
a245b	0.98	0.03
t248g2	0.59	0.01

ID	O^2_{axis}	Err
m249e	0.45	0
i250d1	0.38	0
i250g2	0.56	0.01

Table C-57: Methyl Order Parameters of Galectin bound to Lactose

ID	O^2_{axis}	Err
l114d1	0.51	0.02
l114d2	0.48	0.01
i115d1	0.22	0
i115g2	0.44	0.01
v116g1	0.46	0.01
l120d1	0.63	0.03
v126g1	0.78	0.03
v126g2	0.77	0.05
v127g1	0.25	0.01
m130e	0.48	0.01
l131d1	0.51	0.01
i132d1	0.38	0.01
i132g2	0.67	0.02
i134d1	0.82	0.02
l135d2	0.38	0.01
t137g2	0.55	0.01
v138g1	1	0.1
v138g2	0.9	0.03
a142b	0.92	0.05
i145d1	0.77	0.02
i145g2	0.78	0.02
a146b	0.83	0.01
l147d1	0.52	0.08
l147d2	0.28	0.01
v170g1	0.41	0.02
v170g2	0.49	0.01
i171g2	0.85	0.02
v172g1	0.82	0.05
v172g2	0.87	0.03
t175g2	0.96	0.04
v189g2	0.79	0.05

ID	O^2_{axis}	Err
i200d1	0.78	0.02
i200g2	0.8	0.02
v202g1	0.52	0.01
v202g2	0.69	0.06
l203d2	0.62	0.02
v204g1	0.88	0.03
v204g2	0.91	0.03
v211g1	0.85	0.02
a212b	0.97	0.03
v213g1	0.94	0.05
a216b	0.91	0.02
l218d1	0.74	0.06
v225g1	0.76	0.02
v225g2	0.76	0.02
l228d1	0.61	0.03
l228d2	0.62	0.03
i231d1	0.71	0.02
i231g2	0.89	0.03
l234d1	0.71	0.04
l234d2	0.68	0.06
i236g2	0.82	0.02
i240d1	0.57	0.01
l242d1	0.42	0.04
t243g2	0.68	0.04
a245b	0.68	0.03
t248g2	0.62	0.02
m249e	0.45	0.01
i250d1	0.38	0.01
i250g2	0.55	0.01

Table C-58: Methyl Order Parameters of Apo HEWL

ID	O^2_{axis}	Err
VAL2CG2	0.598	0.021
LEU8CD1	0.767	0.019
LEU8CD2	0.803	0.031
ALA9CB	1	0.029
ALA10CB	0.901	0.018
ALA11CB	0.861	0.009
MET12CE	0.812	0.013
LEU17CD1	0.63	0.016
LEU17CD2	0.632	0.017
LEU25CD1	1	0.028
LEU25CD2	0.609	0.022
VAL29CG1	0.871	0.013
VAL29CG2	0.791	0.032
ALA31CB	0.984	0.018
THR43CG2	0.361	0.003
THR47CG2	0.327	0.021
THR51CG2	0.778	0.005
ILE55CG2	0.739	0.028
ILE55CD1	0.323	0.025
LEU56CD1	0.734	0.01
LEU56CD2	0.681	0.017
ILE58CG2	1	0.024
ILE58CD1	0.16	0.016
THR69CG2	0.984	0.034
LEU75CD2	0.588	0.03
ILE78CG2	0.81	0.014
ILE78CD1	0.416	0.014
ALA82CB	0.88	0.034
LEU83CD1	0.783	0.012
LEU83CD2	0.884	0.029
LEU84CD1	0.879	0.012
LEU84CD2	1	0.022
ILE88CG2	0.697	0.026
ILE88CD1	0.722	0.01
THR89CG2	1	0.037
ALA90CB	0.919	0.013
VAL92CG1	0.764	0.004
VAL92CG2	0.707	0.024
ALA95CB	0.68	0.026
ILE98CG2	0.74	0.016
ILE98CD1	0.815	0.012
VAL99CG1	0.487	0.028
VAL99CG2	0.517	0.028
MET105CE	0.63	0.011
ALA107CB	0.832	0.024
VAL109CG1	0.354	0.01
VAL120CG1	0.66	0.015
ALA122CB	0.879	0.011
ILE124CG2	0.753	0.016
ILE124CD1	0.351	0.003
LEU129CD1	0.525	0.031
LEU129CD2	0.507	0.028

Table C-59: Methyl Order Parameters of HEWL:Chitotriose

ID	O^2_{axis}	Err
VAL2CG2	0.57	0.011
LEU8CD1	0.773	0.021
LEU8CD2	0.658	0.021
ALA9CB	0.962	0.022
ALA10CB	0.931	0.01
ALA11CB	1	0.03
MET12CE	0.932	0.009
LEU17CD1	0.555	0.015
LEU17CD2	0.58	0.025
LEU25CD1	0.87	0.018

ID	O^2_{axis}	Err
LEU25CD2	0.657	0.032
VAL29CG1	0.84	0.019
VAL29CG2	1	0.049
ALA31CB	0.941	0.038
THR43CG2	0.394	0.016
THR47CG2	0.3	0.007
THR51CG2	0.927	0.034
ILE55CG2	1	0.049
ILE55CD1	0.393	0.007
LEU56CD1	0.816	0.022
LEU56CD2	0.815	0.02
ILE58CG2	1	0.028
ILE58CD1	0.262	0.045
THR69CG2	0.702	0.031
LEU75CD2	0.744	0.016
ILE78CG2	0.831	0.028
ILE78CD1	0.599	0.02
ALA82CB	0.868	0.016
LEU83CD1	1	0.035
LEU83CD2	1	0.047
LEU84CD1	0.778	0.021

ID	O^2_{axis}	Err
LEU84CD2	1	0.038
ILE88CG2	0.793	0.021
ILE88CD1	0.655	0.024
THR89CG2	1	0.039
ALA90CB	1	0.027
VAL92CG1	1	0.032
VAL92CG2	0.705	0.025
ALA95CB	0.904	0.023
ILE98CG2	0.61	0.022
ILE98CD1	0.394	0.038
VAL99CG1	0.21	0.038
VAL99CG2	0.248	0.028
MET105CE	1	0.041
ALA107CB	1	0.031
VAL109CG1	0.201	0.037
VAL120CG1	0.736	0.023
ALA122CB	0.831	0.023
ILE124CG2	0.731	0.022
ILE124CD1	0.452	0.019
LEU129CD1	0.615	0.03
LEU129CD2	0.329	0.034

Table C-60: Methyl Order Parameters of the SAP90 PDZ3

ID	O^2_{axis}	Err
i307d1	0.337	0.006
i307g2	0.605	0.019
i314d1	0.303	0.005
i314g2	0.768	0.016
v315g1	0.812	0.018
v315g2	0.771	0.014
i316d1	0.37	0.007
i316g2	0.46	0.01
t321g2	0.576	0.006
l323d1	0.67	0.05
l323d2	0.697	0.027
i327d1	0.725	0.012
i327g2	0.881	0.017
v328g1	0.785	0.03

ID	O^2_{axis}	Err
v328g2	0.728	0.03
i336d1	0.686	0.015
i336g2	0.807	0.023
i338d1	0.501	0.009
i338g2	0.905	0.019
i341d1	0.251	0.005
i341g2	0.857	0.017
l342d1	0.263	0.005
l342d2	0.419	0.021
a343b	0.87	0.011
a347b	0.931	0.022
l349d2	0.368	0.005
l353d1	0.634	0.034
l353d2	0.624	0.016

ID	O^2_{axis}	Err
i359d1	0.505	0.01
i359g2	0.843	0.015
l360d2	0.616	0.012
v362g1	0.575	0.011
v362g2	0.592	0.013
v365g1	0.858	0.018
l367d1	0.55	0.032
l367d2	0.615	0.035
a370b	0.932	0.02
a375b	0.898	0.039
i377d1	0.423	0.005
i377g2	0.622	0.006
l379d1	0.737	0.029
l379d2	0.74	0.023
a382b	0.979	0.021
t385g2	0.783	0.017
i388d1	0.505	0.009
i388g2	0.786	0.015
i389d1	0.255	0.005
i389g2	0.911	0.016
a390b	0.919	0.019
a402b	0.118	0.002

Table C-61: Methyl Order Parameters of the SAP90 PDZ3 bound to the CRIPT peptide

ID	O^2_{axis}	Err
i307d1	0.334	0.007
i307g2	0.581	0.021
i314d1	0.305	0.03
i314g2	0.762	0.016
v315g1	0.739	0.014
v315g2	0.723	0.012
i316d1	0.372	0.006
i316g2	0.415	0.008
t321g2	0.55	0.009
l323d1	0.796	0.079
l323d2	0.724	0.027
i327d1	0.738	0.014
i327g2	0.887	0.023
v328g1	0.57	0.141
v328g2	0.823	0.059
i336d1	0.676	0.014
i336g2	0.827	0.021
i338d1	0.571	0.01
i338g2	0.858	0.021
i341d1	0.221	0.009
i341g2	0.84	0.02
l342d1	0.42	0.01
l342d2	0.505	0.018
a347b	0.937	0.026
l349d2	0.362	0.006
l353d1	0.624	0.05
l353d2	0.632	0.018
i359d1	0.49	0.011
i359g2	0.83	0.02
l360d2	0.603	0.014
v362g1	0.57	0.01
v362g2	0.61	0.012
v365g1	0.857	0.015
l367d1	0.486	0.037
l367d2	0.64	0.029
a370b	0.869	0.016
a375b	0.927	0.035
i377d1	0.412	0.005
i377g2	0.613	0.009
l379d1	0.866	0.03
l379d2	0.844	0.025
a382b	0.923	0.019
t385g2	0.747	0.014
i388d1	0.498	0.008
i388g2	0.777	0.014
i389d1	0.234	0.005

ID	O^2_{axis}	Err
i389g2	0.887	0.016
a390b	0.891	0.016
a402b	0.168	0.002
a402b	0.118	0.002

Table C-62: Methyl Order Parameters of the SAP90 PDZ3Δ7

ID	O^2_{axis}	Err
i307d1	0.25	0.009
i307g2	0.48	0.034
i314d1	0.256	0.013
i314g2	0.668	0.041
v315g1	0.696	0.04
v315g2	0.622	0.028
i316d1	0.316	0.016
i316g2	0.442	0.027
i327d1	0.563	0.026
i327g2	0.767	0.043
v328g2	0.529	0.035
i336d1	0.567	0.03
i336g2	0.632	0.041
i338d1	0.406	0.024
i341g2	0.67	0.041
l342d1	0.306	0.068
l342d2	0.261	0.014
a347b	0.833	0.054
l349d1	0.301	0.036
l349d2	0.317	0.015
l353d1	0.484	0.049
l353d2	0.468	0.032
i359d1	0.343	0.021
i359g2	0.714	0.039
l360d1	0.498	0.032
l360d2	0.525	0.029
v362g1	0.542	0.032
v362g2	0.498	0.025
v365g1	0.709	0.037
l367d1	0.445	0.042
l367d2	0.46	0.059
a370b	0.763	0.046
a375b	0.819	0.079
i377d1	0.358	0.013
i377g2	0.418	0.017
l379d1	0.668	0.068
l379d2	0.574	0.038
t385g2	0.726	0.044
i388d1	0.386	0.019
i389d1	0.227	0.013
i389g2	0.849	0.045
a390b	0.751	0.047

Table C-63: Methyl Order Parameters of the SAP90 PDZ3Δ7 bound to the CRIPT peptide

ID	O^2_{axis}	Err
i307d1	0.307	0.01
i307g2	0.528	0.02
i314d1	0.295	0.007
i314g2	0.758	0.024
v315g1	0.697	0.017
v315g2	0.742	0.022
i316d1	0.37	0.01
i316g2	0.409	0.014
t321g2	0.577	0.01
l323d1	0.826	0.058

ID	O^2_{axis}	Err
l323d2	0.753	0.034
i327d1	0.731	0.02
i327g2	0.887	0.033
v328g1	0.589	0.011
v328g2	0.809	0.046
i336d1	0.786	0.03
i336g2	0.695	0.023
i338d1	0.539	0.015
i338g2	0.846	0.031
i341d1	0.248	0.006
i341g2	0.788	0.025
l342d1	0.487	0.026
a343b	0.863	0.016
a347b	0.886	0.039
l349d1	0.395	0.016
l349d2	0.362	0.009
l353d1	0.567	0.042
l353d2	0.559	0.021
i359d1	0.378	0.011
i359g2	0.805	0.023
l360d1	0.581	0.019
l360d2	0.608	0.017
v362g1	0.599	0.019
v362g2	0.559	0.015
v365g1	0.802	0.013
v365g2	0.835	0.023
l367d1	0.559	0.048
l367d2	0.621	0.042
a370b	0.848	0.027
a375b	0.93	0.051
a376b	0.894	0.023
i377d1	0.382	0.007
i377g2	0.564	0.011
l379d1	0.789	0.034
l379d2	0.789	0.034
t385g2	0.732	0.023
v386g2	0.725	0.016
i388d1	0.474	0.012
i388g2	0.732	0.023
i389d1	0.226	0.006
i389g2	0.852	0.025
a390b	0.867	0.026

Table C-64: Methyl Order Parameters of the ecDHFR:Folate binary complex

ID	O^2_{axis}	Err
m1e	0.1	0.01
i2d1	0.42	0.01
i2g2	0.69	0.02
l4d1	0.43	0.01
l4d2	0.44	0.03
i5d1	0.68	0.07
i5g2	0.82	0.07
a6b	0.71	0.05
a7b	0.83	0.07
l8d1	0.31	0.01
l8d2	0.24	0.01
a9b	0.79	0.06
v10g1	0.63	0.02
v10g2	0.64	0.09
v13g2	0.7	0.04
i14d1	0.69	0.03
i14g2	0.71	0.03
m16e	0.22	0.01
a19b	0.66	0.01
m20e	0.14	0.01
l24d1	0.58	0.12
l24d2	0.47	0.06
a26b	0.86	0.04
l28d1	0.36	0.01
l28d2	0.33	0.01
t35g2	0.75	0.05
l36d1	0.27	0.01
l36d2	0.27	0.01

ID	O^2_{axis}	Err
v40g1	0.75	0.02
v40g2	0.71	0.03
i41d1	0.62	0.02
i41g2	0.8	0.02
m42e	0.82	0.01
t46g2	0.61	0.01
i50d1	0.76	0.03
i50g2	0.61	0.01
l54d2	0.81	0.06
i60d1	0.3	0.01
i60g2	0.82	0.03
i61d1	0.25	0.01
i61g2	0.76	0.04
l62d1	0.38	0.01
l62d2	0.38	0.01
v72g1	0.75	0.04
v72g2	0.74	0.03
t73g2	0.82	0.03
v75g2	0.87	0.03
v78g1	0.8	0.01
v78g2	0.79	0.02
a81b	0.89	0.03
i82d1	0.5	0.01
i82g2	0.83	0.01
a84b	0.8	0.02
v88g1	0.75	0.02
v88g2	0.77	0.02
i91d1	0.76	0.02
i91g2	0.85	0.02
m92e	0.75	0.01
v93g1	0.9	0.03
v93g2	0.92	0.03
i94d1	0.68	0.05
v99g1	0.77	0.03
v99g2	0.8	0.02
l104d2	0.52	0.02
a107b	0.78	0.03
l110d1	0.66	0.07
l110d2	0.65	0.04
l112d1	0.36	0.02
l112d2	0.82	0.06
i115d1	0.59	0.04
i115g2	0.82	0.06
a117b	0.76	0.03
v119g1	0.27	0.01
v119g2	0.25	0.01
t123g2	0.5	0.01
v136g2	0.67	0.02
a143b	0.92	0.02
a145b	0.82	0.02
i155d1	0.73	0.03
i155g2	0.84	0.03
l156d1	0.37	0.01
l156d2	0.37	0.01

Table C-65: Methyl Order Parameters of the ecDHFR:Folate:NADP$^+$ ternary complex

ID	O^2_{axis}	Err
m1e	0.09	0.01
i2d1	0.48	0.01
i2g2	0.74	0.03
l4d1	0.52	0.01
l4d2	0.48	0.05
i5d1	0.8	0.06
i5g2	0.86	0.11
a6b	0.81	0.09
l8d1	0.31	0.02
l8d2	0.28	0.01
a9b	0.77	0.05
v10g1	0.66	0.03
v10g2	0.77	0.06
v13g1	0.79	0.02

ID	O^2_{axis}	Err
v13g2	0.69	0.07
i14g2	0.81	0.1
m16e	0.31	0.01
m20e	0.34	0.01
l24d1	0.52	0.1
l24d2	0.49	0.16
a26b	1	0.01
l28d2	0.32	0.02
a29b	0.91	0.02
t35g2	0.78	0.07
l36d1	0.29	0.01
l36d2	0.29	0.01
v40g2	0.84	0.05
i41d1	0.7	0.03
i41g2	0.79	0.03
m42e	0.84	0.02
t46g2	0.58	0.05
i50d1	0.8	0.04
i50g2	0.65	0.02
l54d1	0.71	0.12
l54d2	0.82	0.04
i60d1	0.29	0.01
i60g2	0.81	0.03
i61d1	0.2	0.01
i61g2	0.75	0.08
l62d1	0.46	0.02
l62d2	0.43	0.04
t68g2	0.7	0.01
v72g1	0.78	0.12
v72g2	0.78	0.06
t73g2	0.79	0.03
v75g1	0.77	0.02
v75g2	0.9	0.04
v78g1	0.85	0.02
v78g2	0.87	0.02

ID	O^2_{axis}	Err
a81b	0.91	0.03
i82d1	0.52	0.01
i82g2	0.78	0.03
a83b	0.9	0.02
a84b	0.84	0.03
v88g2	0.76	0.03
i91d1	0.8	0.02
i91g2	0.85	0.04
m92e	0.76	0.01
v93g1	0.87	0.03
v93g2	0.89	0.03
i94d1	0.67	0.05
i94g2	0.7	0.08
v99g2	0.85	0.05
l104d1	0.47	0.02
l104d2	0.52	0.03
a107b	0.85	0.05
l110d1	0.69	0.12
l112d1	0.36	0.04
l112d2	0.84	0.06
t113g2	0.86	0.04
i115d1	0.63	0.05
i115g2	0.89	0.07
v119g2	0.45	0.02
t123g2	0.69	0.18
v136g1	0.68	0.02
v136g2	0.68	0.02
a143b	0.87	0.04
a145b	0.78	0.03
i155d1	0.77	0.03
i155g2	0.85	0.04
l156d1	0.33	0.01
l156d2	0.32	0.01

Table C-66: Methyl Order Parameters of the SAP SH2 domain

ID	O^2_{axis}	Err
a3b	0.463	0.018
v6g2	0.696	0.022
i11d1	0.808	0.024
i11g2	0.822	0.025
l20d2	0.628	0.021
l21d2	0.572	0.017
t23g2	0.606	0.018
l25d1	0.477	0.009
l25d2	0.444	0.014
l30d1	0.837	0.054
l30d2	0.87	0.106
v37g1	0.743	0.031
v40g2	0.808	0.025
l43d2	0.695	0.027
v45g1	0.495	0.024
l46d1	0.652	0.026
l46d2	0.838	0.041
i51d1	0.235	0.022
i51g2	0.73	0.042
a66b	0.822	0.029
t68g2	0.755	0.052
i80d1	0.22	0.008
i80g2	0.345	0.017
l83d1	0.67	0.044
l83d2	0.72	0.018
i84d1	0.285	0.016
i84g2	0.819	0.017
a86b	0.908	0.022
i94d1	0.747	0.045
i94g2	0.814	0.04
v95g1	0.699	0.026
v95g2	0.708	0.041
i96g2	0.25	0.019
i96g2	0.809	0.027
l98d1	0.931	0.166
l98d2	0.864	0.042
v102g1	0.838	0.034

Table C-67: Methyl Order Parameters of the SAP SH2 domain bound to Y281

ID	O^2_{axis}	Err
a3b	0.432	0.019
v4g2	0.335	0.011
v6g2	0.739	0.026
i11g2	0.782	0.019
l20d2	0.688	0.054
l21d2	0.434	0.013
t23g2	0.648	0.021
l25d1	0.399	0.018
l25d2	0.343	0.01
l30d1	0.751	0.023
l30d2	0.917	0.125
l31d1	0.334	0.02
v37g1	0.717	0.033
v37g2	0.683	0.018
v40g2	0.8	0.021
l43d2	0.604	0.021
v45g1	0.55	0.015
v45g2	0.635	0.026
l46d1	0.787	0.03
i51d1	0.373	0.014
i51g2	0.832	0.058
t53g2	0.855	0.061
v56g1	0.597	0.026
v56g2	0.6	0.017
a66b	0.89	0.037
t68g2	0.618	0.036
a69b	0.908	0.031
v72g1	0.656	0.058

ID	O^2_{axis}	Err
i80d1	0.178	0.012
i80g2	0.302	0.01
l83d1	0.721	0.097
l83d2	0.781	0.027
i84d1	0.329	0.015
a86b	0.903	0.034
i94d1	0.788	0.048
i94g2	0.892	0.029

ID	O^2_{axis}	Err
v95g1	0.648	0.014
v95g2	0.64	0.026
i96d1	0.4	0.012
l98d1	0.796	0.256
l98d2	0.887	0.051
v102g1	0.818	0.014
v102g2	0.83	0.038

Table C-68: Methyl Order Parameters of the SAP SH2 domain bound to pY281

ID	O^2_{axis}	Err
a3b	0.463	0.018
v6g2	0.696	0.022
i11d1	0.808	0.024
i11g2	0.822	0.025
l20d2	0.628	0.021
l21d2	0.572	0.017
t23g2	0.606	0.018
l25d1	0.477	0.009
l25d2	0.444	0.014
l30d1	0.837	0.054
l30d2	0.87	0.106
v37g1	0.743	0.031
v40g2	0.808	0.025
l43d2	0.695	0.027
v45g1	0.495	0.024
l46d1	0.652	0.026
l46d2	0.838	0.041
i51d1	0.235	0.022
i51g2	0.73	0.042

ID	O^2_{axis}	Err
a66b	0.822	0.029
t68g2	0.755	0.052
i80d1	0.22	0.008
i80g2	0.345	0.017
l83d1	0.67	0.044
l83d2	0.72	0.018
i84d1	0.285	0.016
i84g2	0.819	0.017
a86b	0.908	0.022
i94d1	0.747	0.045
i94g2	0.814	0.04
v95g1	0.699	0.026
v95g2	0.708	0.041
i96g2	0.25	0.019
i96g2	0.809	0.027
l98d1	0.931	0.166
l98d2	0.864	0.042
v102g1	0.838	0.034

Table C-69: Methyl Order Parameters of the hPTP1e PDZ2 domain

ID	O^2_{axis}	Err
i6d1	0.256	0.008
i6g2	0.684	0.021
v9g1	0.512	0.027
v9g2	0.506	0.02

ID	O^2_{axis}	Err
l11d2	0.284	0.05
a12b	0.743	0.02
l18d1	0.605	0.071
l18d2	0.541	0.037

ID	O^2_{axis}	Err
i20d1	0.602	0.019
i20g2	0.351	0.012
v22g1	0.803	0.037
v22g2	0.755	0.028
t23g2	0.718	0.05
v26g2	0.563	0.019
t28g2	0.742	0.035
v30g1	0.549	0.021
v30g2	0.529	0.026
i35d1	0.651	0.032
i35g2	0.844	0.039
v37g1	0.881	0.043
a39b	0.872	0.023
v40g1	0.609	0.021
i41d1	0.177	0.013
i41g2	0.78	0.026
a45b	0.91	0.04
a46b	0.92	0.053
i52d1	0.709	0.026
i52g2	0.764	0.032
v58g1	0.805	0.043

ID	O^2_{axis}	Err
v58g2	0.806	0.031
l59d1	0.55	0.043
l59d2	0.535	0.027
v61g2	0.769	0.028
v64g1	0.496	0.014
v64g2	0.484	0.007
l66d2	0.596	0.069
a69b	0.797	0.035
t70g2	0.801	0.036
a74b	0.644	0.049
t77g2	0.814	0.061
l78d2	0.478	0.018
t81g2	0.872	0.059
v84g1	0.692	0.02
v85g1	0.667	0.032
v85g2	0.699	0.034
l87d1	0.427	0.056
l88d1	0.631	0.023
l89d1	0.524	0.078
l89d2	0.581	0.132

Table C-70: Methyl Order Parameters of the hPTP1e PDZ2 domain bound to RA-GEF2

ID	O^2_{axis}	Err
i6d1	0.236	0.005
i6g2	0.635	0.012
v9g1	0.471	0.011
v9g2	0.459	0.016
l11d2	0.234	0.021
l18d1	0.511	0.05
l18d2	0.571	0.015
i20d1	0.646	0.013
i20g2	0.355	0.006
v22g1	0.752	0.019
v22g2	0.704	0.02
t23g2	0.605	0.078
v26g1	0.681	0.013
v26g2	0.65	0.017

ID	O^2_{axis}	Err
v30g2	0.606	0.022
i35d1	0.605	0.015
i35g2	0.783	0.021
a39b	0.841	0.014
v40g1	0.574	0.012
i41d1	0.186	0.004
i41g2	0.698	0.014
a45b	0.841	0.023
a46b	0.871	0.033
i52d1	0.68	0.015
i52g2	0.766	0.021
v58g1	0.779	0.023
v58g2	0.768	0.018
l59d1	0.566	0.051

ID	O^2_{axis}	Err
v61g2	0.67	0.017
v64g1	0.647	0.013
v64g2	0.573	0.009
l66d1	0.589	0.041
l66d2	0.586	0.014
a69b	0.856	0.022
t70g2	0.867	0.021
v75g2	0.803	0.031
t77g2	0.678	0.017
l78d1	0.779	0.037
l78d2	0.791	0.044
t81g2	0.784	0.028
v84g1	0.624	0.012
v84g2	0.622	0.009
v85g1	0.535	0.014
v85g2	0.555	0.015
l87d1	0.434	0.038
l87d2	0.499	0.029
l88d1	0.597	0.013

Table C-71: Methyl Order Parameters of Barnase

ID	O^2_{axis}	Err
ALA1CB	0.351	0.012
VAL3CG2	0.633	0.024
VAL3CG1	0.509	0.008
ILE4CD1	0.578	0.028
ILE4CG2	0.974	0.028
THR6CG2	0.994	0.012
VAL10CG2	0.994	0.044
VAL10CG1	0.851	0.014
ALA11CB	0.994	0.039
LEU14CD2	0.588	0.011
LEU14CD1	0.747	0.02
THR16CG2	0.954	0.032
LEU20CD2	0.821	0.04
LEU20CD1	0.836	0.011
ILE25CD1	0.776	0.03
ILE25CG2	0.242	0.003
THR26CG2	0.979	0.046
ALA30CB	0.994	0.019
ALA32CB	0.994	0.032
LEU33CD1	0.712	0.035
LEU33CD2	0.732	0.028
VAL36CG1	0.905	0.029
LEU42CD2	0.717	0.033
LEU42CD1	0.855	0.012
ALA43CB	0.994	0.013
VAL45CG1	0.964	0.036
VAL45CG2	0.855	0.033
ALA46CB	0.994	0.044
ILE51CD1	0.464	0.014
ILE51CG2	0.841	0.028
ILE55CD1	0.385	0.005
ILE55CG2	0.841	0.033
LEU63CD2	0.697	0.018
LEU63CD1	0.732	0.023
THR70CG2	0.464	0.021
ALA74CB	0.994	0.03
ILE76CG2	0.836	0.027
ILE76CD1	0.648	0.02
THR79CG2	0.846	0.041
ILE88CD1	0.781	0.012
ILE88CG2	0.534	0.024
LEU89CD1	0.722	0.032
LEU89CD2	0.628	0.03
LEU95CD1	0.44	0.017
LEU95CD2	0.494	0.017
ILE96CD1	0.653	0.02
ILE96CG2	0.994	0.045
THR99CG2	0.994	0.019
THR107CG2	0.974	0.042
ILE109CG2	0.747	0.021

Table C-72: Methyl Order Parameters of Barnase bound to dCGAC

ID	O^2_{axis}	Err
ALA1CB	0.291	0.003
VAL3CG2	0.489	0.012
VAL3CG1	0.455	0.022
ILE4CD1	0.484	0.008
ILE4CG2	0.821	0.028
THR6CG2	0.994	0.047
VAL10CG2	0.994	0.031
VAL10CG1	0.9	0.021
ALA11CB	0.93	0.011
LEU14CD2	0.756	0.016
LEU14CD1	0.761	0.036
THR16CG2	0.94	0.034
LEU20CD2	0.752	0.014
LEU20CD1	0.821	0.009
ILE25CD1	0.722	0.016
ILE25CG2	0.148	0.003
THR26CG2	0.895	0.019
ALA30CB	0.994	0.039
ALA32CB	0.994	0.026
LEU33CD1	0.672	0.015
LEU33CD2	0.633	0.017
VAL36CG1	0.86	0.042
LEU42CD2	0.623	0.023
LEU42CD1	0.836	0.023
ALA43CB	0.994	0.047
VAL45CG1	0.86	0.02
VAL45CG2	0.89	0.017
ALA46CB	0.994	0.024
ILE51CD1	0.435	0.009
ILE51CG2	0.964	0.043
ILE55CD1	0.296	0.01
ILE55CG2	0.717	0.023
LEU63CD2	0.712	0.014
LEU63CD1	0.796	0.019
THR70CG2	0.45	0.008
ALA74CB	0.994	0.03
ILE76CG2	0.841	0.023
ILE76CD1	0.653	0.013
THR79CG2	0.697	0.008
ILE88CD1	0.667	0.016
ILE88CG2	0.558	0.013
LEU89CD1	0.727	0.011
LEU89CD2	0.643	0.029
LEU95CD1	0.326	0.004
LEU95CD2	0.455	0.014
ILE96CD1	0.44	0.014
ILE96CG2	0.92	0.011
THR99CG2	0.514	0.02
THR105CG2	0.628	0.01
THR107CG2	0.93	0.03
ILE109CG2	0.687	0.022

Table C-73: Methyl Order Parameters of HBP(D24R)

ID	O^2_{axis}	Err
ALA6CB	0.898	0.032
ALA13CB	0.796	0.025
ALA17CB	0.769	0.01
LEU21CD1	0.668	0.015
ALA23CB	0.93	0.042
VAL25CG2	0.652	0.028
VAL25CG1	0.657	0.031
VAL28CG2	0.652	0.059
MET31CE	0.577	0.041
VAL32CG2	0.421	0.03
VAL32CG1	0.652	0.043
VAL41CG1	0.812	0.009

ID	O^2_{axis}	Err
THR47CG2	0.855	0.05
VAL49CG2	0.812	0.069
MET52CE	0.111	0.045
ALA53CB	0.871	0.058
VAL56CG2	0.437	0.052
VAL56CG1	0.314	0.036
ILE63CD1	0.555	0.045
ILE63CG2	0.855	0.049
LEU68CD1	0.164	0.026
LEU68CD2	0.084	0.033
MET70CE	0.084	0.02
ALA73CB	0.716	0.045
THR75CG2	0.523	0.009
ALA80CB	0.903	0.077
THR81CG2	0.582	0.002
THR85CG2	0.85	0.035
ALA86CB	0.941	0.048
VAL87CG2	0.86	0.019
VAL87CG1	0.909	0.024
MET89CE	0.116	0.039
ALA97CB	0.919	0.018
VAL107CG2	0.598	0.03
THR109CG2	0.716	0.02
VAL111CG2	0.47	0.031

ID	O^2_{axis}	Err
ILE112CD1	0.212	0.074
ILE112CG2	0.764	0.02
ALA113CB	0.903	0.076
VAL121CG1	0.903	0.015
ILE122CG2	0.727	0.044
VAL124CG1	0.582	0.007
THR127CG2	0.346	0.074
LEU136CD2	0.491	0.013
LEU136CD1	0.475	0.04
THR138CG2	0.561	0.044
ILE144CD1	0.652	0.043
ILE144CG2	0.828	0.009
ALA146CB	0.887	0.013
LEU149CD2	0.507	0.038
ALA156CB	0.909	0.008
VAL157CG2	0.33	0.06
VAL157CG1	0.694	0.027
THR161CG2	0.464	0.017
VAL164CG2	0.877	0.024
VAL164CG1	0.828	0.013
ALA168CB	0.759	0.026
LEU170CD2	0.266	0.078
LEU170CD1	0.255	0.068

Table C-74: Methyl Order Parameters of HBP(D24R) bound to histamine

ID	O^2_{axis}	Err
ALA6CB	0.839	0.03
ALA13CB	0.855	0.019
ALA17CB	0.769	0.012
LEU21CD1	0.63	0.021
ALA23CB	0.866	0.037
VAL25CG2	0.652	0.018
VAL25CG1	0.646	0.039
VAL28CG2	0.662	0.03
MET31CE	0.577	0.033

ID	O^2_{axis}	Err
VAL32CG2	0.47	0.023
VAL32CG1	0.641	0.017
VAL41CG1	0.807	0.026
THR47CG2	0.871	0.03
VAL49CG2	0.743	0.025
MET52CE	0.111	0.046
ALA53CB	0.871	0.04
VAL56CG2	0.421	0.047
VAL56CG1	0.277	0.051

ID	O^2_{axis}	Err
ILE63CD1	0.582	0.031
ILE63CG2	0.871	0.038
LEU68CD1	0.191	0.046
LEU68CD2	0.079	0.04
MET70CE	0.084	0
ALA73CB	0.641	0.023
THR75CG2	0.496	0.027
ALA80CB	0.85	0.026
THR81CG2	0.539	0.01
THR85CG2	0.802	0.03
ALA86CB	0.935	0.029
VAL87CG2	0.802	0.008
VAL87CG1	0.855	0.03
MET89CE	0.116	0.046
ALA97CB	0.946	0.035
VAL107CG2	0.593	0.028
THR109CG2	0.689	0.019
VAL111CG2	0.459	0.031
ILE112CD1	0.229	0.08
ILE112CG2	0.78	0.008
ALA113CB	0.839	0.039

ID	O^2_{axis}	Err
VAL121CG1	0.85	0.011
ILE122CG2	0.743	0.024
VAL124CG1	0.598	0.035
THR127CG2	0.346	0.078
LEU136CD2	0.496	0.033
LEU136CD1	0.502	0.018
THR138CG2	0.55	0.034
ILE144CD1	0.63	0.01
ILE144CG2	0.818	0.033
ALA146CB	0.871	0.028
LEU149CD2	0.502	0.023
ALA156CB	0.903	0.03
VAL157CG2	0.314	0.027
VAL157CG1	0.657	0.016
THR161CG2	0.437	0.001
VAL164CG2	0.834	0.022
VAL164CG1	0.812	0.031
ALA168CB	0.732	0.02
LEU170CD2	0.277	0.049
LEU170CD1	0.261	0.015

APPENDIX D: Chapter 4

Materials and Methods

Sample Preparation

BIRB796 and SB203580 were obtained from LC Laboratories (Woburn, MA) and SelleckChem (Houston, TX) respectively. p38α$_{2\text{-}349}$ was expressed and purified as essentially as described previously [129]. The sole exception is that before anion exchange by MonoQ, the protein was treated with Lambda Protein Phosphatase (New England Biolabs) at a ratio of 400U:mg of protein to remove endogenous phosphorylation which was found to occur during expression. The final NMR sample for relaxation measurements contained 0.5 mM protein in 10mM HEPES, 150mM NaCl, 5mM DTT, pH 7.4. To ensure solubilization of the inhibitors, all samples contained 1% v/v DMSO-d6 in the final sample. SB203580 and BIRB796 were solubilized in DMSO-d6 and added at a ratio of 1.2:1 ligand:protein to ensure complete titration, which was confirmed by NMR.

NMR Spectroscopy

Assignment and NMR relaxation data were collected at 600MHz and 750 MHz. Several experiments employed the use of non-uniformly sampled (NUS) data. This involves sampling the indirect dimensions of multidimensional NMR spectra data using a variety of sampling "schedules" followed by data reconstruction during data processing. The details of various approach to NUS NMR are extensively outlined elsewhere [131, 177]. To illustrate briefly how NUS works, let us consider a 2D ^{15}N HSQC experiment. A typical experiment of this nature would contain 2048 x 320 (^{1}H x ^{15}N) total points. In a Cartesian-sampled experiment, the data would be collected as 320 separate FIDs each of 2048 points in the directly detected dimension. In a non-uniformly sampled experiment, one would collect a smaller percentage of these FIDs that are separated by some non-uniform distribution. For example, one could collect 25%, or 80, of these FIDs with a non-uniform spacing. The data in the indirect dimension can then be reconstructed to

320 total points using a variety of algorithms. Of paramount concern, of course, is the fidelity of the reconstruction. Historically, this method was fraught with artifacts in the final reconstructed spectrum. Wagner and colleagues recently overcame these boundaries with the use of a Poisson-Gap sampling schedule and reconstruction using the Iterative Soft Thresholding (IST) algorithm [131]. This approach allows for NMR data to be reconstructed with high fidelity. Unpublished data from our lab have demonstrated that the sampling sparsityrequired for high-quality reconstruction of 2D and 3D spectra are 10% and 25% respectively. . All NUS data collected in this study followed this requirement For ^{15}N and 13C relaxation data, which are Pseudo-3D experiments, a sampling sparsity of 25% was used. All standard (Cartesian) pulse sequences used in this study were converted to NUS by Matthew Stetz, graduate student in the Wand laboratory.

Relaxation Data Analysis

All ^{15}N and ^{13}C relaxation data were collected as NUS experiments. After reconstruction as described above, exponential decays were fit using in-house software to determine T_1 and T_{1p} rates. T_{1p} rates were corrected for the off-resonance tilted field using the relation:

$$R_2 = R_{1\rho} / \cos^2\theta - R_{1\rho} / \tan^2\theta$$

Where tanθ=ω_1/Ω where ω_1 is the spin-lock RF field and Ω is the offset from either the ^{15}N or ^{13}C carrier, depending on the nucleus being probed. Macromolecular tumbling was determined from T_1 and T_2 rates at 2 magnetic fields fitting to the Lipari-Szabo formalism using in-house software [21]. 15N residues were excluded from the molecular tumbling fitting routine if their fits for τ_m, τ_e, and O^2_{NH} produced statistical outliers to the normalized χ^2 values of the fit. Residues displaying statistically significant R_{ex} were also omitted for the determination of molecular tumbling. approximately 115 residues were used to calculate overall tumbling for the apo and drug-bound complexes. Methyl order parameters were determined from T_1 and T_2 rates at two magnetic fields. Model free parameters (O^2 and τ_e) were determined using a grid search approach[155] utilizing software and parameters as described elsewhere.[156] Errors were determined using the Monte

Carlo method. O^2_{axis} values were obtained by division by 0.111, which assumes a tetrahedral geometry of the methyl groups.

Isothermal Titration Calorimetry

Isothermal titration calorimetry (ITC) measurements were carried out on a VP-ITC instrument (Microcal) at the same temperature and buffer conditions as the corresponding NMR relaxation data. The sole exception to the buffer conditions were that 0.2mM DTT was used instead of 5mM DTT to minimize the impact of DTT on the ITC trace. This effect is due to the release of heat upon oxidation of DTT which can cause baseline distortions across the experiment.

p38α was purified as outlined above and dialyzed in NMR buffer. Samples were centrifuged at 4000 RPM for 10 minutes to remove any precipitate. The sample was degassed at 293K for 5 minutes. DMSO-d6 was added to the p38α sample immediately before the experiment.185uM p38α was titrated into 5-15uM inhibitor in 5ul injections. Example traces can be found in Figure 4-2 of the main text. Data analysis was performed using the Origin software. The data were corrected for the heat of dilution as necessary.

Data Tables

Table D-1: Backbone assignments of p38α in the apo and inhibitor-bound states

	Apo		SB203580-Bound		BIRB796-Bound	
Residue	**^{15}N (ppm)**	**^{1}H (ppm)**	**^{15}N (ppm)**	**^{1}H (ppm)**	**^{15}N (ppm)**	**^{1}H (ppm)**
GLY 1	110.55	8.389	110.614	8.398	110.574	8.393
SER 2	115.947	8.187	116.048	8.204		
GLN 3	122.216	8.45	122.275	8.451	122.289	8.459
GLU 4	122.475	8.347	122.486	8.346	122.438	8.334
ARG 5	125.277	8.412	125.357	8.422	125.279	8.414
THR 7	117.457	8.508	117.52	8.503	117.459	8.495
PHE 8	127.248	8.816	127.412	8.836	127.277	8.822
TYR 9	120.059	9.143	120.063	9.13	120.087	9.131
ARG 10	120.093	8.475	120.058	8.445	119.759	8.422

	Apo		**SB203580-Bound**		**BIRB796-Bound**	
Residue	**^{15}N (ppm)**	**^{1}H (ppm)**	**^{15}N (ppm)**	**^{1}H (ppm)**	**^{15}N (ppm)**	**^{1}H (ppm)**
GLN 11	122.264	8.961	122.719	9.002	122.839	9.003
GLU 12	125.452	8.866	125.554	8.865	125.779	8.872
LEU 13	128.539	9.003	128.392	8.999	128.367	9.041
ASN 14	115.956	7.38				
LYS 15	109.9	8.903	110.156	8.893	110.19	8.89
THR 16	115.658	7.854	116.281	7.833	116.297	7.853
ILE 17	125.497	8.636	126.121	8.627	125.992	8.602
TRP 18	131.007	9.297	130.872	9.245	130.888	9.205
GLU 19	128.235	8.315	128.133	8.316	128.087	8.266
VAL 20	112.392	7.649	111.866	7.644	111.72	7.656
GLU 22	118.937	8.132	118.873	8.13	118.721	8.112
ARG 23	117.451	7.485	117.125	7.543	117.163	7.512
TYR 24	118.055	7.793	118.334	7.785	118.266	7.8
GLN 25	122.52	9.191	122.711	9.196	122.6	9.238
ASN 26	117.38	8.839	117.326	8.805	117.403	8.829
LEU 27	120.218	8.565	120.173	8.52	120.215	8.499
SER 28	115.971	8.759	115.759	8.747	115.965	8.817
VAL 30	120.825	8.662	120.263	8.651	121.016	8.561
GLY 31	108.319	7.77	108.743	7.83		
SER 32	115.278	8.398				
GLY 33	110.393	8.174	108.716	7.845	109.782	8.321
ALA 34						
TYR 35	113.363	8.092	113.14	8.163		
GLY 36	108.411	7.31				
SER 37	115.899	8.135			116.519	8.321
VAL 38	122.449	8.715	123.306	8.618		
CYS 39	125.429	9.276	125.667	9.287	124.348	9.207
ALA 40	125.63	8.804	125.734	8.8		
ALA 41	120.598	9.035			119.555	9.018
PHE 42	122.278	9.222	123.423	9.3	123.188	9.336
ASP 43	125.977	8.324	125.675	8.231	125.814	8.227
THR 44	117.282	8.943	117.686	9.257	117.47	9.175
LYS 45	121.715	7.897	121.675	7.811	121.849	7.848
THR 46	104.947	6.586	104.678	6.521	104.912	6.575
GLY 47	112.255	8.373	112.474	8.361	112.295	8.312
LEU 48	119.64	7.105	119.248	7.125	119.407	7.13
ARG 49	119.653	8.243	118.606	8.31	118.536	8.342
VAL 50	116.423	8.81			116.742	8.609

	Apo		SB203580-Bound		BIRB796-Bound	
Residue	**^{15}N (ppm)**	**^{1}H (ppm)**	**^{15}N (ppm)**	**^{1}H (ppm)**	**^{15}N (ppm)**	**^{1}H (ppm)**
ALA 51	122.597	8.825				
VAL 52	122.921	9.222	122.252	9.199	117.892	7.998
LYS 53	129.246	9.569				
LYS 54	128.287	8.624			128.409	8.504
LEU 55	128.582	8.001	128.172	7.829	129.01	8.055
SER 56	117.881	8.038	117.277	8.034	117.632	7.857
ARG 57	123.091	8.74	123.152	8.693	123.164	8.764
PHE 59	112.293	7.908	112.122	7.919	112.297	7.849
GLN 60	115.439	7.085	115.702	7.063	115.667	7.14
SER 61	110.647	7.447	110.508	7.442	110.443	7.437
ILE 62	122.993	9.19				
ILE 63	118.844	7.593	118.934	7.591	119.189	7.601
HIS 64						
ALA 65	123.477	8.612			123.611	8.569
LYS 66	118.165	7.833	117.974	7.851	118.008	7.875
ARG 67	119.22	7.471	119.483	7.526		
THR 68	119.927	8.412				
TYR 69	121.338	7.571			121.435	7.644
ARG 70						
GLU 71						
LEU 72						
ARG 73						
LEU 74						
LEU 75						
LYS 76						
HIS 77						
MET 78						
LYS 79	128.668	8.512	128.335	8.552	128.318	8.492
HIS 80	123.931	8.733	124.63	8.705	123.785	8.59
GLU 81	125.494	8.064	124.722	8.043	124.828	7.998
ASN 82						
VAL 83	119.91	7.697	119.894	7.61	120.532	7.618
ILE 84	129.474	8.373			128.709	8.191
GLY 85	109.526	7.626			108.822	7.679
LEU 86	121.03	8.215			120.583	8.746
LEU 87	126.536	8.973			125.259	9.042
VAL 89	120.227	7.834	120.607	7.701		
PHE 90					119.532	8.209

	Apo		SB203580-Bound		BIRB796-Bound	
Residue	^{15}N (ppm)	^{1}H (ppm)	^{15}N (ppm)	^{1}H (ppm)	^{15}N (ppm)	^{1}H (ppm)
THR 91	113.454	8.956	113.402	8.932	113.675	8.945
ALA 93	122.263	7.718	122.214	7.651	122.313	7.73
ARG 94	121.039	9.277	121.293	9.302	121.038	9.28
SER 95	111.301	7.38	111.223	7.383	111.201	7.369
LEU 96	122.401	8.483	122.396	8.49	122.188	8.45
GLU 97	117.302	8.307	117.329	8.312	117.058	8.269
GLU 98	115.345	7.026	115.289	7.021	115.32	7.024
PHE 99	122.113	7.295	122.13	7.295	122.1	7.255
ASN 100	125.522	8.547	125.523	8.651	126.114	8.779
ASP 101	115.874	7.624	115.7	7.55		
VAL 102	121.129	8.482	121.123	8.514	120.719	8.217
TYR 103						
LEU 104						
VAL 105					120.942	7.65
THR 106	117.977	9.012				
HIS 107	119.39	8.936				
LEU 108	125.256	8.191			124.729	7.927
MET 109	126.102	8.725			127.141	8.252
GLY 110	108.737	8.145			106.425	7.886
ALA 111	123.81	7.879			123.316	8.072
ASP 112	118.501	7.997	118.67	7.967	117.039	7.951
LEU 113	117.325	7.788	116.986	7.85	117.977	7.594
ASN 114	115.536	7.661	116.593	7.703	114.787	7.605
ASN 115	118.176	7.978	117.858	8.043	118.127	7.937
ILE 116	118.784	7.502			119.116	7.477
VAL 117	116.521	7.522	116.33	7.48	116.284	7.509
LYS 118	117.318	7.381	117.566	7.408	117.288	7.389
CYS 119	114.474	7.643	114.476	7.644	114.348	7.646
GLN 120	119.531	8.017	119.426	8.04	119.455	8
LYS 121	121.843	8.244	121.903	8.259	121.769	8.228
LEU 122	126.679	8.541	126.585	8.526	126.587	8.528
THR 123						
ASP 124	120.653	8.982	120.768	8.981	120.59	8.977
ASP 125	115.381	7.945	115.321	7.949	115.49	7.921
HIS 126	119.303	7.518	119.397	7.529	119.149	7.504
VAL 127	119.977	8.137	119.952	8.122	119.894	8.134
GLN 128	118.193	8.402	118.197	8.409	118.188	8.391
PHE 129	116.182	7.438	116.095	7.416	116.276	7.457

	Apo		**SB203580-Bound**		**BIRB796-Bound**	
Residue	**^{15}N (ppm)**	**^{1}H (ppm)**	**^{15}N (ppm)**	**^{1}H (ppm)**	**^{15}N (ppm)**	**^{1}H (ppm)**
LEU 130	120.656	8.798	120.389	8.735	120.837	8.855
ILE 131						
TYR 132					119.654	8.963
GLN 133	116.504	8.584				
ILE 134						
LEU 135						
ARG 136						
GLY 137	107.104	8.129	107.212	8.086	107.186	8.205
LEU 138	121.555	8.687	121.4	8.65	121.67	8.677
LYS 139	119.271	8.688	119.13	8.681	119.264	8.674
TYR 140	118.11	6.818	117.981	6.846	118.097	6.821
ILE 141	120.179	8.454			120.475	8.51
HIS 142	119.585	9.508	120.64	9.539	119.431	9.538
SER 143	116.368	7.858	115.812	7.859	116.046	7.833
ALA 144	126.304	7.421	126.28	7.418	126.47	7.457
ASP 145	115.198	8.207	115.317	8.204	115.194	8.219
ILE 146	119.057	7.246	119.359	7.323	119.479	7.233
ILE 147	122.947	7.852			123.674	7.858
HIS 148	120.813	7.367	120.853	7.368	120.971	7.348
ARG 149						
ASP 150						
LEU 151						
LYS 152						
SER 154	106.09	7.557				
ASN 155	118.95	7.802	119.286	7.829	120.56	7.679
LEU 156	119.092	7.048	119.11	6.865	117.908	7.166
ALA 157	125.766	8.598			127.602	8.818
VAL 158	117.957	8.169	118.031	7.729	119.547	8.731
ASN 159	122.259	7.895	121.358	7.852	123	8.134
GLU 160	117.466	8.852	118.071	8.918	117.663	8.883
ASP 161	118.659	7.519	118.532	7.567	118.834	7.56
CYS 162	111.265	8.298	111.752	8.273	110.715	8.325
GLU 163	117.644	7.669	117.766	7.562	118.432	7.654
LEU 164	125.257	7.981	124.189	7.854	124.195	7.852
LYS 165	122.692	8.984			122.217	9.111
ILE 166	121.863	8.215			121.278	8.089
LEU 167	125.152	8.484			124.088	8.406
ASP 168						

	Apo		SB203580-Bound		BIRB796-Bound	
Residue	^{15}N (ppm)	^{1}H (ppm)	^{15}N (ppm)	^{1}H (ppm)	^{15}N (ppm)	^{1}H (ppm)
PHE 169						
GLY 170					109.818	8.078
LEU 171						
ALA 172	119.232	8.09	119.209	8.102	119.59	8.071
ARG 173	116.995	8.424	117.027	8.426	120.797	8.04
HIS 174						
THR 175	115.494	7.321				
ASP 177	119.989	8.092	119.984	8.099		
GLU 178	120.433	8.124	120.481	8.127		
MET 179	119.823	8.149	119.855	8.139		
THR 180	113.886	7.94	113.724	7.934		
GLY 181	111.201	8.211	111.488	8.224		
TYR 182	120.786	7.87	120.835	7.896	121.001	7.888
VAL 183	123.125	7.811			123.169	7.736
ALA 184						
THR 185						
ARG 186						
TRP 187						
TYR 188						
ARG 189	122.419	7.35	122.443	7.344	122.35	7.358
ALA 190	126.08	8.853	125.567	8.972	126.131	8.866
GLU 192						
ILE 193						
MET 194						
LEU 195	126.488	9.212	126.274	9.215	126.498	9.219
ASN 196	115.24	7.893	115.178	7.881	115.31	7.902
TRP 197	125.08	8.582	124.895	8.536	124.959	8.6
MET 198	120.129	8.691	119.923	8.682	120.061	8.703
HIS 199	115.068	7.207				
TYR 200	126.788	10.114	126.883	10.089	127.289	10.315
ASN 201	124.787	8.78				
GLN 202	118.48	7.218			118.729	7.243
THR 203	115.388	8.358	115.477	8.367	115.376	8.355
VAL 204						
ASP 205						
ILE 206	119.19	7.285	119.364	7.331	119.332	7.286
TRP 207	120.778	7.519	120.904	7.503	120.948	7.53
SER 208	112.511	7.593	112.542	7.556	112.354	7.568

	Apo		SB203580-Bound		BIRB796-Bound	
Residue	^{15}N (ppm)	^{1}H (ppm)	^{15}N (ppm)	^{1}H (ppm)	^{15}N (ppm)	^{1}H (ppm)
VAL 209	119.838	8.009	119.874	8.005	120.023	7.987
GLY 210	110.176	8.512	110.345	8.532	110.141	8.492
CYS 211	119.201	7.89	119.309	7.885	119.126	7.861
ILE 212	124.145	8.44	124.25	8.454	123.827	8.406
MET 213	120.463	9.306	120.626	9.331	120.283	9.275
ALA 214	118.375	8.158	118.461	8.137	118.348	8.173
GLU 215	119.669	7.12	120.058	7.126	119.373	7.081
LEU 216	116.304	7.283	116.367	7.285	116.291	7.281
LEU 217	118.32	8.508	118.353	8.506	118.27	8.509
THR 218	105.961	7.964	105.98	7.956	105.954	7.96
GLY 219	112.584	8.416	112.876	8.491	112.431	8.375
ARG 220	119.037	8.02	119.19	8.035	119.038	8.02
THR 221	119.842	7.954	119.957	7.956	119.816	7.953
LEU 222	117.789	7.86	117.855	7.864	118.163	7.876
PHE 223						
GLY 225	113.546	8.357	113.597	8.36	113.623	8.357
THR 226	116.615	10.123	116.648	10.126	116.665	10.127
ASP 227	130.629	8.648	130.72	8.667	130.565	8.6
HIS 228	114.214	8.574	114.22	8.562	114.261	8.581
ILE 229						
ASP 230						
GLN 231						
LEU 232						
LYS 233						
LEU 234						
ILE 235						
LEU 236						
ARG 237	117.316	8.243				
LEU 238	117.728	7.627	117.736	7.62	117.806	7.608
VAL 239			107.743	8.229	107.672	8.214
GLY 240	113.142	8.152			113.12	8.156
THR 241						
GLY 243	108.622	8.309	108.62	8.315	108.684	8.303
ALA 244	121.283	8.377	121.388	8.383	121.46	8.376
GLU 245	116.35	8.608	116.262	8.611	116.349	8.563
LEU 246	120.434	7.485	120.512	7.487	120.407	7.477
LEU 247	118.013	7.874	117.952	7.875		
LYS 248						

	Apo		SB203580-Bound		BIRB796-Bound	
Residue	^{15}N (ppm)	^{1}H (ppm)	^{15}N (ppm)	^{1}H (ppm)	^{15}N (ppm)	^{1}H (ppm)
LYS 249			120.51	7.498		
ILE 250						
SER 251						
SER 252						
GLU 253						
SER 254	114.114	8.364				
ALA 255	125.676	7.714	125.665	7.722	125.685	7.705
ARG 256			125.497	9.23		
ASN 257						
TYR 258						
ILE 259						
GLN 260	118.107	8.1	118.128	8.119	118.039	8.096
SER 261	113.882	7.44	113.883	7.443	113.92	7.431
LEU 262						
THR 263						
GLN 264	126.745	8.541				
MET 265	124.211	8.694	124.315	8.703	124.215	8.694
LYS 267	120.372	8.285	120.409	8.291	120.37	8.282
MET 268	125.976	8.414	126.054	8.422	126.001	8.412
ASN 269	120.256	8.569	120.319	8.586	120.275	8.582
PHE 270	129.885	9.409	129.916	9.407	129.898	9.407
ALA 271	122.277	8.552	122.354	8.554	122.255	8.546
ASN 272	112.993	7.46	113.06	7.463	112.965	7.453
VAL 273	119.975	7.212	120.02	7.209	119.97	7.212
PHE 274	120.691	7.625	120.751	7.619	120.94	7.624
ILE 275	120.838	6.887	120.88	6.891	120.834	6.881
GLY 276	116.263	9.018	116.318	9.023	116.242	9.012
ALA 277	121.912	7.399	121.945	7.404	121.918	7.399
ASN 278	122.458	9.113	122.548	9.131	122.384	9.081
LEU 280	117.062	8.435	117.092	8.443	117.049	8.429
ALA 281	120.965	7.103	121.078	7.108	120.948	7.1
VAL 282	116.308	7.088	116.316	7.078	116.33	7.083
ASP 283	117.832	7.486	117.869	7.495	117.854	7.474
LEU 284	117.513	7.112	117.604	7.119	117.515	7.114
LEU 285	120.246	8.284				
GLU 286	117.418	7.968	117.269	8.009		
LYS 287	116.211	7.335	116.311	7.34	116.178	7.332
MET 288	118.262	7.569				

	Apo		SB203580-Bound		BIRB796-Bound	
Residue	^{15}N (ppm)	^{1}H (ppm)	^{15}N (ppm)	^{1}H (ppm)	^{15}N (ppm)	^{1}H (ppm)
LEU 289	118.914	7.841	118.849	7.881		
VAL 290						
LEU 291						
ASP 292						
SER 293						
ASP 294	120.913	8.458	121.06	8.484	120.984	8.479
LYS 295	117.429	7.636	117.551	7.622	117.4	7.651
ARG 296	122.422	7.056	122.824	7.075	122.423	7.048
ILE 297	125.032	7.09	124.98	7.006	124.881	7.059
THR 298	109.389	7.397	109.115	7.405	109.161	7.382
ALA 299	122.038	9.498	121.949	9.464	122.028	9.499
ALA 300	116.107	8.619	116.183	8.603	116.098	8.617
GLN 301	115.832	7.424	115.913	7.413	115.795	7.408
ALA 302	123.728	8.673	123.778	8.668	123.708	8.657
LEU 303	116.442	7.648	116.432	7.663	116.52	7.657
ALA 304	114.765	6.555	114.829	6.569	114.672	6.543
HIS 305	122.693	7.964	122.741	7.968	122.692	7.964
ALA 306	132.636	8.343	132.623	8.331	132.694	8.345
TYR 307						
PHE 308	110.39	7.669	110.48	7.671	110.404	7.678
ALA 309	123.434	7.522	123.444	7.517	123.477	7.523
GLN 310	114.006	8.671	114.046	8.663	113.966	8.674
TYR 311	115.987	7.513	116.14	7.509	115.939	7.501
HIS 312	115.898	7.811	116.098	7.807	115.832	7.82
ASP 313	125.029	7.584	125.084	7.545	124.931	7.526
ASP 315	117.274	7.944	117.485	7.975	117.222	7.94
ASP 316	121.2	8.037	121.24	8.025	121.304	8.037
GLU 317	121.456	7.766	121.739	7.831	121.602	7.801
VAL 319	109.141	7.868	109.396	7.878	108.796	7.854
ALA 320	123.478	8.441	123.665	8.415	123.49	8.506
ASP 321	120.91	8.099	120.923	8.107	120.988	8.075
TYR 323						
ASP 324	122.845	6.964	122.91	6.973	122.862	6.962
GLN 325						
GLU 328	114.81	9.912	114.933	9.964	114.549	9.865
SER 329	111.832	7.436	112.175	7.477	111.769	7.442
ARG 330	121.792	7.607	121.805	7.597	121.864	7.615
ASP 331	124.703	8.589	124.532	8.589	124.58	8.586

	Apo		SB203580-Bound		BIRB796-Bound	
Residue	^{15}N (ppm)	^{1}H (ppm)	^{15}N (ppm)	^{1}H (ppm)	^{15}N (ppm)	^{1}H (ppm)
LEU 332	123.015	7.835	123.152	7.844	123.085	7.829
LEU 333	119.762	8.782	119.914	8.803	119.849	8.792
ILE 334	121.681	8.979	121.748	8.995	121.766	8.989
ASP 335	115.76	8.401	116.058	8.383	115.745	8.386
GLU 336	120.419	7.103	120.544	7.125	120.447	7.117
TRP 337	119.669	7.698	119.619	7.707	119.479	7.71
LYS 338	121.384	8.764	121.313	8.772	121.407	8.756
SER 339	114.455	7.62	114.463	7.624	114.506	7.62
LEU 340	120.293	7.927	120.457	7.933	120.159	7.984
TYR 342	124.711	8.818	125.008	8.85	124.905	8.809
ASP 343	117.23	8.086	117.383	8.08	117.402	8.101
GLU 344	118.192	7.491	118.233	7.508	118.007	7.503
VAL 345	121.141	8.082	121.36	8.083	121.326	8.04
ILE 346	114.434	8.105	114.769	8.135	115.087	8.098
SER 347	113.182	7.397	113.153	7.43	112.795	7.418
PHE 348	124.884	7.283	124.914	7.314	124.961	7.308
VAL 349	130.056	6.901	130.008	6.943	130.262	6.938

Table D-2: ILV methyl assignments of p38α in the apo and inhibitor-bound states

	Apo		SB203580-Bound		BIRB796-Bound	
ID	^{13}C (ppm)	^{1}H (ppm)	^{13}C (ppm)	^{1}H (ppm)	^{13}C (ppm)	^{1}H (ppm)
LEU13CD1	23.109	0.142	22.858	0.165	22.732	0.243
LEU13CD2	21.266	0.584	21.342	0.573	21.544	0.553
ILE17CD	7.866	0.624	7.904	0.622	7.999	0.617
VAL20CG1	16.672	0.555	16.472	0.54	16.473	0.515
VAL20CG2	18.811	0.8	18.861	0.794	18.859	0.749
LEU27CD1	21.749	0.453	21.337	0.384	21.285	0.403
LEU27CD2	21.747	0.594	21.656	0.557	21.702	0.559
VAL30CG1	18.544	0.814	17.819	0.817	18.655	0.916
VAL30CG2	17.878	0.736	18.725	0.981		
VAL38CG1	18.865	0.746	19.26	0.501	18.299	0.797
VAL38CG2	18.54	0.687			18.585	0.676
LEU48CD1	22.003	0.698	22.202	0.768	22.262	0.73
LEU48CD2	19.698	0.789	19.635	0.88	20.489	0.921

	Apo		SB203580-Bound		BIRB796-Bound	
ID	^{13}C (ppm)	^{1}H (ppm)	^{13}C (ppm)	^{1}H (ppm)	^{13}C (ppm)	^{1}H (ppm)
VAL50CG1	19.455	0.641	18.885	0.585	19.286	0.63
VAL50CG2	15.642	0.512	15.527	0.491	15.652	0.5
VAL52CG1	19.586	0.958	19.428	0.964	19.718	0.953
VAL52CG2	17.503	0.415	17.028	0.4	17.001	0.443
LEU55CD1	22.883	0.674	22.636	0.647	22.446	0.573
LEU55CD2	19.99	0.638	19.938	0.605		
ILE62CD	10.951	1.135	10.839	1.151	10.857	1.149
ILE63CD	9.544	0.728	9.529	0.731	9.461	0.751
LEU72CD1	24.735	0.783	24.623	0.821	21.824	0.769
LEU72CD2	22.26	0.767	21.987	0.833	25.706	0.807
LEU74CD1	22.307	0.501	22.216	0.512	22.834	0.52
LEU74CD2	21.823	0.316			23.155	0.641
LEU75CD1	23.788	0.737	24.27	1.006	24.553	0.858
LEU75CD2	20.372	0.721	20.719	0.954	22.034	0.664
VAL83CG1	19.563	1.002	19.533	0.997	19.064	1.135
VAL83CG2	18.818	0.609	18.922	0.605	18.992	0.669
ILE84CD	11.498	0.992	12.837	0.719	10.783	-0.602
LEU86CD1	21.535	0.774	21.461	0.696	21.939	0.691
LEU86CD2	23.204	0.483	23.12	0.612	22.44	0.799
LEU87CD1	22.291	0.358	21.978	0.17	22.196	0.316
LEU87CD2	19.868	0.572	19.865	0.614	20.618	0.549
VAL89CG1	16.909	0.581	17.399	0.644	17.999	0.622
VAL89CG2	20.191	0.822	20.396	0.752	20.662	0.619
LEU96CD1	20.177	0.521	20.083	0.534	20.134	0.517
LEU96CD2	22.449	0.684	22.341	0.695	22.412	0.683
VAL102CG1	18.159	0.647	18.258	0.667	18.372	0.641
VAL102CG2	19.658	0.823	19.198	0.84	19.706	0.823
LEU104CD1	22.939	0.619			22.895	0.617
LEU104CD2	21.553	0.621			21.4	0.655
VAL105CG1	18.044	0.734	17.694	0.772	18.107	0.595
VAL105CG2	18.194	0.58	18.484	0.654		
LEU108CD1	20.328	0.778	24.039	0.9	23.504	0.732
LEU108CD2						
LEU113CD1	21.7	0.706	24.275	0.529	22.168	0.463
LEU113CD2	22.919	0.591	24.812	0.486	22.955	0.416
ILE116CD	8.787	0.569	9.064	0.569	8.696	0.575
VAL117CG1	18.494	0.872	18.363	0.883	18.475	0.865
VAL117CG2	19.251	0.892	19.317	0.897	19.095	0.882

	Apo		**SB203580-Bound**		**BIRB796-Bound**	
ID	**^{13}C (ppm)**	**^{1}H (ppm)**	**^{13}C (ppm)**	**^{1}H (ppm)**	**^{13}C (ppm)**	**^{1}H (ppm)**
LEU122CD1	23.854	0.705	23.707	0.707	23.84	0.707
LEU122CD2	19.94	0.479	20.051	0.496	19.887	0.473
VAL127CG1	19.612	1	19.543	0.998	20.742	0.928
VAL127CG2	20.805	0.922	20.684	0.917	19.573	1.003
LEU130CD1	23.823	0.668	23.4	0.705	23.943	0.682
LEU130CD2	21.459	0.612	22.074	0.64	21.557	0.625
ILE131CD	5.619	0.447	5.575	0.435	5.63	0.454
ILE134CD	11.611	0.514	11.497	0.486	11.429	0.522
LEU135CD1	25.862	0.538	25.739	0.539	25.899	0.547
LEU135CD2	19.346	0.627	19.305	0.61	19.897	0.644
LEU138CD1	24.037	0.497	24.03	0.489	23.928	0.515
LEU138CD2	18.905	0.517	18.801	0.527	18.983	0.563
ILE141CD	11.51	0.574			11.736	0.784
ILE146CD	10.091	0.394	10.067	0.489	10.061	0.502
ILE147CD	10.169	0.726	10.544	0.729	10.29	0.71
LEU151CD1	22.203	0.428				
LEU151CD2	22.744	0.319	22.641	0.734		
LEU156CD1	25.084	0.543			25.005	0.563
LEU156CD2	23.212	0.676	20.996	0.312	22.842	0.688
VAL158CG1	17.911	0.529	17.619	0.436	18.134	0.537
VAL158CG2	19.389	0.694	19.206	0.606	19.196	0.755
LEU164CD1	24.203	0.581	23.242	0.593	23.972	0.594
LEU164CD2	21.434	0.377	21.8	0.389	21.522	0.382
ILE166CD	11.216	0.69	10.764	0.621	11.721	0.742
LEU167CD1	21.538	0.715	18.8	0.756	24.578	0.311
LEU167CD2	22.807	0.754	21.461	0.696	20.542	0.513
LEU171CD1	22.295	0.537	22.492	0.385	23.611	0.837
LEU171CD2						
VAL183CG1	18.241	0.705	18.142	0.742	18.264	0.686
VAL183CG2	17.74	0.736			17.732	0.709
ILE193CD	8.802	0.366	8.709	0.401	8.727	0.354
LEU195CD1	20.075	0.739	19.939	0.748	20.03	0.749
LEU195CD2	22.076	0.84			22.134	0.857
ILE202CD						
VAL204CG1	19.746	1.185	19.762	1.196	19.823	1.175
VAL204CG2	16.963	1.074	16.996	1.078	17.022	1.057
ILE206CD	5.284	0.499	5.317	0.499	5.366	0.503
VAL209CG1	22.11	0.865	22.139	0.87	22.128	0.889

	Apo		SB203580-Bound		BIRB796-Bound	
ID	**^{13}C (ppm)**	**^{1}H (ppm)**	**^{13}C (ppm)**	**^{1}H (ppm)**	**^{13}C (ppm)**	**^{1}H (ppm)**
VAL209CG2	20.25	0.723	19.947	0.716	20.158	0.748
ILE212CD	10.2	0.175	9.998	0.138	10.206	0.205
LEU216CD1	19.888	0.847	19.877	0.851	19.832	0.847
LEU216CD2	23.542	0.411	23.434	0.411	23.519	0.412
LEU217CD1	23.319	0.723	23.406	0.737	23.466	0.717
LEU217CD2						
LEU222CD1	25.621	0.131	25.493	0.14	25.594	0.127
LEU222CD2	18.937	0.331	18.837	0.337	18.929	0.331
ILE229CD	7.743	0.443	7.698	0.449	7.71	0.436
LEU232CD1			22.818	0.623		
LEU232CD2						
ILE235CD	11.087	0.487	10.964	0.5	11.034	0.49
LEU236CD1	23.481	0.731				
LEU236CD2	20.021	0.701	19.986	0.698	19.937	0.715
LEU238CD1	21.054	0.504	20.965	0.507	21.028	0.503
LEU238CD2	23.648	0.638	23.581	0.641	23.602	0.639
VAL239CG1	19.563	1.332	19.468	1.344	19.533	1.334
VAL239CG2	16.772	1.181	16.629	1.189	16.764	1.189
LEU246CD1					22.764	0.74
LEU246CD2						
LEU247CD1	20.771	0.79	20.69	0.792	20.758	0.799
LEU247CD2						
ILE250CD						
ILE259CD	10.102	0.682	10.01	0.705	10.181	0.672
LEU262CD1	22.063	0.675	21.984	0.69	21.989	0.657
LEU262CD2	20.895	0.623	20.792	0.64	20.805	0.619
VAL273CG1	16.801	-0.26	16.694	-0.254	16.784	-0.257
VAL273CG2	18.507	0.574	18.422	0.582	18.487	0.579
ILE275CD	9.606	0.759	9.502	0.766	9.568	0.76
LEU280CD1	22.739	0.858	22.649	0.864	22.718	0.861
LEU280CD2	19.845	0.795	19.765	0.8	19.821	0.8
VAL282CG1	19.93	0.895	19.846	0.901	19.903	0.898
VAL282CG2	20.888	0.863	20.773	0.868	20.845	0.866
LEU284CD1	20.045	0.572	19.844	0.581	20.017	0.584
LEU284CD2	25.182	0.579	25.167	0.58	25.194	0.586
LEU285CD1	21.613	-0.19	21.492	-0.195	21.579	-0.187
LEU285CD2	21.899	0.432	21.789	0.441	21.879	0.434
LEU289CD1	23.71	0.399	23.6	0.41	23.728	0.4

	Apo		SB203580-Bound		BIRB796-Bound	
ID	^{13}C (ppm)	^{1}H (ppm)	^{13}C (ppm)	^{1}H (ppm)	^{13}C (ppm)	^{1}H (ppm)
LEU289CD2	19.108	-0.377	18.999	-0.374	19.056	-0.378
VAL290CG1	18.001	0.812	18.035	0.816	17.98	0.816
VAL290CG2	19.202	0.978	19.035	0.984	19.177	0.982
LEU291CD1						
LEU291CD2	21.268	0.682	21.04	0.682	21.246	0.696
ILE297CD	11.067	0.708	11.025	0.705	11.097	0.705
LEU303CD1	24.062	0.583	23.88	0.574	24.134	0.598
LEU303CD2	22.529	0.302	22.463	0.287	22.556	0.303
VAL319CG1	19.716	0.966	19.599	0.97	19.752	0.978
VAL319CG2	14.74	0.826	14.709	0.831	14.664	0.83
LEU332CD1	21.163	-0.829	21.117	-0.804	21.162	-0.823
LEU332CD2	19.193	0.342	19.123	0.349	19.192	0.342
LEU333CD1	22.495	0.822	22.389	0.834	22.476	0.826
LEU333CD2	19.291	0.83	19.439	0.822	19.281	0.834
ILE334CD	11.047	0.823	10.938	0.823	11.04	0.822
LEU340CD1	22.726	0.124	22.716	0.142	22.706	0.153
LEU340CD2	20.046	0.563	19.935	0.616	20.322	0.525
VAL345CG1	18.693	0.804	18.507	0.811		
VAL345CG2	20.198	1.009	20.129	1.027	20.442	1.001
ILE346CD	9.709	0.448	9.503	0.456	9.361	0.439
VAL349CG1	17.549	0.746	17.494	0.773	17.552	0.758
VAL349CG2	18.611	0.756	18.52	0.782	18.558	0.767

Table D-3: ILV Methyl Order Parameters of p38α in the apo and inhibitor-bound states

Residues which are spectrally resolved but not assigned are appended to the end of this table. They were included in the calculation of <O^2_{axis}> for the entropy meter.

ID	Apo	SB203580-Bound	BIRB796-Bound
	O^2_{axis}	O^2_{axis}	O^2_{axis}
LEU13CD1	0.441±0.005	0.391±0.012	0.345±0.046
LEU13CD2	0.323±0.016	0.287±0.013	
ILE17CD	0.162±0.051	0.171±0.056	0.158±0.052
VAL20CG1	0.56±0.021	0.622±0.01	0.762±0.03
VAL20CG2		0.734±0.018	
LEU27CD1	0.293±0.002	0.317±0.035	0.289±0.018

ID	**Apo**	**SB203580-Bound**	**BIRB796-Bound**
	O^2_{axis}	**O^2_{axis}**	**O^2_{axis}**
LEU27CD2	0.339±0.031	0.241±0.001	
VAL30CG1	0.317±0.012		0.385±0.035
VAL30CG2		0.576±0.011	
VAL38CG1		0.857±0.045	0.79±0.031
VAL38CG2	0.572±0.025		
LEU48CD1	0.552±0.001	0.65±0.026	
LEU48CD2	0.473±0.009	0.574±0.012	0.638±0.035
VAL50CG1			
VAL50CG2	0.784±0.04	0.832±0.016	0.818±0.025
VAL52CG1			
VAL52CG2	0.768±0.043	0.776±0.02	0.77±0.01
LEU55CD1	0.506±0.015	0.522±0.024	0.383±0.005
LEU55CD2			
ILE62CD	0.281±0.011	0.333±0.035	0.251±0.01
ILE63CD	0.162±0.051	0.231±0.037	
LEU72CD1	0.381±0.028		0.489±0.029
LEU72CD2	0.451±0.016	0.51±0.013	0.437±0.005
LEU74CD1	0.806±0.022	0.784±0.022	0.596±0.007
LEU74CD2	0.702±0.01		0.325±0.038
LEU75CD1		0.816±0.03	0.734±0.022
LEU75CD2		0.877±0.048	
VAL83CG1			0.971±0.031
VAL83CG2	0.792±0.016		0.83±0.017
ILE84CD	0.556±0.005		0.738±0.038
LEU86CD1	0.522±0.011	0.524±0.014	
LEU86CD2	0.61±0.026	0.411±0.027	0.558±0.025
LEU87CD1	0.469±0.002	0.487±0.005	0.443±0.005
LEU87CD2	0.546±0.027		0.463±0.005
VAL89CG1	0.548±0.016	0.526±0.02	0.357±0.01
VAL89CG2	0.5±0.033	0.369±0.03	0.349±0.032
LEU96CD1	0.616±0.025	0.586±0.023	0.622±0.023
LEU96CD2	0.604±0.021	0.586±0.021	0.58±0.017
VAL102CG1	0.395±0.012	0.425±0.002	0.415±0.013
VAL102CG2	0.417±0.016	0.485±0.007	0.562±0.013
LEU104CD1	0.514±0.006		0.491±0.007
LEU104CD2			0.648±0.004
VAL105CG1			
VAL105CG2	0.849±0.035	0.425±0.016	

ID	Apo	SB203580-Bound	BIRB796-Bound
	O^2_{axis}	O^2_{axis}	O^2_{axis}
LEU108CD1	0.421±0.022	0.81±0.025	0.696±0.037
LEU108CD2			
LEU113CD1		0.901±0.035	0.427±0.017
LEU113CD2	0.598±0.01	0.889±0.033	0.425±0.019
ILE116CD	0.231±0.031	0.219±0.012	0.303±0.017
VAL117CG1	0.313±0.018	0.269±0.012	0.333±0.036
VAL117CG2	0.371±0.044	0.413±0.028	0.427±0.037
LEU122CD1	0.469±0.011	0.385±0.034	0.487±0.043
LEU122CD2		0.465±0.046	
VAL127CG1	0.83±0.043		0.895±0.055
VAL127CG2		0.774±0.025	0.865±0.026
LEU130CD1	0.786±0.021	0.636±0.017	0.461±0.03
LEU130CD2		0.291±0.028	0.648±0.004
ILE131CD	0.616±0.031	0.642±0.032	0.626±0.028
ILE134CD			
LEU135CD1	0.959±0.036	0.889±0.026	0.961±0.053
LEU135CD2			
LEU138CD1	0.965±0.061	0.997±0.029	0.917±0.024
LEU138CD2	0.58±0.029	0.552±0.017	0.612±0.011
ILE141CD			0.686±0.023
ILE146CD			0.269±0.034
ILE147CD			0.662±0.033
LEU151CD1	0.766±0.032		0.887±0.021
LEU151CD2		0.604±0.028	
LEU156CD1	0.832±0.009		0.818±0.024
LEU156CD2	0.764±0.025	0.724±0.021	0.73±0.02
VAL158CG1	0.339±0.065		0.411±0.058
VAL158CG2	0.399±0.014	0.315±0.051	0.419±0.026
LEU164CD1		0.65±0.032	
LEU164CD2	0.67±0.029		0.343±0.064
ILE166CD			
LEU167CD1	0.467±0.014	0.518±0.015	0.516±0.038
LEU167CD2		0.997±0.05	
LEU171CD1	0.812±0.025		
LEU171CD2			0.766±0.016
VAL183CG1	0.361±0.033	0.409±0.036	0.419±0.055
VAL183CG2			0.413±0.046
ILE193CD			

ID	**Apo**	**SB203580-Bound**	**BIRB796-Bound**
	O^2_{axis}	**O^2_{axis}**	**O^2_{axis}**
LEU195CD1	0.814±0.022		
LEU195CD2		0.714±0.008	
ILE202CD			
VAL204CG1	0.997±0.064	0.997±0.049	0.997±0.068
VAL204CG2			
ILE206CD	0.425±0.002		0.489±0.014
VAL209CG1		0±0.006	
VAL209CG2			
ILE212CD	0.794±0.013	0.798±0.016	0.786±0.038
LEU216CD1	0.524±0.02	0.558±0.026	0.584±0.012
LEU216CD2			0.688±0.01
LEU217CD1		0.732±0.012	0.688±0.031
LEU217CD2			
LEU222CD1	0.837±0.051	0.826±0.016	0.863±0.051
LEU222CD2	0.65±0.018	0.764±0.029	0.702±0.028
ILE229CD	0.415±0.047	0.441±0.019	0.429±0.034
LEU232CD1		0.614±0.014	
LEU232CD2			
ILE235CD			
LEU236CD1			
LEU236CD2	0.778±0.021		0.62±0.029
LEU238CD1	0.64±0.029	0.678±0.027	0.658±0.019
LEU238CD2	0.808±0.031	0.889±0.027	0.837±0.022
VAL239CG1	0.865±0.009	0.863±0.023	0.857±0.014
VAL239CG2	0.76±0.019	0.708±0.028	0.784±0.021
LEU246CD1			0.596±0.017
LEU246CD2			0.497±0.024
LEU247CD1	0.512±0.035	0.371±0.025	
LEU247CD2			
ILE250CD			
ILE259CD	0.437±0.003	0.423±0.001	
LEU262CD1		0.584±0.03	
LEU262CD2	0.361±0.026	0.389±0.008	
VAL273CG1	0.674±0.028	0.65±0.014	0.702±0.012
VAL273CG2	0.758±0.014	0.75±0.017	0.732±0.011
ILE275CD	0.164±0.059	0.124±0.083	
LEU280CD1	0.612±0.021	0.6±0.01	0.628±0.018
LEU280CD2	0.473±0.035	0.445±0.032	0.508±0.039

ID	Apo	SB203580-Bound	BIRB796-Bound
	O^2_{axis}	O^2_{axis}	O^2_{axis}
VAL282CG1	0.788±0.041	0.61±0.019	0.788±0.028
VAL282CG2	0.746±0.013	0.718±0.023	0.8±0.025
LEU284CD1			
LEU284CD2	0.835±0.03	0.837±0.033	0.843±0.028
LEU285CD1	0.558±0.024	0.55±0.019	0.572±0.019
LEU285CD2		0.554±0.018	0.548±0.029
LEU289CD1	0.74±0.009	0.704±0.027	0.694±0.021
LEU289CD2	0.722±0.028		0.738±0.012
VAL290CG1	0.736±0.013		0.698±0.013
VAL290CG2	0.323±0.02	0.297±0.035	0.317±0.046
LEU291CD1			
LEU291CD2	0.808±0.03	0.794±0.019	0.676±0.021
ILE297CD		0.72±0.02	0.832±0.028
LEU303CD1		0.804±0.028	
LEU303CD2	0.744±0.023	0.758±0.017	0.744±0.023
VAL319CG1			
VAL319CG2	0.977±0.033	0.997±0.025	0.917±0.019
LEU332CD1	0.774±0.016	0.744±0.032	0.79±0.015
LEU332CD2	0.624±0.014	0.594±0.027	0.61±0.018
LEU333CD1	0.614±0.018	0.58±0.025	0.604±0.027
LEU333CD2	0.481±0.019	0.489±0.027	0.495±0.024
ILE334CD	0.333±0.055	0.265±0.056	0.331±0.05
LEU340CD1	0.652±0.019	0.6±0.041	0.686±0.013
LEU340CD2			0.495±0.055
VAL345CG1			
VAL345CG2	0.845±0.02	0.893±0.039	0.853±0.022
ILE346CD	0.391±0.038	0.419±0.013	0.379±0.041
VAL349CG1	0.07±0.062	0.058±0.047	0.05±0.059
VAL349CG2	0.092±0.046	0.064±0	0.06±0.049
UNASS	0.508±0.028	0.542±0.014	0.461±0.011
UNASS	0.997±0.044		0.656±0.004
UNASS			0.5±0.042
UNASS			0.853±0.046
UNASS			0.351±0.033
UNASS			0.51±0.006
UNASS			0.632±0.035
UNASS			0.526±0.009

BIBLIOGRAPHY

1. Koshland, D.E., *Application of a Theory of Enzyme Specificity to Protein Synthesis.* Proceedings of the National Academy of Sciences of the United States of America, 1958. **44**(2): p. 98-104.
2. Lichtenthaler, F.W., *100 Years Schlussel-Schloss-Prinzip - What Made Fischer,Emil Use This Analogy.* Angewandte Chemie-International Edition, 1994. **33**(23-24): p. 2364-2374.
3. Ma, B.Y., et al., *Folding funnels and binding mechanisms.* Protein Engineering, 1999. **12**(9): p. 713-720.
4. Keskin, O., et al., *Principles of protein-protein interactions: what are the preferred ways for proteins to interact?* Chem Rev, 2008. **108**(4): p. 1225-44.
5. Janin, J., R.P. Bahadur, and P. Chakrabarti, *Protein-protein interaction and quaternary structure.* Q Rev Biophys, 2008. **41**(2): p. 133-80.
6. England, J.L., *Statistical physics of self-replication.* Journal of Chemical Physics, 2013. **139**(12).
7. Velazquez-Campoy, A., S.A. Leavitt, and E. Freire, *Characterization of protein-protein interactions by isothermal titration calorimetry.* Methods Mol Biol, 2015. **1278**: p. 183-204.
8. Tanford, C., *The hydrophobic effect and the organization of living matter.* Science, 1978. **200**(4345): p. 1012-8.
9. Harpole, K.W. and K.A. Sharp, *Calculation of configurational entropy with a Boltzmann-quasiharmonic model: the origin of high-affinity protein-ligand binding.* J Phys Chem B, 2011. **115**(30): p. 9461-72.
10. Frederick, K.K., et al., *Conformational entropy in molecular recognition by proteins.* Nature, 2007. **448**(7151): p. 325-329.
11. Wand, A.J., *The dark energy of proteins comes to light: conformational entropy and its role in protein function revealed by NMR relaxation.* Curr Opin Struct Biol, 2013. **23**(1): p. 75-81.
12. Wand, A.J., V.R. Moorman, and K.W. Harpole, *A surprising role for conformational entropy in protein function.* Top Curr Chem, 2013. **337**: p. 69-94.
13. Tzeng, S.R. and C.G. Kalodimos, *Protein activity regulation by conformational entropy.* Nature, 2012. **488**(7410): p. 236-240.
14. Karplus, M., T. Ichiye, and B.M. Pettitt, *Configurational Entropy of Native Proteins.* Biophysical Journal, 1987. **52**(6): p. 1083-1085.
15. Henzler-Wildman, K. and D. Kern, *Dynamic personalities of proteins.* Nature, 2007. **450**(7172): p. 964-72.
16. Igumenova, T.I., K.K. Frederick, and A.J. Wand, *Characterization of the fast dynamics of protein amino acid side chains using NMR relaxation in solution.* Chem Rev, 2006. **106**(5): p. 1672-99.
17. Jarymowycz, V.A. and M.J. Stone, *Fast time scale dynamics of protein backbones: NMR relaxation methods, applications, and functional consequences.* Chem Rev, 2006. **106**(5): p. 1624-71.
18. Dyson, H.J. and P.E. Wright, *Unfolded proteins and protein folding studied by NMR.* Chem Rev, 2004. **104**(8): p. 3607-22.
19. Kay, L.E., *NMR studies of protein structure and dynamics - a look backwards and forwards.* Journal of Magnetic Resonance, 2011. **213**(2): p. 492-4.
20. Palmer, A.G., *NMR characterization of the dynamics of biomacromolecules.* Chemical Reviews, 2004. **104**(8): p. 3623-3640.
21. Lipari, G. and A. Szabo, *Model-Free Approach to the Interpretation of Nuclear Magnetic-Resonance Relaxation in Macromolecules .1. Theory and Range of Validity.* Journal of the American Chemical Society, 1982. **104**(17): p. 4546-4559.
22. Kasinath, V., K.G. Valentine, and A.J. Wand, *A 13C labeling strategy reveals a range of aromatic side chain motion in calmodulin.* J Am Chem Soc, 2013. **135**(26): p. 9560-3.

23. Sharp, K.A., et al., *On the relationship between NMR-derived amide order parameters and protein backbone entropy changes.* Proteins: Structure, Function, and Bioinformatics, 2015. **83**(5): p. 922-930.
24. Muhandiram, D.R., et al., *Measurement of 2H T1 and T1.rho. Relaxation Times in Uniformly 13C-Labeled and Fractionally 2H-Labeled Proteins in Solution.* Journal of the American Chemical Society, 1995. **117**(46): p. 11536-11544.
25. Tugarinov, V. and L.E. Kay, *Quantitative 13C and 2H NMR relaxation studies of the 723-residue enzyme malate synthase G reveal a dynamic binding interface.* Biochemistry, 2005. **44**(49): p. 15970-7.
26. Lee, A.L. and A.J. Wand, *Microscopic origins of entropy, heat capacity and the glass transition in proteins.* Nature, 2001. **411**(6836): p. 501-4.
27. Sharp, K.A., V. Kasinath, and A.J. Wand, *Banding of NMR-derived methyl order parameters: Implications for protein dynamics.* Proteins, 2014.
28. Li, Z.G., S. Raychaudhuri, and A.J. Wand, *Insights into the local residual entropy of proteins provided by NMR relaxation.* Prot. Sci., 1996. **5**(12): p. 2647-2650.
29. Yang, D.W. and L.E. Kay, *Contributions to conformational entropy arising from bond vector fluctuations measured from NMR-derived order parameters: Application to protein folding.* Journal of Molecular Biology, 1996. **263**(2): p. 369-382.
30. Marlow, M.S., et al., *The role of conformational entropy in molecular recognition by calmodulin.* Nat. Chem. Biol., 2010. **6**(5): p. 352-358.
31. Hilser, V.J., et al., *A statistical thermodynamic model of the protein ensemble.* Chem Rev, 2006. **106**(5): p. 1545-58.
32. Krushelnitsky, A., D. Reichert, and K. Saalwachter, *Solid-state NMR approaches to internal dynamics of proteins: from picoseconds to microseconds and seconds.* Acc Chem Res, 2013. **46**(9): p. 2028-36.
33. Vugmeyster, L., et al., *Slow motions in the hydrophobic core of chicken villin headpiece subdomain and their contributions to configurational entropy and heat capacity from solid-state deuteron NMR measurements.* Biochemistry, 2011. **50**(49): p. 10637-46.
34. Agarwal, V., et al., *Protein side-chain dynamics as observed by solution- and solid-state NMR spectroscopy: a similarity revealed.* J Am Chem Soc, 2008. **130**(49): p. 16611-21.
35. Tamura, A., et al., *Dynamics of the three methionyl side chains of Streptomyces subtilisin inhibitor. Deuterium NMR studies in solution and in the solid state.* Protein Sci, 1996. **5**(1): p. 127-39.
36. Dunbrack, R.L., Jr., *Sequence comparison and protein structure prediction.* Curr Opin Struct Biol, 2006. **16**(3): p. 374-84.
37. Hughes, J.P., et al., *Principles of early drug discovery.* Br J Pharmacol, 2011. **162**(6): p. 1239-49.
38. Michel, J., *Current and emerging opportunities for molecular simulations in structure-based drug design.* Phys Chem Chem Phys, 2014. **16**(10): p. 4465-77.
39. Anderson, A.C., *The process of structure-based drug design.* Chem Biol, 2003. **10**(9): p. 787-97.
40. Ewing, T.J., et al., *DOCK 4.0: search strategies for automated molecular docking of flexible molecule databases.* J Comput Aided Mol Des, 2001. **15**(5): p. 411-28.
41. Zoete, V., A. Grosdidier, and O. Michielin, *Docking, virtual high throughput screening and in silico fragment-based drug design.* J Cell Mol Med, 2009. **13**(2): p. 238-48.
42. Davis, A.M. and S.J. Teague, *Hydrogen bonding, hydrophobic interactions, and failure of the rigid receptor hypothesis.* Angewandte Chemie-International Edition, 1999. **38**(6): p. 737-749.
43. Mobley, D.L. and K.A. Dill, *Binding of Small-Molecule Ligands to Proteins: "What You See" Is Not Always "What You Get".* Structure, 2009. **17**(4): p. 489-498.
44. Baron, R. and J.A. McCammon, *Molecular recognition and ligand association.* Annu Rev Phys Chem, 2013. **64**: p. 151-75.

45. Stone, J.E., et al., *GPU-accelerated molecular modeling coming of age.* Journal of Molecular Graphics & Modelling, 2010. **29**(2): p. 116-125.
46. Gilli, P., et al., *Enthalpy-Entropy Compensation in Drug-Receptor Binding.* Journal of Physical Chemistry, 1994. **98**(5): p. 1515-1518.
47. Sharp, K., *Entropy-enthalpy compensation: Fact or artifact?* Protein Science, 2001. **10**(3): p. 661-667.
48. Lafont, V., et al., *Compensating enthalpic and entropic changes hinder binding affinity optimization.* Chem Biol Drug Des, 2007. **69**(6): p. 413-22.
49. Ladbury, J.E., G. Klebe, and E. Freire, *Adding calorimetric data to decision making in lead discovery: a hot tip.* Nature Reviews Drug Discovery, 2010. **9**(1): p. 23-7.
50. Freire, E., *A thermodynamic approach to the affinity optimization of drug candidates.* Chem Biol Drug Des, 2009. **74**(5): p. 468-72.
51. Chaires, J.B., *Calorimetry and thermodynamics in drug design.* Annu Rev Biophys, 2008. **37**: p. 135-51.
52. Freire, E., *Do enthalpy and entropy distinguish first in class from best in class?* Drug Discovery Today, 2008. **13**(19-20): p. 869-874.
53. Kasinath, V., K.A. Sharp, and A.J. Wand, *Microscopic insights into the NMR relaxation-based protein conformational entropy meter.* J Am Chem Soc, 2013. **135**(40): p. 15092-100.
54. Gabel, F., et al., *Protein dynamics studied by neutron scattering.* Q. Rev. Biophys., 2002. **35**: p. 327–367.
55. Wood, K., et al., *Protein surface and core dynamics show concerted hydration-dependent activation.* Angew Chem Int Ed Engl, 2013. **52**(2): p. 665-8.
56. Bazari, W.L., et al., *Villin sequence and peptide map identify six homologous domains.* Proc Natl Acad Sci U S A, 1988. **85**(14): p. 4986-90.
57. McKnight, C.J., P.T. Matsudaira, and P.S. Kim, *NMR structure of the 35-residue villin headpiece subdomain.* Nat Struct Biol, 1997. **4**(3): p. 180-4.
58. Duan, Y., L. Wang, and P.A. Kollman, *The early stage of folding of villin headpiece subdomain observed in a 200-nanosecond fully solvated molecular dynamics simulation.* Proc Natl Acad Sci U S A, 1998. **95**(17): p. 9897-902.
59. Vugmeyster, L., et al., *Temperature-dependent dynamics of the villin headpiece helical subdomain, an unusually small thermostable protein.* J Mol Biol, 2002. **320**(4): p. 841-54.
60. Tang, Y., et al., *Peptide models provide evidence for significant structure in the denatured state of a rapidly folding protein: the villin headpiece subdomain.* Biochemistry, 2004. **43**(11): p. 3264-72.
61. Chiu, T.K., et al., *High-resolution x-ray crystal structures of the villin headpiece subdomain, an ultrafast folding protein.* Proc Natl Acad Sci U S A, 2005. **102**(21): p. 7517-22.
62. Tang, Y., M.J. Goger, and D.P. Raleigh, *NMR characterization of a peptide model provides evidence for significant structure in the unfolded state of the villin headpiece helical subdomain.* Biochemistry, 2006. **45**(22): p. 6940-6.
63. Reiner, A., P. Henklein, and T. Kiefhaber, *An unlocking/relocking barrier in conformational fluctuations of villin headpiece subdomain.* Proc Natl Acad Sci U S A, 2010. **107**(11): p. 4955-60.
64. Urbanek, D.C., et al., *The Two Dimensional Vibrational Echo of a Nitrile Probe of the Villin HP35 Protein.* J Phys Chem Lett, 2010. **1**: p. 3311-3315.
65. Beauchamp, K.A., et al., *Quantitative comparison of villin headpiece subdomain simulations and triplet-triplet energy transfer experiments.* Proc Natl Acad Sci U S A, 2011. **108**(31): p. 12734-9.
66. Vugmeyster, L. and D. Ostrovsky, *Temperature dependence of fast carbonyl backbone dynamics in chicken villin headpiece subdomain.* J Biomol NMR, 2011. **50**(2): p. 119-27.
67. Serrano, A.L., O. Bilsel, and F. Gai, *Native state conformational heterogeneity of HP35 revealed by time-resolved FRET.* J Phys Chem B, 2012. **116**(35): p. 10631-8.

68. Piana, S., K. Lindorff-Larsen, and D.E. Shaw, *Protein folding kinetics and thermodynamics from atomistic simulation.* Proc Natl Acad Sci U S A, 2012. **109**(44): p. 17845-50.
69. Meng, W., et al., *Native like structure in the unfolded state of the villin headpiece helical subdomain, an ultrafast folding protein.* Protein Sci, 2009. **18**(8): p. 1692-701.
70. Vugmeyster, L. and C.J. McKnight, *Slow motions in chicken villin headpiece subdomain probed by cross-correlated NMR relaxation of amide NH bonds in successive residues.* Biophys J, 2008. **95**(12): p. 5941-50.
71. Hu, K.N., et al., *Quantitative determination of site-specific conformational distributions in an unfolded protein by solid-state nuclear magnetic resonance.* J Mol Biol, 2009. **392**(4): p. 1055-73.
72. Havlin, R.H. and R. Tycko, *Probing site-specific conformational distributions in protein folding with solid-state NMR.* Proc Natl Acad Sci U S A, 2005. **102**(9): p. 3284-9.
73. Song, X.J., et al., *Temperature dependence of fast dynamics in proteins.* Biophys J, 2007. **92**(6): p. L43-5.
74. Sabo, T.M., et al., *Thermal coefficients of the methyl groups within ubiquitin.* Protein Sci, 2012. **21**(4): p. 562-70.
75. Mittermaier, A. and L.E. Kay, *Measurement of methyl H-2 quadrupolar couplings in oriented proteins. How uniform is the quadrupolar coupling constant?* J. Am. Chem. Soc., 1999. **121**(45): p. 10608-10613.
76. Ming, D.M. and R. Bruschweiler, *Prediction of methyl-side chain dynamics in proteins.* Journal of Biomolecular Nmr, 2004. **29**(3): p. 363-368.
77. Chevelkov, V., et al., *Comparison of solid-state dipolar couplings and solution relaxation data provides insight into protein backbone dynamics.* J Am Chem Soc, 2010. **132**(14): p. 5015-7.
78. Li, D.W. and R. Bruschweiler, *NMR-based protein potentials.* Angew. Chem. Intl. Ed., 2010. **49**(38): p. 6778-6780.
79. Li, D.W. and R. Bruschweiler, *Certification of molecular dynamics trajectories with NMR chemical shifts.* J. Phys. Chem. Lett., 2010. **1**(1): p. 246-248.
80. Krishnan, M. and J.C. Smith, *Reconstruction of protein side-chain conformational free energy surfaces from NMR-derived methyl axis order parameters.* J. Phys. Chem. B, 2012. **116**: p. 4124−4133.
81. Krushelnitsky, A., et al., *13C and 15N NMR study of the hydration response of T4 lysozyme and alphaB-crystallin internal dynamics.* J Phys Chem B, 2009. **113**(29): p. 10022-34.
82. Nakagawa, H., et al., *Hydration affects both harmonic and anharmonic nature of protein dynamics.* Biophys J, 2008. **95**(6): p. 2916-23.
83. Roh, J.H., et al., *Influence of hydration on the dynamics of lysozyme.* Biophys J, 2006. **91**(7): p. 2573-88.
84. Zhou, H.X. and M.K. Gilson, *Theory of free energy and entropy in noncovalent binding.* Chem. Rev., 2009. **109**(9): p. 4092-107.
85. Steinberg, I.Z. and H.A. Scheraga, *Entropy changes accompanying association reactions.* J. Biol. Chem., 1963. **238**: p. 172-181.
86. Wodak, S.J. and J. Janin, *Structural basis of macromolecular recognition.* Adv. Protein. Chem., 2002. **61**: p. 9-73.
87. Clackson, T. and J.A. Wells, *A hot spot of binding energy in a hormone-receptor interface.* Science, 1995. **267**(5196): p. 383-6.
88. Welch, G.R., B. Somogyi, and S. Damjanovich, *The role of protein fluctuations in enzyme action: A review.* Prog. Biophys. Molec. Biol., 1982. **39**: p. 109-146.
89. Cooper, A. and D.T.F. Dryden, *Allostery without conformational change - a plausible model.* Eur. Biophys. J. Biophys. Lett., 1984. **11**(2): p. 103-109.
90. Gilson, M.K., et al., *The statistical-thermodynamic basis for computation of binding affinities: A critical review.* Biophys. J., 1997. **72**(3): p. 1047-1069.

91. Luo, H. and K. Sharp, *On the calculation of absolute macromolecular binding free energies.* Proc Natl Acad Sci U S A, 2002. **99**(16): p. 10399-10404.
92. Singh, N. and A. Warshel, *A comprehensive examination of the contributions to the binding entropy of protein-ligand complexes.* Proteins, 2010. **78**(7): p. 1724-35.
93. Sturtevant, J.M., *Heat-capacity and entropy changes in processes involving proteins.* Proc. Natl Acad. Sci. USA, 1977. **74**(6): p. 2236-2240.
94. Hilser, V.J., et al., *A statistical thermodynamic model of the protein ensemble.* Chem. Rev., 2006. **106**(5): p. 1545-58.
95. Akke, M., R. Bruschweiler, and A.G. Palmer, *NMR order parameters and free-energy - an analytical approach and Its application to cooperative Ca2+ binding by calbindin-D(9k).* J. Am. Chem. Soc., 1993. **115**(21): p. 9832-9833.
96. Kasinath, V., K.A. Sharp, and A.J. Wand, *Microscopic Insights into the NMR relaxation-based protein conformational entropy meter.* J. Am. Chem. Soc., 2013. **135**(40): p. 15092-15100.
97. Leavitt, S. and E. Freire, *Direct measurement of protein binding energetics by isothermal titration calorimetry.* Curr Opin Struct Biol, 2001. **11**(5): p. 560-6.
98. Ben-Naim, A. and Y. Marcus, *Solvation thermodynamics of nonionic solutes.* J. Chem. Phys., 1984. **81**(4): p. 2016-2027.
99. Makhatadze, G.I. and P.L. Privalov, *Contributions of hydration to protein-folding thermodynamics. 1. The enthalpy of hydration.* J. Mol. Biol., 1993. **232**(2): p. 639-659.
100. Marcus, Y., *A simple empirical model describing the thermodynamics of hydration of ions of widely varying charges, sizes, and shapes.* Biophys. Chem., 1994. **51**(2-3): p. 111-127.
101. Prabhu, N.V. and K.A. Sharp, *Heat capacity in proteins.* Annu. Rev. Phys. Chem., 2005. **56**: p. 521-48.
102. Sabo, T.M., et al., *Thermal coefficients of the methyl groups within ubiquitin.* Protein Sci., 2012. **21**(4): p. 562-70.
103. Wintrode, P.L. and P.L. Privalov, *Energetics of target peptide recognition by calmodulin: a calorimetric study.* J Mol Biol, 1997. **266**(5): p. 1050-62.
104. Igumenova, T.I., A.L. Lee, and A.J. Wand, *Backbone and side chain dynamics of mutant calmodulin-peptide complexes.* Biochemistry, 2005. **44**(38): p. 12627-39.
105. Cohen, P., *The origins of protein phosphorylation.* Nat Cell Biol, 2002. **4**(5): p. E127-30.
106. Adams, J.A., *Kinetic and catalytic mechanisms of protein kinases.* Chem Rev, 2001. **101**(8): p. 2271-90.
107. Xiao, Y., et al., *Dynamics of protein kinases: insights from nuclear magnetic resonance.* Acc Chem Res, 2015. **48**(4): p. 1106-14.
108. Taylor, S.S. and A.P. Kornev, *Protein kinases: evolution of dynamic regulatory proteins.* Trends Biochem Sci, 2011. **36**(2): p. 65-77.
109. Kornev, A.P., S.S. Taylor, and L.F. Ten Eyck, *A helix scaffold for the assembly of active protein kinases.* Proc Natl Acad Sci U S A, 2008. **105**(38): p. 14377-82.
110. Huse, M. and J. Kuriyan, *The conformational plasticity of protein kinases.* Cell, 2002. **109**(3): p. 275-82.
111. Xiao, Y., et al., *Phosphorylation releases constraints to domain motion in ERK2.* Proc Natl Acad Sci U S A, 2014. **111**(7): p. 2506-11.
112. Masterson, L.R., et al., *Dynamics connect substrate recognition to catalysis in protein kinase A.* Nat Chem Biol, 2010. **6**(11): p. 821-8.
113. Henzler-Wildman, K.A., et al., *Intrinsic motions along an enzymatic reaction trajectory.* Nature, 2007. **450**(7171): p. 838-44.
114. Zhang, P., et al., *Structure and allostery of the PKA RIIbeta tetrameric holoenzyme.* Science, 2012. **335**(6069): p. 712-6.
115. McClendon, C.L., et al., *Dynamic architecture of a protein kinase.* Proc Natl Acad Sci U S A, 2014. **111**(43): p. E4623-31.
116. Cohen, P. and D.R. Alessi, *Kinase drug discovery--what's next in the field?* ACS Chem Biol, 2013. **8**(1): p. 96-104.

117. Meharena, H.S., et al., *Deciphering the structural basis of eukaryotic protein kinase regulation.* PLoS Biol, 2013. **11**(10): p. e1001680.
118. Zarubin, T. and J. Han, *Activation and signaling of the p38 MAP kinase pathway.* Cell Res, 2005. **15**(1): p. 11-8.
119. Kumar, S., J. Boehm, and J.C. Lee, *p38 map kinases: Key signalling molecules as therapeutic targets for inflammatory diseases.* Nature Reviews Drug Discovery, 2003. **2**(9): p. 717-726.
120. Barnes, P.J., *New anti-inflammatory targets for chronic obstructive pulmonary disease.* Nature Reviews Drug Discovery, 2013. **12**(7): p. 543-559.
121. Quan, L.D., et al., *The development of novel therapies for rheumatoid arthritis.* Expert Opinion on Therapeutic Patents, 2008. **18**(7): p. 723-738.
122. Hanks, S.K. and T. Hunter, *Protein Kinases .6. The Eukaryotic Protein-Kinase Superfamily - Kinase (Catalytic) Domain-Structure and Classification.* Faseb Journal, 1995. **9**(8): p. 576-596.
123. Wang, Z., et al., *Structural basis of inhibitor selectivity in MAP kinases.* Structure, 1998. **6**(9): p. 1117-28.
124. Pargellis, C., et al., *Inhibition of p38 MAP kinase by utilizing a novel allosteric binding site.* Nat Struct Biol, 2002. **9**(4): p. 268-72.
125. Vogtherr, M., et al., *NMR characterization of kinase p38 dynamics in free and ligand-bound forms.* Angew Chem Int Ed Engl, 2006. **45**(6): p. 993-7.
126. Casper, D., M. Bukhtiyarova, and E.B. Springman, *A Biacore biosensor method for detailed kinetic binding analysis of small molecule inhibitors of p38alpha mitogen-activated protein kinase.* Anal Biochem, 2004. **325**(1): p. 126-36.
127. Kroe, R.R., et al., *Thermal denaturation: A method to rank slow binding, high-affinity p38 alpha MAP kinase inhibitors.* Journal of Medicinal Chemistry, 2003. **46**(22): p. 4669-4675.
128. Privalov, P.L. and G.I. Makhatadze, *Contribution of Hydration to Protein-Folding Thermodynamics .2. The Entropy and Gibbs Energy of Hydration.* Journal of Molecular Biology, 1993. **232**(2): p. 660-679.
129. Francis, D.M., et al., *Structural basis of p38alpha regulation by hematopoietic tyrosine phosphatase.* Nat Chem Biol, 2011. **7**(12): p. 916-24.
130. Tokunaga, Y., et al., *Allosteric enhancement of MAP kinase p38alpha's activity and substrate selectivity by docking interactions.* Nat Struct Mol Biol, 2014. **21**(8): p. 704-11.
131. Hyberts, S.G., et al., *Application of iterative soft thresholding for fast reconstruction of NMR data non-uniformly sampled with multidimensional Poisson Gap scheduling.* Journal of Biomolecular Nmr, 2012. **52**(4): p. 315-327.
132. Sprangers, R. and L.E. Kay, *Quantitative dynamics and binding studies of the 20S proteasome by NMR.* Nature, 2007. **445**(7128): p. 618-22.
133. Sinha, K., L. Jen-Jacobson, and G.S. Rule, *Divide and conquer is always best: sensitivity of methyl correlation experiments.* Journal of Biomolecular Nmr, 2013. **56**(4): p. 331-5.
134. Chang, C.I., et al., *Crystal structures of MAP kinase p38 complexed to the docking sites on its nuclear substrate MEF2A and activator MKK3b.* Mol Cell, 2002. **9**(6): p. 1241-9.
135. Lakomek, N.A., J.F. Ying, and A. Bax, *Measurement of N-15 relaxation rates in perdeuterated proteins by TROSY-based methods.* Journal of Biomolecular Nmr, 2012. **53**(3): p. 209-221.
136. Wang, Z., et al., *The structure of mitogen-activated protein kinase p38 at 2.1-A resolution.* Proc Natl Acad Sci U S A, 1997. **94**(6): p. 2327-32.
137. Nielsen, G., et al., *Kinase in motion: insights into the dynamic nature of p38alpha by high-pressure NMR spectroscopic studies.* Chembiochem, 2013. **14**(14): p. 1799-806.
138. Aoto, P.C., et al., *Accurate scoring of non-uniform sampling schemes for quantitative NMR.* Journal of Magnetic Resonance, 2014. **246**: p. 31-35.
139. Kneller, J.M., M. Lu, and C. Bracken, *An effective method for the discrimination of motional anisotropy and chemical exchange.* J Am Chem Soc, 2002. **124**(9): p. 1852-3.

140. Aragon, S., *A precise boundary element method for macromolecular transport properties.* Journal of Computational Chemistry, 2004. **25**(9): p. 1191-1205.
141. Aragon, S. and D.K. Hahn, *Precise boundary element computation of protein transport properties: Diffusion tensors, specific volume, and hydration.* Biophys J, 2006. **91**(5): p. 1591-603.
142. Bae, S.H., H.J. Dyson, and P.E. Wright, *Prediction of the rotational tumbling time for proteins with disordered segments.* J Am Chem Soc, 2009. **131**(19): p. 6814-21.
143. Garcia de la Torre, J., M.L. Huertas, and B. Carrasco, *HYDRONMR: prediction of NMR relaxation of globular proteins from atomic-level structures and hydrodynamic calculations.* Journal of Magnetic Resonance, 2000. **147**(1): p. 138-46.
144. Mauldin, R.V., M.J. Carroll, and A.L. Lee, *Dynamic dysfunction in dihydrofolate reductase results from antifolate drug binding: modulation of dynamics within a structural state.* Structure, 2009. **17**(3): p. 386-94.
145. DeLorbe, J.E., et al., *Thermodynamic and structural effects of conformational constraints in protein-ligand interactions. Entropic paradoxy associated with ligand preorganization.* J Am Chem Soc, 2009. **131**(46): p. 16758-70.
146. Gomez, J., et al., *The heat capacity of proteins.* Proteins, 1995. **22**(4): p. 404-12.
147. Bi, Y., et al., *Efficient high level expression of peptides and proteins as fusion proteins with the N-terminal domain of L9: application to the villin headpiece helical subdomain.* Protein Expr Purif, 2006. **47**(1): p. 234-40.
148. Marley, J., M. Lu, and C. Bracken, *A method for efficient isotopic labeling of recombinant proteins.* J Biomol NMR, 2001. **20**(1): p. 71-5.
149. Sattler, M., J. Schleucher, and C. Griesinger, *Heteronuclear multidimensional NMR experiments for the structure determination of proteins in solution employing pulsed field gradients.* Progress in Nuclear Magnetic Resonance Spectroscopy, 1999. **34**(2): p. 93-158.
150. Sklenar, V., *Suppression of Radiation Damping in Multidimensional Nmr Experiments Using Magnetic-Field Gradients.* J. Magn. Reson. A, 1995. **114**(1): p. 132-135.
151. O'Connell, N.E., et al., *Partially folded equilibrium intermediate of the villin headpiece HP67 defined by 13C relaxation dispersion.* J Biomol NMR, 2009. **45**(1-2): p. 85-98.
152. Millet, O., et al., *Deuterium spin probes of side-chain dynamics in proteins. 1. Measurement of five relaxation rates per deuteron in (13)C-labeled and fractionally (2)H-enriched proteins in solution.* J Am Chem Soc, 2002. **124**(22): p. 6439-48.
153. Rahi, S.J. and K. Sharp, *Mapping complicated surfaces onto a sphere.* Int. J. Comp. Geo. Appl., 2007. **17**(04): p. 305-329.
154. Cho, C.H., et al., *Thermal offset viscosities of liquid H2O, D2O, and T2O.* J. Phys. Chem. B, 1999. **103**(11): p. 1991-1994.
155. Dellwo, M.J. and A.J. Wand, *Model-independent and model-dependent analysis of the global and internal dynamics of cyclosporine-A.* J. Am. Chem. Soc., 1989. **111**(13): p. 4571-4578.
156. Moorman, V.R., K.G. Valentine, and A.J. Wand, *The dynamical response of hen egg white lysozyme to the binding of a carbohydrate ligand.* Protein Sci, 2012. **21**(7): p. 1066-73.
157. Phillips, J.C., et al., *Scalable molecular dynamics with NAMD.* J Comput Chem, 2005. **26**(16): p. 1781-802.
158. Brooks, B.R., et al., *CHARMM: the biomolecular simulation program.* J Comput Chem, 2009. **30**(10): p. 1545-614.
159. Jorgensen, W.L., et al., *Comparison of Simple Potential Functions for Simulating Liquid Water.* Journal of Chemical Physics, 1983. **79**(2): p. 926-935.
160. Humphrey, W., A. Dalke, and K. Schulten, *VMD: Visual molecular dynamics.* J. Mol. Graph. Model., 1996. **14**(1): p. 33-38.

161. Ryckaert, J.P., G. Ciccotti, and H.J.C. Berendsen, *Numerical-Integration of Cartesian Equations of Motion of a System with Constraints - Molecular-Dynamics of N-Alkanes.* J. Comp. Phys., 1977. **23**(3): p. 327-341.
162. Kranz, J.K., et al., *A direct test of the reductionist approach to structural studies of calmodulin activity: relevance of peptide models of target proteins.* J. Biol. Chem., 2002. **277**(19): p. 16351-4.
163. Finerty, P.J., Jr., R. Muhandiram, and J.D. Forman-Kay, *Side-chain dynamics of the SAP SH2 domain correlate with a binding hot spot and a region with conformational plasticity.* J. Mol. Biol., 2002. **322**(3): p. 605-20.
164. Bhabha, G., et al., *Identification of endogenous ligands bound to bacterially expressed human and E. coli dihydrofolate reductase by 2D NMR.* FEBS Lett., 2011. **585**(22): p. 3528-32.
165. Ishima, R., et al., *Comparison of methyl rotation axis order parameters derived from model-free analyses of* ^{2}H *and* ^{13}C *longitudinal and transverse relaxation rates measured in the same protein sample.* J. Am. Chem. Soc., 2001. **123**(25): p. 6164-6171.
166. Moorman, V.R., et al., *Dynamic and thermodynamic response of the Ras protein Cdc42Hs upon association with the effector domain of PAK3.* J Mol Biol, 2014. **426**(21): p. 3520-38.
167. Bailey, S., *The CCP4 suite - programs for protein crystallography.* Acta. Cryst. D Biol. Cryst., 1994. **50**: p. 760-763.
168. Diehl, C., et al., *Protein flexibility and conformational entropy in ligand design targeting the carbohydrate recognition domain of galectin-3.* J Am Chem Soc, 2010. **132**(41): p. 14577-89.
169. Garcia-Hernandez, E., et al., *Structural energetics of protein-carbohydrate interactions: Insights derived from the study of lysozyme binding to its natural saccharide inhibitors.* Protein Science, 2003. **12**(1): p. 135-142.
170. Petit, C.M., et al., *Hidden dynamic allostery in a PDZ domain.* Proc Natl Acad Sci U S A, 2009. **106**(43): p. 18249-54.
171. Schnell, J.R., H.J. Dyson, and P.E. Wright, *Effect of cofactor binding and loop conformation on side chain methyl dynamics in dihydrofolate reductase.* Biochemistry, 2004. **43**(2): p. 374-83.
172. Fuentes, E.J., C.J. Der, and A.L. Lee, *Ligand-dependent dynamics and intramolecular signaling in a PDZ domain.* Journal of Molecular Biology, 2004. **335**(4): p. 1105-1115.
173. Milev, S., et al., *Energetics of peptide recognition by the second PDZ domain of human protein tyrosine phosphatase 1E.* Biochemistry, 2007. **46**(4): p. 1064-78.
174. Kozlov, G., et al., *Solution structure of the PDZ2 domain from cytosolic human phosphatase hPTP1E complexed with a peptide reveals contribution of the beta2-beta3 loop to PDZ domain-ligand interactions.* J Mol Biol, 2002. **320**(4): p. 813-20.
175. Marlow, M.S., et al., *The role of conformational entropy in molecular recognition by calmodulin.* Nature Chem. Biol., 2010. **6**(5): p. 352-358.
176. Wintrode, P.L., G.I. Makhatadze, and P.L. Privalov, *Thermodynamics of ubiquitin unfolding.* Proteins, 1994. **18**(3): p. 246-53.
177. Hyberts, S.G., et al., *Perspectives in magnetic resonance: NMR in the post-FFT era.* Journal of Magnetic Resonance, 2014. **241**: p. 60-73.